GENERAL ATOMIC

GA-A13815
UC-77

GAS-COOLED FAST BREEDER REACTOR

QUARTERLY PROGRESS REPORT

FOR THE PERIOD NOVEMBER 1, 1975 THROUGH January 31, 1976

by

Project Staff

Prepared under
Contract E(04-3)-167
Project Agreement No. 23
for the
San Francisco Operations Office
U.S. Energy Research and Development Administration

General Atomic Project 3228

Date Published: March 22, 1976

[redacted]

PROGRESS REPORT SERIES

GA-5537	November 1, 1963 to July 31, 1964
GA-6667	August 1, 1964 to July 31, 1965
GA-7645	August 1, 1965 to July 31, 1966
GA-8107	August 1, 1966 to July 31, 1967
GA-8787	August 1, 1967 to July 31, 1968
GA-8895	August 1, 1968 through October 31, 1968
GA-9229	November 1, 1968 through January 31, 1969
GA-9359	February 1, 1969 through April 30, 1969
GA-9639	May 1, 1969 through July 31, 1969
GA-9811	August 1, 1969 through October 31, 1969
GA-9838	November 1, 1969 through January 31, 1970
GA-10517	February 1, 1970 through January 31, 1971
GA-10645	February 1, 1971 through April 30, 1971
GA-A10803	May 1, 1971 through July 31, 1971
GA-A10906	August 1, 1971 through October 31, 1971
GA-A12003	November 1, 1971 through January 31, 1972
GA-A12252	May 1, 1972 through July 31, 1972
GA-A12421	August 1, 1972 through October 31, 1972
GA-A12530	November 1, 1972 through January 31, 1973
GA-A12728	May 1, 1973 through July 31, 1973
GA-A12824	August 1, 1973 through October 31, 1973
GA-A12894	November 1, 1973 through January 31, 1974
GA-A13021	February 1, 1974 through April 30, 1974
GA-A13148	May 1, 1974 through July 31, 1974
GA-A13238	August 1, 1974 through October 31, 1974
GA-A13379	November 1, 1974 through January 31, 1975
GA-A13458	February 1, 1975 through April 30, 1975
GA-A13565	May 1, 1975 through July 31, 1975
GA-A13766	August 1, 1975 through October 31, 1975

ABSTRACT

The tasks of the gas-cooled fast breeder reactor (GCFR) program that are supported by the U.S. Energy Research and Development Administration include development of GCFR fuel, blanket, and control elements; development of the pressure equalization system for GCFR fuel; out-of-pile loop facility test program planning; fuels and materials development; fuel, blanket, and control rod analyses and development; nuclear analysis and reactor physics for GCFR core design; shielding requirements for the GCFR; reactor engineering to assess the thermal, hydraulic, and structural performance of the core and the core support structure; plant systems control; development of reactor components, including reactor vessel, control and locking mechanisms, fuel handling equipment, core support structure, shielding assemblies, main helium circulator, steam generator, and auxiliary circulator; development of a helium circulator test facility; and reactor safety, including an in-pile safety evaluation program.

CONTENTS

FIGURES

FIGURES (Continued)

FIGURES (Continued)

FIGURES (Continued)

TABLES

TABLES (Continued)

TABLES (Continued)

TABLES (Continued)

I. INTRODUCTION

The various tasks of the gas-cooled fast breeder reactor (GCFR) program for the period November 1, 1975 through January 31, 1976 sponsored by the U.S. Energy Research and Development Administration (ERDA) are discussed in this quarterly progress report. The GCFR utility program, which is supported by a large number of electric utility companies, rural electric cooperatives, and General Atomic, is primarily directed toward the development of a GCFR demonstration plant. The utility-sponsored work and the ERDA-sponsored work are complementary.

Analytical, experimental, and fabrication development is being accomplished under the core element development task to establish the basis for the design of GCFR fuel, blanket, and control element assemblies. Analytical methods development for structural and thermal-hydraulic analyses is discussed, and the results of structural analysis of the fuel assembly components and thermal-hydraulic analysis of the blanket element during low power are presented. Current progress on rod spacer interaction tests, fuel element seismic and vibration test planning, and development of assembly fabrication techniques is also presented. The various subtasks of core element development and the work accomplished during this reporting period are discussed in Section II.

The technology to support the design and construction of the pressure equalization system for GCFR fuel is being developed. This includes (1) the development of analytical models and computer codes that will be verified by test programs and testing of materials and seals and (2) the development of fabrication processes for the pressure equalization system. These are discussed in Section III.

To demonstrate the ability of GCFR fuel, control, and blanket assembly designs to meet design goals and verify predictions of analytical models, a series of out-of-pile simulation tests will be performed. The emphasis of the tests will be on obtaining thermal-structural data for steady-state, transient, and margin conditions using electrically heated rod bundles in a dynamic helium loop. These are discussed in Section IV.

In the fuels and materials development program, thermal flux and fast flux irradiation programs are being conducted to establish conditions and design features specific to GCFR fuel rods, such as vented fuel, fission product traps, and surface-roughened cladding. In addition, a test program of smooth and surface-roughened GCFR cladding specimens is being conducted to determine how materials behave under irradiation. The fuels and materials tests, the analytical studies, and the results to date are presented in Section V.

Under the fuel rod engineering task, performance of the fuel and blanket rods under steady-state and transient conditions is being evaluated to determine performance characteristics, operating limits, and design criteria. In addition, surveillance of the fuel rod and blanket rod technology of other programs is being carried out. These studies are presented in Section VI.

The objectives of the nuclear analysis and reactor physics task are to verify and validate the nuclear design methods which will be applied to the GCFR core design. A critical experiments program is being carried out on the ZPR-9 facility at Argonne National Laboratory for this purpose. Critical assembly design, analysis, and methods development are discussed in Section VII.

Verification of the physics and engineering analytical methods and the data for design of the GCFR shields is being conducted under the shielding requirements task along with an evaluation of the effectiveness of various shield configurations. The results of radial shield analyses and the work being done on structural analysis are presented in Section VIII.

To assess the thermal-hydraulic performance of the GCFR reactor core, analytical methods and models are being developed and utilized to define operating strategies. These, together with the development of GCFR plant control systems and an evaluation of the capability of the PCRV internal structures to provide postaccident fuel containment, are discussed in Section IX.

Section X presents the evaluation and development of the main components of the GCFR which are currently in progress, including reactor vessel, control and locking mechanisms, fuel handling, core support structure, shielding assemblies, main helium circulator, steam generator, and auxiliary circulator.

Development of a test facility for qualification testing of the main helium circulator is discussed in Section XI. This task includes the responsibility for (1) evaluation studies of alternative test facility concepts, (2) preparation of specifications for the selected facility, and (3) final design, construction, and checkout of the facility.

The objective of the reactor safety task, which is discussed in Section XII, is to study the safety aspects of the GCFR using logical probabilistic methods to determine the probabilities associated with accident initiation and progression sequences.

The gas reactor in-pile safety test (GRIST) program is being studied as a potential follow-on to the analytical and experimental programs covering design basis accidents. The objective of the GRIST program is to provide information related to beyond-design-basis accidents, particularly the behavior of melted cladding and fuel. Progress in test assembly analysis and design is discussed in Section XIII.

II. CORE-ELEMENT DEVELOPMENT (189a No. SU006)

2.1. FUEL- AND CONTROL-ASSEMBLIES ANALYSIS

The analytical basis, in conjunction with experimental evaluation, for the design and development of the GCFR fuel and control assemblies is being developed. Because complete prototype in-pile tests cannot be conducted, a strong analytical base supported by development tests is required to design the core assemblies. The current emphasis is on developing an adequate steady-state and transient analysis capability and performing both thermal-hydraulic and structural steady-state and transient analyses in order to provide a basis for the assembly design criteria and for specific test requirements.

During the previous quarterly period, the programming of the first-order, outer temperatures in FLOMAX was completed, the subchannel temperatures were compared with COBRA results, and the programming of the first-order, outer flow rates was initiated. Formal inner solutions were obtained for the complete thermal-hydraulic problem, but the coding of these solutions was not begun. The thermal-hydraulic analyses for that period included the calculation of subchannel and rod surface temperatures in an assembly with a dilated duct, and the determination of assembly pressure drops by hand calculations and with the COBRA code. The dilation resulted in increased thermal gradients across the edge rods of the assembly. The hand calculations of assembly pressure drops were found to give results comparable with COBRA and the CALIOP core systems code.

During the present quarterly period the subroutine for calculating the first-order, outer flow rates in FLOMAX was developed, with some debugging still in progress. The chopped cosine power distribution was incorporated in the code, and preparations were begun for programming

the inner solutions. The thermal-hydraulic analysis for this period concentrated on a more accurate determination of the effect of the rod-to-duct spacing of the fuel assembly. Using the rough-rod data from the Swiss Federal Institute as a basis, a calculational scheme was developed, but further analysis is required for this complicated problem.

2.1.1. Development of the Rod-Bundle Thermal-Hydraulic Analysis Code FLOMAX

The primary mathematical problem of rod-bundle codes is to determine for each subchannel i, and as a function of the axial coordinate x, the mass velocities $G_i(x)$, and pressures $P_i(x)$, and the temperatures $T_i(x)$. In FLOMAX this is done by expanding these variables into the asymptotic series,

$$G_i(x) \sim G_{oi} + \mu G_{1i}(x) + \nu g_i(\xi) \quad ,$$

$$P_i(x) \sim P_o(x) + \mu P_1(x) + \pi p_i(\xi) \quad , \tag{1}$$

$$T_i(x) \sim T_o(x) + \mu T_{1i}(x) + \tau t_i(\xi) + \mu^2 T_{2i}(x) \quad ,$$

where the upper case letters denote what are called outer solutions (valid away from spacers and transitions), and the lower case letters denote the inner solutions (valid near the spacers and transitions). The Greek letters denote small parameters, and the stretched coordinate is $\xi = x/\varepsilon$. Previously the functions G_{oi}, P_o, T_o and T_{1i} were obtained. During this quarter the coefficients of the functions G_{1i} and P_1 were determined. In FLOMAX the above functions are determined analytically as a linear combination of functions $F_\beta(x)$ related to the axial power functions $\psi_\beta(x)$. For example, the first-order velocities, G_{1i}, and pressures, P_{1i}, were programmed as

$$G_{1i}(x) = \sum_\beta A_{i\beta} F_\beta(x) \quad ,$$

and

$$P_1(x) = \sum_{\beta} B_\beta F_\beta(x) \quad .$$

It is the coefficients $A_{i\beta}$ and B_β which have been determined; work is now in progress to combine these coefficients with the functions, as shown above.

Previously, the sequence of functions built into FLOMAX was a polynomial:

$$\psi_\beta(x) = x^{(\beta-1)} \quad , \qquad \beta = 1, 2, 3, \cdots$$

During this quarter, the code was expanded to include the common chopped cosine function:

$$\psi(\eta) = a \cos \omega(2\eta-1) \quad , \tag{2}$$

where η is the normalized axial coordinate, which has the range 0-1 over the length of the fueled section of the assembly; the parameter, a, is the axial peaking factor of the power distribution, which is specified by the user; the parameter ω is determined in the code by requiring the integral of $\psi(\eta)$ over the fueled section to be equal to one. With

$$\int_0^1 \psi(\eta)d\eta = 1 \quad ,$$

there results the transcendental equation to solve for ω: $a \sin \omega = \omega$. By plotting this equation, it was found to be well approximated by the function $\omega^o = 1.9(a-1)^{0.38}$; a closer approximation to the root is determined in FLOMAX by Newton-Raphson iteration: $\omega^1 = \omega^o - (a \sin \omega^o - \omega^o)/(a \cos \omega^o - 1)$.

In the last quarterly report,[1] the subchannel temperatures were calculated for a uniform axial power distribution for the case of two adjoining subchannels. This calculation was repeated this quarter with

the chopped cosine power distribution, and the results are shown in Fig. 2.1 in comparison with COBRA calculations. The FLOMAX results include the functions $T_o(x)$ and $T_{1i}(x)$, and it can be seen that there is good agreement between the results, except near x/L = 0. Better agreement will be obtained near x/L = 0 with the programming of the $t_i(\xi)$ solutions. Near x/L = 1, improved agreement would require the programming of the $T_{2i}(x)$ solution, but this is planned only as a code improvement task subsequent to user experience with the code. As discussed in the last quarterly report, the subchannel temperatures are sensitive to uncertainties in the turbulent mixing factors, and the $T_{2i}(x)$ functions may not yield a substantially better solution in the practical sense.

Preparation for the inner solutions $g_i(\xi)$, $p_i(\xi)$, and $t_i(\xi)$ was initiated this quarter by programming the input required for the spacer locations, and by reworking the output routine to include the additional solutions. In the code, the user will specify the desired number of axial printing positions between the spacers and the axial location of the spacers; the code then divides the spacer/spacer interval in equal parts and constructs and prints the solution at these axial increments. The logic for accomplishing this output printing was completed, but further development is required as the inner solutions become available. During the next quarter, the debugging of the outer solutions will be completed and the programming of the inner solution will be started.

2.1.2. Thermal-Hydraulic Analysis

One of the most important aspects of the GCFR fuel assembly analysis is the flow and temperature relationship between the side and central subchannels of the rod bundle. Failure to have an appropriate relationship may result in excessive rod temperature gradients and resulting rod bowing and grid spacer loads. An appropriate relationship may be obtained by design of the duct-to-rod spacing, but first the consequences of the spacing must be determined analytically. In the last quarterly report, an approximate analysis was done to determine the effect of duct dilation.

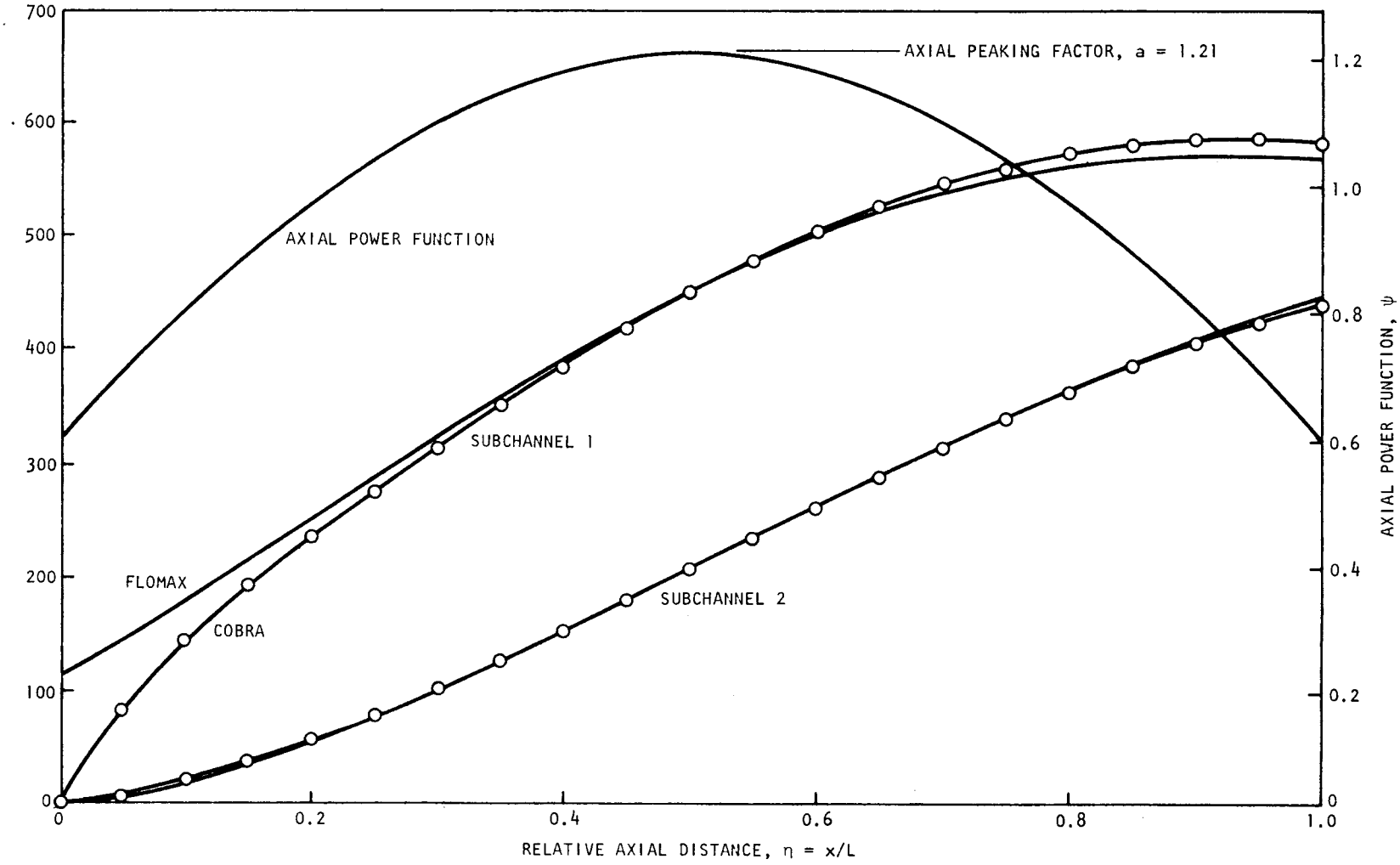

Fig. 2.1 Comparison of FLOMAX outer subchannel temperatures and COBRA results for a chopped cosine power distribution

During this quarter, a more accurate analysis was begun to determine the appropriate friction factors and Stanton numbers for the side subchannels.

Presently the analysis can only be done with the COBRA code, which is limited to three types of subchannels in the roughened section of the rod bundle; these types are the center, side, and corner subchannels, as bounded by the heavy lines in Fig. 2.2. In the side subchannel in particular, there will be a significant variation in flows and temperatures and, therefore, it is desirable to subdivide this subchannel into sub-subchannels as indicated by the four annulus-segments in the figures. These segments should really be treated as individual subchannels, as they will be in the FLOMAX code; but because of the limitation of the COBRA code, the friction factors and Stanton numbers for each segment must be combined into single functions for the whole side subchannel.

In each of the sub-subchannel segments shown in Fig. 2.2, the friction factors f, and Stanton numbers St, will be different functions of the Reynolds number Re, because the rod surface exhibits different effective, or relative, roughnesses in these segments. Each annulus segment is bounded by a rough surface ($r = r_1$) and either a smooth surface ($r = r_2$) or a symmetry surface ($r = r_o$). In segments 3 and 4 the equivalent symmetry radius of zero shear stress r_o is known and f and St can be obtained from the transformation of the basic annulus experiments with roughened rods, which have been performed at the Swiss Federal Institute (EIR) as part of a cooperative program with GA. In segments 1 and 2, r_2 is known instead of r_o, which lies somewhere between r_1 and r_2; and f and St must be determined from the inverse transformation of transformed results. After f^i and St^i were obtained for each sub-subchannel i, they were then combined into f^s and St^s functions for the entire side subchannel.

The basic data obtained from the EIR experiments of a roughened rod in a smooth tube were transformed using a simple method based on equal axial pressure drops near r_1 and r_2. The effect of this transformation is to separate at $r = r_o$ the effect of the smooth surface at $r = r_2$ from

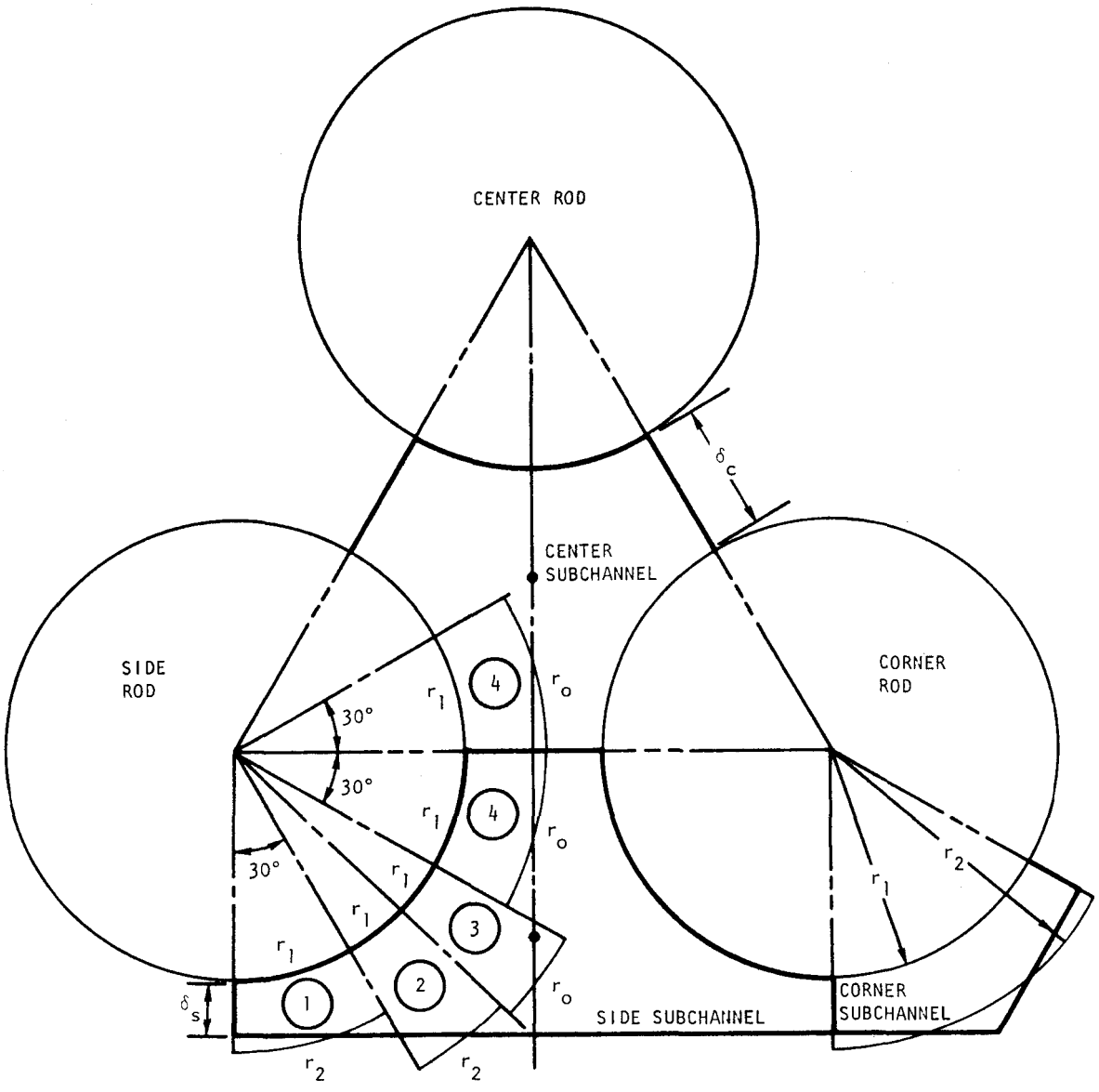

Fig. 2.2 Layout of center, side, and corner subchannels and sub-subchannel divisions of the side subchannel

the effect of the rough surface at $r = r_1$, such that the results will be applicable to segments 3 and 4. If the subscripts 1 and 2 denote the quantities associated with the rough and smooth surfaces, respectively, then the transformation equation can be written as follows:

$$Re_1 = Re\ \phi(\varepsilon_1) \quad , \qquad f_1 = f\ \phi(\varepsilon_1) \quad ,$$

$$Re_2 = Re\ \psi(\varepsilon_1) \quad , \qquad f_2 = f\ \psi(\varepsilon_1) \quad , \tag{3}$$

$$f_1 = g(re_1, \varepsilon_1) \quad , \qquad f_2 = h(re_2) \quad ,$$

where ε_1 is the effective, or relative, roughness which depends on r_o and where ϕ, ψ, and h are known functions. In the forward transformation, f and Re are known from the experimental data, but g is unknown, and an explicit formula was derived at EIR to determine the transformed data f_1, Re_1, and ε_1. The transformed Stanton number was determined from a simple formula from the literature: $St_1 = St\ \theta(Re_1, f_1)$. To apply these data to segments 3 and 4, least-squares curve fits were made to obtain the functions g and k:

$$f_1 = g(Re_1, \varepsilon_1) \quad , \qquad St_1 = k(Re_1, \varepsilon_1) \quad . \tag{4}$$

Since ε_1 is known for segments 3 and 4, e.g., $\varepsilon_1 = \varepsilon^i$, then f^i and St^i are as follows:

$$f^i = g(Re^i, \varepsilon^i) \quad , \qquad St^i = k(Re^i, \varepsilon^i) \quad , \qquad i = 3, 4 \quad . \tag{5}$$

These curve fits, or correlations, were required because Re^i and ε^i of the analysis did not correspond to Re_1 and ε_1 of the experiments.

In the inverse transformation g is a known function, but f is unknown. To obtain the unknowns f_1, Re_1, f_2, Re_2, f, and ε_1 from the above six equations, the equations were combined into the following single function of ε_1:

$$F(\varepsilon_1) \equiv \psi(\varepsilon_1)g(Re\phi(\varepsilon_1),\varepsilon_1) - \phi(\varepsilon_1)h(Re\psi(\varepsilon_1)) = 0$$

Given the total annulus Reynolds number, Re, $F(\varepsilon_1) = 0$ was solved by Newton-Raphson iteration, with the new ε_1's given by

$$\varepsilon_1^n = \varepsilon_1^o - F(\varepsilon_1^o)/F'(\varepsilon_1^o) \quad ,$$

where the derivative is given by

$$F'(\varepsilon_1) = \psi'g + \psi(\phi' Re \frac{\partial g}{\partial Re_1} + \frac{\partial g}{\partial \varepsilon_1}) - \phi'h - \phi h'\psi' Re \quad .$$

This scheme converged very well, and with ε_1 known from solving $F(\varepsilon_1) = 0$, f, Re, and St were determined from Eqs (3), etc. Thus, for segments 1 and 2, the functions p and q were determined:

$$f^i = p(Re^i, r_2^i) \quad , \quad St^i = q(Re^i, r_2^i) \quad , \quad i = 1, 2 \quad . \tag{6}$$

This rather involved process of transformation-correlation-inverse transformation is still under development; it is required because the roughness rib height and r_2^i, etc., of the GCFR design studies do not, and cannot, correspond to the values of the EIR experiments.

For the analysis, each of segments 1 to 4 should be treated as individual subchannels. In COBRA this is not presently possible, and the above results must be combined. For the friction factors, combining was done by assuming equal pressure drops for the i = 1, 2, 3, 4 segments. For the Stanton numbers, a function was derived to produce an average rough surface temperature for the four segments. Finally, curve fits were made of these functions in the forms

$$f = x_1 + x_2 Re^{x_3} \quad ,$$

$$Nu = x_4 + x_5 Re^{x_6} \quad ,$$

which are appropriate for COBRA input. The Nusselt number was taken as $Nu = St \cdot Re \cdot Pr$, with $Pr = 0.7$.

The above correlations are presently being used with COBRA to study the effect of the rod-to-duct spacing (δ_s in Fig. 2.2). For small δ_s's the ε^i's for $i = 1$ are much larger than the ε_1's of the EIR experiments, and large extrapolations of the data are necessary. This requires further study of the best forms of the functions g and k to ensure correct behavior in the extrapolated region, and this study is now in progress. The COBRA code needs further development to simplify the application of the above type of roughness functions. In the FLOMAX development, sufficient latitude will be provided to include a wide class of roughness functions and arbitrary subchannel divisions.

2.1.3. Distortion Analysis

During the previous quarterly reporting period it was shown that the dilation of the duct of the fuel assembly could lead to significant temperature gradients across the peripheral rods of the assembly, resulting in the distortion of these rods. During this quarter, the effect of the duct-to-rod spacing (whether produced by dilation or as a design variable) was analyzed further. By adjusting the spacing and determining the rod temperature gradients with the COBRA code, it was found that approximately a 40% spacing ($\delta_s = 0.4\ \delta_c$ in Fig. 2.2) gave the minimum gradients across the side rods; however, the gradient across the corner rods was increased. Among other reasons, the fact that the gradients of the side and corner rods are in opposite directions led to changing the corner rods from fuel rods to grid-spacer support rods.

With the corner rods as support rods instead of fuel rods, a further analysis with COBRA was done to determine the best support rod diameter to use. The preliminary results indicated that a 10-mm rod would be appropriate when including gamma heating in the rod and in the duct (by comparison, the fuel-rod diameter is 7.2 mm). The values of the duct-to-rod spacing and the support rod diameter are very preliminary, and further analysis will be done using the methods described in Section 2.1.2.

2.1.4. Hot-Spot Factors for the GCFR Fuel Element

The hot-spot factors that have been used previously in GCFR analyses were revised, and an extensive list of parameters that contribute to the hot-spot factors in the GCFR fuel element has been drawn up (Table 2.1). The uncertainties of the parameters were classified into two types: (1) spatially statistical, and (2) temporally statistical and non-random. Each parameter was analyzed according to this classification and for the effect it has on the coolant temperature rise and the temperature gradients across the film, cladding, cladding-to-fuel gap, and the fuel. Subfactors f define these effects quantitatively and are used for their respective temperature drops as shown by the general equation $\partial\Delta T_\beta = f_\beta \Delta T$, where $\partial\Delta T_\beta$ is the contribution of the parameter β on the coolant, and where ΔT is the nominal coolant temperature rise. These subfactors will be combined by a semi-statistical method to obtain the overall hot-spot factors. The hot-spot factors will be used as multipliers for their respective temperature drops, e.g.,

$$T = T_i + F_c \Delta T_c$$

where T = coolant hot spot temperature,

T_i = coolant inlet temperature,

ΔT_c = coolant nominal temperature rise,

F_c = coolant hot spot factors.

2.2. BLANKET ASSEMBLY ANALYSIS

The purpose of this task is to develop and verify the analytical techniques for blanket assembly analyses. These analytical techniques will be applied to obtain preliminary and final designs of the blanket assembly and to determine the design margin requirements. The task includes the thermal-hydraulic, structural, and dynamic analyses and the evaluation of handling and shipping of the blanket assembly.

Table 2.1

HOT-SPOT FACTORS FOR THE GCFR FUEL ELEMENT

	Coolant	Film	Cladding	Gap	Film
Statistical Components					
Fuel rod pitch	X	X			
Grid spacer tolerances	X	X			
Bowing	X	X			
Cladding outside diameter	X	X			
Cladding thickness			X		
Cladding swelling (and duct swelling)	X	X	X		
Fuel pellet diameter	X	X	X	X	X
Fuel density, Fuel enrichment } fuel fissile content	X	X	X	X	X
Fuel eccentricity			X		
Orifice tolerance	X	X			
Non-Random Cumulative Components					
Specific heat of coolant	X	X			
Density of coolant	X	X			
Specific heat of cladding			X		
Density of cladding			X		
Conductivity of cladding			X		
Specific heat of fuel					X
Conductivity of fuel					X
Film heat transfer coefficient		X			
Gap heat transfer coefficient				X	
Friction factor correlation	X	X			
Axial peaking factor	X	X	X	X	X
Radial peaking factor	X	X	X	X	X
Core blanket shift	X	X	X	X	X
Control-rod peaking	X	X	X	X	X
New-to-average power	X	X	X	X	X
γ-heating	X				
Coolant inlet temperature[a]	X	X			
Coolant flow rate	X	X			
Inlet flow maldistribution	X	X			
Bundle mixing	X	X			
Pressure drop calculations	X	X			
Power measurement and system deadband	X	X	X	X	X

[a]In addition to affecting the coolant and film temperature gradients, this uncertainty directly raises the temperatures of all the five components.

During the previous quarterly reporting period, a sizing study for the blanket assembly, and thermal-hydraulic and structural analyses for the blanket assembly were initiated.

Thermal-hydraulic analysis of the radial blanket assembly was continued. An evaluation of the proposed design compared to the reference design was continued and a new configuration and management scheme for the radial blanket were proposed, reviewed, and approved.

2.2.1. Thermal-Hydraulic Analysis

2.2.1.1. Circumferential Variation of Mid-Wall Cladding Temperature in the Radial Blanket.

As discussed in Ref. 1, a small pitch/diameter ratio is desirable in the GCFR radial blanket assembly. However, for rod bundles with small pitch/diameter ratios, the local heat transfer coefficients vary considerably around the periphery of the rod.

The effect of circumferential variation of heat transfer coefficients on the mid-wall cladding temperature was analyzed with a two-dimensional conduction code. The model used in the analysis is shown in Fig. 2.3. A conservative estimate of the variation of local heat transfer coefficient for the hottest rod in the assembly was obtained from Ref. 2. The analysis shows that when the average ($\sim$4000 $W/m^2 \cdot °C$) to minimum heat transfer coefficient varied by a factor of 1.8, the temperature drop between bulk fluid to mid-wall cladding temperature varied by a factor of 1.18. These results are shown in Fig. 2.4.

With the wire-wrapped spacer, a possibility of very small heat transfer coefficient over a small portion of the cladding exists. This situation was simulated by analyzing 10% of the average heat transfer coefficient over a six degree sector of the cladding. For this case, the maximum temperature drop was 37% higher than the average temperature drop (Fig. 2.5). The results of this analysis are significant for evaluating the hot spot factors for the radial blanket assembly.

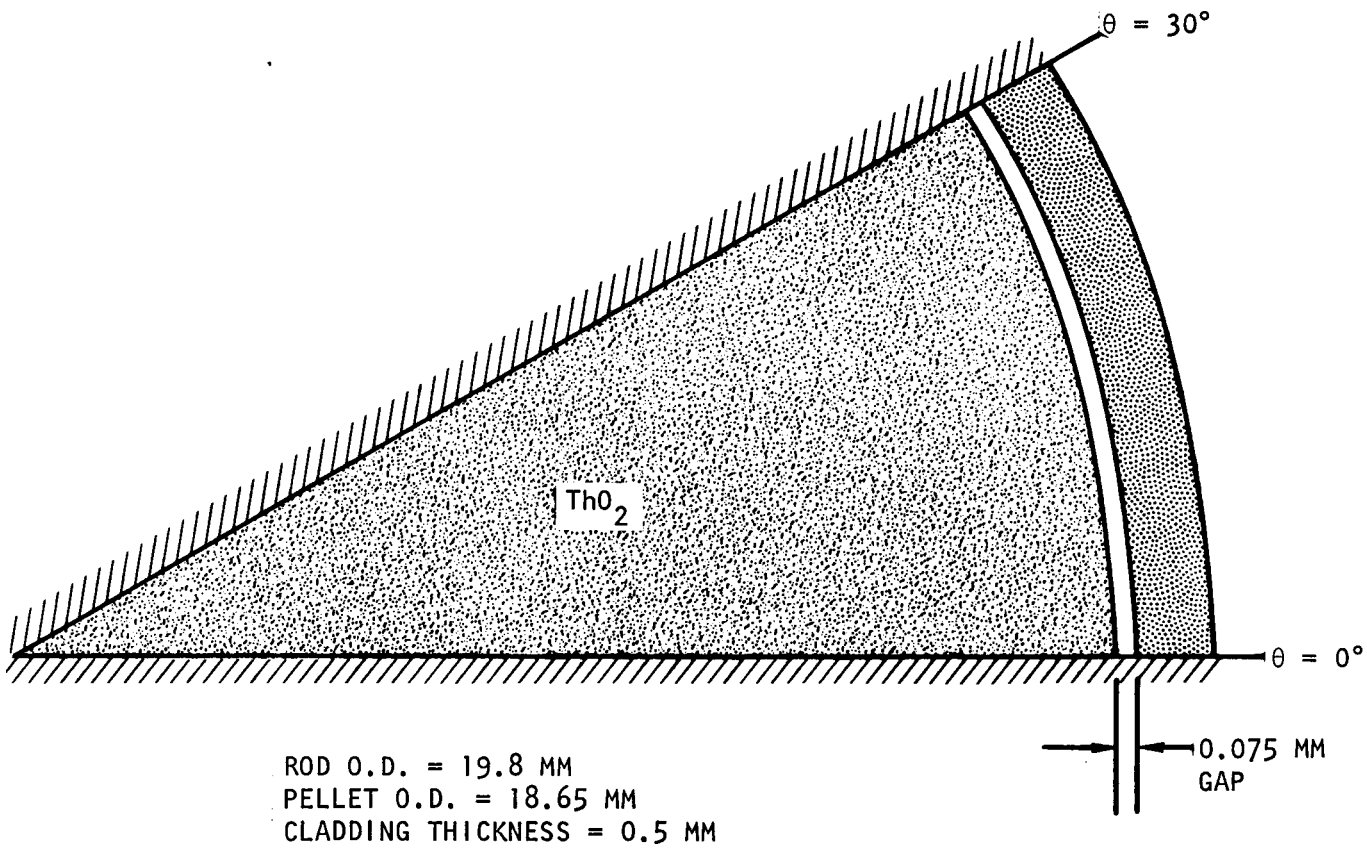

Fig. 2.3 Model of the GCFR blanket rod

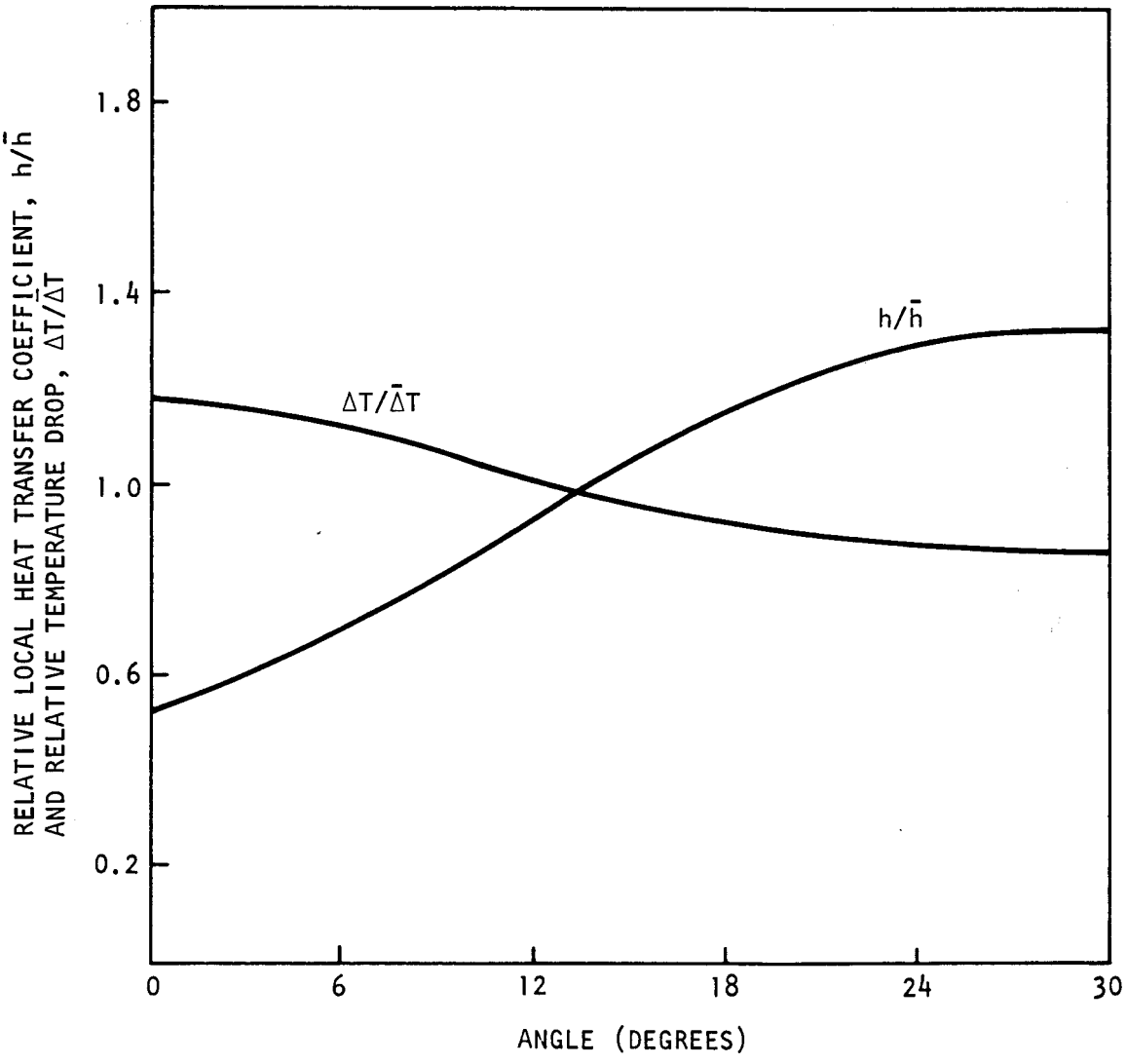

Fig. 2.4 Effect of variation of local heat transfer coefficient on mid-wall cladding temperature of blanket rod

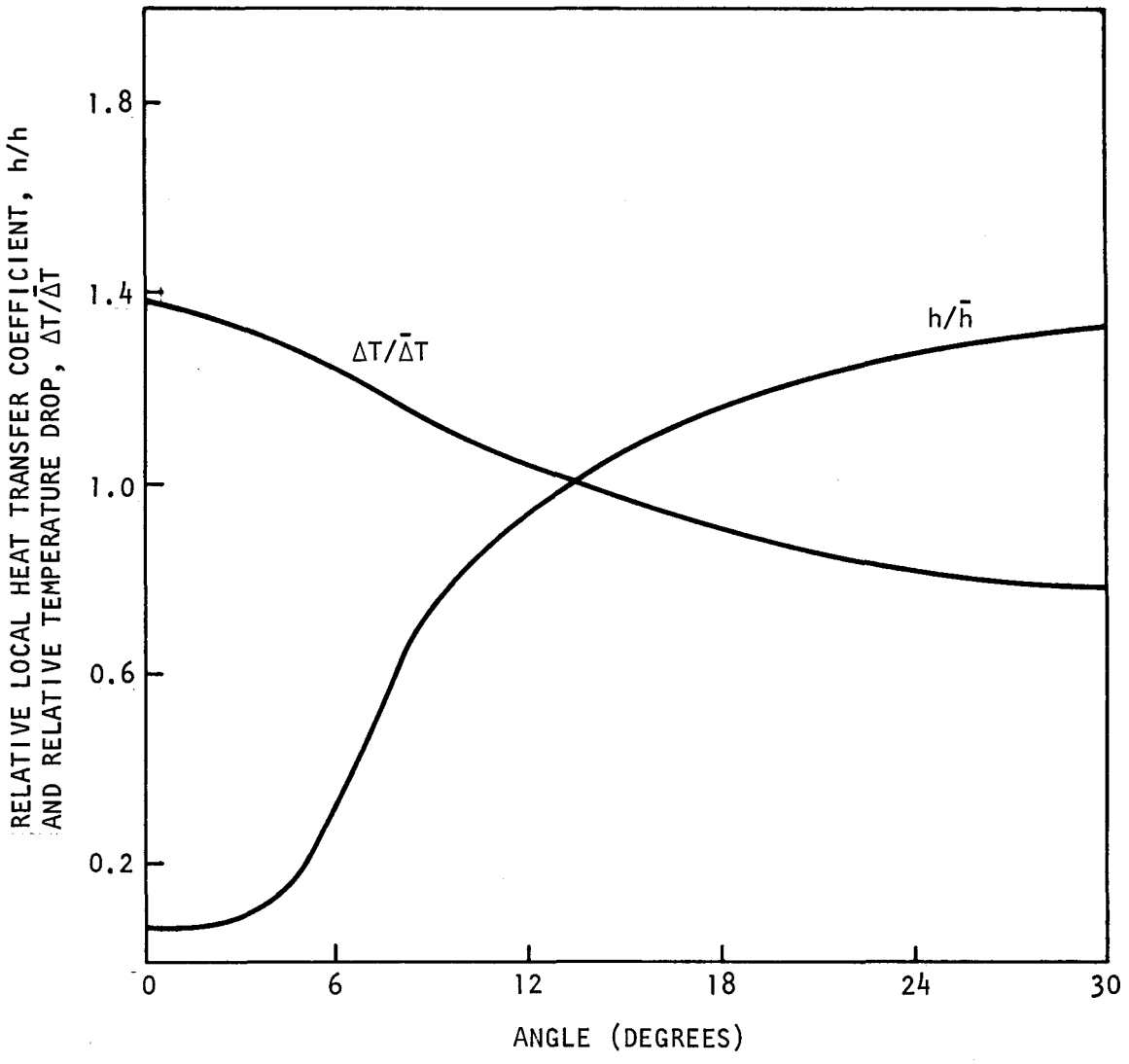

Fig. 2.5 Effect of variation of local heat transfer coefficient on mid-wall cladding temperature of blanket rod

2.2.1.2. Thermal Effects on the Reactor System. A new configuration and management scheme proposed for the radial blanket assembly of the GCFR is discussed in Section 2.2.2. The proposed design uses essentially parallel flow in the blanket assembly. Due to the steep radial power gradients in the blanket assembly, it is necessary to overcool the lower power side of blanket assemblies in order to limit the mid-wall hot spot cladding temperature to 700°C on the high power side. This in turn results in a reduced assembly outlet temperature and affects the reactor system as shown in Table 2.2.

Table 2.2

THERMAL EFFECTS OF THE RADIAL BLANKET ON THE REACTOR SYSTEM

	Beginning of Equilibrium Cycle	End of Equilibrium Cycle
Mixed mean outlet temperature from the blanket assemblies (°C)	391	482
Fraction of total reactor power in the radial blanket (%)	1.37	3.18
Degradation of mixed mean core outlet temperature (°C)	7.3	3.3

These degradations can be compared to a theoretical case where a design of the blanket might be possible with no overcooling at the end of equilibrium cycle. Even in this case, the degradation of the mixed mean core outlet temperature at the beginning of the equilibrium cycle will be 4.1°C due to smaller power at the beginning than at the end of the cycle. Hence, the parallel flow design of the blanket assembly contributes, at most, 3.2°C to the degradation of the core outlet temperature. An analysis of economics shows that 3.2°C degradation represents an increase of capital cost by $0.6 M for 300-MW(e) GCFR due to the increase in the heat transfer area of the steam generator and the other major components (PCRV, etc.).

2.2.2. Recommended Radial Blanket Assembly Configuration and Management

The reference design of the GCFR radial blanket (Ref. 3) is based on a management scheme that does not involve shuffling or rotation of the blanket assemblies. Review of the management schemes of the LMFBR radial blanket resulted in a re-examination of the reference management scheme. A management scheme involving in-out shuffling (similar to the CRBR scheme) with rotation was chosen as the most desirable. This scheme reduces the peak powers in the radial blanket and also reduces the difference in powers between the first and second rows.

Along with the above change in the management scheme, it was found that the pitch/diameter ratio used in the reference design of the radial blanket assembly was so small that there were design difficulties for the baffles, and, at the same time it was too large for the use of wire wrap spacers.

Thermal-hydraulic and structural analyses together with an evaluation of fuel cycle costs led to the changes in configuration and management scheme of the radial blanket assembly shown in Table 2.3.

The recommended design of the radial blanket assembly represents the following advantages over the reference design:

1. The fabrication cost of the blanket assembly is a strong function of the number of rods per assembly. Compared to the reference design, cost per assembly for the proposed design will be 35% lower. This represents a $1.6 M saving in the first core cost and $0.4 M/year saving in reloads.

2. The proposed design will increase the volume fraction of the fertile material in the radial blanket from 0.513 to 0.595. This will increase the breeding ratio of the GCFR from 1.40 to 1.44 and fissile material production by 10%. This represents an additional revenue of $0.3 M/year.

Table 2.3

COMPARISON OF REFERENCE DESIGN AND RECOMMENDED DESIGN OF GCFR RADIAL BLANKET

	Reference Design	Recommended Design
Blanket Management	Fresh elements loaded in both rows with a residence time of three years in the first row and six years in the second row.	Fresh elements loaded in the first row, rotated at EOC[a] 1, shuffled to the second row at EOC 2. Discharged from row 2 at EOC 4 (Fig. 2.6).
Average Residence Time	4.6 years	4 years
Configuration	127 rods/assembly pitch/diameter ratio = 1.12 rod diameter = 12.8 mm cladding thickness = 0.375 mm central thermocouple rod eight baffles to cause flow mixing	61 rods/assembly pitch/diameter ratio = 1.05 rod diameter = 19.8 mm cladding thickness = 0.5 mm central thermocouple rod wire wrap spacers to cause mixing
Spacer	eight grid spacers	wire wrap spacer with wire

[a]EOC = End-of-Cycle

3. Increased volume fraction of the fertile material in the radial blanket will reduce the shielding requirements.

4. Absence of baffles in the proposed design will reduce the possibility of local recirculation during low flow.

5. The proposed design will have a lower peak burnup (<5,000 MWD/MTM) and fluence (~5 x 10^{22} nvt) than the reference design and management scheme.

CYCLE		TIME (DAYS)	BLANKET ELEMENT AGE (DAYS) ROW 1	ROW 2
1	BOC*	0	0	
	EOC*	250	250	250
2	BOC	250	250 (ROTATED)	250
	EOC	500	500	500 → OUT
3	BOC	500	SHUFFLE TO ROW 2; REPLACE WITH FRESH ELEMENT	500
	EOC	750	250	750
4	BOC	750	250 (ROTATED)	750
	EOC	1000	500	1000

*BOC = BEGINNING OF CYCLE; EOC = END OF CYCLE.

Fig. 2.6 Radial blanket management scheme for 4-yr residence time

6. Unlike the reference design, the proposed design is directionally independent (i.e., the baffle design required orientation with respect to the radial power gradient).

7. Due to the in/out shuffling scheme of the proposed design, the second row of the blanket assembly operates at a higher power than the reference scheme, thus reducing the possibility of local recirculation.

2.3. ASSEMBLY MECHANICAL TESTING

The current phase of assembly mechanical testing is the testing of element components. The fuel rod/spacer interaction was the initial long term component test and is scheduled for completion in FY-76. Additional tests are being planned for components such as the spacer grids, rod support grid, and element nozzle parts and subassemblies.

2.3.1. Fuel Rod/Spacer Interaction Tests

The purpose of the rod/spacer interaction tests is to evaluate the interaction between the rod and the spacer in the ranges of temperature and impurity levels (primarily water and hydrogen) expected in the GCFR helium coolant. These interactions arise from the relative motion between the rod and the spacer due to temperature variations during reactor transients. These tests will provide a data base for standards of acceptable friction and wear and the elimination of the possibility of adhesion between the rod and the spacer.

Initially, the combinations of pressed spacers with convex contact surfaces and smooth or ribbed rods were tested. Both spacers and rods were of type 316 stainless steel. Adhesion was observed in tests on smooth rods in an environment containing 900/90 μatm of H_2/H_2O in helium. No adhesion was observed when the H_2/H_2O ratio was increased to 100 at the same absolute level of H_2O. Additional tests were conducted using spacers

fabricated by the electrodischarge machining (EDM) technique. These spacers had flat or concave contact surfaces with 2 μm R_a surface roughness. No adhesion was observed under the same conditions at which pressed spacers showed adhesion. In addition, adhesion has not been observed with Inconel 718, Inconel 625, or Hastelloy spacers against type 316 SS smooth rods.

During this quarterly reporting period, tests to determine the reproducibility of the friction coefficient and wear measurements of fuel rods and electrodischarge machined (EDM) spacers were initiated. The tests are conducted in a helium environment at 550°C and 325°C containing 3000 μatm of H_2 and 850 μatm of H_2O. The EDM spacers used have flat contact surfaces with a surface roughness range of 2 to 2.5 μm R_a. The interaction occurs during a relative motion between the rod and spacer and the test parameters include two stroke lengths of 0.76 mm and 3.8 mm. The tests using combinations of smooth surface fuel rods and EDM spacers at 550°C and 325°C were completed and the results are tabulated in Table 2.4. The average values for the short stroke tests (0.76 mm) at 550°C were not computed because of a difficulty that occurred with the cam drive mechanism. These tests may be repeated at a later date.

The following general conclusions can be made from the test results of Table 2.4.

1. The coefficient of friction appears to be lower for the short stroke (0.76 mm) tests. This may be the effect of a shorter dwell time (one minute versus one hour).

2. The average wear appears to be independent of the stroke length and dwell time. It is noted that the total linear motion of the short stroke test is 3050 mm; it is 380 mm for the long stroke tests. It is possible that wear reaches an equilibrium value very early during the long and short stroke tests. This tends to agree with similar tests done by Kraftwerk Union (KWU)

Table 2.4

REPRODUCIBILITY TEST RESULTS

Temperature (°C)	Stroke[a] (mm)	Coefficient of Friction			Wear (μm)		
		Maximum	Average	σ[b]	Maximum	Average	σ
550	3.8	0.6			40		
550	3.8	1.1	0.85	0.24	36	34	6.4
550	3.8	0.7			25		
550	3.8	1.0			36		
550	0.76	0.5			--		
550	0.76	0.5	—[c]	--	20	--	--
550	0.76	0.5			16		
550	0.76	0.4			10		
325	3.8	1.3			36		
325	3.8	0.7			31		
325	3.8	1.0	1.14	0.54	25	30	4.3
325	3.8	2.0			31		
325	3.8	0.7			25		
325	0.76	0.7			25		
325	0.76	0.5	0.55	0.13	31	31	7.1
325	0.76	0.6			41		
325	0.76	0.4			25		
550	3.8[d]	2.0	--	--	62	--	--

[a]The short stroke tests have a dwell time of one minute between strokes, and the long stroke tests have a dwell time of one hour between strokes.

[b]σ = standard deviation

[c]These tests were affected by faulty drive mechanism. Smooth rods and EDM spacers were used in all tests.

[d]Long dwell time test results.

for the BR-2 tests, where a transfer of material was observed from roughened fuel rods to spacer contact surfaces. This material buildup reached an equilibrium value and so did the rod wear depth. However, the equilibrium wear was much greater, i.e., 100 to 160 μm.

The reproducibility testing was initiated for roughened tubing (CW type 316 tubes with mechanically ground roughening) against EDM spacers, which is the reference design fabrication process.

The long dwell time tests were continued, and one short stroke test on the smooth tube at 550°C was completed. The stroke length was 3.8 mm and the total number of strokes was 100. The total test duration was 1000 hrs, in order to complete a reasonable number of tests in the current year. This resulted in the following testing sequence: the test was initiated with 25 strokes with a four-hour dwell between strokes followed by six strokes with a 100-hour dwell time between strokes, and finally a series of 74 strokes with a four-hour dwell between strokes. It was observed as expected in this initial test that the breakaway friction was greater than the dynamic friction. However, the dynamic friction coefficient tended to increase during the stroke until it equaled or exceeded the breakaway coefficient. The maximum coefficient of friction was about 2 with a maximum wear of about 62 μm. It is noted that there has never been any tendency for adhesion between the rod and spacer during these tests.

If this degree of cladding wastage is determined to be unacceptable from a strength point of view, the wear pads or short-ribbed sections can be provided at the spacer locations in the fuel rod design.

2.3.2. Component Mechanical Testing

Other mechanical testing included initiation of an experimental stress analysis on a small scale hexagonal duct for correlation with structural analyses. The test will use water as the pressurizing medium at room temperature, with strain gages and dial indicators for measuring wall deflections. Preliminary test specifications were initiated for component mechanical testing, including fuel assembly spacers and fuel cladding strength and distortion tests.

2.4. CORE TEMPERATURE MONITORING

The preliminary design requirements were prepared for the core element assembly based on the current GA-KWU fuel element design concept.

In this concept, the temperature monitor is a single large diameter Chromel-Alumel thermocouple. The replaceability requirement is facilitated by inclusion of a thermocouple guide tube into a central fuel rod position of the fuel assembly. A similar guide tube in the element latching mechanism must align with the guide tube in the element. The replacement is accomplished by disconnecting the lead wires above the PCRV and withdrawing the entire thermocouple. Since the guide tube O.D. is about 7 mm, the thermocouple sheath diameter can be 5 mm, thus providing a relatively stiff thermocouple assembly to facilitate the remote insertion into the guide tube for replacement.

It is expected that this thermocouple design concept will be included in the blanket assemblies. The blanket assembly design has changed to fewer (from 91 to 61) and larger blanket rods (~19 mm). This provides an opportunity for a much stiffer thermocouple assembly. However, it also represents a decrease of blanket material, i.e., one of 61 rods or 1.6 percent.

The thermocouple assembly conceptual design requirements may be difficult to meet for the control rod fuel element assemblies. This is

because of the central location of a solid section control rod, which precludes a central thermocouple location. If the thermocouple or thermocouples are located off-center, then it becomes increasingly difficult to design for remote replaceability and an in-core connector may be required. However, a conceptual design study is in progress on a private program to devise alternative control rod designs that could accommodate a centrally located thermocouple location. One concept being considered is an annular control rod design that would have a thermocouple guide tube in the central location. The thermocouple junction would be located in a position in the exit nozzle that would be representative of the average element outlet temperature.

2.5. HEAT TRANSFER AND FLUID FLOW TESTS

Test planning for the pressure drop measurements of the element assembly inlet nozzle section has continued. Test specifications are being prepared, and the conceptual design of a test model was completed. It is planned to design a plastic model simulating the metal part with ducting that can be assembled to the GA experimental engineering air blower ducts. The detailed component drawings are being prepared and are near completion. The machining of parts in the laboratory machine shop is planned for early 1976.

REFERENCES

1. "Gas-Cooled Fast Breeder Reactor Quarterly Progress Report for the Period August 1, 1975 through October 31, 1975," USERDA Report GA-A13766, General Atomic, January 1976.

2. Palmer, L. D. and L. L. Swanson, "Measurements of Heat Transfer Coefficients, Friction Factors, and Velocity Profiles for Air Flowing Parallel to Closely Spaced Rods," Paper No. 63, International Heat Transfer Conference held at the University of Colorado, Boulder, Colorado, ASME, 1961.

3. "300-MW(e) Gas Cooled Fast Breeder Reactor Demonstration Plant," General Atomic Report GA-A13045, July 15, 1974.

III. PRESSURE-EQUALIZATION SYSTEM FOR FUEL (189a No. SU006)

3.1. FUEL-ELEMENT AND VENT-CONNECTION SEALS

In the GCFR reference design, the core (fuel, control, and blanket) elements and their vent connections are sealed to the grid plate by clamping the conical surfaces of the elements to the matching surfaces in the grid plate with a force sufficient to effect a seal and to support the elements, which are cantilevered from the grid plate. These element seals must function at the coolant pressure difference between the reactor core inlet and exit plenums. The effectiveness of the seals over the life of the core is uncertain, not only because each element may be rotated or relocated several times over its useful life, but also because the seals must be effective in a high-purity, high-temperature helium environment while subject to mechanical, vibrational, and thermal effects. Most of the uncertainties are expected to be resolved in a two-part program: (1) a materials screening test program for study of static adhesion of simulated fuel-element and grid-plate parts clamped together, and (2) leakage tests of fuel-element and vent-connection seals to the grid plate. Current progress in these activities is given below.

3.1.1. Static Adhesion Tests

Preparations were completed for testing of the static adhesion properties of the alternate materials representing the grid plate and fuel elements as described in the previous report.[1] Pre-exposure testing and characterization were completed. Exposure of the samples to high temperature helium with controlled levels of impurities began in November 1975. By the end of 1975, more than 1000 hours had been accumulated toward the 3000 hour exposure goal that is expected to be reached about mid-March 1976.

3.1.2. Fuel Element Seal Leakage Tests

An alternative to the conical metal-to-metal reference element seal design is being developed in which piston rings are used as sealing members. The piston ring seal tests are in preparation and are based on the design incorporated into the joint Kraftwerk Union-General Atomic model core element to be built to KWU in Germany. Test equipment and test grid plate and fuel element parts used for metal-to-metal conical seal testing will be modified to test the piston ring seals.

The piston-ring seal design drawings for the model fuel element were completed. The drawings for the piston-ring seal test fixtures to be inserted into the test autoclave previously used for the conical seal tests were completed. Alternative designs are being drawn based on the piston ring designs developed in vendors' quotations. The basic piston (fuel-element head test piece) will be retained for all tests, and various attachments will be designed for each piston ring design with detailed dimensional requirements.

Materials are on hand and fabrication for modification of the test fixture and equipment has been ordered.

The piston-ring-leakage test program was reviewed and a detailed schedule developed. The critical path item is the delivery of the piston rings from suppliers. Delivery is now scheduled for about mid-April 1976. Piston rings of a KWU design are also expected to be procured.

3.1.3. Vent Connection and Vent Port Valve Seals

A vent connection and vent port valve assembly previously described are being developed for connecting the GCFR fuel elements to the vent passages in the grid plate and for sealing the vent port of the core elements when removed from the grid plate for handling, storage, and transport.

Vent assemblies were assembled by electron beam (EB) and tungsten insert gas (TIG) welding techniques. The first EB-welded assembly resulted in unsatisfactory weld appearance and leaks. The second EB-welded assembly was completed successfully and will be tested as discussed below. The first TIG-welded vent assembly also leaked, but the weld quality was noticeably superior. A second vent assembly is being prepared for the TIG welding. TIG welding has been chosen for future assemblies.

Load-deflection calibration tests of the Belleville washer springs for the vent assembly design were conducted. The results agreed, well within the nominal ranges specified by the manufacturer, and are repeatable within 2%. The manufacturer's ranges are $\pm$10% to $\pm$15% around nominal values and appear to be overly conservative unless batch or lot variations are large. However, similar calibration tests on larger Belleville washer springs for the static adhesion tests were conducted on different springs that were procured on two orders placed 18 months apart. The load deflection measurements agree within 1% between the two groups of washers. It is not known whether the washers came from different manufacturing lots.

Modification of the apparatus for separate leak testing of the valve seat in the vent assemblies is in progress. Adaptors for installing the vent assemblies in the fuel-rod seal test apparatus have been made. All required equipment is available for installation, and testing is expected to start in the next reporting period.

The vent assemblies are also to be tested in separate leakage tests of the vent connection seal. Vent assemblies subsequently will be installed in the fuel-element test piece for integral tests with conical and piston ring core-element seals. The design for integral testing of the vent assemblies with the piston-ring seals is in progress and should be completed early in the next quarter. The design for mounting the vent assembly in the conical transition section of the core elements is a critical design item that has not yet been resolved. Resolution of the vent assembly mounting design is expected in the next quarter.

3.2. ANALYSIS, MODELS AND CODE DEVELOPMENT

Development of a computer code for transient analysis of the pressure equalization system (PES) flow network continued during this reporting period.

3.2.1. Transient Flow Code

During the previous quarter, a model for simulating the transient thermal-hydraulic behavior of the helium purification system (HPS) in the PES was developed. This model is capable of analyzing the thermal-hydraulic behavior of the HPS during severe transients including depressurization accidents.

The HPS consists of a series of components such as heaters, coolers, and filters, which are idealized as volumes interconnected by pipes, with the resistances of the components lumped into the pipe resistances (see Fig. 3.1). With such an idealization, for each volume it is possible to write three differential equations, representing the one-dimensional energy, momentum, and continuity equations.

The equations have been programmed using the SYSL system simulation code, and some initial studies have been done. For these preliminary studies a simplified model was used. The simplified model, shown schematically in Fig. 3.2, consisted of five equal volumes, connected by equal-length pipes. The first and last volumes were connected by pipe to large plenums, the gas pressures and temperatures of which were specified functions of time. The particular transient considered was a rapid depressurization of the two plenums from 100% pressure to 2% pressure in 20 seconds.

It should be emphasized that this transient is more severe than any considered credible for the GCFR. Also, the model being analyzed here bears only superficial resemblence to the GCFR HPS, and is being used only for qualitative studies of different system configurations.

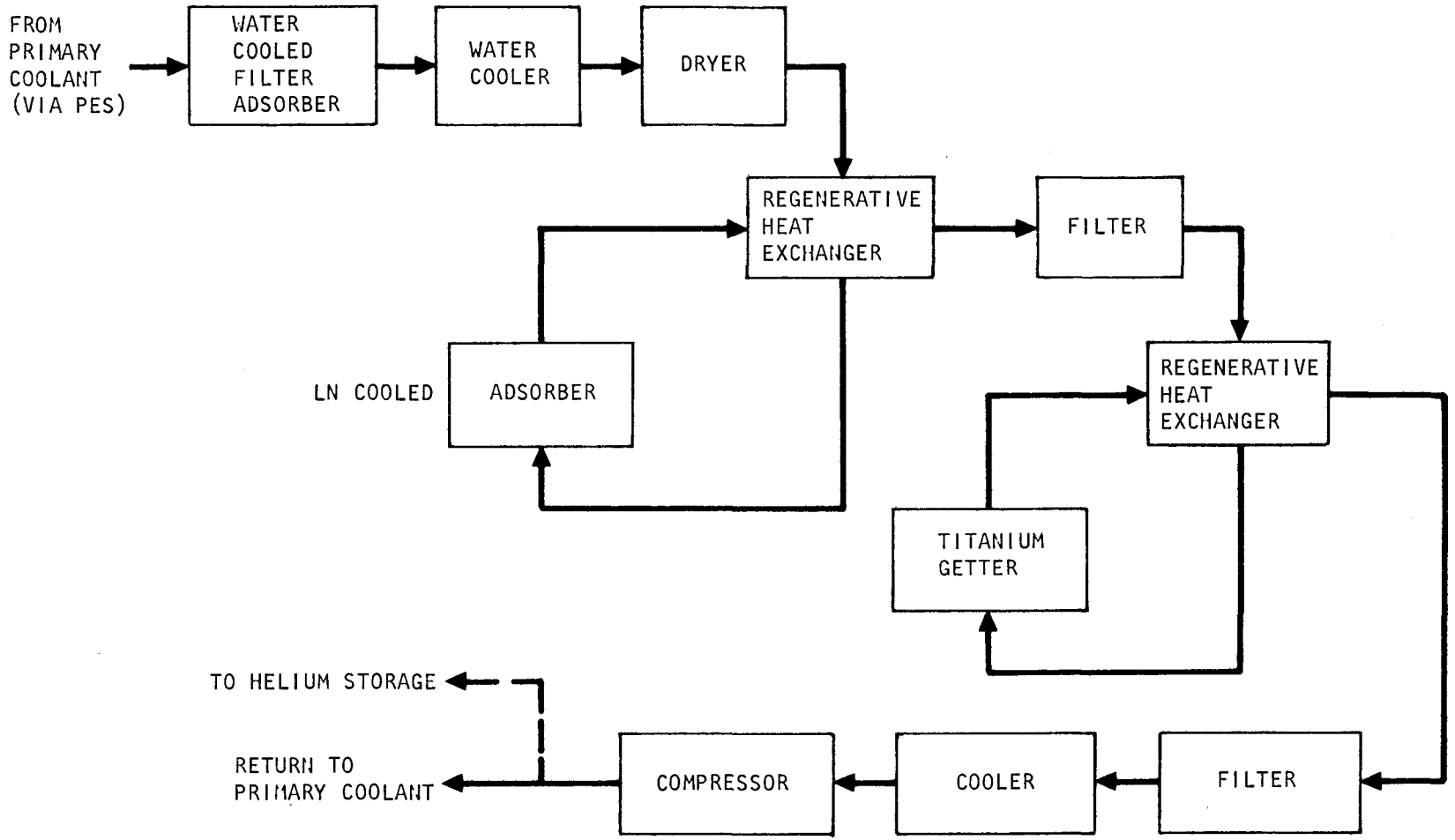

Fig. 3.1 Helium purification system train, two trains per unit

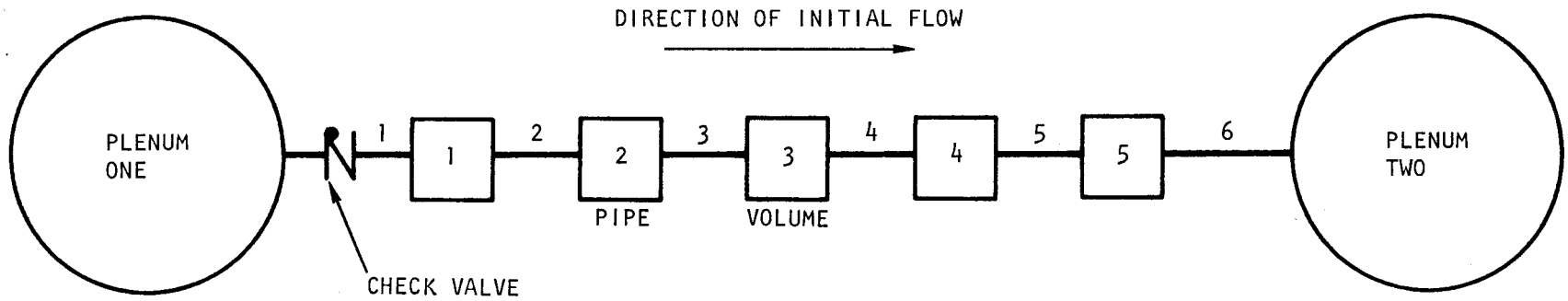

Fig. 3.2 Simplified HPS test model

Four cases were run: two considered uniform pipes with and without the check valve shown in Fig. 3.2, and two cases set pipe one as half the diameter and pipes two through six as twice the diameter of the pipes in the uniform case, and again considered the system with and without the check valve.

Figures 3.3 through 3.6 depict the gas flows through the system for the four cases. As can be seen from Figs. 3.3 and 3.4, reverse flow occurs for both cases without check valves, although it is severe only for the case of uniform pipes. Figure 3.5 shows that if a check valve is installed in the system, for the case of uniform pipes, the valve closes at about 5 seconds and remains closed for about 30 seconds. In the case of non-uniform pipes, the valve does not close until about 17 seconds, and remains closed for only about 6 seconds.

Particularly evident in the nonuniform pipe cases, but a characteristic of all the curves, is a "ringing" behavior, i.e., a superposition of a low amplitude, high frequency signal upon the main response. This has not yet been explained, and is currently under investigation.

The results obtained with the code to date appear qualitatively correct, but no effort has yet been made to check the validity of the code quantitatively. Such validation will need to be done before the code is used for quantitative analysis of the GCFR HPS.

Data are being assembled on the volumes, pipe sizes and lengths, and valve sizes and types in the HPS in the Fort St. Vrain HTGR as a basis for developing a realistic model of the HPS in the GCFR-PES. Data gathering and modeling will continue in the next reporting period.

3.3. PLATEOUT AND PLUGGING

During this reporting period, qualification of the high pressure water saturators was completed and testing of the helium circulators for

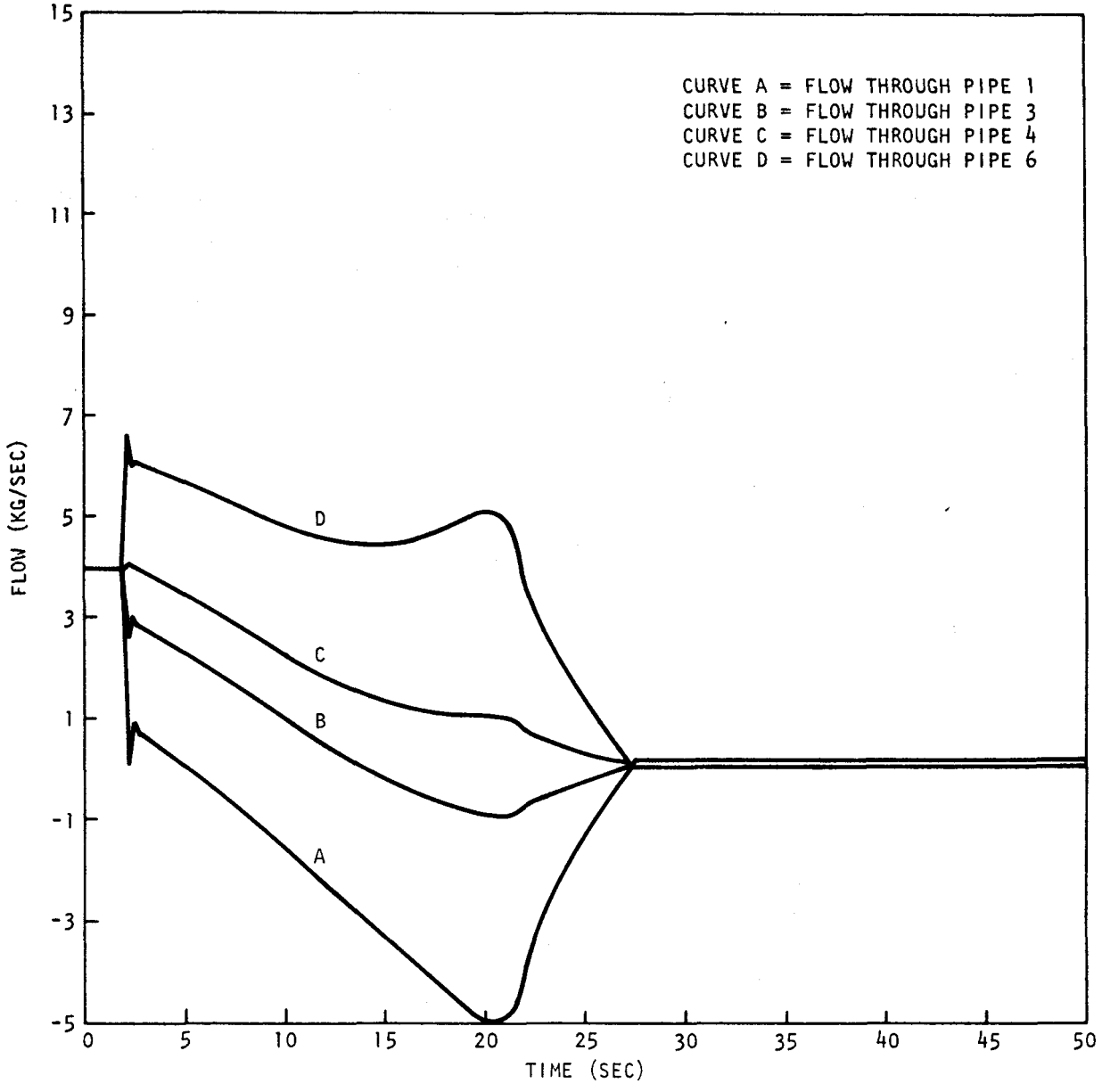

Fig. 3.3 HPS model during depressurization: case 1, uniform pipes, no check valve

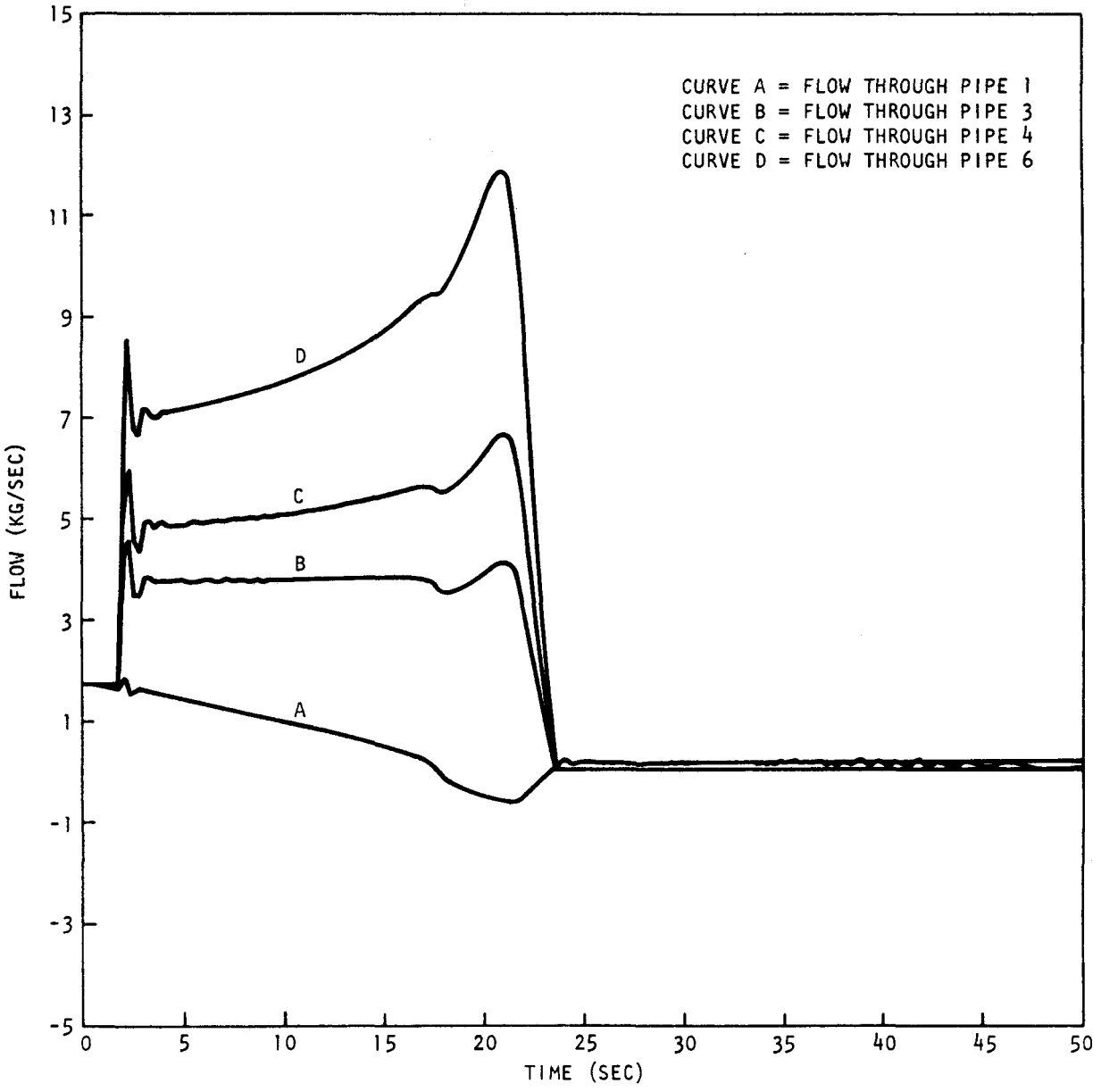

Fig. 3.4 HPS model during depressurization: case 2, nonuniform pipes, no check valve

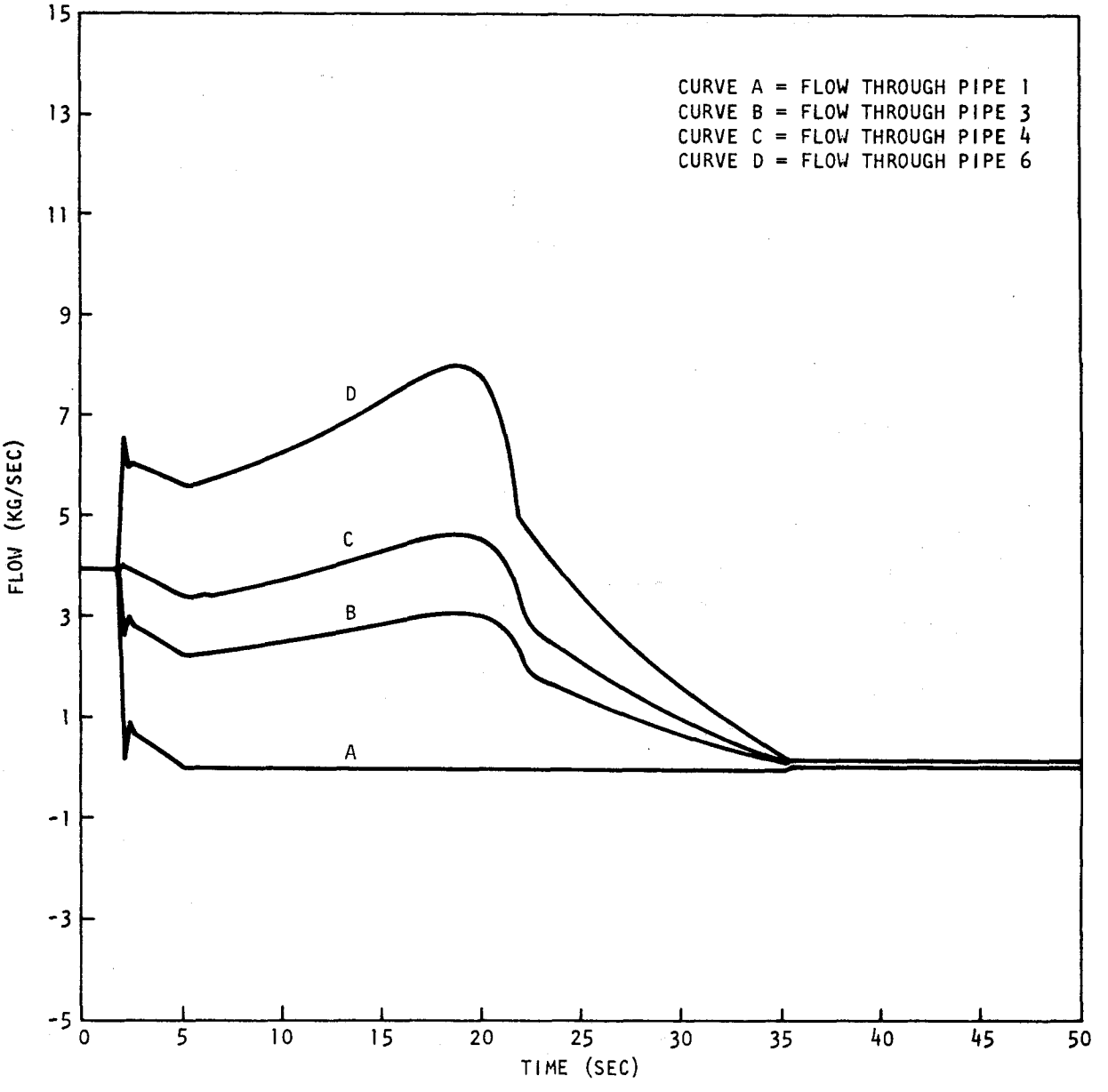

Fig. 3.5 HPS model during depressurization: case 3, uniform pipes, with check valve

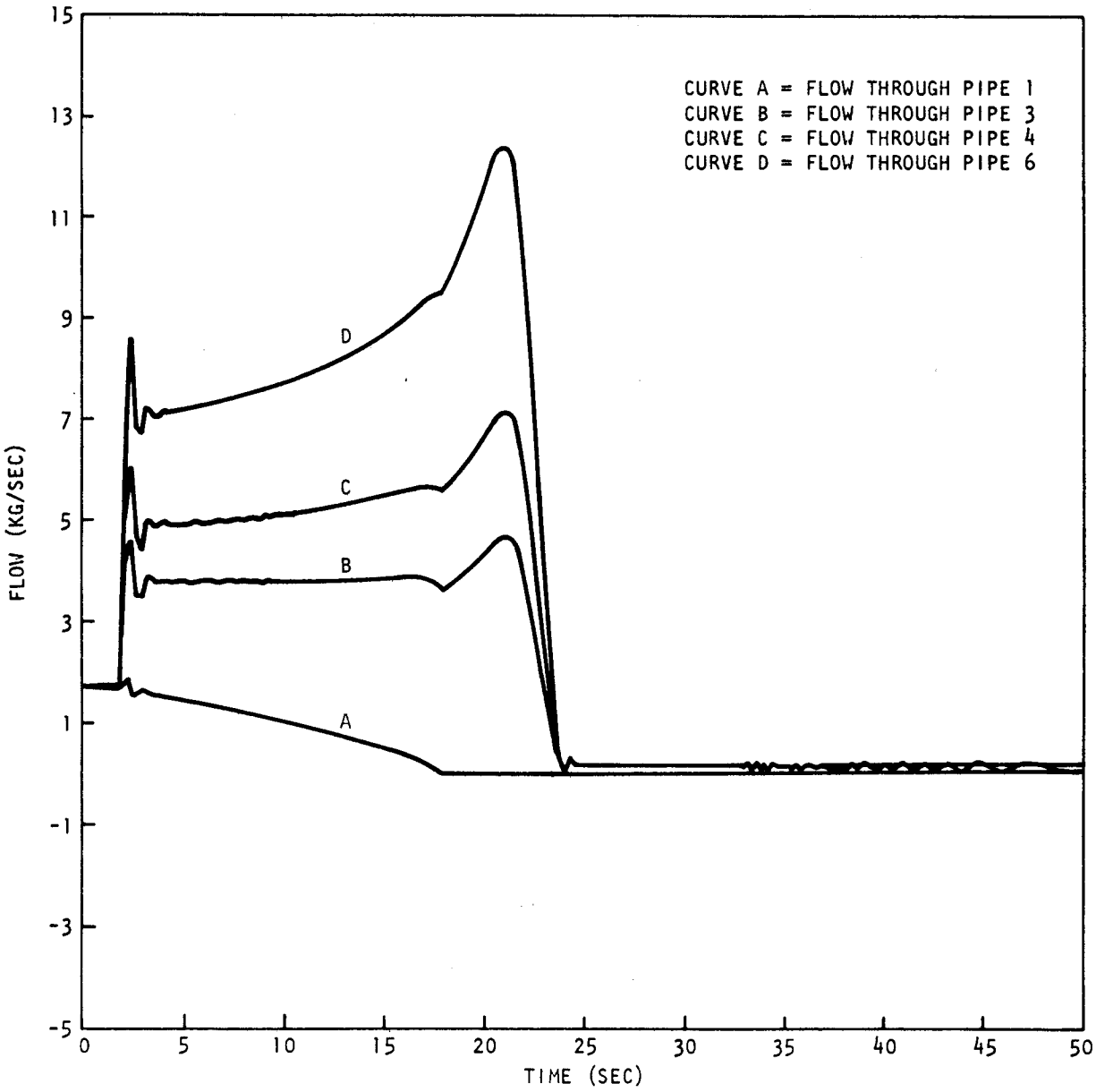

Fig. 3.6 HPS model during depressurization: case 4, nonuniform pipes, with check valves

the plateout and plugging test loop progressed satisfactorily. These developments are detailed below.

3.3.1. High Pressure, Water Vapor Saturator

A new filling procedure was developed for the saturators that allows for freezing of the water without plugging of the flow path by the ice that is formed. Differential pressure versus helium flow curves were obtained at 253°K (-20°C) and 213°K (-60°C) of a helium flow rate range of 100-4000 mℓ/min (23°C, 1 atm). The maximum differential pressures (ΔP) obtained at an ice temperature of 253°K (-20°C) and helium flow of 4000 mℓ/min was 106 and 86 Pa for saturators No. 1 and No. 2 respectively.

A series of measurements was made of the moisture levels produced by the saturators via a ThO_2-EMF-cell oxygen potential meter. Helium gas containing 500 $\pm$ 5 ppm H_2 (analyzed with a gas chromatograph) was used. The gas was rendered oxygen free by passing it through an 0.16 g activated charcoal trap, cooled to liquid-nitrogen temperature prior to flowing it through the saturator at a flow rate of 100 mℓ/min. The oxygen potential (i.e., H_2/H_2O ratio) of the resultant gas was then measured with the EMF cell. Both saturators were tested over an ice temperature range of ∿253°K to 213°K (-20°C to -60°C), resulting in H_2/H_2O ratios from ∿0.55 to 46.0 respectively. Plots of cell EMF versus log of the calculated H_2/H_2O ratio (Fig. 3.7) are quite linear. The values of the slopes and E_o (a fundamental cell constant) were 98 mV/272 mV and 97 mV/274 mV for saturators No. 1 and No. 2 respectively.

Saturator No. 1 has been connected to the EGG Model 440 dew point hygrometer for several weeks, and the performance of the hygrometer as a function of saturator temperature and helium gas flow was measured. The data indicated that the hygrometer reads a frost point approximately 3°K higher than the saturator temperature at the 203°K (-70°C) level while at the 213°K (-20°C) range, the hygrometer reads about 0.3°K higher than the saturator temperature. It was also observed that the hygrometer takes a long time to equilibrate with the gas stream in order to give a stable

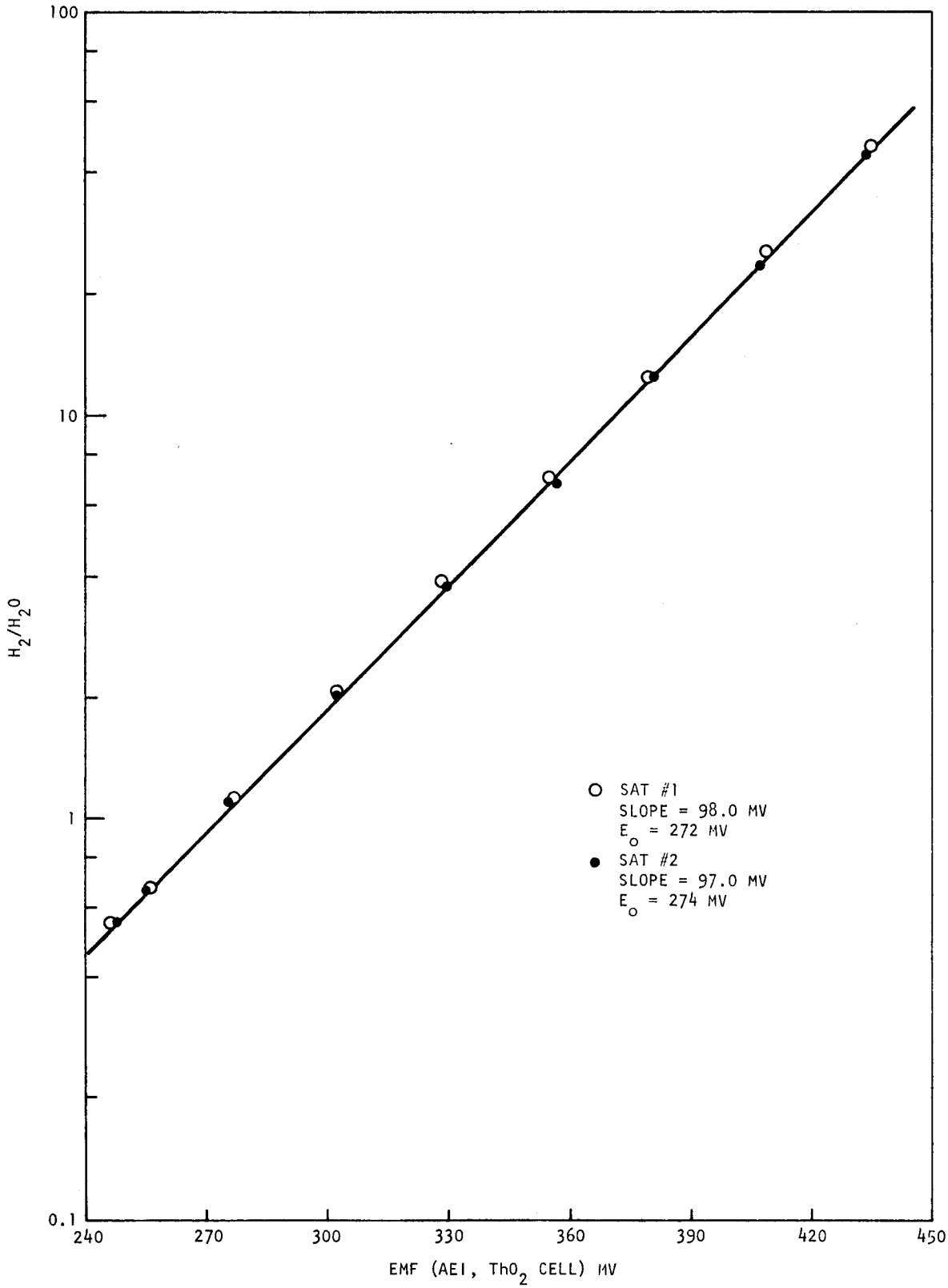

Fig. 3.7 H_2/H_2O ratio vs ThO_2 EMF cell response

reading (sometimes as much as two days were required at a helium flow rate of 100 mℓ/min).

The saturators behave well and produce the desired moisture levels over the range of ice temperatures from 253°K to 213°K (-20°C to -60°C). The saturators are now qualified for application and use in the high pressure plateout and plugging loop under development and on irradiation capsule GB-10 for which they were built.

3.3.2. Helium Circulators for the Plateout and Plugging Test Loop

A series of characteristic pump curves (flow rate versus ΔP) were run for two Spectrex AS-121 diaphragm pumps: individually, in series connection, and in parallel connection in room air. The parallel arrangement was selected and the pumps were mounted in a pressure vessel. Characteristic curves were obtained at 101, 239, 515, 6480 kPa of total helium pressure. At a helium pressure of 6.48 MPa, characteristic curves with the application of 40 and 20 V (peak to peak) were obtained as shown in Fig. 3.8. Pump performance of 22 kPa pressure rise at a flow rate of 4 ℓ/min compares favorably with the design criteria of a pressure rise of 14 kPa at 2.5 ℓ/min set for the loop circulators.

During the next quarterly reporting period pumping characteristics will be obtained on helium pressures up to 9.0 MPa, and a 100-hour endurance test will be performed.

3.4. PES MANIFOLD FABRICATION

Manifold fabrication development during this period consisted of:

1. Evaluation of methods for hole locations, dimensions, and surface finish in investment-cast, one-third segment manifolds.

2. Evaluation of three full size investment-cast manifolds.

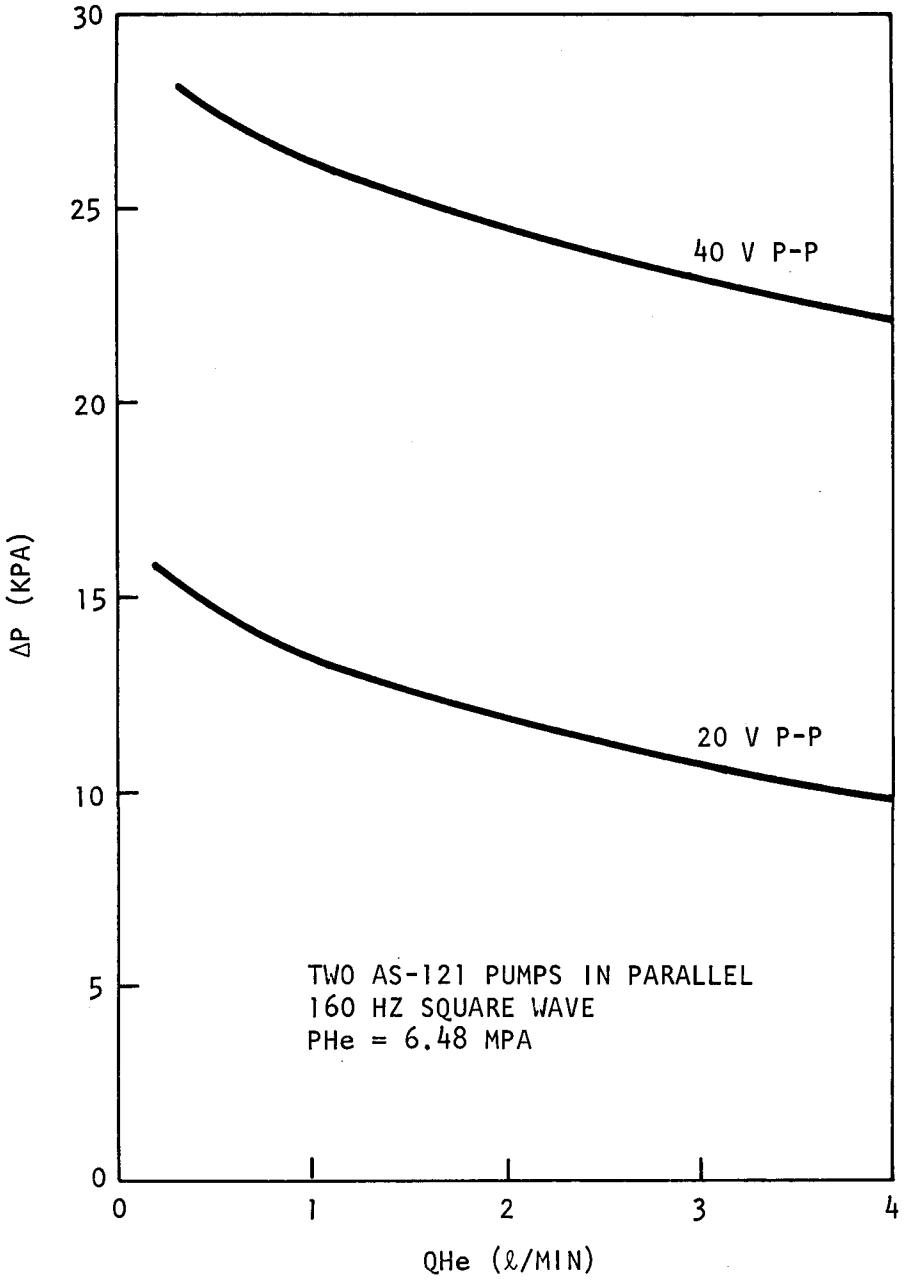

Fig. 3.8 ΔP vs flow characteristics, parallel pump combination

3. Three methods were evaluated for drilling fission gas passage holes into one-third segment manifolds by three different vendors:

   a. Electrochemical machining (ECM) by Metem,

   b. Electrical discharge machining (EDM) by L. C. Miller and Associates,

   c. Gun drilling by Deep Hole Specialists.

4. Leak testing of double rod/manifold seals that would allow making the connection between the rod and manifold from the top of the manifold.

5. Evaluation of diffusion bonding a one-third segment of a manifold in which a cover plate with milled fission gas passages was bonded to the main manifold structure.

6. Evaluation of non-destructive techniques for characterizing manifolds.

3.4.1. Hole Drilling

The one-third manifold segment into which 1.27 mm (0.050 inch) diameter fission gas passages were drilled by ECM is still at Metem for installation of the threaded fuel rod connection holes. A one-third manifold segment into which fission gas passages (2 mm [0.079 in.] diameter) were formed by gun drilling was received and evaluated.

Preliminary inspection showed that in several places the initial drilling broke through the side of the webs in the manifold segment. The breaks were repaired by welding, and the holes were redrilled. Therefore, some steps appeared inside the holes from the restart of the holes in a slightly different direction. One of the holes was plugged and a drill that was broken off in it was removed by EDM. The locations of the 1.98 mm (0.0781 in.) diameter holes were measured relative to the upper surface of the manifold by a magnetometer. A number of the holes

were out of tolerance at one or more locations by 2 or 3 times the allowable tolerance. This part was returned to the vendor for performance of the balance of the machining.

A one-third manifold segment into which fission gas passages were formed by electrical discharge machining (EDM) and rod connection holes were formed by conventional drilling (by L. C. Miller and Associates) was inspected prior to threading of the rod connection holes. The locations of the 1.27 mm (0.50 in.) holes were determined by the magnetometer method, and the locations were generally within tolerance. The fuel rod/manifold sealing surface smoothness was determined for eight locations by a replication technique. (The holes are too deep for direct stylus measurement.) The measured values had an average of 1.8 μm R_a (71 μin. AA) with a range of 0.9 μm R_a (37 μin.) to 2.7 μm R_a (105 μin.) while the specified value on the engineering drawing is 1.6 μm R_a (63 μin. AA). This part was also returned to the vendor for tapping of the threaded holes. The threaded holes have been completed (see Fig. 3.9), and the part is undergoing quality control inspection.

3.4.2. Full Size Investment-Cast Manifolds

Three GCFR 330 MW(e) demonstration plant size fuel element fission gas manifolds have been received from the vendor. These manifolds were investment cast in 316 stainless steel. The initial qualitative observation was that the castings looked good except for excessive cupping of the part where the gates were removed. This should have been corrected by hot straightening, but up to 1.5 mm (0.06 in.) deviation from flatness was observed. The full size investment-cast manifolds are being inspected in the GA Quality Control Department. X-radiography indicates some voids or inclusions, but the report is not yet complete.

3.4.3. Electron Beam Welding

Four sample sections of a manifold design with fuel rod/manifold connections and a cover plate (with milled fission gas passages) electron

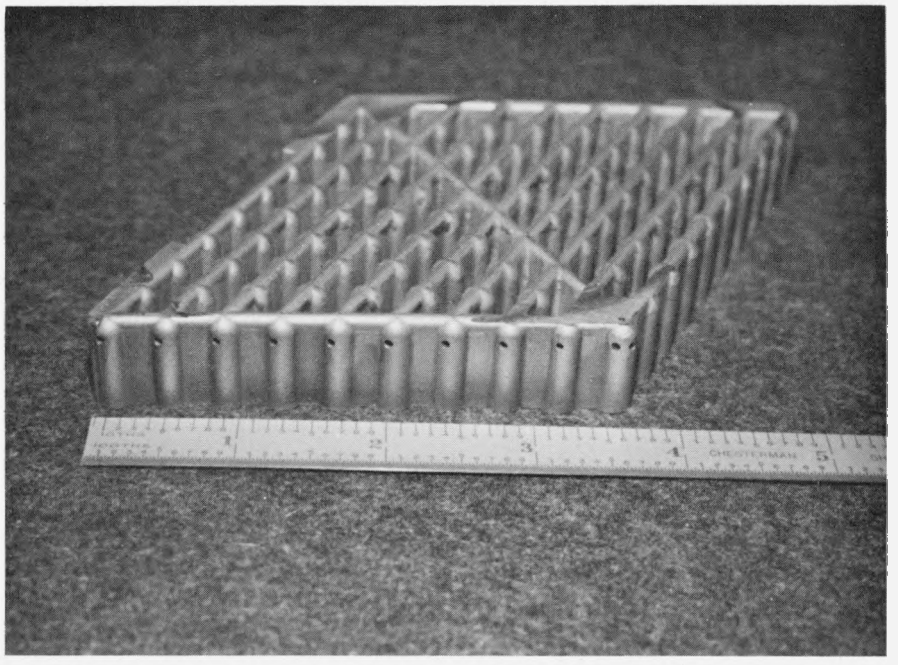

(a)

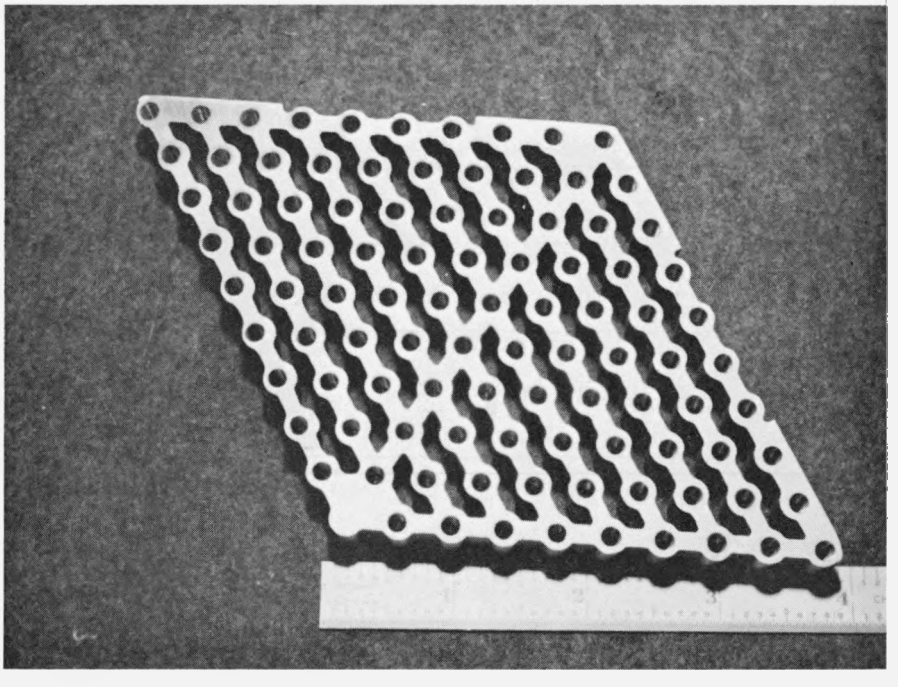

(b)

Fig. 3.9 Manifold segment with holes drilled by conventional methods (a) top view, (b) bottom view

beam welded to the manifold were received from Chemtronics. While two of the four samples appeared to have sound welds, the general condition of the samples was poor. The samples were warped and discolored, indicating excessive heat input (to cause warping) and a contaminated atmosphere (discoloration) during welding. Because of limited funding, no further work on the electron beam welding of the manifold is planned.

3.4.4. Leak Testing of Rod/Manifold Seals

Three double cone rod/manifold seals have been leak tested on a helium mass spectrometer at room temperature. All seals were found to be helium leak tight to the leak detector limit of 5×10^{-12} scc/sec.

Three double flat bottom seals previously tested were also rechecked on the helium mass spectrometer. All were found to be leak tight. The small leaks apparent during tests in the vacuum decay measurement in the seals were from non-constant outgassing in the leak rate test apparatus rather than actual leaks.

3.4.5. Diffusion Bonding

Under private funding, the diffusion bonding of a cover plate with milled fission gas passages to the manifold structure of a one-third segment of a GCFR fission gas manifold (see Figs. 3.10 and 3.11) has been investigated. The manifold parts were prepared by machining, EDM, and milling at GA. The parts were pinned with SS dowels at the corners to maintain their alignment during handling in preparation for bonding, and then were deburred and cleaned.

The manifold parts were then diffusion bonded at DWA Composite Specialties, Inc. in Chatsworth, California. The bonding was done in an evacuated retort in a hydraulic press equipped with heated platens.

Visual inspection showed that the cover plate had experienced some deformation. The bosses showed "barreling" and were wider in the cover

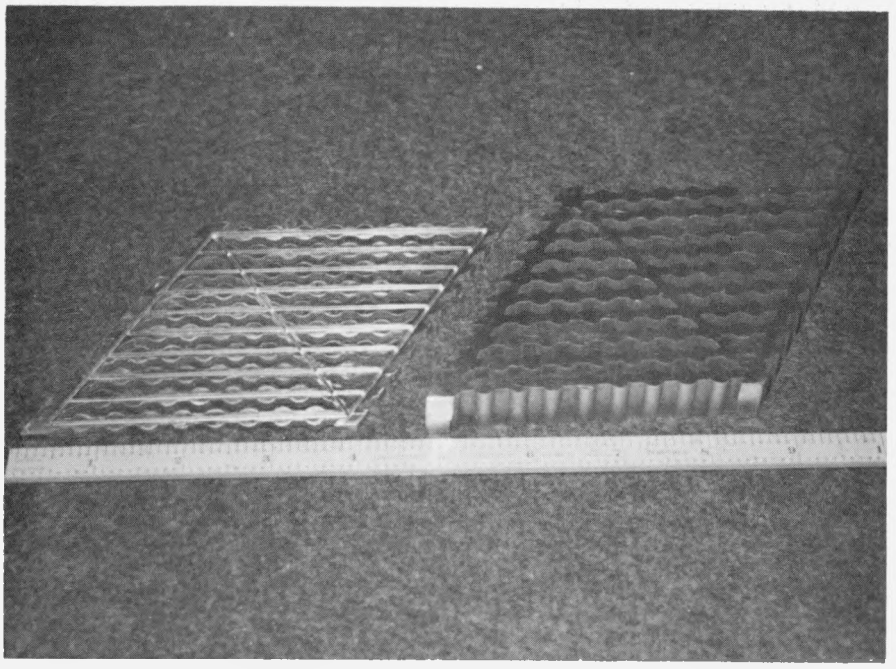

Fig. 3.10 Cover plate with milled fission gas passages and main manifold structure prior to bonding

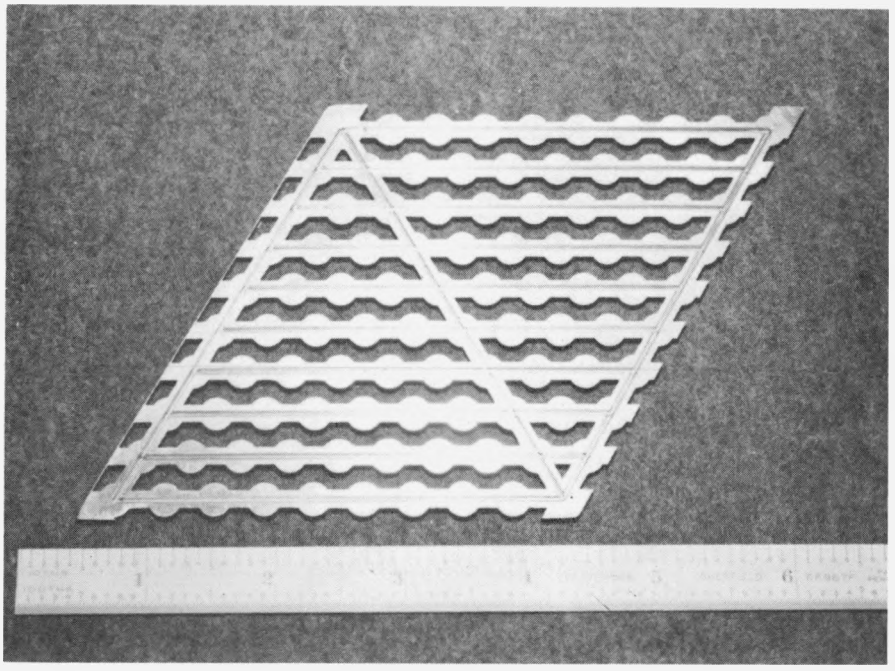

Fig. 3.11 Cover plate with milled fission gas passages

plate than in the manifold structure (see Fig. 3.12). The manifold segment was cleaned to remove the stop-off on its top and bottom surfaces prior to further evaluation.

The evaluation of the diffusion bonded manifold by helium mass spectrometer leak check and helium pressure check (bubble check in alcohol) at 7.0 kPa (1000 psig) has been done. The bond showed several large leaks and numerous smaller leaks. A dimensional check of change in web dimensions manifold thickness, and top and bottom surface parallelism is being evaluated.

Metallographic examination of selected sections from the diffusion bonded manifold segment was performed (see Figs. 3.13, 3.14, and 3.15). Some sections were not bonded at all and in general only partial bonding occurred. It appeared that some foreign material was present in the bond line or interface (see Fig. 3.15) and that the atmosphere in the bonding retort was not adequately cleaned. The use of a roughing pump to evacuate the retort may not have been adequate to remove all of the gases; and also the stop-off that was used may have introduced contaminants while outgassing.

Some deformation of the material at or near the bond line was evident (see Fig. 3.14) as the cover plate had increased locally in width and decreased in thickness by ~0.5 mm.

To improve the bonding, the following changes are recommended:

1. Evaluate using a pumping station that includes a diffusion pump to remove gases from the retort. Backfilling of the retort with high purity helium-hydrogen mixture would help prevent ingress of air should leaks in the retort occur during bonding.

2. Pre-baking of the stop-off to remove gases prior to bonding may also remove a source of bonding surface contaminants.

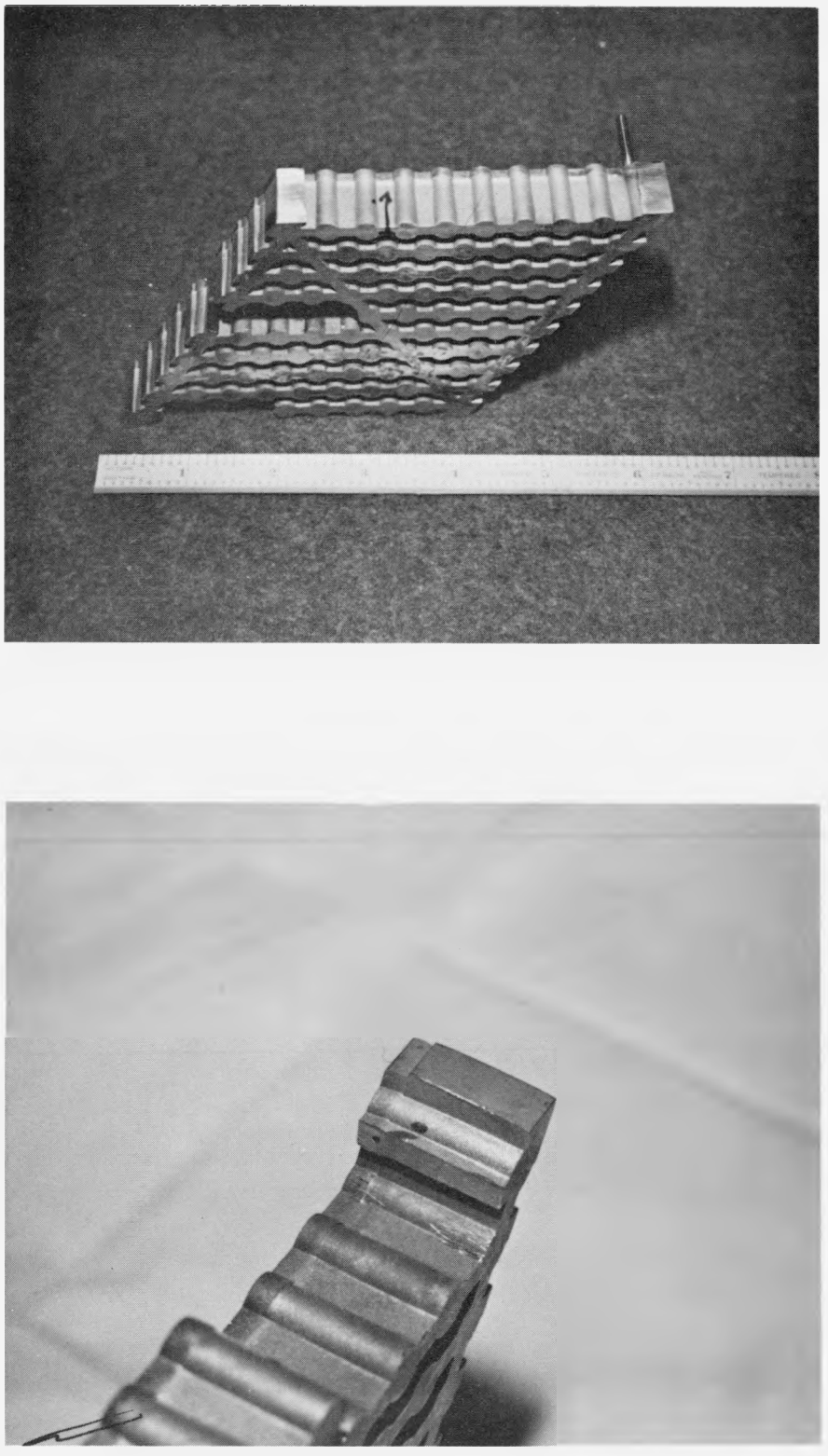

Fig. 3.12 Manifold after diffusion bonding (and sectioning), showing "barreling" of cover plate

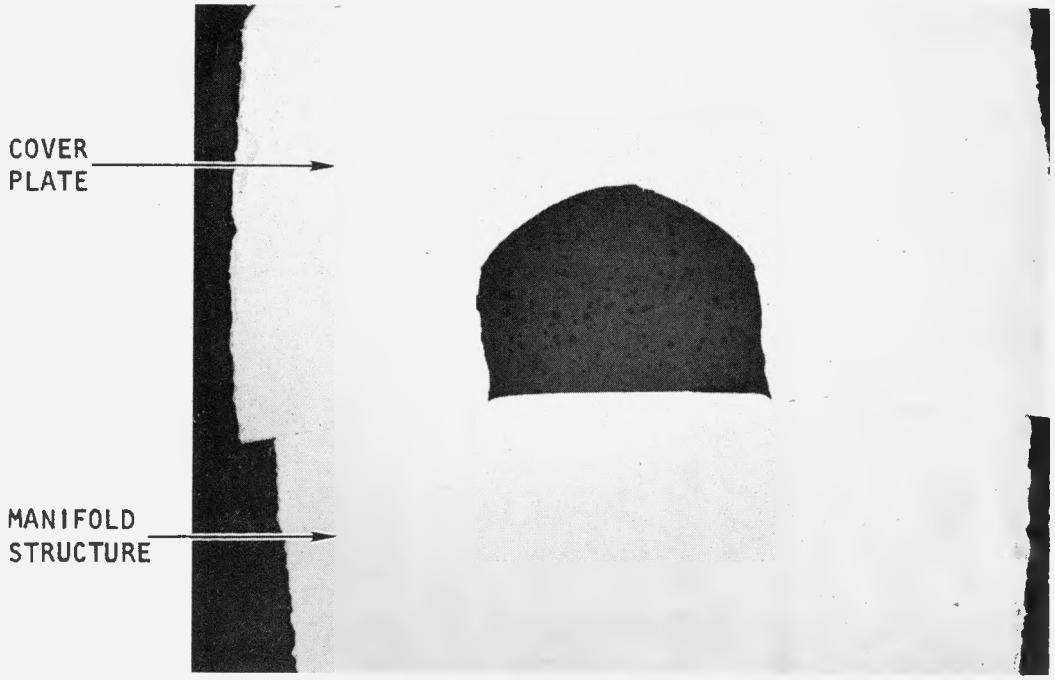

Fig. 3.13 Diffusion bonding of cover plate with milled fission gas passage to manifold structure. Note that deformation, primarily of cover plate, has occurred (both parts were initially the same in width) and only partial bonding has taken place.

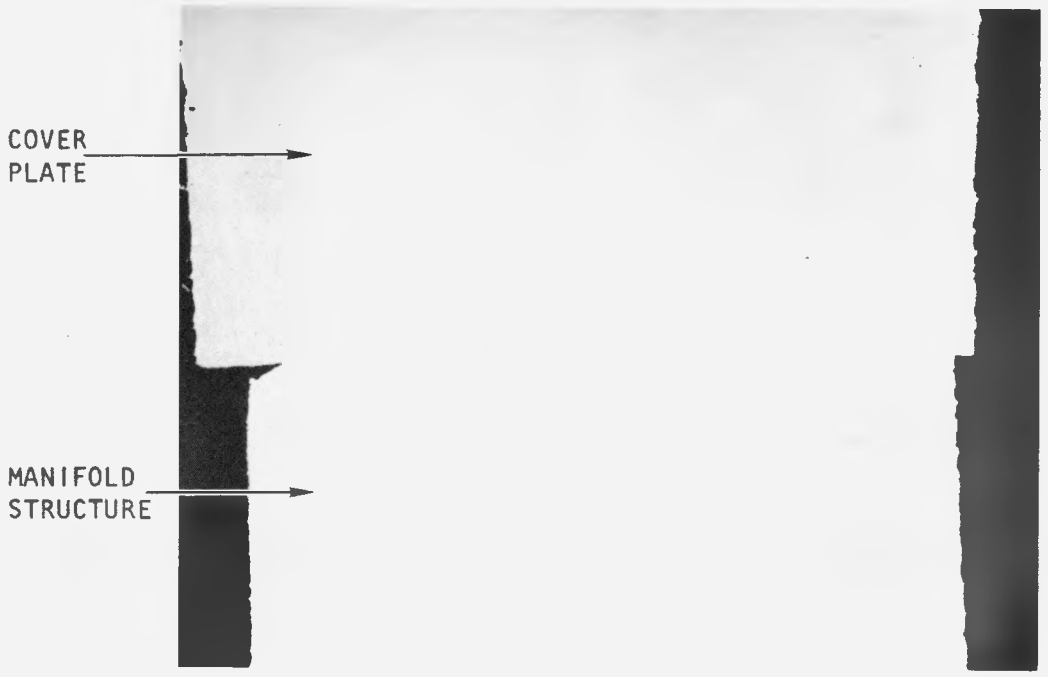

Fig. 3.14 Partial bonding between cover plate and manifold structure

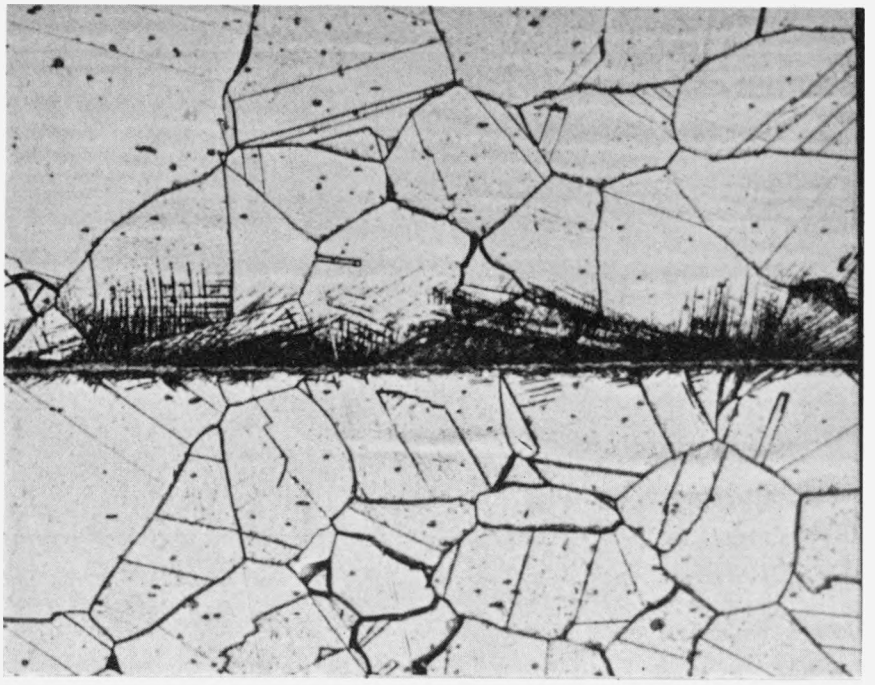

ETCHED

250X

Fig. 3.15 Presence of foreign material in bond line between cover plate and manifold structure. Material is believed to have resulted from contaminants in retort atmosphere.

3. In addition to the above, DWA Composite Specialties, Inc. suggests use of a 0.05 mm thick Ni foil at the interface to improve bonding characteristics. The foil would deform in shear more readily than the parent material and provide more uniform intimate contact of the surfaces to enhance diffusion across the interface.

After bonding, a long term high temperature vacuum heat treatment to increase the amount of diffusion may also be considered.

3.4.6. Non-Destructive Methods

A report was received from GA Quality Control Engineering on the evaluation of several non-destructive inspection methods for the GCFR fission product manifolds. The results are summarized below:

1. Radiography

   Neutron radiography showed poor resolution for flaw detection because of metal thickness and neutron absorption properties, but it should be a good method for determination of location of fission gas passage holes.

   X-radiography was not satisfactory in resolving flaws of the sizes required (i.e., those which could cause sealing problems at the rod/manifold seal surface). One problem is that large and variable grain size in the castings create x-ray diffraction patterns.

2. Ultrasonic

   Flaw calibration of artificial defect holes 1.2 mm (0.047 in.) and 1.98 mm (0.078 in.) in diameter were resolvable in the manifold segments, and the castings could be examined to within ~5 mm (0.2 in.) of the top, rounded surfaces.

3.5 PES PROGRAM PLANNING

No reportable results were achieved during this quarter.

REFERENCE

1. "Gas-Cooled Fast Breeder Reactor Quarterly Progress Report for the Period August 1, 1975 through October 31, 1975," USERDA Report GA-A13766, General Atomic, January 1976.

IV. CORE ASSEMBLIES STRUCTURAL-THERMAL-FLOW TESTS (189a No. SU006)

A series of out-of-pile simulation tests are to be performed to demonstrate the ability of the GCFR fuel-, control-, and blanket-assembly designs to meet design goals and to verify predictions of analytical models that describe design operation and accident behavior. The test emphasis will be on obtaining thermal-structural data for steady-state, transient, and margin conditions using electrically heated rod bundles in a dynamic helium loop. The requirements include testing in the range of cladding melting and the consequences of local initiation of melting.

The "Program Plan for the GCFR Core Flow Test Loop"[1] contains the requirements for the test program to be conducted in the core flow test loop (CFTL) that will be constructed and operated by Oak Ridge National Laboratory (ORNL). Principal work during this quarterly period has included:

1. The study of budget and schedule options.
2. The preparation of a computer code to aid in evaluating proposed test conditions.
3. The specification of the steady-state tests for the preliminary test series.
4. The recommendation of a maximum test section space envelope.

4.1. PROGRAM PLANNING

4.1.1. Budget/Schedule Options

During this quarter, the planning effort has concentrated on developing budget/schedule options to make the CFTL available at the earliest

possible date with various funding assumptions. A review of the CFTL has indicated that it qualifies under ERDA guidelines for operating funding. Thus the options that were considered are (1) funding the CFTL as a "Line Item" in FY-77 or FY-78 and (2) a high or low level of operating funding in FY-77 with follow-on operating funding in subsequent years. Approximately equally time-consuming in establishing the CFTL schedule, according to recent information from ORNL, are the following three parallel activities: general loop design and construction (29 months), circulator procurement (31 months) and heater development (~30 months). This balance of program activities is being accomplished by concentrating current ORNL efforts on the circulator development. Either FY-77 line-item funding or a high level of FY-77 operating funding will provide for initial loop operation in mid-1979. FY-78 line-item funding will delay operation to mid-1980 while a low level of FY-77 operating funding will allow initial loop operation in the first quarter of 1980. ORNL accounting practices will require 10% more funding for CFTL construction on operating funding.

4.1.2. PERT* Network

The draft PERT type schedule for CFTL was reviewed with ORNL during this quarter. An improved GA version of RECS* was run with CFTL input and provided a clearer picture of network slack times. Further PERT development is being continued as a low priority activity.

4.2. TEST ANALYSIS AND PREDICTION

4.2.1. Bundle Performance

The preparation of test specifications (Section 4.3) required test analysis and prediction to aid in adequately identifying and modeling the test range. To facilitate these computations, a special purpose computer code "TSPEC" is being developed to process test input parameters

*The PERT program in use at GA employs PERT, CPM, and cost control techniques and is referred to as the Resource Evaluation and Control System (RECS).

and predict the dependent performance parameters for each test condition. The initial approach is to predict overall bundle geometry, coolant temperatures, surface temperatures, pressure drops, and bundle thermal expansion, on a simplified analytic basis. The code has been developed to the point where steady-state bundle performance is predicted over the range of operating conditions, from laminar flow to fully developed turbulent flow, with and without power generation in the heater rods. Predictive performance data have been generated for the steady-state test conditions listed in Section 4.3, "Test Specification," and a sample code output is included in Section 4.3 corresponding to a particular test run.

4.2.2. Transient Modeling

The predicted GCFR scram transients were examined to determine how to create an adequate yet simple mathematical model for the power and flow variation with time. The objective is to provide an accurate, simple functional relationship in the test specification in which only a few parameters need be specified to cover the range of possible GCFR operating and margin transients. The initial criterion of adequacy was that the coolant outlet temperature duplicate the GCFR predicted condition by $\pm 10°C$, out to 60 seconds after scram. It was determined that a single-linear transient relationship was adequate for decreasing power to an afterheat level of 10% and that flow would require two linear functions to approach the above simulation criteria.

The initial mathematical approximation model is:

$P = 1.0$	$\theta < 0.2s$		
$P = C + C_2 * \theta$	$0.2 \leq \theta \leq 0.7s$	$C_1 = 1.36$	$C_2 = -1.80$ 1/s
$P = 0.1$	$\theta > 0.7s$		
$F = 1.0$	$\theta < 0.2s$		
$F = C_3 + C_4 * \theta$	$2.2 \leq \theta \leq 6.0s$	$C_3 = 1.411$	$C_4 = -0.187$ 1/s
$F = C_5 + C_6 * \theta$	$6.0 < \theta \leq 45s$	$C_5 = 0.319$	$C_6 = -0.00487$ 1/s
$F = 0.1$	$\theta > 45s$		

where P = power fraction,

F = flow fraction,

θ = time in seconds.

The initial evaluation neglected the stored energy in the heater rods, and to compensate for the difference between heater rods and fuel rods it will probably be necessary to increase the power to the heater rods during the first few seconds of the transient. The loop and bundle simulation models (see Section 4.2.3) are being used to determine the necessary model modification to account for stored energy effects.

4.2.3. CFTL Dynamic Simulation

Work has been completed on the code for the transient thermal-hydraulic simulation of the CFTL. The code has been placed on the catalog file "CFTL*SIM." The portion of the code that models the rod bundles is capable of simulating either nuclear heated GCFR rods or electrically heated CFTL heater rods, and has been placed in a separate file called "GCFR-RODS* CFTL-HEATERS." Two studies have been done using "GCFR-RODS*CFTL-HEATERS." The first involved determining the time constants of a GCFR fuel rod and a CFTL heater rod and the second study investigated an approach to compensating for the thermal response difference between a GCFR fuel rod and a CFTL heater rod.

The determination of cladding thermal response time constants* was done for two transients: a 10% reduction in power and a 10% reduction in flow. Table 4.1 lists the average cladding thermal response time constants for both the GCFR rods and the CFTL heaters. The CFTL heater rods respond to changes in power approximately 48% faster than GCFR fuel rods. This is due partly to the higher heat capacity of the GCFR fuel, when compared to the CFTL heater element, and partly to the presence of a gap between the fuel and the cladding, and its absence on the CFTL heaters.

*The time constant is defined as the time in seconds for the transient term to be reduced to $1/e = 0.368$ of its initial value. It is a measure of the speed of response to a transient.

Table 4.1

COMPARISON OF CLADDING THERMAL RESPONSE TIMES FOR GCFR FUEL RODS AND CFTL HEATERS

Average Response Time Constant[a] (Seconds)			
Power Changes		Flow Changes	
GCFR Rods	CFTL Heaters	GCFR Rods	CFTL Heaters
4.02	2.07	0.84	1.21

[a]The time constant is defined as the time in seconds for the transient term to be reduced to 1/e = 0.368 of its initial value.

(The gap conductance for the GCFR fuel rods was taken to be 11.3 $kW/m^2/°K$ [2000 $BTU/hr/ft^2/°F$] for this study.) For flow changes, it was found that the cladding thermal response of the CFTL heaters was approximately 44% slower than that of the GCFR rods. The gap between the fuel and cladding increases the radial thermal resistance of the GCFR fuel rods, and therefore the cladding responds more independently.

For the second study, the bundle simulation model was used to determine the response of the CFTL heater rod bundles to the power and flow transient corresponding to the GCFR scram. It was also used to examine how to modify the power transient to account for the different response characteristics of the CFTL heaters compared to GCFR fuel rods. Three transients were considered: first, the GCFR scram, second a linearized scram, whose power and flow transients are discussed in Section 4.2.2, and third, a modified linearized scram that added power to compensate for the smaller heat capacity of the heaters. The three transients and the resulting cladding thermal responses are shown in Fig. 4.1. Figure 4.1a shows the power and flow variation during a reactor scram, and Fig. 4.1b shows the cladding temperature response of nuclear heated GCFR rods to this transient. As can be seen, there is an initial period of overcooling during which the cladding temperatures drop rapidly, followed by a brief period of undercooling as the stored heat in the fuel rod heats the cladding, followed

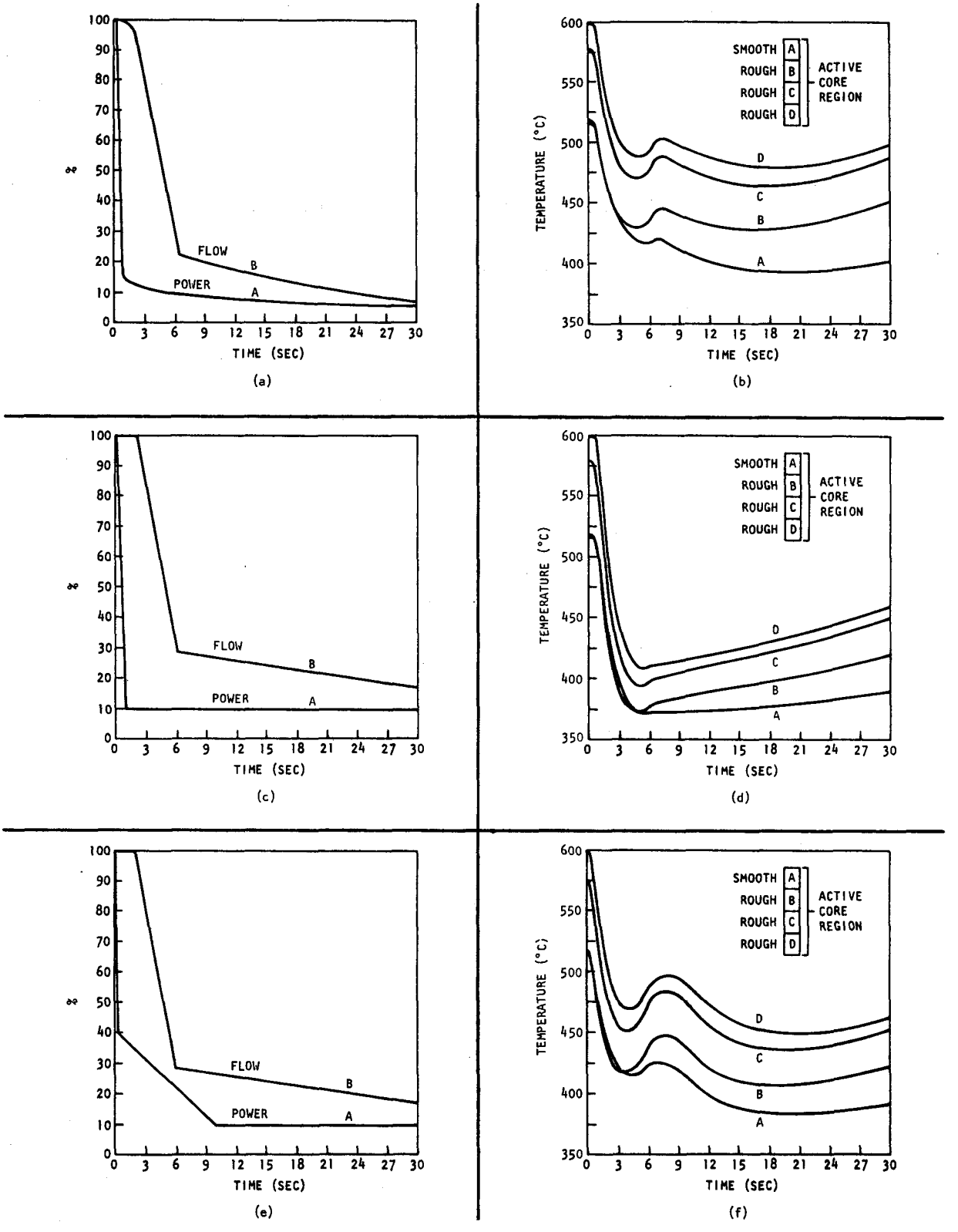

Fig. 4.1 Power and flow transients and cladding thermal response: (a) and (b) for GCFR scram; (c) and (d) for linearized scram; (e) and (f) for modified scram

again by overcooling, and then finally a gradual rise in temperature towards equilibrium. It is desirable that the cladding temperature transient experienced by the CFTL electrically heated rods exhibits a similar behavior.

Figure 4.1c shows the power and flow variation for the linearized version of the GCFR scram transient, and Fig. 4.1d shows the cladding temperature response of the CFTL electrical heaters to this transient. As can be seen, the initial cladding temperature drop is more severe in this case, and the dip in cladding temperatures following the peak occurring at about 8 seconds in the GCFR case is absent. In order to obtain a heater rod response more closely resembling the GCFR rod response, a modification of the power transient was made. This consisted of adding power to the heaters during the initial 10 seconds of the transient, as shown in Fig. 4.1e. The temperature response of the electrical heaters, Fig. 4.1f, is now a more satisfactory simulation of the response expected of the GCFR rods shown in Fig. 4.1b.

4.3. TEST SPECIFICATION

4.3.1. Format

A draft of the test specification format was distributed for review and comments during last quarter. Most of the suggestions by ORNL have been resolved. The format shown in Table 4.2 is being adopted to prepare the specification for the first group of tests, the Preliminary Test Series.

4.3.2. Preliminary Steady-State Test

There are five main groups of steady-state tests in the Preliminary Test Series as outlined in the Program Plan.[1]

1. P-1.1, zero power.
2. P-2.1, uniform power.
3. P-2.2, skewed power.

Table 4.2

TEST SPECIFICATION FORMAT FOR CFTL TESTS

Title and Issue Summary Sheet (GA Form 777):

- Title of Document
- Document Number
- Issue Letter
- Issue Date
- Name of Document Preparer (Initialed to show approval)
- Names, Signatures, and Dates of GA Departmental Approvals
- Purpose of the Issue or of the Change Thereto
- Document Control Center Release Date
- (This sheet will be Page 1 of the document.)

Table of Contents

- Title of Each Section of the Document
- Title of Each Major Sub-Section
- (This section will be Page 2 of the document; required additional pages will be numbered in sequential order.)

Introduction

- Statement about the CFTL Test Program in Relation to the GCFR Program
- Statement about the Specific Test Series and Purpose of Each Test
- Number of Planned Tests
- Description of Test Bundles:
  - Type of rod bundle - simulated fuel, control, or blanket
  - Bundle identification letter
  - Number of rods
- References:
  - Program plan
  - Test bundle drawings
  - Applicable pre-test analyses

Test Requirements

- Test Number
- (The following items will apply to each test number.)
  - Bundle configuration (e.g., number of heater rods; heated or unheated bundle)
  - Specific test objectives
  - Design-related reason for the specific test
  - Operating conditions and limitations:
    - Heater power distribution
    - Helium mass flow
    - Helium impurity
    - Bundle inlet helium pressure
    - Bundle inlet helium temperature
  - Test data to be measured (sensors at specified locations):
    - Temperatures
    - Helium flow
    - Helium pressures and differential pressures

Table 4.2 (continued)

Test Requirements (continued)

- Strain, Vibration, Displacement } (where applicable)
- Special measurements
- Table of measurements:
  - Points of measurement - test condition
  - Range of measurements
  - Required accuracy of measurements
  - Number of data runs
- Criteria for acceptable data
- Statement(s) of the importance of the specific measurements
- Description of interim and post-test examinations

Data Format

This section will include the detailed requirements for data presentation to GA, such as magnetic tape, computer printout, raw data. Compatibility requirements between GA and ORNL data processing and data reduction equipment, if any, will be stated.

Description of Measurement

Type (Temperature, Pressure, etc.)
Location - Drawings and Table Combined

Safety Requirements

A statement to the effect that the test procedures will follow acceptable ORNL safety standards.

Special Requirements

Statement that ORNL will prepare a test procedure for each test, and that the procedure will be reviewed by GA.

Statement(s) in reference to test bundle handling, cleanliness, etc., where applicable.

Statement(s) on schedule constraints, such as: certain test information is required before continuing or initiating other scheduled activity.

Quality Assurance Requirements

Statement(s), where applicable, on such items as:
- Pre-test and post-test inspection of test bundles
- Identification of "hold-points" to be incorporated into the test procedure
- Acceptable criteria for the test
- Monitoring of the test procedure

(In addition to the above information, each page will contain the document title and/or document number and issue letter and document page number.)

4. P-2.3, single powered rod.
5. P-2.7, full uniform power-reduced coolant flow.

The groups consist of as many as 21 tests, each of which contains a number of runs as specified in the input information. Tables 4.3 through 4.7 list values for the following input information applicable to the individual tests: heater rod power, bundle coolant flow, bundle inlet temperature, bundle inlet pressure, power factor range, flow factor range, and number of runs. For a particular test, the power and flow condition for the runs are linearly distributed from the initial to final range values.

Table 4.3 lists the input information for the initially planned group of steady-state tests. The four tests are for unheated rods, i.e., zero power. Only the coolant flow is varied through turbulent, transition, and laminar conditions to measure the pressure drops within the bundle for correlation with the Reynolds numbers. Measured output information will give an indication of an upper flow limit based on the total obtainable pressure drop for the CFTL.

Table 4.4 lists the input information for the first group of tests with uniformly powered (transversely) heater rods. The input conditions represent those expected for fuel bundles at various locations within a reactor, i.e., temperature, pressure, and flow conditions in the turbulent, transition, and laminar flow ranges.

Table 4.5 lists input information for steady-state flow with skewed power distribution for various bundle positions within a reactor, and for representative conditions of core maximum and average power and afterheat power.

Table 4.6 lists the input for tests with a single heated rod under steady-state turbulent, transition, and laminar flow conditions. The predicted data for Tests P-2.3.1 and P-2.3.2 will be compared to that obtained for the actual test data for each of the 31 heater-rod positions

Table 4.3

TEST CONDITION INFORMATION FOR CFTL TEST SERIES GROUP P-1.1 STEADY-STATE FLOW - ZERO POWER - FUEL BUNDLE C

Test No.	Heater Rod Power (kW)			Bundle Flow (kg/s)	Inlet Temp. (°C)	Inlet Press. (MPa)	Power Factor		Flow Factor		No. of Runs	Simulation - Comments
	Average	Maximum	Minimum				Maximum	Minimum	Maximum	Minimum		
P-1.1.1	0.0	0.0	0.0	0.868	325	9.0	1.0	1.0	1.3	0.1	13	General operating flow conditions - 10% to 110% of GCFR flow
P-1.1.2	0.0	0.0	0.0	0.868	325	9.0	1.0	1.0	1.0	0.7	30	50% to 85% of GCFR flow - small incremental flow changes, study for flow induced vibrations
P-1.1.3	0.0	0.0	0.0	0.868	325	9.0	1.0	1.0	0.1	0.02	9	Detection of and operation in the transition flow range
P-1.1.4	0.0	0.0	0.0	0.868	325	9.0	1.0	1.0	0.25	0.005	8	Detection of and operation in the laminar flow range

Table 4.4

TEST CONDITIONS INPUT INFORMATION FOR CFTL TEST SERIES GROUP P-2.1 STEADY-STATE FLOW - UNIFORM POWER - FUEL BUNDLE C

Test No.	Heater Rod Power (kW)			Bundle Flow (kg/s)	Inlet Temp. (°C)	Inlet Press. (MPa)	Power Factor		Flow Factor		No. of Runs	Simulation - Comments
	Average	Maximum	Minimum				Maximum	Minimum	Maximum	Minimum		
P-2.1.1	28.0	28.0	28.0	0.75	325	9.0	1.1	0.1	1.1	0.1	11	Center GCFR assembly - predicted operation.
P-2.1.2	28.0	28.0	28.0	0.75	325	9.0	1.1	0.1	1.1	0.1	11	Center GCFR assembly - 7% undercooled.
P-2.1.3	28.0	28.0	28.0	0.80	325	9.0	1.1	0.1	1.1	0.1	11	Center GCFR assembly - 7% overcooled.
P-2.1.4	24.0	24.0	24.0	0.64	325	9.0	1.1	0.1	1.1	0.1	11	Ring 3 GCFR assembly - predicted operation.
P-2.1.5	24.0	24.0	24.0	0.75	325	9.0	1.1	0.1	1.1	0.1	11	Ring 3 GCFR assembly - 15% overcooled.
P-2.1.6	21.0	21.0	21.0	0.56	325	9.0	1.1	0.1	1.1	0.1	11	Ring 7 GCFR assembly - predicted operation.
P-2.1.7	21.0	21.0	21.0	0.75	325	9.0	1.1	0.1	1.1	0.1	11	Ring 7 GCFR assembly - 30% overcooled.
P-2.1.8	28.0	28.0	28.0	0.75	325	9.0	1.0	0.1	1.0	1.0	10	Overcooling study.
P-2.1.9	2.91	2.91	2.91	0.08	325	9.0	1.0	0.05	1.0	0.05	20	Transition and laminar flow study - full pressure
P-2.1.10	28.0	28.0	28.0	0.75	325	6.0	1.0	0.1	1.0	0.1	11	Center GCFR assembly - reduced pressure ~60 atm.
P-2.1.11	28.0	28.0	28.0	0.75	325	3.0	1.0	0.1	1.0	0.1	11	Center GCFR assembly - reduced pressure ~30 atm.
P-2.1.12	2.91	2.91	2.91	0.08	325	0.2	1.0	0.05	1.0	0.05	20	Transition and laminar flow study - 2 atm.
P-2.1.13	2.91	2.91	2.91	0.08	325	0.1	1.0	0.05	1.0	0.05	20	Transition and laminar flow study - 1 atm.

Table 4.5

TEST CONDITION INPUT INFORMATION FOR CFTL TEST SERIES GROUP P-2.2 STEADY-STATE FLOW - SKEWED POWER - FUEL BUNDLE C

Test No.	Heater Rod Power (kW)			Bundle Flow (kg/s)	Inlet Temp. (°C)	Inlet Press. (MPa)	Power Factor		Flow Factor		No. of Runs	Simulation - Comments
	Average	Maximum	Minimum				Maximum	Minimum	Maximum	Minimum		
P-2.2.1	28.0	28.3	27.7	0.75	325	9.0	1.1	0.1	1.1	0.1	11	GCFR assembly 2.01 - 0.1 kW/row skew.
P-2.2.2	26.0	26.6	25.4	0.70	325	9.0	1.1	0.1	1.1	0.1	11	GCFR assembly 4.02 - 0.2 kW/row skew.
P-2-2-3	21.0	22.2	19.8	0.56	325	9.0	1.1	0.1	1.1	0.1	11	GCFR assembly 6.01 - 0.4 kW/row skew.
P-2.2.4	18.0	19.8	16.2	0.50	325	9.0	1.1	0.1	1.1	0.1	11	GCFR assembly 7.06 - 0.6 kW/row skew.
P-2.2.5	25.0	26.8	23.2	0.67	325	9.0	1.1	0.1	1.1	0.1	11	Core average power - 0.6 kW/row skew, margin-max.
P-2.2.6	25.0	27.7	22.3	0.67	325	9.0	1.1	0.1	1.1	0.1	11	Core average power - 0.9 kW/row skew, margin-max. + 50%.
P-2.2.7	25.0	28.6	21.4	0.67	325	9.0	1.1	0.1	1.1	0.1	11	Core average power - 1.2 kW/row skew, margin-max. + 100%.
P-2.2.8	2.91	3.06	2.76	0.08	325	9.0	1.0	0.05	1.0	0.05	20	Afterheat power - 50 W/row, margin-max.
P-2.2.9	2.91	3.21	2.61	0.08	325	9.0	1.0	0.05	1.0	0.05	20	Afterheat power - 100 W/row, margin-max. + 100%
P-2.2.10	2.91	3.06	2.76	0.08	325	0.2	1.0	0.05	1.0	0.05	20	Afterheat power - 2 atm - 50 W/row skew, margin-max.
P-2.2.11	2.91	3.06	2.76	0.08	325	0.1	1.0	0.05	1.0	0.05	20	Afterheat power - 1 atm - 50 W/row skew, margin-max.

Table 4.6

TEST CONDITION INPUT INFORMATION FOR CFTL TEST SERIES GROUP P-2.3 STEADY-STATE FLOW - SINGLE HEATED ROD - FUEL BUNDLE C

Test No.	Single Heated Rod Power (kW)	Bundle Flow (kg/s)	Inlet Temp. (°C)	Inlet Press. (MPa)	Power Factor		Flow Factor		No. of Runs	Simulation - Comments
					Maximum	Minimum	Maximum	Minimum		
P-2.3.1	30.0	0.75	325	9.0	1.0	1.0	1.0	1.0	31	Each rod at full power and flow.
P-2.3.2.	3.0	0.08	325	9.0	0.05	0.05	0.05	0.05	31	Each rod at afterheat power and flow.
P-2.3.3.	30.0	0.75	325	9.0	1.1	0.1	1.1	0.1	11	Each of 5 unique rod positions - operating range.
P-2.3.4	3.0	0.08	325	9.0	1.0	0.05	1.0	0.05	20	Each of 5 unique rod positions - transition to laminar flow.
P-2.3.5	30.0	0.75	325	6.0	1.0	0.1	1.0	0.1	10	Each of 5 unique positions - reduced pressure, 2/3.
P-2.3.6	30.0	0.75	325	3.0	1.0	0.1	1.0	0.1	10	Each of 5 unique positions - reduced pressure, 1/3.
P-2.3.7	3.0	0.08	325	0.2	1.0	0.05	1.0	0.05	20	Each of 5 unique positions - transition and laminar flow study at 2 atm.
P-2.3.8	3.0	0.08	325	0.1	1.0	0.05	1.0	0.05	20	Each of 5 unique rod positions - transition and laminar flow study at 1 atm.

Table 4.7

TEST CONDITION INPUT INFORMATION FOR CFTL TEST SERIES GROUP P-2.7 STEADY-STATE FLOW - MARGIN UNDERCOOLING - FUEL BUNDLE D

Test No.	Heater Rod Power (kW)			Bundle Flow (kg/s)	Inlet Temp. (°C)	Inlet Press. (MPa)	Power Factor		Flow Factor		No. of Runs	Simulation - Comments
	Average	Maximum	Minimum				Maximum	Minimum	Maximum	Minimum		
P-2.7.1	28.0	28.0	28.0	0.75	325	9.0	1.1	0.1	1.1	0.1	11	For comparison to P-2.2.1.
P-2.7.2	25.0	28.6	21.4	0.67	325	9.0	1.1	0.1	1.1	0.1	11	For comparison to P-2.2.7.
P-2.7.3	2.91	3.06	2.76	0.08	325	0.1	1.0	0.05	1.0	0.05	20	For comparison to P-2.2.11.
P-2.7.4	30.0	—	—	0.75	325	9.0	1.0	1.0	1.0	1.0	31	Single heated rod for comparison to P-2.3.1.
P-2.7.5	28.0	28.0	28.0	0.67	325	9.0	1.1	0.5	1.1	0.5	7	This and subsequent tests are to check for performance shift with variation in flow.
P-2.7.6	28.0	28.0	28.0	0.61	325	9.0	1.2	0.6	1.2	0.6	4	
P-2.7.7	28.0	28.0	28.0	0.56	325	9.0	1.25	0.75	1.25	0.75	5	
P-2.7.8	28.0	28.0	28.0	0.52	325	9.0	1.25	0.75	1.25	0.75	5	
P-2.7.9	28.0	28.0	28.0	0.48	325	9.0	0.6	1.2	0.6	1.2	4	
P-2.7.10	28.0	28.0	28.0	0.45	325	9.0	0.6	1.2	0.6	1.2	4	
P-2.7.11	28.0	28.0	28.0	0.42	325	9.0	0.6	1.2	0.6	1.2	4	
P-2.7.12	28.0	28.0	28.0	0.40	325	9.0	0.6	1.2	0.6	1.2	4	
P-2.7.13	28.0	28.0	28.0	0.38	325	9.0	0.6	1.2	0.6	1.2	4	
P-2.7.14	28.0	28.0	28.0	0.36	325	9.0	0.8	1.1	0.8	1.1	4	
P-2.7.15	28.0	28.0	28.0	0.35	325	9.0	0.8	1.1	0.8	1.1	4	
P-2.7.16	28.0	28.0	28.0	0.34	325	9.0	0.8	1.1	0.8	1.1	4	
P-2.7.17	28.0	28.0	28.0	0.33	325	9.0	0.8	1.1	0.8	1.1	4	
P-2.7.18	28.0	28.0	28.0	0.32	325	9.0	0.8	1.0	0.8	1.0	3	
P-2.7.19	28.0	28.0	28.0	0.31	325	9.0	0.8	1.0	0.8	1.0	3	
P-2.7.20	28.0	28.0	28.0	0.30	325	9.0	0.8	1.0	0.8	1.0	3	
P-2.7.21	28.0	28.0	28.0	0.29	325	9.0	0.8	1.0	0.8	1.0	3	

at full power and afterheat power with the corresponding flows. There are five unique rod positions within a 37-rod bundle. Therefore, the predicted data obtained for Tests P-2.3.2 through P-2.3.7 will be used for comparison to actual data obtained for each of the five positions.

The first four tests listed in Table 4.7 denote repeat testing on a second bundle. The predicted data obtained for bundle C in the tests noted in the comments column of the table will be used for comparison to actual test data that will be obtained for bundle D. The remaining tests listed are for obtaining data for determining the predicted margin undercooling limit.

The computer code "TSPEC" (Section 4.2) was used to obtain predicted data for the steady-state tests. Table 4.8 lists the input parameters and predicted results for a single run on Test P-2.2, which is a test with a transverse skewed power distribution.

4.4. TEST BUNDLE DESIGN

Based on the need for flexibility to cover possible design changes to GCFR core assemblies, a maximum size test section envelope was established. The envelope is defined as a cylinder 2420 mm long and 288 mm outside diameter. Table 4.9 lists the current dimensions and the likely maximum values for length, diameter, and clearances for the largest test section, which would be for a full-size blanket assembly. Allowance has been made for clearance to accommodate twice the margin duct bowing that is predicted for a GCFR assembly.

Figures 4.2 and 4.3 delineate the current reference fuel and blanket rod designs. The dimensions are those that are required for fabrication of the heaters that will be used to simulate the fuel and blanket rods.

Among the conceptual requirements for heater simulation of GCFR fuel and blanket rods is the axial distribution of heat within the rods. The

Table 4.8

CFTL TEST SPECIFICATION FOR TEST, SAMPLE P-2.2.1, BUNDLE C
(Skewed Power, GCFR Assembly 2.01 - 0.1 kW/Row Skew)

BUNDLE DESIGN
BUNDLE TYPE = FUEL
BUNDLE IDENTIFICATION = C

BUNDLE DATA
RODS PER BUNDLE = 37. HEATED = 31. UNHEATED = 6.
BUNDLE OD = 75.0 MM
DUCT WALL THICKNESS = 2.500 MM
BUNDLE FLOW AREA = 1613. MM**2
DUCT PERIMETER = 210.00 MM
AVG BUNDLE HYDRAULIC DIAMETER = 6.05 MM

ROD DATA
ROD DIAMETER = 7.40 MM
ROD PITCH = 10.00 MM
HEIGHT OF ROUGHENING = .100 MM
PITCH OF ROUGHENING = 1.20 MM
FLOW AREA PER ROD = 43.59 MM**2
H T PERIMETER PER ROD = 23.25 MM
LOCAL HYDRAULIC DIAMETER = 7.50 MM
UPPER BLANKET LENGTH = 650.5 MM
HEATED LENGTH = 1000.0 MM
LOWER BLANKET LENGTH = 450.0 MM
TOTAL LENGTH = 2100.5 MM

ROUGHENING DATA
ROUGHENED FRACTION OF HEATED LENGTH = .750
ROUGHENED LENGTH = 750.0 MM
FRICTION FACTOR MULTIPLIER = 4.40
HEAT TRANSFER MULTIPLIER = 2.30
REFERENCE REYNOLDS NO = 100000.

SPACER AND FLOW COEFFICIENT DATA
NUMBER OF SPACER = 10.
SPACER COEFFICIENT = .600
SPACER SOLIDITY = .179
INLET COEFFICIENT = .100
OUTLET COEFFICIENT = .500

HEATER AXIAL POWER PROFILE
AXIAL QMAX/QAVG = 1.210
QX/QMAX = COS(1.049*(2*X/L - 1))

X/L	QX/QMAX
.000	.4984
.100	.6681
.200	.8084
.300	.9133
.400	.9781
.500	1.0000
.600	.9781
.700	.9133
.800	.8084
.900	.6681
1.000	.4984

Table 4.8 (continued)

```
STEADY STATE TEST SERIES                    NO. OF RUNS = 11
                          POWER      FLOW
  SERIES FACTOR = MAX     1.100     1.100
  SERIES FACTOR = MIN      .100      .100

INPUT PARAMETERS FOR TEST RUN =   5
  TOTAL BUNDLE HEAT INPUT = 607.600 KW
  AVG POWER PER ROD = 19.600 KW
  MAX POWER PER ROD = 19.810 KW
  MIN POWER PER ROD = 19.390 KW
  MAX POWER DENSITY =  239.7 W/CM
  FLOW PER BUNDLE =  .5250 KG/SEC
  HELIUM INLET TEMPERATURE =  325.0 C
  HELIUM INLET PRESSURE =  9.000 MPA

THERMAL OUTPUT PARAMETERS
  AVERAGE BUNDLE OUTLET TEMPERATURE =  547.9 C      TEMPERATURE RISE =    222.9 C
  OUTLET TEMPERATURE - AVG POWER ROD =  591.1 C      TEMPERATURE RISE =    266.1 C
  OUTLET TEMPERATURE - MAX POWER ROD =  593.9 C      TEMPERATURE RISE =    268.9 C
  OUTLET TEMPERATURE - MIN POWER ROD =  588.2 C      TEMPERATURE RISE =    263.2 C
  MAX SURFACE TEMPERATURE =  636.5 C
  MAX SURFACE TEMPERATURE AT X/L = 1.000
  SMOOTH ROD H. T. COEF.( X/L =  .249 ) =  4733. W/M*M/C     FILM DROP =   188.3 C
  ROUGHENED ROD H. T. COEF.(X/L =  .500 ) = 11669. W/M*M/C     FILM DROP =    88.4 C
  ROUGHENED ROD H. T. COEF.(X/L = 1.000 ) = 12353. W/M*M/C     FILM DROP =    41.6 C

FLOW OUTPUT PARAMETERS
  AVG. BUNDLE RE =  55346.    LOCAL RE =  60271.
  BUNDLE PRESSURE DROP
    INLET =    .778 KPA
    UPPER BLANKET =  16.992 KPA
    SMOOTH CORE LENGTH =   8.020 KPA
    ROUGHENED CORE LENGTH =  94.056 KPA
    LOWER BLANKET =  64.552 KPA
    ACCELERATION LOSS =   2.934 KPA
    SPACERS LOSS =  14.879 KPA
    OUTLET LOSS =   5.341 KPA
  TOTAL BUNDLE PRESSURE DROP = 207.553 KPA

THERMAL EXPANSION PARAMETERS
  THERMAL INPUT     AS FABRICATED          TEST TEMPERATURES
                                          DUCT      ROD     DIFFERENTIAL
    AVERAGE            2100.5           2116.4    2117.7      1.3 MM
    HOTTEST            2100.5           2116.4    2117.7      1.3 MM
    COLDEST            2100.5           2116.3    2117.6      1.2 MM
  MAX BOW DISPLACEMENT =   2.2 MM
  DIAMETRAL CLEARANCE =   78.8 MM
  MINIMUM DIAMETRAL CLEARANCE =   76.9 MM
```

Table 4.8 (continued)

STEADY STATE RUN = 5

AXIAL PRESSURE, POWER, AND TEMPERATURE VALUES

LOCATION	X MM	X/L	DP KPA	AVERAGE POWER W/CM	AVERAGE HELIUM C	AVERAGE CLAD C	MAXIMUM POWER W/CM	MAXIMUM HELIUM C	MAXIMUM CLAD C	MINIMUM POWER W/CM	MINIMUM HELIUM C	MINIMUM CLAD C
INLET	.0		.778	.0	325.0	325.0	.0	325.0	325.0	.0	325.0	325.0
CORE INLET	650.5	.000	22.378	118.2	325.0	427.5	119.5	325.0	428.6	116.9	325.0	426.3
SMOOTH	775.5	.125	27.290	167.5	349.4	498.7	169.3	349.6	500.8	165.7	349.1	496.7
SMOOTH	899.5	.249	32.163	205.0	380.9	567.0	207.2	381.5	569.8	202.8	380.3	564.2
ROUGH	901.5	.251	32.163	205.5	381.5	457.1	207.7	382.1	458.5	203.3	380.9	455.6
ROUGH	1150.5	.500	65.195	237.2	458.0	545.4	239.7	459.5	547.8	234.6	456.6	543.0
ROUGH	1250.5	.600	78.461	232.0	490.0	575.2	234.4	491.8	577.9	229.5	488.2	572.4
ROUGH	1350.5	.700	91.726	216.6	520.5	599.6	218.9	522.6	602.6	214.3	518.5	596.7
ROUGH	1450.5	.800	104.992	191.7	548.4	617.9	193.8	550.8	621.1	189.7	546.0	614.7
ROUGH	1550.5	.900	118.258	158.4	572.2	629.2	160.1	574.9	632.5	156.7	569.6	625.9
ROUGH	1600.5	.950	124.891	139.1	582.3	632.1	140.6	585.1	635.4	137.6	579.6	628.8
CORE OUTLET	1650.5	1.000	131.524	118.2	591.1	633.2	119.5	593.9	636.5	116.9	588.2	629.9
OUTLET	2100.5		207.553	.0	591.1	591.1	.0	593.9	593.9	.0	588.2	588.2

Table 4.9

TEST SECTION SIZE ENVELOPE[a] FOR BLANKET ASSEMBLY

	Current Design (mm)	Likely Upper Range Value (mm)
Length Parameters		
Length from top of inlet grid to top of blanket	130	130
Blanket length	1970.5	1970.5
Lower end plug	9	9
Outlet nozzle and instrumentation	280	280
Total as fabrication	2389.5	2389.5
Total - hot (1100°C)	2420	2420
Blanket OD (across corners)[a]		
As fabricated	195	212
Hot (1100°C)	199	216
Clearance Circle		
Margin bow with $\Delta T = 260°C$	80	80
Envelope diameter (bundle offset from center)	271	288

[a]Values are based on GCFR fuel assembly. The test blanket assembly will have the same outside diameter.

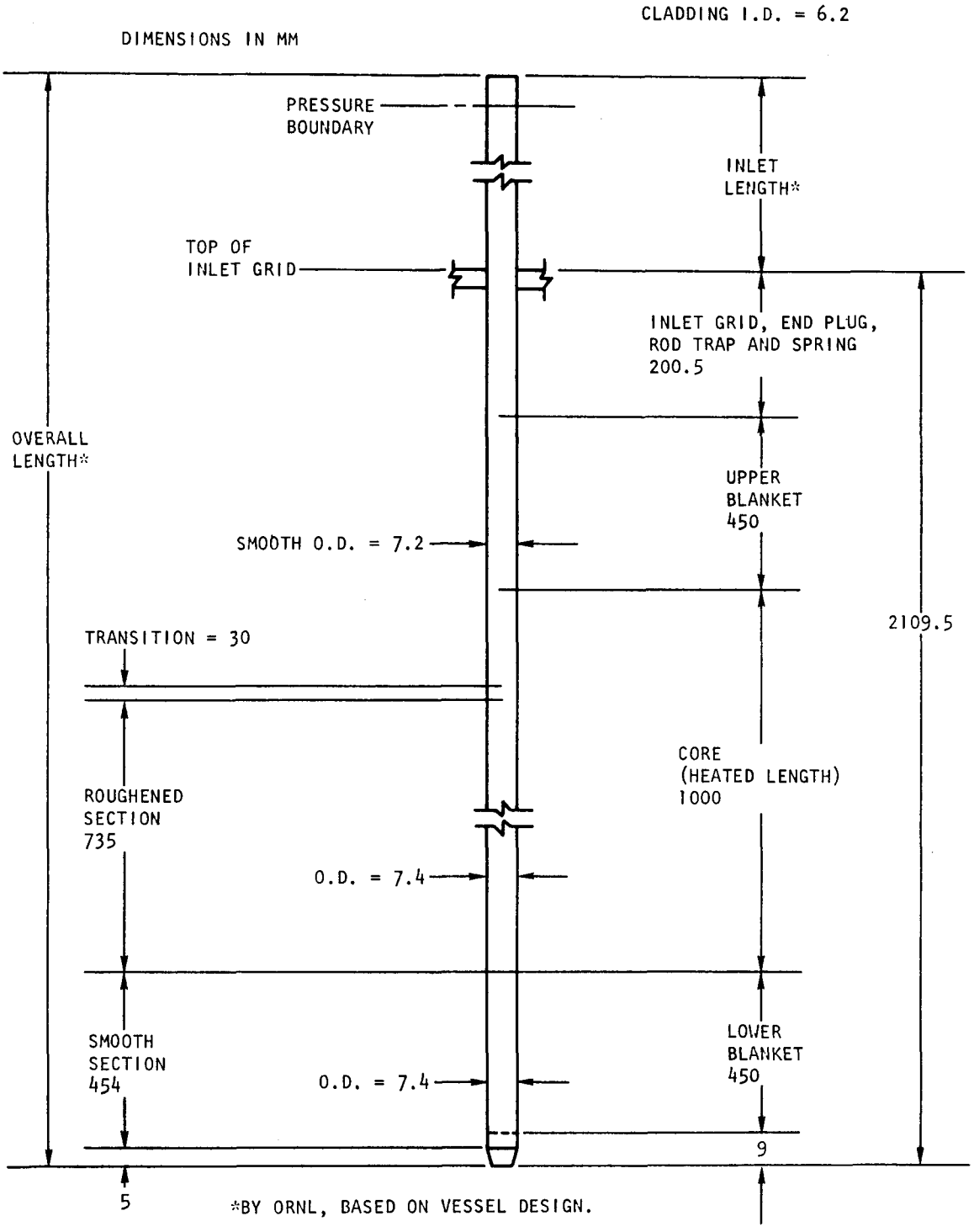

Fig. 4.2 GCFR reference fuel rod design for CFTL

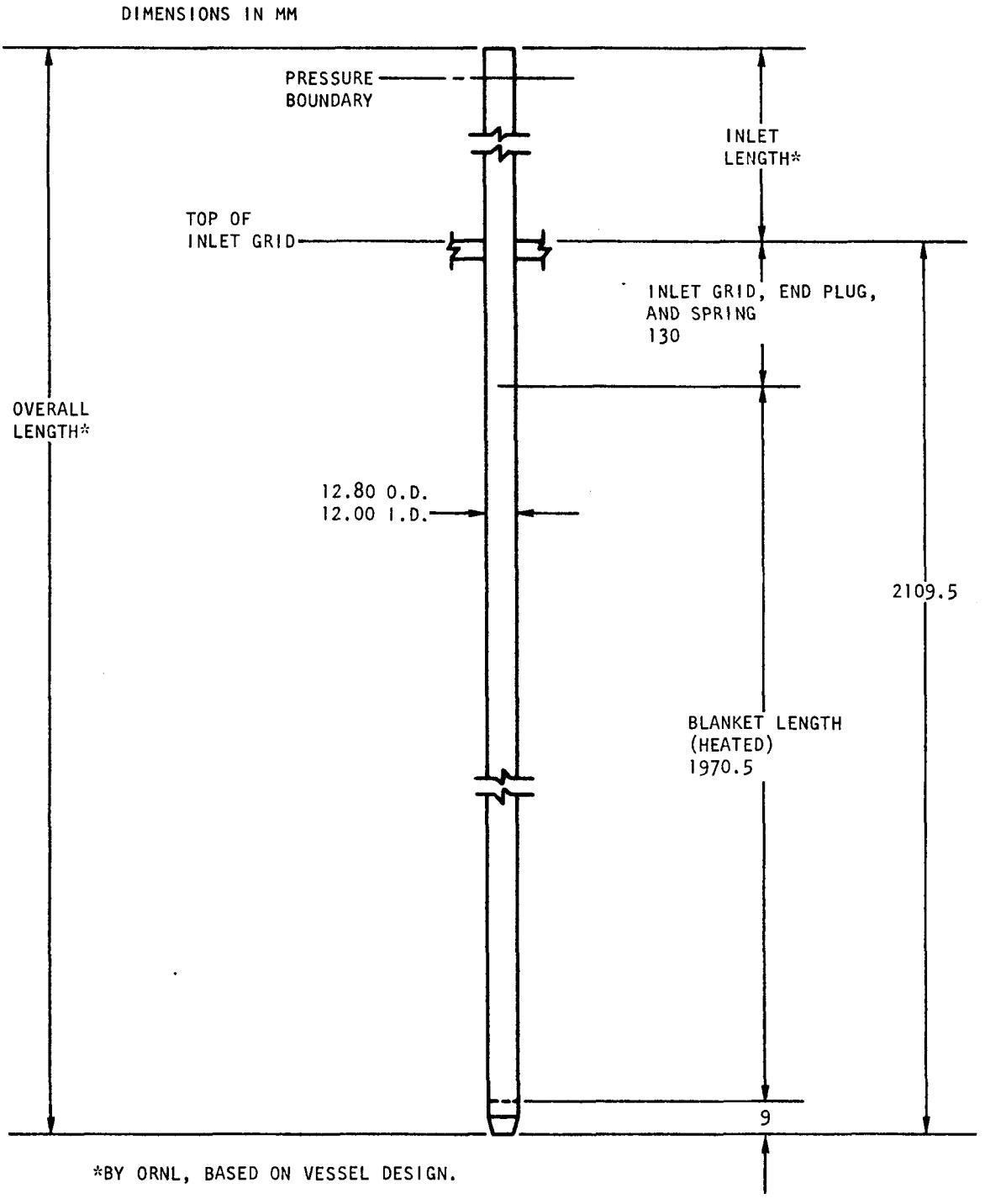

Fig. 4.3 GCFR reference blanket rod design for CFTL

heat distribution for a fuel rod must be the chopped cosine value with maximum/average ratio of 1.21. This is equivalent to a heat distribution ratio of

$$Q = \text{COS } 1.049 \left(\frac{2X}{L} - 1 \right) ,$$

where X = distance from start of the heated zone,
L = total length of the heated zone,
(independent variable is in radians).

The heat distribution for a blanket rod must be the cosine distribution. The analytic expression for the heat distribution ratio is

$$Q = 0.52 + 0.48 \text{ COS } 1.570 \left(\frac{2X}{L} - 1.86 \right) ,$$

where X = distance from start of the heated zone in mm,
L = 1100 mm,
(independent variable is in radians).

4.5. LIAISON WITH ORNL

There was no CFTL review meeting held during this quarter. However, contact was continued by exchange of reports and phone conversations. The last review meeting was held in mid-September 1975 as discussed in the last quarterly report[2], and the next review meeting is scheduled for March, 1976. In the interim, GA has provided ORNL with specific information on: desired low flow test operation of CFTL bundles for safety studies, a definition of the maximum test size envelope, and current reference fuel and blanket rod designs. ORNL has provided GA with specific information on: a proposal to study reliability and accuracy of small-diameter thermocouples, review of the test specification format, and revised loop completion schedules based on various proposed funding options with an earliest start-up date of mid-1979.

REFERENCES

1. Hopkins, H. C., Jr., "Program Plan for GCFR Core Flow Test Loop," USAEC Report GA-A13080, General Atomic, August 1974.

2. "Gas-Cooled Fast Breeder Reactor Quarterly Progress Report for the Period August 1, 1975 through October 31, 1975," USERDA Report GA-A13766, General Atomic, January 1976.

V. FUELS AND MATERIALS ENGINEERING (189a No. SU007)

5.1. OXIDE FUEL, BLANKET, AND GRID PLATE SHIELDING MATERIALS TECHNOLOGY

It is the responsibility of this subtask to maintain liaison with and surveillance of other ERDA and non-ERDA programs, especially the LMFBR program, to ensure the availability of all relevant information for the GCFR design. The areas included in this subtask are

1. Oxide fuel technology.
2. UO_2 (axial) blanket technology.
3. ThO_2 (radial) blanket technology.
4. Grid plate shielding technology.

During this quarterly reporting period, updated test matrices of current GCFR fast-flux irradiations F-1 (X094) and F-3 (X206) were provided to the national Fuel-Cladding Chemical Interaction Program (FCCI) steering group for use in their compilation of data on fast-flux irradiations and in planning for future programs of research and development in the area of fuel/cladding chemical interactions. The current status of these irradiations was also reviewed.

A tentative test matrix for the planned F-5 (prototype) irradiation test was also submitted to the FCCI steering group.

The evaluation of the results of the Kr-85 annealing technique for the determination of in-pile cladding operating temperatures using data obtained under the irradiation task (see Section 5.4) has been completed; a final report has been prepared and is currently undergoing review. Our

assessment indicates that although the technique shows promise for fuel rods not subjected to cladding corrosion or interaction with the fuel, the latter effects when extensive have the potential for producing highly erroneous results and thus destroying the potential of the method.

A review of the LWBR Environmental Impact Statement to obtain data on the irradiation of thoria as a radial blanket material is under way. However, completion of the review will be delayed by recent funding reductions in this task.

5.2. CLADDING TECHNOLOGY

5.2.1. Mechanical Testing Program at Argonne National Laboratory

The purpose of this program is to determine the effects of the following factors on the behavior and mechanical properties of GCFR cladding:

1. Ribs, rib geometry, and fabrication technique.
2. Impurity levels in helium typical of the GCFR.

These tests are being conducted in a quasi-static helium environment at Argonne National Laboratory. General Atomic participates in an advisory, consultative, and evaluative role. Testing of the initial test matrix has been completed.

During this reporting period, tests using the second test matrix were initiated and are in progress at ANL. The test matrix is shown in Table 5.1 for reference. Ribbed cladding produced by mechanical grinding by Superior Tube Company and by electrochemical etching by GA are included in this test. For comparison purposes, smooth cladding with an outside diameter equal to the root diameter of the ribbed cladding, produced by electrochemical etching and by centerless grinding, is also included. The tests

Table 5.1

GENERAL TEST MATRIX FOR THE SECOND TEST SERIES AT ANL

Group	Specimen Quantity[a]	Nominal Length (cm)	Nominal ID (cm)	Nominal Stress[b] (MPa)	Temperature (°C)
A - Chemically Etched Smooth	9	9.83	0.668	238	650
B - Chemically Etched Ribbed	8	4.45	0.668	238	650
C - Chemically Etched Smooth	8	4.45	0.668	238	650
D - Mechanically Ground Ribbed	4	4.45	0.711	238	650
E - Mechanically Ground Smooth	5	4.45	0.711	238	650

[a] Commercially bottled helium (99.99% pure). Activated carbon at liquid nitrogen temperature is used for additional purification. Cover gas is also pure helium, purified in the same way, at atmospheric pressure and at a flow rate of ~400 c^3/min.

[b] The nominal stress is based on the root diameter for the ribbed specimens.

are being conducted in purified helium at 650°C. The helium gas was purified by passing through a liquid nitrogen cooled charcoal trap, but the specimens are being oxidized. These tests are being conducted at the same stress levels (34 ksi nominal) used in the initial tests.

Based on the initial test results and the data from the "Nuclear Systems Materials Handbook," failures were expected in 500 to 700 hours. The failures were expected to be of the intergranular pinhole type. But within ~100 hours of initiation of testing, seven chemically etched smooth specimens had failed. Five of the failures were by rupture and the other two by pinhole leak. Mechanically ground specimens have not failed, and the oxidation behavior of the etched specimens differs from the behavior of the ground specimens as seen by visual examination.

Small non-metallic inclusions have been observed on the fracture surface of the ruptured specimens. Initial analysis indicates that these inclusions contain P, S, Cl, and Si. Detailed investigations are in progress.

Unusual etching behavior was observed upon etching the new tubing (Heat #90126) purchased from Carpenter Technology. This behavior showed up as surface anomolies or scabs upon electrochemical etching of the tubing (see Fig. 5.1). Previous lots of tubing (Heat #88229) did not show any such defects. These scabs were seen in three out of four tubes processed by etching. The scabs were examined by Carpenter Technology Labs. No evidence of voids, inclusions, and/or foreign material was observed. Even the microstructure of the area of the scabs is similar to the rest of the tubing. Additional investigation is planned.

Ribbed cladding fabricated by mechanical grinding at Kraftwerk Union has been received. Visual inspection here and non-destructive examination at ANL show no defects. Metallography and hardness tests show no significant effect of the grinding process. The delivery date for the cladding ribbed by electrochemical grinding, previously expected by January 1976, is now uncertain. This may delay the Pacific Northwest Laboratories (PNL) helium loop test program or it may have to proceed without electrochemically ground specimens.

Agreement was reached on the design of the third test matrix with ANL. The test matrix is given in Table 5.2, and the corresponding test matrix for the initial tests at PNL is also shown in the same table.

The following points were taken into consideration in the design of the test matrices:

1. The third test at ANL and the first test at PNL are being conducted under identical conditions in terms of temperature, stress, impurity levels, etc. This will make it possible to compare

Fig. 5.1 Surface anomolies or scabs upon electrochemical etching of the tubing

Table 5.2

TEST MATRIX FOR THE THIRD TEST AT ANL AND THE FIRST TEST AT PNL

Number of Specimens			Stress (KSI)	Temperature (°C)	H_2/H_2O (μatm)	Expected Life (Hrs)	Remarks
MGS[a]	MGR[b]	ECGR[c]					
6	5	5	34	650	3000/850	~800	ANL Test
6	5	5	38	650	3000/850	~200	ANL Test
7	7	6	34	650	3000/850	~800	PNL Test

[a]MGS - mechanically ground smooth.

[b]MGR - mechanically ground ribbed.

[c]ECGR - electrochemically ground ribbed.

the mechanical behavior in quasi-static helium and in recirculating helium as early as possible in the test program (during FY-77).

2. The effect of environment will be investigated by performing the fourth test in purified helium at ANL and comparing the results to the third test.

3. The only fabrication processes included in the third test at ANL are mechanical grinding and electrochemical grinding. Electrochemical etching is not capable of producing the reference rib configuration at the present time. Some specimens fabricated from ribbed cladding by electrochemical etching are included in the second test, which is currently in progress.

4. For purposes of comparing smooth versus ribbed cladding, smooth cladding with O.D. equal to the rib root diameter, produced by centerless grinding, is included in the test. The surface conditions may be slightly different from the mechanically ground ribbed cladding.

5. All future tests will use 44.45-mm long specimens with HEDL design end caps and reinforcing collars.

6. The end caps for the PNL test specimens will be welded at ANL to reduce uncertainties in the test program.

5.2.2. Helium Loop Test Program at PNL

The primary objective of this program is to permit comparison of mechanical properties in recirculating helium at PNL to those in quasi-static helium, measured in the Mechanical Properties Testing Program at ANL, to ensure that the ANL tests are in fact representative of the conditions in a GCFR. The scope of work has been agreed upon, and the evaluation of techniques for detection of pinhole leaks and ruptures has been completed.

The modification of the loop for unattended operation has been completed. The water and hydrogen injection systems and impurity monitoring system have been installed, and the loop has been operated with impurity levels typical of the GCFR demonstration plant. The analysis of the simulation of the steam inleakage accident has been completed. The analysis indicates that the molybdenum heaters will interfere with this type of operation.

In this reporting period, ANL was requested to perform the welding of the end caps for the PNL test specimens, and ANL has agreed. This will avoid any unknown differences in the test specimens at ANL and PNL and improve the confidence in the comparison of the test results from these laboratories. The testing has not been started due to a delay in the delivery of ribbed cladding.

5.3. F-1 FAST FLUX IRRADIATION EXPERIMENT

Irradiation of the encapsulated seven-fuel-rod F-1 (X094B) experiment has now achieved a maximum burnup exposure of 116.5 MW/kg (12.7 at-%). Irradiation will continue to the burnup goal for the experiment of 125 MWd/kg (13.4 at-%). The goal is expected to be reached (or exceeded slightly) at the end of EBR-II run 82 in June 1976.

The post-irradiation work under way or remaining to be done at GA is outlined below. Work at GA during this quarter was aimed at cladding operating temperature determination, tritium yield measurements on U-238, Th-232, and U-235, neutron dosimetry, and charcoal trap analysis. A final report describing the Kr-85 cladding temperature measurement was initiated during the quarter.

5.3.1. Charcoal Trap Analysis

Cesium analyses of the active charcoal trap from rod G-6 were completed. A review of the analytical cesium data was undertaken to assess the consistency between data based on quantitative gamma spectrometry and data based on chemical analysis.

Isotopic cesium loadings of the charcoal trap were obtained by two procedures:

1. Absolute gamma spectrometry was used to obtain Cs-137 (and Cs-134*) loadings for each axial section of the charcoal trap. The combination of the gamma spectrometry data with relative mass spectrometric determinations of the isotopic ratios of Cs-133, Cs-134, Cs-135, and Cs-137 in each axial section yielded results on the absolute loading of each isotope in each charcoal sample section. These data are given in Table 5.3 and plotted in Figs. 5.2 and 5.3.

2. Determinations of the absolute levels of total cesium (and rubidium) in axial sections of the trap by atomic absorption spectrometry were combined with the relative mass spectrometric isotopic distributions to yield absolute loadings of each cesium and rubidium isotope in several of the axial sections. Unfortunately, atomic absorption spectrometry was not carried out on all axial sections. The results obtained by the atomic absorption and mass spectrometry procedures are given in Table 5.4.

*The Cs-137 levels were used for data normalization.

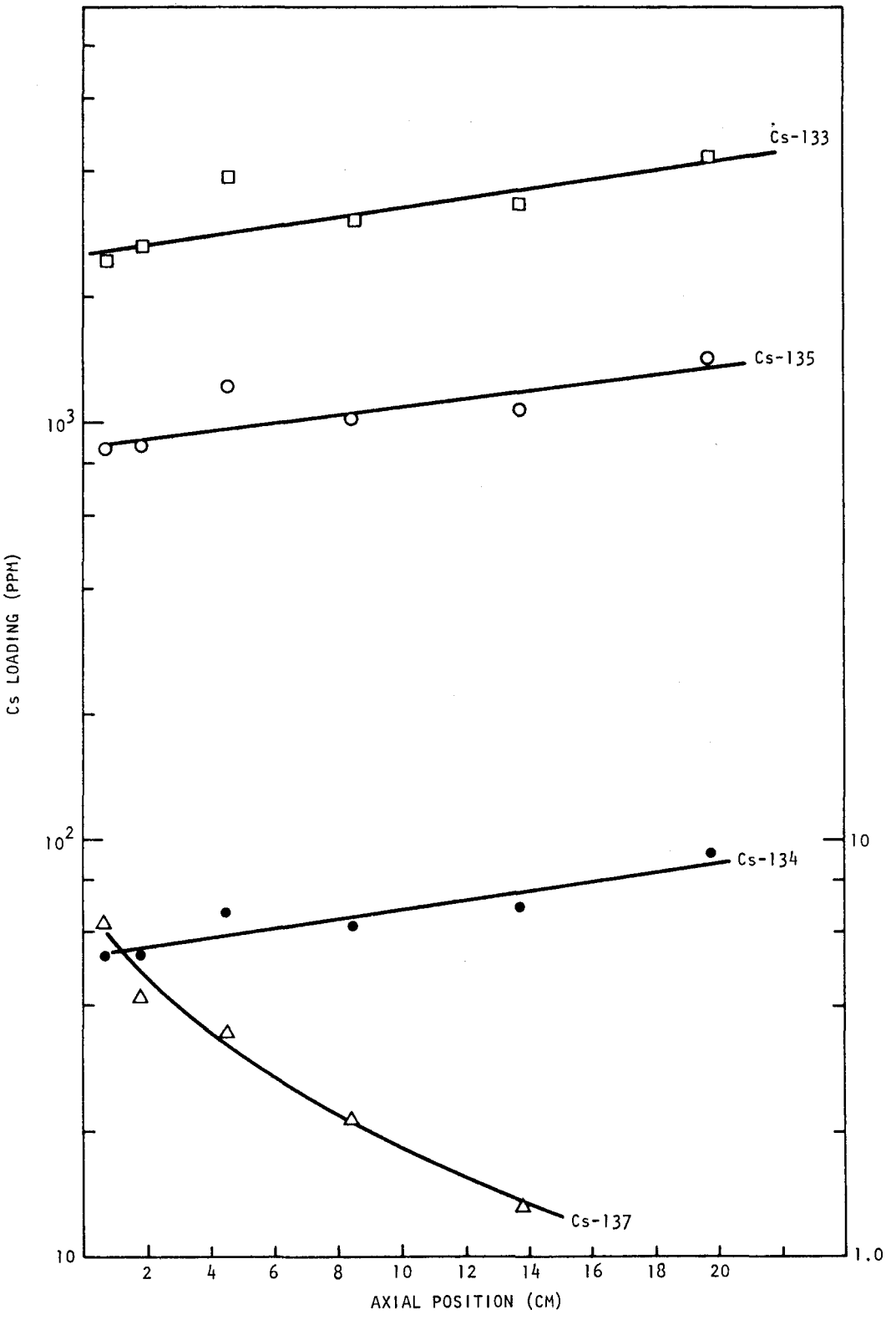

Fig. 5.2 G-6 upper trap cesium isotopic loading vs axial position

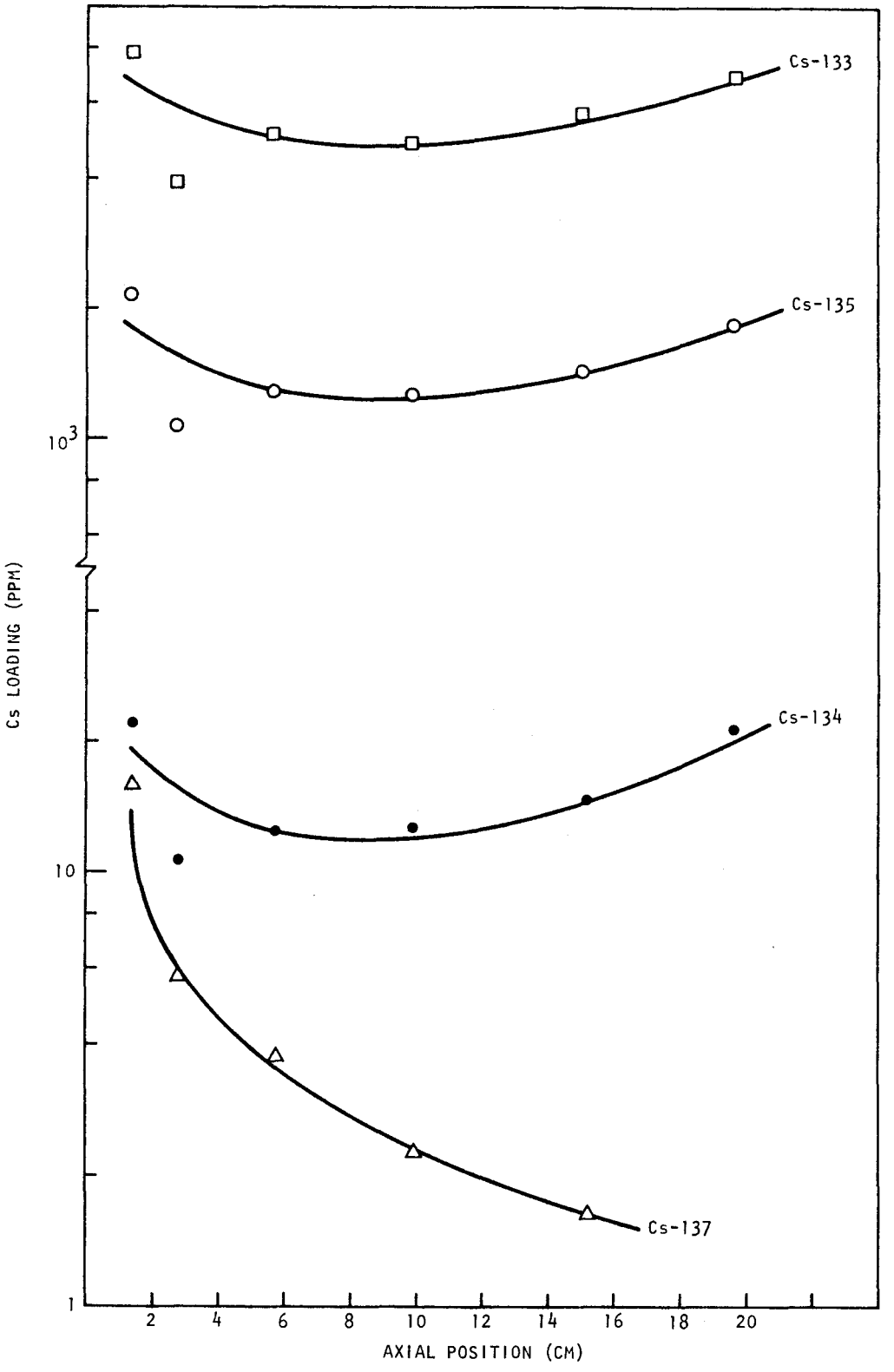

Fig. 5.3 G-6 lower trap cesium isotopic loading vs axial position

Table 5.3

CESIUM ISOTOPIC LOADING IN CHARCOAL AXIAL SECTIONS

Sample	Axial[a] Position (cm)	Cesium Isotope (ppm)			
		133	134[b]	135	137
Upper Trap 846	0.63	2488	5.26	872	6.24
Upper Trap 845	1.91	2690	5.30	884	4.25
Upper Trap 844	4.57	3914	6.76	1238	3.47
Upper Trap 842	8.50	3108	6.22	1004	2.14
Upper Trap 841	13.7	3378	6.95	1095	1.30
Upper Trap 840	19.3	4273	9.37	1424	N.D.
Lower Trap 834	1.52	7964	22.0	2185	16.0
Lower Trap 835	2.92	3942	10.5	1044	5.78
Lower Trap 836	5.72	5194	12.3	1296	3.79
Lower Trap 837	10.0	4872	12.6	1256	2.23
Lower Trap 838	15.2	5737	14.9	1438	1.61
Lower Trap 839	19.8	6944	21.7	1873	N.D.

[a]The axial position is measured from the fuel end of the trap to the section midpoint.

[b]Cs-134 content was normalized to the data of mass spectrometric analysis.

The results of the two methods are compared in Table 5.5 for those trap sections for which both methods of analysis were used.

Scatter in the gamma counting data introduced large uncertainties in total cesium isotopic loadings since Cs-137 is being used to normalize the mass spectrometric data. The differences between the results obtained with the two analytical techniques was further exacerbated by differences in isotopic distribution in aliquots of various axial sections determined by (1) leaching or (2) total sample dissolution. These differences are shown in Table 5.6, which compares the isotopic distributions of leached and totally dissolved aliquots from several axial sections.

Table 5.4

CESIUM AND RUBIDIUM DISTRIBUTIONS IN CHARCOAL TRAP SECTIONS

Location (cm)[a]	Sample Number	Total Rb[b] (ppm)	Isotopic Distribution (at-%)		Total Cs[c] (ppm)	Isotopic Distribution (at-%)			
			Rb-85	Rb-87		Cs-133	Cs-134	Cs-135	Cs-137
Upper Trap - 0.63	846	140	64.29	35.71	1540	71.87	0.259	27.57	0.292
Upper Trap - 1.91	845	141	65.80	34.20	1380	72.46	0.321	26.92	0.301
Lower Trap - 1.52	834	1.52	60.67	39.33	5770	74.79	0.363	24.601	0.247
Lower Trap - 1.91	835	1.91	66.28	33.72	2000	75.30	0.439	23.995	0.65

[a]Distance from fuel end of the trap.

[b]Atomic absorption spectrometry.

[c]Mass spectrometric isotopic dilution analysis.

Table 5.5

COMPARISON OF CESIUM ISOTOPIC LOADINGS BY DIFFERENT ANALYTICAL AND SAMPLING PROCEDURES

Axial Position (cm)	Sample Number	Analytical and Sampling Technique[a]	Total Cesium (ppm)	Isotopic Content (ppm)			
				Cs-133	Cs-134	Cs-135	Cs-137[c]
Upper Trap							
0.63	846	AA + MS dissolved	1540	1106	9.12	424	4.77
		γ + MS dissolved[b]		1356	11.16	520	5.84
		γ + MS leached[b]		1115	8.72	428	4.78
1.91	845	AA + MS dissolved	1380	1000	10.11	371	4.39
		γ + MS dissolved[b]		685	6.91	254	3.02
		γ + MS leached[b]		941	9.04	350	4.13
Lower Trap							
1.52	834	AA + MS dissolved	5770	4315	20.9	1419	15.1
		γ + MS dissolved[b]		3556	39.5	1170	12.4
		γ + MS leached[b]		3497	36.9	1150	12.2
2.92	835	AA + MS dissolved	2000	1506	20.0	480	5.61
		γ + MS dissolved[b]		1339	17.79	427	4.99
		γ + MS leached[b]		1372	17.35	437	5.10

[a]Values listed as AA and MS were determined by atomic absorption analysis and mass spectrometry on dissolved samples. γ + MS refers to gamma spectral analysis and mass spectrometry.

[b]Cs-137 absolute gamma count used as standard.

[c]Cs-137 data corrected to end-of-irradiation, 2/19/73.

The errors associated with atomic absorption analysis and mass spectrometry (MS) analysis are $\pm$2%. This compares to gamma spectral analysis errors of $\pm$3% for Cs-134 and 4%-25% for Cs-137. But a mean value of the gamma samples in an axial section generates average reference isotope contents with errors of $\pm$20%. Errors on the MS values derived from leach

Table 5.6

COMPARISON OF Cs ISOTOPIC ANALYSIS FOR LEACH VERSUS DISSOLVED CHARCOAL SAMPLES

	Cs Isotope (at-%)							
	133		134		135		137	
Sample	Leach	Dissolve	Leach	Dissolve	Leach	Dissolve	Leach	Dissolve
Upper Trap 846	73.800	71.873	0.156	0.259	25.852	27.566	0.193	---
Upper Trap 845	75.126	72.462	0.148	0.321	24.674	26.917	0.052	0.301
Lower Trap 834	78.200	74.789	0.216	0.363	21.458	24.601	0.126	0.247
Lower Trap 835	78.824	75.296	0.210	0.439	20.870	23.995	0.096	0.265

samples versus dissolved samples are factors on the order of 2 to 6 for the reference isotopes. Thus, it is clear that precise fission isotopic values can only be obtained on totally dissolved samples. The irradiation shrinkage of the charcoal has caused unexpected difficulties, not only in the processing of the samples but also in the precision of results, by distorting the isotopic composition.

5.3.2. Iodine Analyses

Three samples from the upper charcoal trap of rod G-6 were examined for I-129 content. The I-129 was determined by neutron activation analysis following destruction of the charcoal by perchloric acid dissolution. The results are shown in Table 5.7.

The loading in this charcoal trap is ~1/10 of the average I-129 loading found in the GB-9 trap. It is believed this difference is not entirely real. Rather, it reflects possible error in technique and the difficulty of removal of the fission species due to charcoal shrinkage. The GB-9 charcoal was leachable.

This analysis has been particularly difficult because of entrapment of the fission products within the structural mass of charcoal. This phenomenon was first observed during analysis for cesium isotopes by leaching. The shrinkage of the charcoal during irradiation apparently occluded any fission elements that had been deposited in fractures (and nonsurface sites). Hence, the greater fraction (~90%) of the iodine may not be readily removed by leaching.

One further difficulty is presented with iodine: carrier-exchange chemistry is a prerequisite for assuring quantitative recovery of the desired species. Because of the entrapment of I-129 within the charcoal matrix, it is believed that the carrier exchange was not complete because the free exchange can only be effected where the species can interchange. The carrier species was only in contact with <<20% of the I-129 species and probably did not effect a true carrier exchange. The entrapped I-129

Table 5.7

I-129 CONTENT IN G-6 UPPER CHARCOAL TRAP[a]

Sample	Axial Position[b] (cm)	I-129 (ppm)	I-129 Cs-137 Ratio
845-10	1.91	0.61	0.14
844-1	4.57	0.14	0.0402
842-3	8.50	0.25	0.12

[a]As a comparison, note the GB-9 charcoal trap average loading of 4.4 ppm.

[b]The axial position is measured from the fuel end of the trap to the sample compartment midpoint.

species once in contact with the hot perchloric would probably be distilled off as I-129 to atmosphere. Thus, in order to ensure quantitative measurement of the I-129, the charcoal should be oxidized by means of an alkaline fusion technique with the carrier present.

5.3.3. Strontium-89 and Strontium-90 Analyses

The Sr-89 and Sr-90 analyses have been completed, and the data are shown in Table 5.8. The credibility of the Sr-89 data remains uncertain. The data should be viewed in a qualitative sense because the values derived are the result of a small difference between large counting data values. The reason for the large error is the decay factor due to the long interval between the end of irradiation and the analyses. The decay factor for the 50.4-day Sr-89 isotope is 6.7×10^{-5}, while the Sr-90 had decayed about 5%.

The relative constancy of the ratio Sr-89/Sr-90 implies a uniformly decreasing loading factor for both isotopes across each trap. The Sr-90 concentration profile in each of the traps is shown in Fig. 5.4. This

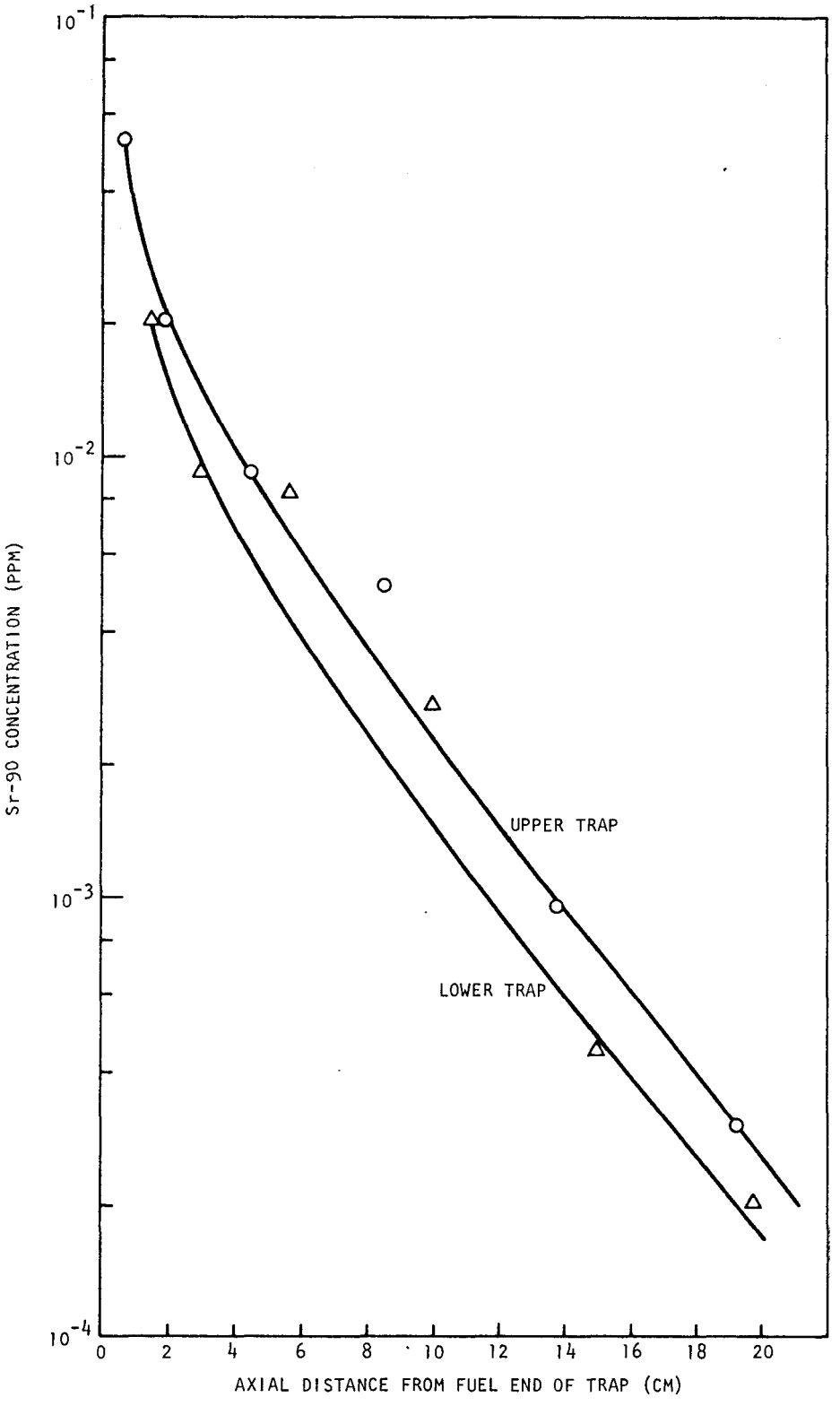

Fig. 5.4 Sr-90 concentration for upper and lower charcoal traps

Table 5.8

STRONTIUM LOADING IN THE G-6 CHARCOAL TRAPS[a]

Sample Number	Axial Position[b] (cm)	Sr-90 (ppm)	Sr-89 (ppm)	Sr-89/ Sr-90 Ratio
Upper Trap				
846	0.63	0.053	N.D.	---
845	1.91	0.0202	30.1	1490
844	4.57	0.00904	16.4	1814
842	8.50	0.0051	N.D.	---
841	13.7	0.00097	N.D.	---
840	19.3	0.000302	1.35	4470
Lower Trap				
834	1.52	0.0211	98.5	4668
835	2.92	0.0093	37.4	4022
836	5.72	0.0088	N.D.	---
837	10.0	0.0027	N.D.	---
838	15.2	0.00045	2.12	4711
938	19.8	0.00020	0.689	3445

[a]The isotopic activities have been normalized to February 19, 1973, the end-of-irradiation date.

[b]The axial position is measured from the fuel end of the trap to the sample compartment midpoint.

concentration gradient appears to be nearly exponential for essentially the same Sr-90 levels in both the upper and lower traps.

5.3.4. Rubidium Isotopic Loadings

It is frequently forgotten that the lower mass inert gas, krypton, transports even more readily than its high-mass analogue, xenon. This is due primarily to the difficulties associated with analysis for the

daughter of rubidium. Rubidium cannot be detected by gamma counting but must be determined chemically (e.g., by atomic adsorption) and the isotopic distribution determined by mass spectrometry

The isotopic rubidium analyses of four axial sections of the trap are given in Table 5.9. Of special interest is the ratio of Rb-85 to Rb-87, which is nearly 2. The long lived precursor, Kr-85, probably dictates the mobility of this species. However, the Rb-85/87 ratio appears higher than expected since the yield ratio is 0.718 based on fast fission yields. The 10.7-year half-life of Kr-85 should also tend to decrease the Rb-85/87 ratio because less than half of the Kr-85 will have decayed to Rb-85 prior to analysis. These data therefore require further consideration and analyses.

Table 5.9

RUBIDIUM ISOTOPIC LOADINGS IN CHARCOAL TRAP AXIAL SECTIONS[a]

Location (cm)	Sample Number	Total Rb (ppm)	Rubidium Isotopic Loadings (ppm)	
			Rb-85	Rb-87
Upper Trap				
0.63	846	140	90.0	50.0
1.91	845	141	92.8	48.2
Lower Trap				
1.52	834	275	166.8	108.2
1.91	835	151	100.1	50.9

[a]Mass spectrometric isotopic dilution analysis.

[b]Distance from the fuel end of the trap to trap section midpoint.

The absolute rubidium loading for the lower charcoal trap sections given in Table 5.9 is 1.5 to 2 times higher than the upper trap. By comparison, the cesium loadings given in Tables 5.3 and 5.5 are three to four times higher in the lower trap than in the upper trap. This is believed to be due to the apparently lower temperature (~100°C) of the lower trap. The rubidium comprises about 10% of the fission product content of the trap loading.

5.3.5. Dosimetry

Coated fuel particles were used in the F-1 fuel rods as part of a neutron dosimetry packet. Selected particles have been examined by mass spectrometric isotopic dilution analysis. These results can be used to calculate the burnup exposure and also the neutron flux incident on the rod. Burnup values have been calculated and are shown in Table 5.10. Burnup values have also been obtained by ANL by fission monitor analysis of the irradiated fuel. The derivation of the neutron flux is dependent on cross section values for the EBR-II core spectra, which are to be provided by ANL personnel.

The ANL and GA burnup values, while not comparable at identical locations, are in reasonable accord when equivalent rods and axial positions are taken into account. Other sample particles are being processed and will furnish more specific data for the rod flux profiles.

Thorium conversion to U-233 has been measured for fuel particle samples in the EBR-II fuel and axial blanket regions. These data are shown in Table 5.11.

The conversion values shown in Table 5.11 indicate an expected marked neutron energy dependence. The transmutation occurs by neutron capture by Th-232 forming Th-233 with subsequent decay to Pa-233 and finally U-233. The values listed for a burnup of 50 MWd/kg are only slightly lower than those previously expected (0.0151, see Ref.1) in the end of cycle equilibrium mass balances for U-233 and Th-232 for a three-row ThO_2 blanket of the GCFR demonstration plant.

Table 5.10

MEASURED BURNUP VALUES FOR F-1 RODS

Sx	Axial Position Relative to Mid-Plane (cm)	Burnup (at-%)	
		GA Value[a]	ANL Value[b]
G-1-3 (blanket)	-21.2	4.27	---
G-1-ANL	0.0		5.35
G-1-4	-12.2	4.39	
G-1-ANL	+15.3		4.35
G-7-3 (blanket)[c]	-21.2	4.22	
G-2-ANL	-12.2		4.91
G-2-ANL	0.0		5.19
G-2-ANL	+15.3		4.26

[a]Based on analysis of coated fuel particles in neutron dosimetry packets.

[b]Based on fission monitor analysis of the irradiated fuel.

[c]The blanket samples are ~4 cm from the fuel blanket interface.

5.3.6. Operating Temperature Determination

All the Kr-85 cladding anneal samples have been completed. A final report has been written and is undergoing review. A preliminary summary is presented here comparing the measured values from Kr-85 anneals with the calculated values as derived from LAMBDA and TAK codes. The O.D. cladding temperatures are presented in Fig. 5.5 for rods G-1, G-2, and G-3.

G-1 upper and midsection samples were apparently affected by cladding attack and show lower than calculated temperatures. This same observation is made for the G-2 midsection sample; however, metallographic examination fails to confirm the presence of cladding attack at this location.

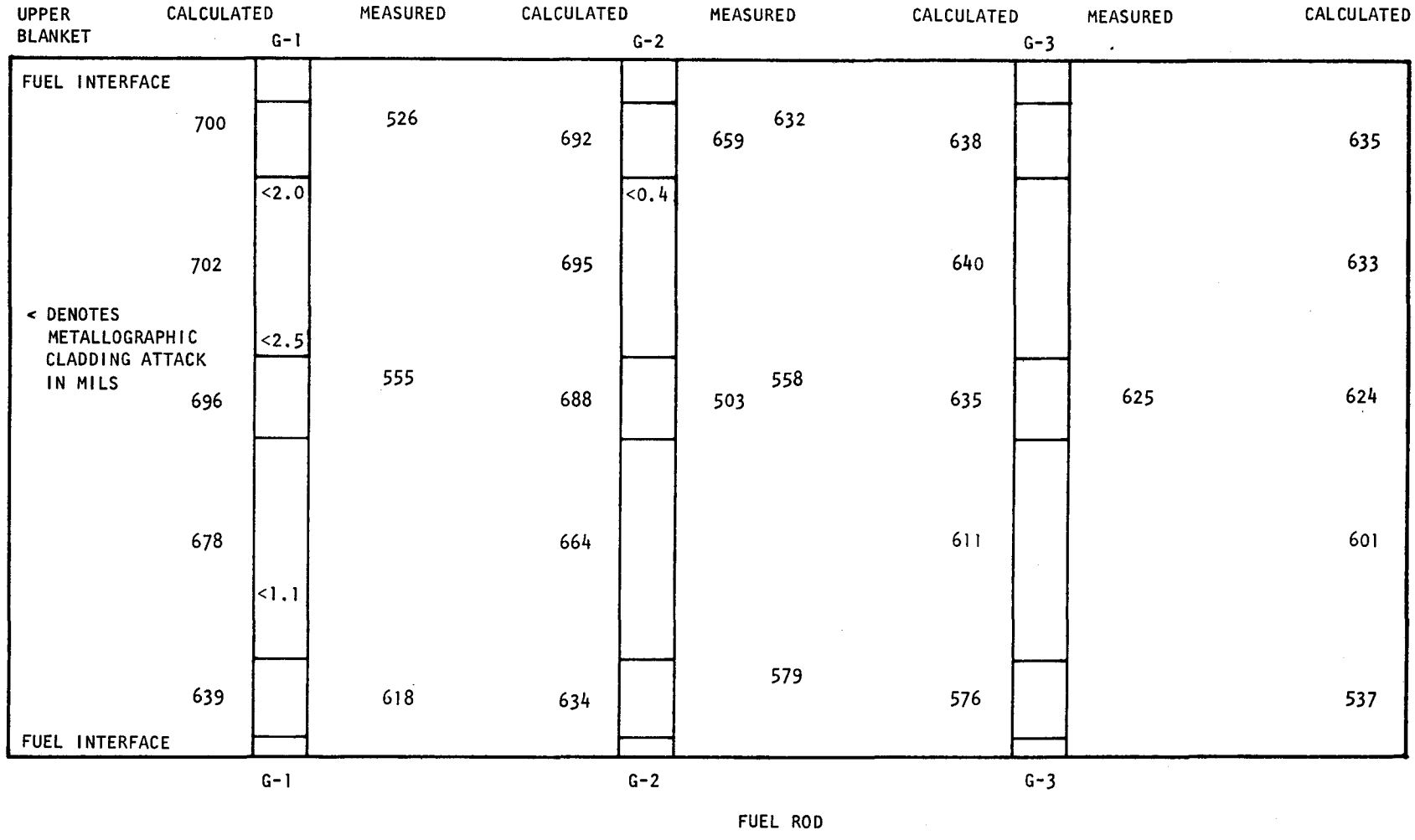

Fig. 5.5 Summary of cladding temperature data, comparison of calculated o.d. temperatures (°C) vs Kr-85 anneal

Table 5.11

CONVERSION OF THORIUM-232 TO URANIUM-233 IN THE EBR-II SPECTRUM[a]

Sample	Axial Position[b] (cm)	Mean Neutron Energy (KeV)[c]	Total Fluence	Conversion Fraction
G-2-38	-20 (lower blanket)	400	2.82×10^{22}	0.0140
G-1-7	13 (fuel core)	420	2.97×10^{22}	0.00366
G-1-9	30 (upper blanket)	325	2.20×10^{22}	0.0112

[a]Experiment F-1 (X094) is located in row 7 in the radial reflector of the EBR-II core.

[b]The distance is measured from the midplate.

[c]These energy values relate to axial positions in Row 8 of EBR-II and are given here to indicate the relative profile in Row 7, which would be somewhat more difficult to calculate. Energy values are taken from Ref 2.

Since the annealing technique relies on the Kr-85 inventory, which is confined to $\lesssim$10 μ of the inner cladding surface, the surface layer is the controlling factor in this method. Moderate cladding attack imposes a constraint on this method since the original stainless steel surface is transmuted to one impregnated with metallic fission products. This disruption of surface integrity in cases of cladding attack apparently destroys the efficacy of the method. It has been tentatively concluded that further work on this technique is not justified.

5.3.7. Fast Fission Tritium Measurements on U-235

Fuel particles irradiated on both sides of the upper fuel/blanket interface in the G-1 rod have been examined for tritium content. The analyses were performed by the GA HTGR Fuel Chemistry Branch. These coated fuel particles are part of the neutron dosimetry assembly that will also provide information on the fast neutron fission yield of tritium for the various fissile isotopes to be used in the GCFR program.

The fuel particles were analyzed by gamma spectrometry using one or more fission isotopes to determine total fission product inventory. Cs-137 was selected for this calculation, although other species can be used. Both cesium and tritium are believed to be quantitatively retained in these fuel particles under the irradiation temperature of 500°C.

The tritium content of these particles was determined by liquid scintillation counting. The particles are burned in a sweep stream of HeO_2 containing 90 ppm carrier water. The H-3 released is converted to HTO on passage through a CuO bed. The tritiated water is then collected in a freeze trap and subsequently diluted and counted. The data are presented in Table 5.12. The preliminary tritium yield value obtained for U-235 appears to be $1.5 \pm 0.02 \times 10^{-4}$ t/fission for the G-1 rod (row 7). Table 5.13 presents fuel particle characterization and irradiation history for the samples analyzed in Table 5.12.

Tritium yield values have been reported by workers at ANL. They report a spectrum averaged fast-neutron tritium yield from U-235 of 2.1×10^{-4} t/f for EBR-II.

5.3.8. Fast Fission Tritium Measurements on U-238 and Th-232 Isotopes

Measurements of the tritium content in EBR-II irradiated fuel particles in the form of $U\text{-}238C_2$ and $Th\text{-}232C_2$ were also made. Particles containing U-238 and Th-232 tend to produce significantly higher values: preliminary estimates are $\sim 2.8 \times 10^{-3}$ t/f.

These values are higher than fission yields reported in the literature by a factor of 10 to 20. A survey of the literature reveals that the fast fission yields of these isotopes have never been measured. Only previously reported values were calculated. Most of the ternary fission yield work has been performed by Dudley at ANL, but the principal effort of the tritium yield work has been focused on U-235 and Pu-239. The fast fission yield value for these nuclides is $\sim 1.5 \times 10^{-4}$.

Table 5.12

TRITIUM FISSION YIELDS FOR U-235 FROM FAST FISSION
(400-500 KeV)

Sample[a]	Atoms Cs-137 (γ Counting)	Cs-137 Fast Fission Yield	Calculated Total Fissions	Measured H-3 Atoms (β Counting)	Mean N_{energy} (KeV)	Tritium Fission Yield (H-3 atoms/ fission)	Error			
							b	c	d	e
G-1-3C(A)	1.652×10^{14}	6.17	2.677×10^{15}	4.147×10^{11}	400	$1.55 \pm 0.02 \times 10^{-4}$	0.36	1	1	0.6
G-1-3C(B)	2.468×10^{14}	6.17	4.000×10^{15}	7.22×10^{11}		$1.80 \pm 0.03 \times 10^{-4}$	0.36	1	1	0.45
G-1-4C(A)	1.125×10^{14}	6.17	1.823×10^{15}	2.555×10^{11}	450	$1.40 \pm 0.02 \times 10^{-4}$	0.41	1	1	0.75
G-1-4C(B)	1.105×10^{14}	6.17	1.791×10^{15}	2.298×10^{11}		$1.28 \pm 0.02 \times 10^{-4}$	0.41	1	1	0.80
G-1-4C(C)	7.90×10^{13}	6.17	1.280×10^{15}	1.728×10^{11}		$1.35 \pm 0.02 \times 10^{-4}$	0.41	1	1	0.92

[a](A), (B), (C) denote duplicate samples.

[b]Error on gamma counting.

[c]Error on pipette dilution of sample.

[d]Error due to incomplete recovery.

[e]Error on beta count.

Table 5.13

FUEL PARTICLE CHARACTERIZATION DATA AND IRRADIATION HISTORY

Sample	Kernel Type	Coating Type	Kernel Diameter (μm)	Buffer Thickness (μm)	Irradiation	
					Time (days)	Position[a] (cm)
G-1-3C	UC_2[b]	BISO-PL	95.0	40.0	312	21
G-1-4C	UC_2[b]	BISO-PL	95.0	40.0	312	13

[a]Samples irradiated in EBR-II. Distances refer to sample location above reactor midplane.

[b]Enriched to 90% U-235.

Detailed calculations of tritium production for fast breeder reactors are now necessary based on these values for the yield. Tritium yield measurements at ANL were curtailed in 1972 on the premise that Pu-239 and U-235 as tritium production sources were insignificant compared to the production in control rods.

More detailed work should be pursued to unambiguously resolve the yields for U-238 and Th-232. Our preliminary results are probably reasonably reliable; however, re-examination of all work performed is deemed reasonable.

5.4. FAST FLUX IRRADIATION EXPERIMENT F-3

The F-3 experiment being irradiated in location 4B3 in EBR-II to date has reached an exposure of 42.3 MWd/kg (4.6 at-%) of a goal exposure to 100 MWd/kg (10.8 at-%). As previously reported, these capsules have been designed for irradiation in an EBR-II core position (row 4) and share a type J19A subassembly (designated X206) with an ANL Group-08 high-temperature chemistry experiment. The experiment will reach a burnup of 50 MWd/kg burnup, or 300 full-power days, on or about February 10, 1976, at which time a planned interim examination will occur. The final maximum burnup goal for the experiment is 100 MWd/kg (11.0 at-%), and a neutron exposure goal of 1.5×10^{23} n/cm^2.

ANL-E reports that the fabrication of the three F-3 replacement rod capsules to be installed in X206 after the interim examination is expected to occur in time for scheduled reconstitution of the F3-08 (X206) subassembly for EBR-II Run 84.

5.5. F-5 PROTOTYPE IRRADIATION EXPERIMENT

The F-5 prototype design fuel rod experiment is to be performed for experimental study of the performance of fuel rods irradiated under simulated GCFR conditions to high burnups for the purposes of (1) determining the reliability of the GCFR fuel rod design, (2) discovering what failure modes may exist, and (3) studying the effect of a step power increase that simulates the 180° rotation of a subassembly at the core-blanket interface in the proposed GCFR demonstration plant.

The "approval in principal" for the F-5 experiment was received from RRD by ANL-E on December 7, 1975, and efforts to establish fuel specifications are under way.

5.6. GB-10 VENTED FUEL ROD EXPERIMENT

Fission product release and transport in GCFR fuel are being measured and studied in capsule GB-10, which is being irradiated in the Oak Ridge Research Reactor (ORR). The burnup of the pressure-equalized and vented fuel rod in capsule GB-10 has reached approximately 85 MWd/kg (9.3 at-%) of the exposure goal of 100 MWd/kg (10.9 at-%). The first 27 MWd/kg (3.0 at-%) were accumulated at a heat generation rate of 39.4 kW/m (12 kW/ft) at a cladding outside surface temperature of 565°C (1049°F); from 27 MWd/kg (3.0 at-%) to 75 MWd/kg (8.2 at-%) have been accumulated at 44.3 kW/m (13.5 kW/ft) at a cladding outside surface temperature of 630°C (1166°F), and from 75 MWd/kg (8.2 at-%) to the current burnup at 47.6 kW/cm (14.5 kW/ft) and a cladding outside temperature of 685°C (1265°F).

Because of funding limitations, it was necessary to postpone or cancel special tests (tritium measurements, power cycling, and simulated leak flow-rate tests). In addition it is necessary to postpone further routine measurements of fission gas release and venting and flow conductance measurements until the end of the irradiation. The capsule will continue to be irradiated and accumulate burnup because this procedure is the best means of storage until post-irradiation examination (PIE) is to be done, and it retains the option for resumption of test data acquisition if funding should be made available. The capsule is expected to reach its revised goal of 100 MWd/kg in June 1976, at which time it is planned to terminate the irradiation and start the PIE with fiscal year transition-quarter funds.

5.6.1. Tritium Measurements in Irradiation Capsule GB-10

The release and transport of fission products in GCFR fuel are being measured and studied in capsule GB-10, which is being irradiated in the Oak Ridge Research Reactor (ORR). The burnup of the pressure-equalized and vented fuel rod in capsule GB-10 has reached approximately 75MWd/kg (8.1 at-%) of the exposure goal of 100 MWd/kg (10.9 at-%). The first 27 MWd/kg were accumulated at a heat generation rate of 39 kW/m (12 kW/ft) at a cladding outside surface temperature of 565°C; the remainder have been accumulated at 44.0 kW/m (13.5 kW/ft) at a cladding outside surface temperature of 630°C.

Activity during this report period was principally expended in supporting the tritium measurements being conducted at ORNL. These included monitoring, consultation, and observation of the tritium monitor calibration and debugging tests; tritium venting experiments at ORNL; design and construction of a high-pressure water saturator; laboratory tests to define operating conditions for the magnesium converter; and development of a method for sampling low levels of H_2 using a liquid-nitrogen-cooled charcoal trap.

5.6.1.1. Tritium Instrumentation Calibration and Debugging. Laboratory tests of tritium monitor components and the system were performed at ORNL prior to installation on the capsule sweep gas system. However, the bench components and the installed components were not identical in all cases. In addition, some conditions (e.g., radioactive fission gases) could not be tested in the laboratory. Thus, a series of in situ calibration and debugging tests were performed, as described below.

5.6.1.1.1. Run 1. The baseline output with helium gas flowing directly to the ion chamber at 3.3 ml STP/sec confirmed laboratory measurements. The baseline reading of 0.66 mV was unaffected by the presence of a fission gas radiation source of 250 to 450 mr/hr brought to the outer surface of the Pb shielding around the ion chamber.

5.6.1.1.2. Run 2. Calibration gas at 5×10^{-5} μCi/ml was directly passed to the ion chamber and the CuO converter at 3.3 ml STP/sec. An output of 55 ± 3 mV was observed in accordance with laboratory measurements. Tritiated water samples from the molecular sieve tray indicated values 20% lower.

5.6.1.1.3. Run 3. Calibration gas was first passed through the tritium monitor at 3.3 ml STP/sec with the magnesium converter off stream. A charcoal trap breakthrough was observed at 70 min with 3 g of charcoal in the trap; 30 min was expected from adsorption measurements. The ion chamber output registered 55 ± 3 mV 4 hr later. Tritiated water samples taken from the molecular sieve trap were again 20% lower. The magnesium converter was brought on stream, and output fell to near the baseline values. The tritiated water sample was omitted because of lack of time. The decay of the ion chamber signal with the magnesium converter on stream was interpreted as little or no HTO in the calibration gas.

5.6.1.1.4. Run 4. Capsule sweep gas flowed at 3.3 ml STP/sec into the top of the trap and back out again (TT-TT flow mode) and into the tritium monitor with the magnesium converter off stream. The capsule operated at 44 kW/m. The ion chamber response was ~2 mV with no delay.

This was a surprising event. The signal corresponded to a tritium concentration of 1.8×10^{-6} μCi/ml in the gas. Tritiated water samples indicated a concentration in the 10^{-7} μCi/ml range, an order of magnitude lower. The magnesium converter was brought on stream and breakthrough was observed in about 40 min with an ion chamber output signal of ~9 mV. Although continuing to operate with unchanged conditions, the 9-mV signal decayed to ~4 mV over a 6-hr period.

5.6.1.1.5. Run 5. Capsule sweep gas flowed at 0.417 ml STP/sec into the bottom of the capsule, through the fuel rod, and into the tritium monitor with the magnesium converter off stream. With the capsule operating at 44 kW/m, this was the maximum flow capacity with a maximum 1.72-MPa pressure drop allowed across the rod. As in run 4, an immediate 2-mV ion chamber output signal was observed with no breakthrough indication after more than 2 hr of continuous operation.

The magnesium converter was then brought on stream, and ~40 min later, breakthrough was observed. The signal rose to ~5 mV and then decayed to ~1 mV in ~2 hr. Contamination of the magnesium converter was postulated as a probable cause of signal degradation.

5.6.1.1.6. Run 6. Pure helium gas flowed directly to the ion chamber at a rate of 3.3 ml STP/sec, and a background signal of 0.45 mV was observed. The input of the gas was then valved to the charcoal trap entrance, and the output of the ion chamber was unchanged. Next, the input flow was conducted to the magnesium converter. A breakthrough signal was observed ~54 min later, passed through a peak of ~2 mV, and decayed to <1 mV over a 3-hr period. The magnesium converter was then bypassed, and after a delay of ~40 min, the ion chamber output signal fell to 0.45 mV. A tritiated water sample taken from the molecular sieve trap indicated a concentration of 4×10^{-7} μCi/ml in the gas.

There were two possible interpretations of the data: (1) fission product contamination of the magnesium converter (e.g., cesium) reacted with the tritium during run 5 and slowly released the tritium; (2) the

magnesium converter trapped tritium from the calibration gas during the calibration tests, and tritium accumulated in the gas phase when the converter was off stream (at 500°C) and was swept through the system when the converter was brought on stream. Thus, the converter was progressively depleted of trapped tritium.

5.6.1.1.7. Run 7. Capsule power level was lowered from 44 kW/m to 39 kW/m to permit increased flow rate through the fuel rod in an attempt to get a clear indication of vented tritium. Sweep gas with a 1.38-MPa pressure loss across the fuel rod flowed at 12.4 ml STP/sec, entering the bottom of the fuel and exiting from the top of the charcoal rod trap (BF-TT flow mode) into the tritium monitor. The charcoal trap in the tritium monitor was operated with an 8-g bed.

An immediate signal of 450 mV registered at the output of the ion chamber. No evidence of a further breakthrough was observed after more than 2 hr of operation, but a slow increase of ~10 mV was seen. The ion chamber was valved off, and a decay curve was recorded which showed a half-life of ~4 min. This is interpreted to be Ne-24 ($T_{1/2}$ + 3.38 min). The molecular sieve trap sample indicated 1.4 x 10^{-6} μCi/ml of gas, or 0.27% of the expected value.

Flow through the monitor was resumed and the magnesium converter was brought on stream. A breakthrough response of the ion chamber was observed ~40 min later. The ion chamber output rose to a peak of ~500 mV, decayed to the ~480-mV level over a 3-hr period, and then began to slowly rise again until the test was terminated. No molecular sieve sample was taken.

As the tritium monitor was swept with clean helium gas, the ion chamber output signal was found to decay with a 15-hr half-life for more than a day. This is interpreted to result from the Na-24 daughter product of Ne-24 deposited in the chamber while sweeping the fuel rod.

5.6.1.1.8. Run 8. As a result of laboratory indications that tritium in low total hydrogen (tritium plus normal H_2) impurity in helium carrier

gas will be significantly trapped in the magnesium converter, tests were conducted with the magnesium converter in the tritium monitor on the capsule. First, calibration gas with a concentration of 5×10^{-5} μCi/ml flowed directly at 3.3 ml STP/sec to the ion chamber, and an output signal of 55 mV was measured. The flow was then introduced at the magnesium converter. An ion chamber output signal of 70 mV was initially recorded, followed by decay to 0.7 mV over a 3-hr period. Breakthrough of the tritium occurred after 86 min, compared with an expected 40-min delay time based on the measured charcoal adsorption coefficients. This confirmed the trapping of tritium in the magnesium converter at low total hydrogen levels in the helium.

5.6.1.1.9. Run 9. Hydrogen was added to the helium gas flowing through the tritium monitor to reduce tritium trapping in the magnesium converter. First, residual tritium was cleaned out of the magnesium converter when helium with 10,000 ppm of H_2 flowed at 8.3 ml STP/sec into the tritium monitor at the magnesium converter. A peak of ~450 mV was observed in the ion chamber output and fell to background level in about 2 hr.

Calibration gas with a concentration of 5×10^{-4} μCi/ml of tritium in helium flowing at 6.7 ml STP/sec was mixed with a stream of helium containing 10,000 ppm of H_2 flowing at 1.67 ml STP/sec and produced a stream with a concentration of 4×10^{-4} μCi/ml flowing at 8.3 ml STP/sec and containing 2000 ppm of H_2. Breakthrough of the 3-g charcoal trap occurred in 31 min; 12 min was the expected time. The ion chamber signal reached ~200 mV; 400 mV was expected.

The flow rates in the confluent gas streams were interchanged, producing a mixture with a concentration of 1×10^{-4} μCi/ml and 8000 ppm of H_2 at the same total flow rate as before. Breakthrough occurred at 12.5 min (as expected). After slight peaking in the output signal from the ion chamber, the signal dropped and leveled off at ~53 mV; ~100 mV was expected. Next, helium with 1% H_2 (10,000 ppm) flowed through the

monitor at 8.3 ml STP/sec, and after 12 min, the ion chamber output started to fall to the baseline output.

The tritiated gas mixture with 8000 ppm of H_2 was again applied to the monitor, and breakthrough was again observed in 12 min. The ion chamber output reached 55 mV in about 30 min and remained steady. Helium with 1% H_2 was again substituted, with the same results given above.

Finally, the gas mixture was directly sent to the ion chamber, bypassing the magnesium converter and the charcoal trap. A signal of 51 mV was measured, indicating that the tritium entering the monitor was not 1×10^{-4} μCi/ml as supposed, but ~5×10^{-5} μCi/ml. A deoxidizer trap placed in the gas stream to remove oxygen and other impurities from the gas also trapped the tritium. Thus, the measured and expected values of the ion chamber output after correction for the oxidizer trapping are in agreement. It is also apparent that at H_2 levels of 2000 ppm and below, the magnesium converter acted as a delay bed and dominated the delay in the charcoal trap.

The Ne-24 interference with measurement of tritium is of little consequence to measurements of venting in the TT-TT flow mode and the BF-TT flow mode at low flow rates. The ~2-mV signal represents only 0.35% of the expected tritium if all is released from the solid state of the fuel. At high flow rates through the fuel, the large Ne-24 signal (~450 mV at 12.5 ml STP/sec) and the oscillations of ~20 mV maximum on 10-min periods from charcoal trap temperature cycling raise the threshold of detectability for tritium to about 50 mV, or 10% of the expected concentration. This completed the calibration and debugging effort.

5.6.1.2. Tritium Venting Tests. After calibration and debugging of the tritium monitoring equipment as described above, two runs were made (1) to measure H_2/H_2O ratio and tritium released and vented from the capsule under its operating conditions over the whole irradiation period to date, i.e., ~75 MWd/kg, and (2) to determine the extent of tritium permeation through

the fuel rod cladding or chemical reaction and absorption in the fuel rod and capsule sweep gas lines.

5.6.1.2.1. Run 10. The power level of the capsule was lowered to 39 kW/m (12 kW/ft) to assure a high flow rate while sweeping the capsule in the BF-BT flow mode. Thus, it was possible to sweep the fuel and blanket regions throughout these tests at ~12.8 ml STP/sec while bypassing the charcoal trap in the fuel rod. The vented gas was diluted with 5.0 ml STP/sec of helium containing 4% H_2 and sweep gas (~2.8 ml STP/sec) prior to entering the tritium monitor, bypassing the capsule to bring the total flow into the monitor to 20 ml STP/sec. Under these conditions and with 8 g of charcoal in the trap, a breakthrough time for the charcoal trap was estimated to be ~20 min and ~10,000 ppm (or 1%) H_2 was contained in the gas to be monitored.

The monitor was first used to measure the HT content of the vented gas; i.e., the magnesium converter was bypassed. Immediately upon flowing the vented gas into the monitor, the IC output rose to ~450 mV, thus duplicating the Ne-24 signal measured under the same venting conditions in a previous test. A 20-mV cyclic variation corresponding to ~3°C peak-to-peak temperature cycling of the charcoal trap was observed with a 10-min period. A slow updrift of the output was observed, which was attributed to the Na-24 daughter product of Ne-24. Under these circumstances, a signal of ~50 mV from tritium would be the minimum discernible signal superimposed on the 450-mV Ne-24 signal. The 50-mV signal corresponds to 5×10^{-5} μCi/ml of tritium in the ion chamber. The expected value at a power level of 44 kW/m (13.5 kW/ft) and a flow rate of 3.3 ml STP/sec was calculated to be 2.23×10^{-3} μCi/ml (Ref. 4). Correcting to the measuring conditions,

$$2.23 \times 10^{-3} \frac{39}{44} \frac{3.3}{12.8} = 5.15 \times 10^{-4} \text{ μCi/ml} \quad .$$

Thus, the Ne-24 signal increases the minimum level of tritium measurable with the ion chamber from ~2.5% to 10% of the expected level. However,

no discernible breakthrough of tritium was observed over a 2-hr period of operation. Thus, the tritium vented as HT or T^2 was $\leq$10% of that expected. A molecular sieve sample was collected for ~1 hr.

The monitor was valved to measure total tritium (HT, T_2, and HTO) and vented by passing the vented gas through the magnesium converter. There was no discernible difference in the ion chamber output signal. Thus, the total tritium vented was 10% of the tritium calculated to be generated in the capsule and expected to be vented while sweeping the fuel. A second molecular sieve sample was collected for ~1 hr.

Analyses of the molecular sieve samples after distillation to eliminate Na-24 from the samples produced the following results for the tritium levels in the monitored (not vented) gas:

$$\text{HT } (\mu\text{Ci/ml}) = 1.40 \times 10^{-5} \ ,$$

$$\text{HT + HTO } (\mu\text{Ci/ml}) = 1.71 \times 10^{-5} \ .$$

The volumes, however, are the STP volumes. These are corrected to the vented gas concentrations as follows:

$$\frac{M(\mu\text{Ci}) \mid (14.7 + 10)\text{ml STP}}{\text{Ml STP} \mid 14.7 \text{ ml vented gas}} = 1.68\ M \ ,$$

where M is the molecular sieve sample values. Therefore,

HT		HT + HTO		
(μCi/ml)	(%)	(μCi/ml)	(%)	HT/HTO
2.35×10^{-5}	4.6	2.87×10^{-5}	5.6	4.52

The level of HTO is $(2.87 - 2.35)10^{-5} = 0.52 \times 10^{-5}$ (1.0%), assuming that molecular tritium is only HT (i.e., no T_2 is present). The levels of tritium present are thus seen to be below the level of ion chamber detectability in the presence of a strong Ne-24 signal. Operation at lower

sweep gas flow rates would enhance the capability to measure the tritium by reducing the Ne-24 signal via decay during transport from the capsule to the monitor because of its short (3.4 min) half-life relative to that of tritium (12.3 yr). This assumes that changes in the permeation or adsorption of tritium in the capsule are less sensitive to flow than radioactive decay of Ne-24.

The measurement of the HT/HTO ratio is believed to be a valid measure of the ratio of H_2/H_2O or the oxidation potential of the capsule. This belief is based on the validity of the assumption that the levels of H_2 and H_2O are so large relative to those of HT and HTO that their equilibrium ratio determines that of the HT and HTO since tritium is exchanging with normal hydrogen. It does not appear likely that oxidation potential of the capsule is the same as that of the fuel rod. Only ~5% of the tritium has been swept from the capsule, strongly suggesting that adsorption in the capsule and/or the sweep gas lines is important. Thus, as anticipated in the original planning, the addition of H_2 to the sweep gas will be required. The addition of H_2O will be necessary to maintain the system near present oxidation potential or to approach expected GCFR conditions.

5.6.1.2.2. Run 11. In this series of tests, tritium in a known concentration in the helium sweep gas flowed through the capsule using four different flow modes to measure the reactivity or absorption of tritium of the various-path elements. The capsule was operated at 39 kW/m and the monitor charcoal bed contained 8 g. The gas swept from the capsule flowed through the magnesium converter, charcoal trap, and ion chamber. No molecular sieve samples of tritiated water were taken. The sweep gas contained a tritium concentration of 1×10^{-3} μCi/ml and flowed at 15 ml STP/sec through the capsule, and 5 ml STP/sec of helium with 4% H_2 was added to make a total of 20 ml STP/sec entering the tritium monitor (at the magnesium converter). Thus, a concentration of 7.5×10^{-4} μCi/ml would enter the monitor if no tritium removal or addition were made to the sweep gas while passing through the capsule. The corresponding ion chamber signal expected would be $7.5 \times 10^{-4}/5 \times 10^{-5}$ 55 mV (11/10) $\simeq$908 mV,

where the ion chamber pressure was 11 psig instead of the calibration pressure of 10 psig.

The sweep gas was first passed through the capsule bypass line to the monitor and an output of 1000 mV was measured. The flow was then valved to the TT_1-TT_2 flow mode, where TT_1 is the incoming line to the trap top and TT_2 is the outgoing line from the trap top. After a suitable delay in the charcoal trap, the output signal fell to ~100 mV. Thus, there was a clear indication of tritium loss in the capsule sweep gas lines.

Next, the flow was valved for the BT_1-TT_2 flow mode, where BT_1 is the incoming sweep gas line to the bottom of the rod's charcoal trap. Again, after suitable delay, the ion chamber output fell to 25 mV, indicating even more tritium losses in the BT_1 line and fuel rod charcoal trap than occurred in the TT_1 line.

Finally, the flow was valved for the TT_1-BT_2 flow mode, where the BT_2 is the outgoing sweep gas line from the bottom of the fuel rod charcoal trap. The ion chamber output returned to ~100 mV. Thus, the rod trap and BT_2 line are equivalent to the TT_2 line in removing tritium from the sweep gas stream.

These tests confirm that even if all the tritium formed in fission were released from the solid to the gas phase in the fuel, the rod trap and the sweep gas lines would be major sinks for tritium when the total hydrogen (i.e., tritium plus normal hydrogen) in the sweep gas was very low (<40 ppm). Thus, the lines and trap mask what is occurring in the fuel rod. It seems apparent, however, that the same effects must be operating in the fuel rod as well. In that case, the tritium distribution in capsule GB-10 and its fuel rod is not typical of GCFRs. Again, as with the results of venting tests without tritiated sweep gas (run 9), it is necessary to add H_2 and H_2O to the sweep gas upstream of the capsule to measure the tritium permeation, venting, and distribution typical of pressure-equalized and vented GCFR fuel rods.

5.7. HEDL CLADDING IRRADIATIONS

Inclusion of GCFR ribbed and smooth cladding specimens now being irradiated in a materials test experiment that was designed and fabricated by Hanford Engineering Development Laboratories (HEDL) was reported in a previous report. The test matrix has since been revised to include specimens ribbed by mechanical grinding (see Table 5.14). Initially, specimens ribbed by etching (and smooth specimens) were included.

Table 5.14

GCFR CLADDING IRRADIATION TEST MATRIX (HEDL CAPSULES)

Irradiation Temperature [°C (°F)]	Fluence (n/cm^2)	Type of Specimen	Scheduled Removal From EBR-II
538 (1000)	$6.9 - 9.4 \times 10^{22}$	5 smooth, 5 ribbed by mechanical grinding	9/78
704 (1300)	$2.6 - 3.6 \times 10^{22}$	5 smooth, 5 ribbed by etching	9/75
704 (1300)	$4.2 - 6 \times 10^{22}$	2 smooth, 3 ribbed by etching	3/76
704 (1300)	$4.2 - 6 \times 10^{22}$	2 smooth, 3 ribbed by mechanical grinding	8/77

Ten cladding specimens irradiated in EBR-II to 3×10^{22} n/cm^2 are now scheduled for de-encapsulation and preliminary examination by HEDL in early February 1976. General Atomic's requirements on post-irradiation testing have been forwarded to HEDL. The conditions most representative of the GCFR require a hoop/axial stress ratio of unity since the load to the cladding will be mainly from fuel cladding mechanical interaction rather than from fission gas pressure. HEDL reports planning is under

way to provide a capability for adding a tensile load to a pressurized specimen to allow tests under the above conditions.

REFERENCES

1. "Gas-Cooled Fast Breeder Reactor Preliminary Environmental Report on 300-MW(e) Demonstration Plant," v. I, General Atomic Report GA-A12957, May 1974.

2. Marck, Wm. J., "Fast Reactor Fission Yields for U-233, U-235, U-238, and Pu-238," Idaho Chemical Programs Report ICP-50-I, December 1974.

3. Meek, M. E., and B. T. Rider, "Compilation of Fission Product Yields, Vallecitos Nuclear Center," General Electric Report NEDO 12154-1, 1974.

4. Campana, R. J., and B. D. Epstein, "Considerations in the Planning of Tritium Measurements in Irradiation Capsule GB-10," General Atomic, unpublished data.

VI. FUEL-ROD ENGINEERING (189a No. SU007)

The steady-state and transient performances of the fuel-, blanket-, and control-rods are being evaluated under this task to determine the performance characteristics, operating limits, and design criteria. Analytical tools (such as the LIFE-III code) are being adapted, updated, and/or developed, and applied to the analysis of the rods and the evaluation of GCFR irradiation experiments. Continuous surveillance of the LMFBR fuels and materials development programs and technology is maintained to maximize the use of developing technology and material properties. Support is provided in the planning and designing of irradiation experiments.

The objectives of the analytical task are to adapt and assess the ability of analytical behavioral models and computer codes (such as LIFE-III) to analyze the GCFR fuel-, blanket-, and control-rods and to evaluate irradiation experiments. The definition of design criteria, operating margins, failure criteria, and mechanisms under steady-state, transient, and load-following conditions will follow from these analyses.

6.1. FUEL, BLANKET, AND CONTROL ROD ANALYTICAL METHODS

6.1.1. Updating and Calibration of LIFE-III Code

The post-calibration checkout of the LIFE-III code using the experimental results of rods G-1 and G-3 from the F-1 series irradiation has been completed. The results have been distributed to all members of the National LIFE Code Working Group (ERDA, GE, WARD, HELD, AI, and GA). This fulfilled GA's commitment in Phase I of the thermo-mechanical calibration of the LIFE code.

The experimental conditions and the pre- and post-irradiation data and results for these rods are described in Section 6.2. The results of

the comparison of code prediction to experimental results are given in Tables 6.1 and 6.2.

The agreement of predicted to experimental results appears to be good; however, some of the parameters need further discussion to justify this statement:

1. The small amount of central melting observed in the bottom 127 mm of rod G-1 cannot be unequivocably explained and was not expected to occur. We believe that this was either the result of a short duration off-normal operating condition (such as the sharp upturn in flux and power curves at the rod end, which occurred after the insertion of the reflector in EBR-II) or a localized heat transfer problem due to coolant flow reduction during one of the flow reduction tests. Another likely explanation is that the solid fission products migrated toward the central void and formed a low melting eutectic, which then collected toward the bottom (a molybdenum ingot about 0.5 mm in diameter was observed there).

2. The code predicted no residual fuel/cladding gap at end-of-life while ceramography showed that gaps of less than 0.025 mm existed at the ends of the fuel column. This disagreement is not considered to be significant in view of the fact that no gaps were observed in the middle sections of the fuel column (this agrees with the code's prediction).

   One explanation for this observation is local conditions, i.e., stronger fuel/cladding mechanical interactions occurred in the end sections where fuel collected by vapor transport closed the central voids, resulting in a higher central temperature and higher thermal expansion causing the fuel to creep inward. This would result in a larger EOL cold gap due to both relaxation of the higher thermal expansion and fuel creep. Some

Table 6.1

COMPARISON OF EXPERIMENTAL RESULTS TO LIFE CODE PREDICTIONS FOR ROD G-1 FROM THE F-1 SERIES IRRADIATIONS IN EBR-II
(5.4 at-% Burnup)

	Fuel Axial Section	Central Void Diameter (mm)[b]	Columnar Grain Region Diameter (mm)	Equiaxed Grain Region Diameter (mm)	Fuel Center Melt Diameter (mm)	Residual Fuel Cladding Gap (mm)	Total O.D. Increase (%)	Total Inelastic Strain (ΔD-Swell) (%)	Room Temperature EOL Plenum Pressure (MPa)	Fission Gas			
										Total Released (cm^3)	Released (%)	End of Life Composition (%)	
												Fission Gas	He
Life Code Predicted	(Bottom) 1	1.875	5.039	5.64	0	0	0.310	0.146					
	2	1.948	5.33	5.82	0	0	0.310	0.091					
	3	1.979	5.43	5.92	0	0	0.241	0.101	0.70	100.4	92.5	80	20
	4	1.968	5.36	5.87	0	0	0.230	0.119					
	(Top) 5	1.935	5.10	5.74	0	0	0.236	0.128					
Experimentally Measured	(Bottom) 1	1.829	4.77	5.59	1.524[c]	0.023	0.160	(d)					
	2	1.879	4.83	5.41	0	0.018	0.200	(d)					
	3	1.879	4.75	5.33	0	0	0.253	(d)	0.78	117.2	93.0	84.1	15.9
	4	1.829	4.62	5.16	0	0	0.247	(d)					
	(Top) 5	1.676	4.95	5.84	0	0.006	0.190	(d)					

[a] Each axial section is 68.6 mm long.

[b] At top and bottom of the fuel column the central void was completely closed (fuel bridged over by evaporation-condensation), the occlusion was only in the end 2.5 mm of the fuel.

[c] Observed only in the bottom <12.7 mm of fuel column.

[d] Cannot be determined. Only one cladding density measurement made, and it indicated no change in density.

Table 6.2

COMPARISON OF EXPERIMENTAL RESULTS TO LIFE CODE PREDICTIONS FOR ROD G-3 FROM THE F-1 SERIES IRRADIATIONS IN EBR-II
(2.65 at-% Burnup)

	Fuel Axial Section	Central Void Diameter (mm)[b]	Columnar Grain Region Diameter (mm)	Equiaxed Grain Region Diameter (mm)	Fuel Center Melt Diameter (mm)	Residual Fuel Cladding Gap (mm)	Total O.D. Increase (%)	Total Inelastic Strain (ΔD-Swell) (%)	Room Temperature EOL Plenum Pressure (MPa)	Fission Gas			
										Total Released (cm^3)	Released (%)	End of Life Composition (%)	
												Fission Gas	He
Life Code Predicted	(Bottom) 1	1.656	4.420	5.156	0	0	0.126	0.126					
	2	1.740	4.877	5.410	0	0	0.119	0.119					
	3	1.773	5.055	5.537	0	0	0.144	0.139	0.37	41.6	81.6	62.2	37.8
	4	1.757	4.877	5.436	0	0	0.151	0.143					
	(Top) 5	1.689	4.470	5.258	0	0	0.154	0.150					
Experimentally Measured	(Bottom) 1	1.524	4.318	4.953	0	0.013	0.247	(c)					
	2	1.727	4.572	5.054	0	0	0.273	(c)					
	3	1.829	4.648	5.105	0	0	0.290	(c)	0.29	38.4	60.0	65.4	34.6
	4	1.727	4.521	5.004	0	0	0.273	(c)					
	(Top) 5	1.524	3.988	4.826	0	0.018	0.226	(c)					

[a] Each axial section is 68.6 mm long.

[b] At top and bottom of the fuel column the central void was completely closed (fuel bridged over by evaporation-condensation). The occlusion was only in the end 2.5 mm of the fuel.

[c] Cannot be determined. Only one cladding density measurement made, and it indicated no change in density.

central melting in the bottom section of G-1 where the largest residual gap was observed would indicate an increase in fuel creep rate due to the higher temperature.

3. The total ΔD (cladding diametral increase) predicted by the code is about 50% smaller than that observed experimentally for rod G-3. A better agreement exists for rod G-1 except for the bottom section where central melting and the fuel/cladding gap were observed. While the difference at first seems to be large, considering that the numbers being compared are small (0.12% to 0.3%), that the accuracy of measurement from profilometry is $\pm$0.005 mm (nearly 0.1%), and that the baseline measurement (obtained from profilometry measurements of the lower plenum) was subject to the same inaccuracy (nearly 0.1%), then these results compare quite favorably because the differences are within the limits of accuracy of the measurements performed.

   In this area, another point that may come into question is the fact that larger ΔD increases were measured for rod G-3 (2.65 at-% burnup) than for rod G-1 (5.4 at-% burnup). This is probably due to the fact that the ΔD's were relative to the baseline measurement, which was taken on the lower plenum region where, due to the low temperature (~316°C) and low flux, no swelling was assumed to have occurred. It has been shown that cold-worked 316 stainless steel cladding undergoes some densification (with a consequent slight decrease in diameter) at the beginning of irradiation due to annealing out of loops and dislocations put in by the cold work. In the higher burnup rod (G-1), some or all of the initial shrinkage due to densification might have been overcome by some small but finite swelling since the integrated flux was at least twice that of rod G-3. To give an example, a very small linear radial swelling, say 0.0025 mm, would correspond to a diametral increase of the baseline measurement of nearly 0.1%. This would result in a similar apparent decrease in the ΔD measurement obtained by difference

with the above baseline measurement. Again it should be remembered that these numbers are still within the limits of accuracy of the experimental measurements.

4. The experimentally measured total inelastic strain cannot be assessed. Only one density measurement, from about the mid-section of the rod, was made. The method used (immersion density measurements) was not able to detect changes of less than 0.1%; since no change in density was detected, it follows that if any change occurred it was less than 0.1%.

The conclusion from the foregoing is that the LIFE code is in good agreement with the experimental observations made on rods G-1 and G-3 from the F-1 series irradiations in EBR-II. This is significant in that it fills in the confidence data in the higher cladding temperature range (693°C and 760°C) at relatively high power (472 W/cm and 492 W/cm) and at burnup extending to 5.4 at-%.

Figure 6.1 shows where these rods fit in with the rest of the rods used in Phase I of the post-calibration checkout of the code.

6.1.2. Gas Cooled Version of the LIFE Code

The identification of the program changes, coolant properties, and models substitutions to be made to the LIFE code (subroutine GOLDN and constants in QQ array) in order to obtain a gas-cooled version of the LIFE-III code has been completed. These changes are now being implemented, and the heat transfer correlation has been set up for incorporation into the code.

6.1.3. Control Rod Analytical Methods

A listing of the CONROD code (Control Rod Thermal Hydraulics Design code) had previously been obtained. Most of the changes necessary to

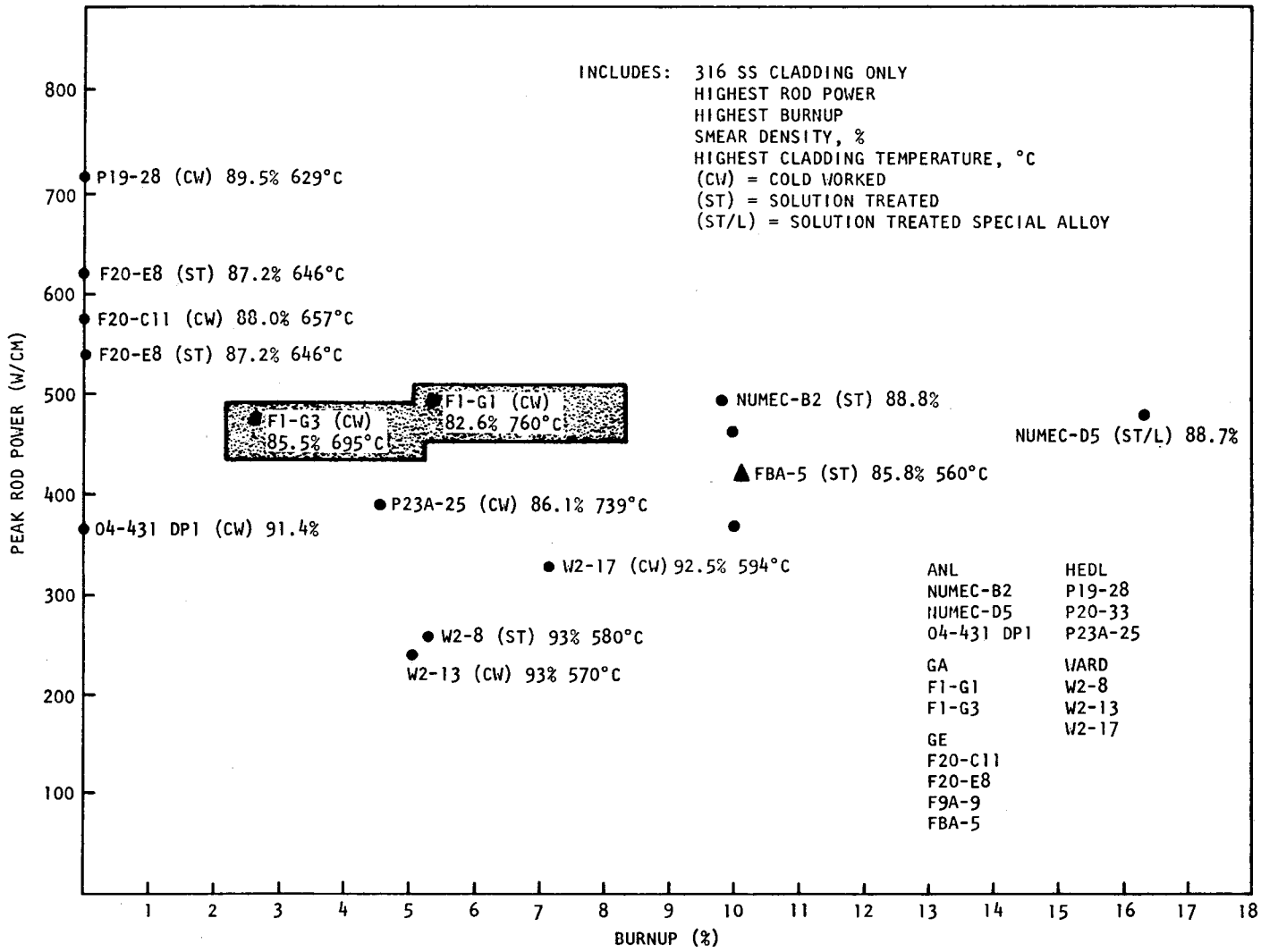

Fig. 6.1 Fuel pins used for Phase I of LIFE-III checkout

make it amenable to the analysis of a gas cooled control rod have been identified. A complete punched deck of the code has been obtained from HEDL.

6.1.4. Blanket Rod Analytical Methods

The material properties (UO_2 and ThO_2) to be integrated in the LIFE code for the analysis of radial blanket rods have been identified, and an evaluation has been made. Using the properties now in the LIFE code to analyze either UO_2 or ThO_2 blanket rods will result in slightly conservative performance predictions. The LIFE-III code is now being modified for application to the analysis of radial blanket rods.

6.2. ANALYSIS OF IRRADIATION TESTS

6.2.1. Analysis of Rods G-1 and G-3 from the F-1 Irradiations

A complete updated package of pre- and post-irradiation data and measurements for rods G-1 and G-3 from the F-1 series has been completed and mailed to all the other members of the National LIFE Code Working Group (HEDL, WARD, GE, AI, and ERDA). This data was used in the post-calibration checkout of the LIFE code and fills in the gap in the high cladding temperature and high power region.

Rods G-1 and G-3 have been discharged from a type B7B capsule (subassembly X094), which is being irradiated in EBR-II to a projected maximum burnup of 125,000 MWD/MTM (13.4 at-%). The accumulated maximum burnup for rods G-1 and G-3 were 5.4 at-% and 2.65 at-% respectively at discharge.

The fuel is sol-gel derived mixed oxide (15% Pu) annular pellets, highly enriched in U-235 (~93% of U). The pre-irradiation data (rod and fuel geometry, composition, dimensions, etc.) are given in Tables 6.3 and 6.4. The irradiation data (such as power, coolant flow, peak neutron flux, peak cladding temperature, etc.) are given in Tables 6.5 and 6.6.

Table 6.3

PRE-IRRADIATION DATA - ROD G-1

Outer rod diameter, mm	7.62
Inner cladding diameter, mm	6.68
Pellet diameter, mm	6.57
Central void diameter, mm	1.52
Fuel column length, mm	346.2
Initial total void volume in rod (measured), cm^3	19.8
Pellet dishing diameter, mm	5.84
Pellet dishing depth, mm	0.152
Fuel pellet density, % TD	90.3
Fuel smear density, % TD	82.64
Initial PuO_2 concentration (fractional)	0.1515
Fill gas	Helium
Initial fill gas pressure (MPa at 25°C)	0.129
Cladding material	20% CW - 316 SS
O/M ratio	1.992
Fractional U-235 content	0.93
Stagnant Na annulus between cladding and thermal barrier, mm	0.952
304 SS thermal barrier thickness, mm	3.85
Stagnant Na annulus between thermal barrier and capsule wall, mm	0.597
304 SS outside capsule wall thickness, mm	0.698
Stagnant sodium pressure on cladding wall, MPa	~0.648 (at power) 0.129 (at 25°C)
Total weight of (U, Pu)O_2 in fuel column, g	109.508
Plenum length (does not include dishes, central void, and fuel-cladding gap)	535.0
Equivalent cladding length (fuel plus plenum), mm	881.4

Table 6.4

PRE-IRRADIATION DATA - ROD G-3

Outer rod diameter, mm	7.62
Inner cladding diameter, mm	6.68
Pellet diameter, mm	6.596
Central void diameter, mm	1.506
Fuel column length	343.9
Initial total void volume in rod (measured), cm^3	19.8
Pellet dishing diameter, mm	5.84
Pellet dishing depth, mm	0.152
Fuel pellet density, % TD	91.0
Fuel smear density, % TD	85.52
Initial PUO_2 concentration (fractional)	0.1515
Fill gas	Helium
Initial fill gas pressure, MPa at 25°C	0.129
Cladding material	20% CW - 316 SS
O/M ratio	1.987
Fractional U-235 content	0.93
Stagnant Na annulus between cladding and thermal barrier, mm	1.715
304 SS thermal barrier thickness, mm	2.413
Stagnant Na annulus between thermal barrier and capsule wall, mm	1.27
304 SS outside capsule wall thickness, mm	0.698
Stagnant sodium pressure on cladding wall	~94 (at power) 0.129 (at 25°C)
Total weight of (U, Pu)O_2 in fuel columns, g	111.585
Plenum length (does not include dishes, central void, and fuel/cladding gap)	539.0
Equivalent cladding length (fuel plus plenum)	882.9

Table 6.5

IRRADIATION DATA FOR ROD G-1 FROM F-1 SERIES IRRADIATIONS IN EBR-II[1]

EBR-II Run No.	Peak Reactor Thermal Power[a] (MW_t)	Rod Peak Linear Power[b] (W/cm)	Peak Cladding Temperature (°C)			Sodium Coolant Flow Through Assembly[b] (liters/sec)	Peak Fast Neutron Flux ($\eta/cm^2 \cdot sec$) x 10^{-14})
			OD	ID	Mid-Wall		
47 (B)	62.5	480	712	752	732	1.00	12.14
48 (A,B)	62.5	445	690	729	710	1.00	11.26
49 (A,B,C)	62.5	487	717	758	738	1.00	12.31
49 (D,E)	40.0	312	604	632	618	1.00	7.87
50 (B)	50.0	302	598	625	612	1.00	7.65
50 (C,F,H)	62.5	378	647	679	663	1.00	9.56
51 (A,C)	62.5	491	719	760	740	1.00	12.42
52 (A,C)	62.5	457	696	735	716	1.00	11.56
52 (B)	30.0	219	546	568	557	1.00	5.55
53 (A,B,C,D,E)	62.5	457	696	736	716	1.00	11.56
54 (A)	62.5	436	684	721	703	1.00	11.03
56 (C)	62.5	469	709	749	729	1.06	11.67
57 (A)	62.5	452	699	737	718	1.06	11.15
58 (A,B,C)	62.5	472	712	752	732	1.06	11.66
59 (A,B)	62.5	462	705	745	725	1.06	11.49
60 (A)	62.5	462	705	745	725	1.06	11.50
61 (A,B)	62.5	466	708	748	728	1.06	11.41

[a]Not corrected by the -9% suggested by ANL-E.

[b]Corrected by the -9% suggested by ANL-E.

Table 6.6

IRRADIATION DATA FOR ROD G-3 FROM F-1 SERIES IRRADIATIONS IN EBR-II[1]

EBR-II Run No.	Peak Reactor Thermal Power[a] (MW_t)	Rod Peak Linear Power[b] (W/cm)	Peak Cladding Temperature (°C)			Sodium Coolant Flow Through Assembly[b] (liters/sec)	Peak Fast Neutron Flux ($\eta/cm^2 \cdot sec \times 10^{-14}$)
			OD	ID	Mid-Wall		
47 (B)	62.5	462	649	688	669	1.00	11.22
48 (A,B)	62.5	431	632	669	651	1.00	10.45
49 (A,B,C)	62.5	468	653	692	673	1.00	11.36
49 (D,E)	40.0	300	559	586	563	1.00	7.27
50 (B)	50.0	291	552	580	566	1.00	7.04
50 (C,F,H)	62.5	363	594	626	610	1.00	8.81
51 (A,C)	62.5	472	655	695	675	1.00	11.43
52 (A,C)	62.5	439	637	674	656	1.00	10.62
52 (B)	30.0	211	508	530	519	1.00	5.10
53 (A,B,C,D,E)	62.5	439	638	675	657	1.00	10.65
54 (A)	62.5	420	626	662	644	1.00	10.17

[a]Not corrected by the -9% suggested by ANL-E.

[b]Corrected by the -9% suggested by ANL-E.

The actual time-power history and the suggested "filtered" power history (time averaged) are given in Tables 6.7 and 6.8. Given in Table 6.9 are the power and flux profiles for six axial sections (five in the fuel and one for the plenum). These profiles were derived from ANL-E data and from the results of post-irradiation zirconium isotope scans of the cladding. The cladding OD axial temperature distribution for the six axial sections (including the plenum temperature) are given in Table 6.10. These temperatures were obtained by calculations using the TAC-2D code and independently confirmed by ANL-E using both the HECTIC-III and the THTB codes.

The post-irradiation data (including measurements of central void, melt diameter, columnar, and equiaxed grain growth regions, residual fuel/

Table 6.7

TIME-POWER HISTORY FOR ROD G-1 FROM THE F-1 SERIES IRRADIATIONS IN EBR-II

EBR-II Run No.	Reactor Thermal Power (MW_t)														
	0.05	0.5	10	20	30	40	50	56	62.5	0.1	20	30	40	50	62.5
	Total Time (Hours) at Indicated Reactor Thermal Power (MW_t)														
	Actual Time-Power History									Suggested Filtered Power History (Time-Averaged)					
47 (B)	25.5	8.0	2.5	3.5	6.5	1.5	4.5	4.5	180.5	12.5	15.0		13.3		180.5
48 (A,B)	24.0	5.5	3.5	5.0	7.5	6.5	1.5	1.5	18.0	12.0	18.0		16.8		18.5
49 (A,B,C)	36.0	0.5	7.0	3.0	16.0	4.5	5.5	14.5	336.0	16.0	30.5		22.0		336.0
49 (D,E)	15.0		5.0	5.0	2.5	5.5				7.5	9.0		5.5		
50 (B)	6.0		3.0		2.0	1.5	2.5			3.0	9.0			3.0	
50 (C,F,H)	19.5	7.5	3.5	4.0	5.5	4.0	3.0	2.5	523.5	10.0	14.3		11.0		523.5
51 (A,C)	28.0	12.5	11.5	8.5	13.5	6.0	10.0	16.0	559.0	14.0	25.0		41.0		559.0
52 (A,C)	11.0	8.0	3.0	2.5	9.5	2.5	2.5	3.5	580.5	5.5	18.7		10.5		580.5
52 (B)	1.0		2.0	1.5	2.5					0.5	2.5	3.0			
53 (A,B,C,D,E)	17.5	5.0	8.0	11.5	16.5	11.0	6.0	4.0	567.5	8.0	41.0		24.0		567.5
54 (A)	12.0	3.5	2.0	1.0	2.0	0.5	1.5	3.5	578.0	6.0	3.5		5.5		578.0
56 (C)	10.5	8.0	7.0	4.5	10.0	12.0	3.0	3.0	575.0	5.0	23.4		20.0		575.0
57 (A)	15.0		3.0	3.0	6.0	5.5	8.0	3.0	530.5	7.5	13.5		19.0		530.5
58 (A,B,C)	12.5	12.0	5.0	10.0	9.0	6.0	5.5	5.0	574.0	6.0	24.5		19.0		574.0
59 (A,B)	16.0	11.0	5.5	5.5	5.5	7.5	5.5	7.0	545.0	8.0	17.0		27.5		545.0
60 (A)	19.5	4.5	3.0	5.5	3.5	2.5	3.5	2.0	585.0	10.0	17.0		9.5		585.0
61 (A,B)	9.0	11.0	12.5	14.0	16.5	12.5	14.5	13.0	584.0	4.5	45.5		44.0		584.0

Table 6.8

TIME-POWER HISTORY FOR ROD G-3 FROM THE F-1 SERIES IRRADIATIONS IN EBR-II

EBR-II Run No.	Reactor Thermal Power (MW_t)														
	0.05	0.5	10	20	30	40	50	56	62.5	0.1	20	30	40	50	62.5
	Total Time (Hours) at Indicated Reactor Thermal Power (MW_t)														
	Actual Time-Power History									Suggested Filtered Power History (Time-Averaged)					
47 (B)	25.5	8.0	2.5	3.5	6.5	1.5	4.5	4.5	180.5	12.5	15.0		13.3		180.5
48 (A,B)	24.0	5.5	3.5	5.0	7.5	6.5	1.5	1.5	18.0	12.0	18.0		16.8		18.5
49 (A,B,C)	36.0	0.5	7.0	3.0	16.0	4.5	5.5	14.5	336.0	16.0	30.5		22.0		336.0
49 (D,E)	15.0		5.0	5.0	2.5	5.5				7.5	9.0		5.5		
50 (B)	6.0		3.0		2.0	1.5	2.5			3.0	9.0			3.0	
50 (C,F,H)	19.5	7.5	3.5	4.0	5.5	4.0	3.0	2.5	523.5	10.0	14.3		11.0		523.5
51 (A,C)	28.0	12.5	11.5	8.5	13.5	6.0	10.0	16.0	559.0	14.0	25.0		41.0		559.0
52 (A,C)	11.0	8.0	3.0	2.5	9.5	2.5	2.5	3.5	580.5	5.5	18.7		10.5		580.5
52 (B)	1.0		2.0	1.5	2.5					0.5	2.5	3.0			
53 (A,B,C,D,E)	17.5	5.0	8.0	11.5	16.5	11.0	6.0	4.0	567.5	8.0	41.0		24.0		567.5
54 (A)	12.0	3.5	2.0	1.0	2.0	0.5	1.5	3.5	578.0	6.0	3.5		5.5		578.0

Table 6.9

POWER AND FLUX PROFILES FOR SIX AXIAL SECTIONS FOR RODS G-1 AND G-3
(F-1 Series)

	Axial Sections					
	1 (Bottom)	2	3	4	5	6 (Plenum)
Prior to Run #55 (Same for G-1 and G-3)						
Relative Power Profile	0.900	0.975	0.995	0.935	0.855	---
Relative Flux Profile	0.885	0.968	0.990	0.930	0.833	0.35
After Run #55 (G-1 Rod Only)						
Relative Power Profile	0.935	0.970	1.00	0.970	0.895	---
Relative Flux Profile	0.910	0.976	1.00	0.965	0.870	0.35

cladding gap, cladding OD, etc.) are given in Table 6.11. Tables 6.12 and 6.13 give the end-of-life gas analysis, internal void volume, cladding density measurements, and fission gas released.

The data, tables and diagrams were developed at GA and all references from which data were obtained are available.

A complete punched and interpreted computer deck for LIFE code runs for each rod with the "filtered" power history and six axial sections (including plenum) have been prepared and sent to the LIFE Code Committee Working Group and put on the RODS computer file on the Berkeley CDC-7600 computer.

These have been successfully run on the Berkeley CDC-7600, and the results have been compared against the experimental measurements (see Section 6.1).

Table 6.10

AVERAGED CLADDING OD AXIAL TEMPERATURE DISTRIBUTION FOR RODS G-1 AND G-3 FROM THE F-1 SERIES IRRADIATIONS IN EBR-II (6 AXIAL SECTIONS)

Run Number	Peak Power (W/cm)	Peak Mid-Wall Temperature (°C)	OD Cladding Temperatures Axial Section (°C)					
			1 (Bottom)	2	3	4	5	6 (Plenum) (Estimated)
Rod G-1								
47 (B)	480	732	639	681	707	710	705	536
48 (A,B)	445	710	612	661	685	688	684	514
49 (A,B,C)	487	738	644	685	711	715	710	544
49 (D,E)	312	618	553	582	602	603	600	453
50 (B)	302	612	547	576	597	598	596	453
50 (C,F,H)	378	663	588	621	643	646	640	475
51 (A,C)	491	740	646	688	714	717	711	543
52 (A,C)	457	716	620	661	692	695	690	513
52 (B)	219	557	500	527	546	546	544	430
53 (A,B,C,D,E)	457	716	620	661	692	695	690	445
54 (A)	436	703	607	654	680	683	679	510
56 (C)	469	729	635	675	708	707	707	538
57 (A)	452	718	618	660	694	697	693	521
58 (A,B,C)	472	732	638	678	707	710	706	535
59 (A,B)	462	725	630	669	701	704	700	520
60 (A)	462	725	630	669	701	704	700	520
61 (A,B)	466	728	634	674	704	707	703	533
ANL-E								
51 (G-1)	491	745	633	682	718	721	710	
Rod G-3								
47 (B)	462	669	582	618	642	647	645	480
48 (A,B)	431	651	568	598	625	630	628	462
49 (A,B,C)	468	673	585	623	648	651	650	485
49 (D,E)	300	563	498	533	554	559	557	415
50 (B)	291	566	493	527	548	552	551	410
50 (C,F,H)	363	610	539	568	589	594	592	440
51 (A,C)	472	675	586	623	648	655	653	486
52 (A,C)	439	656	572	609	632	636	634	480
52 (B)	211	519	455	485	504	508	507	400
53 (A,B,C,D,E)	439	659	572	612	635	637	636	480
54 (A)	420	644	566	600	623	625	624	470

Table 6.11

POST-IRRADIATION DATA ON RODS G-1 AND G-3 (F-1 SERIES)

Rod No.	Axial[a] Position (mm)	Sample Type	Central Void Diameter (mm)		Melt Diameter (mm)	Columnar Grain Zone Diameter (mm)	Equiaxed Grain Zone Diameter (mm)	Residual Cold Diametral Gap (mm)	Maximum Internal Cladding Attack (mm)	Cladding O.D.[c] Measurement (mm)	Peak Cladding O.D. Temperature for Peak Power[d] Run (°C)	Peak Burnup a/o
			Maximum	Minimum								
	Bottom	Long.	---	Closed[b]	---	4.85	5.92	0.152	None			
	4.06	Long.	1.09	1.04	1.68			0.127				
	6.35	Long.	1.09	1.04	1.60			0.076				
G-1	8.64	Long.	1.14	1.09	1.32					7.627	719	5.4
	83.8	Trans	1.93	1.62	---	4.72	5.46	0.038	0.028	7.633		
	171.5	Trans	2.03	1.73	---	4.75	5.33	None	0.063	7.639		
	287.0	Trans	1.73	1.57	---	4.52	5.05	0.013	0.051	7.635		
	Top	Long.	---	Closed[b]	---	4.85	5.76	0.051	0.066			
	Bottom	Long.	Closed		---	3.56	4.80	0.063				
	3.43	Long.	1.24		---			0.063				
	5.08	Long.	1.32		---			0.063		7.637		
G-3	85.73	Trans	1.62		---	4.50	5.00	<0.005		7.640	655	2.65
	174.6	Trans	1.83		---	4.65	5.10	None		7.642		
	273.0	Trans	1.60		---	4.39	4.95	<0.005		7.640		
	340.6	Long.	Closed		---			0.051		7.634		
	Top	Long.	Open (1.24)		---	3.58	4.65	0.051				

[a] Distance above fuel stack bottom.

[b] Central void closed by fuel evaporation and recondensation for about 3.2 mm at top and bottom of fuel column.

[c] Average of 0°, 45°, 70°, and 135° measurements.

[d] See also run-by-run data (Tables 6.7 and 6.8).

Table 6.12

POST-IRRADIATION GAS ANALYSES FOR ROD G-1

Gas	Volume (%)	Volume of Gas at STP (cm^3)
H_2	< 0.1	< 0.14
He	16.2	22.6
H_2O	< 0.1	< 0.14
N_2	0.2	0.3
O_2	< 0.02	< 0.03
A	0.06	0.08
CO_2	< 0.1	< 0.14
Kr	12.4	17.3[a]
Xe	71.7	99.9[a]
	Total	140.63

End-of-life total internal gas pressure (MPa at 25°C	0.782
Measured end-of-life internal void volume (cold, cm^3)	22.1
Change in cladding density (immersion density measurements)[b]	None

[a]Fission gas release based upon 0.2055 cm^3/g fuel/at-%; burnup = 93%.

[b]Results are from one sample only at about fuel midplane.

6.2.2. Evaluation of General Electric F-20 Rods

Review of the data and decks for the GE F-20 rods (E-1, E-2 and S-4) has been initiated. The analysis is being carried out using the calibrated version of the LIFE-III code.

6.2.3. Evaluation of Rods from F-1 Series Irradiation

The collection and analysis of the pre- and post-irradiation data for the remaining rods in the F-1 series irradiations in EBR-II (rods

Table 6.13

POST-IRRADIATION GAS ANALYSIS FOR ROD G-3

Gas	Volume (%)	Volume of Gas at STP (cm^3)
H_2	< 0.1	< 0.06
He	33.9	19.8
N_2, CO	0.09	0.05
O_2	0.01	0.006
A	0.2	0.12
CO_2	< 0.1	< 0.06
Kr	9.2	5.3[a]
Xe	56.2	33.1[a]
	Total	58.496

End-of-life internal gas pressure (MPa at 25°C)	0.291
Measured end-of-life internal void volume (cold, cm^3)	21.6
Change in cladding density (immersion density measurements)[b]	None

[a]Fission gas release, based upon 0.2055 cm^3/g fuel/at-%; burnup = 60%.

[b]Results are from one sample only at about fuel midplane.

G-2, G-4, G-5, G-6, G-7, G-8, G-9, G-10, G-11, G-12, G-13) have been initiated.

6.3. CLADDING STRUCTURAL CRITERIA

Work is continuing on publication of a draft version of the GCFR fuel-, blanket-, and control-rod cladding structural criteria. Recently ERDA has established a National Working Group for design guidelines criteria for LMFBR core components. The purpose of the group is to assemble a unified set of core component structural criteria from the various existing criteria for use throughout the industry. General Atomic has been

asked to join this effort. Consequently, the GCFR cladding structural criteria will become identical, or nearly identical, to the unified LMFBR criteria. In response to recommendations made at the third meeting of the National Working Group on design criteria, three areas have been changed:

1. A limit is now imposed on secondary stress limits, depending on the material ductility at the time under consideration as determined by the plastic component of uniform elongation (ε_u) at failure, for the given conditions of temperature and fluence. A transition point of $\varepsilon_u = 1\%$ determines ductile, $\varepsilon_u > 1\%$, and non-ductile, $\varepsilon_u < 1\%$, behavior. The limit on combined primary membrane plus bending ($P_L + P_B$) and secondary (Q) stress intensity ranges is a function of the ultimate stress for non-ductile behavior. For ductile behavior, a specified combination of these stress intensities must be within 80% of the conventional Brec elastic-plastic shakedown boundary for axisymmetric sections removed from discontinuities. The stable cyclic yield stress at 2% offset is now used as a normalization factor on these stress intensities.

2. The elastic peak stress is now also limited based on ductility considerations. Using the true strain at facture (ε_f) as an index, peak stresses in non-ductile materials ($\varepsilon_f < 10\%$) shall not exceed S_u. No limit is imposed for ductile ($\varepsilon_f > 10\%$ material behavior.

3. The component design margins specified as a function of operation conditions were modified in the case of control components and other critical assemblies under emergency conditions. Since the intent has been that in such cases the control components must maintain functional adequacy without loss of reliability, the design margins for emergency conditions for these components were the same as for normal and upset. In some instances, this

may be overly restrictive. Consequently these limits are now left to the discretion of the designer.

Two additional areas are under further investigation by General Electric: the feasibility of using unirradiated materials to simulate the limit load and shape factors for irradiated stainless steel is being explored, and test recommendations to quantify these items are being formulated; and a possible correlation between shape factors (for brittle fracture analysis) and the yield and ultimate stresses is also being evaluated.

At the next meeting (March 30-31, 1976) of the National Working Group, these investigations will be reviewed and recommendations incorporated into the preliminary design criteria. The approved preliminary documents will then be issued for trial use along with material correlations not contained in the NSM Handbook.

The remaining funding of this subtask will be used to evaluate the additional investigations discussed above. The final draft of the preliminary design criteria will be reviewed for approval at the March meeting. These criteria will then be applied to GCFR fuel rods and fuel assemblies.

6.4. ROD ANALYSIS AND PERFORMANCE

6.4.1. Fuel Rod Cladding Stress Analysis

The creep collapse study of simulated accidentally sealed GCFR fuel rod cladding continued during this quarterly period. The cladding collapse analysis is being performed using a modified version of the COLLAPSE code, modified to accept histogram pressure and temperature input. LIFE-III runs were made to provide data on internal fission gas buildup in the simulated sealed rods for combinations including low (143 W/cm) and high (364 W/cm) power rods (one run with three transients of 15% overpower), with cladding 0.5 mm and 0.38 mm thick, and subject to ~9 MPa external coolant pressure.

These data are currently being used to determine a better approximation for the collapse time of low power rods (small fission gas buildup over life) and an estimate of the possibility of a burst failure in the high power rods (large gas buildup).

The internal pressure in the low power rods builds up to approximately the external pressure at EOL. The pressure in the high power rods equals the external pressure after about 6,000 hours and builds up to less than 20.7 MPa at EOL. This pressure buildup in the high power rods is not enough to cause fuel rod failure due to cladding yielding (the maximum circumferential stress at EOL does not exceed 2/3 of the allowable yield stress). The initial out-out-roundness (defined as $OD_{max} - OD_{min}/4$) was taken as 0.006 mm, based on the maximum tolerance specified for vendor's tubing.

The debugging of the modified COLLAPSE code is now in progress using the internal pressure buildup from fission gases obtained from the LIFE code for the low power rods.

6.4.2. Blanket Rod Evaluation

The steady-state behavior of radial blanket rods of 25.4 and 20.3 mm in diameter with 0.15 and 0.18 mm fuel/cladding diametral gaps have been evaluated using the LIFE code. Four and six year management schemes were considered.

For conservatism, the peak cladding temperatures associated with the peak nominal power in each cycle were used. These are shown in Figs. 6.2 and 6.3. The linear power history and associated fast flux used for each management scheme and rod diameter are given in Figs. 6.4, 6.5, and 6.6.

Since the analysis was performed using the LIFE-III code, the properties of $(U, Pu)O_2$ were used because they are very nearly the same as those

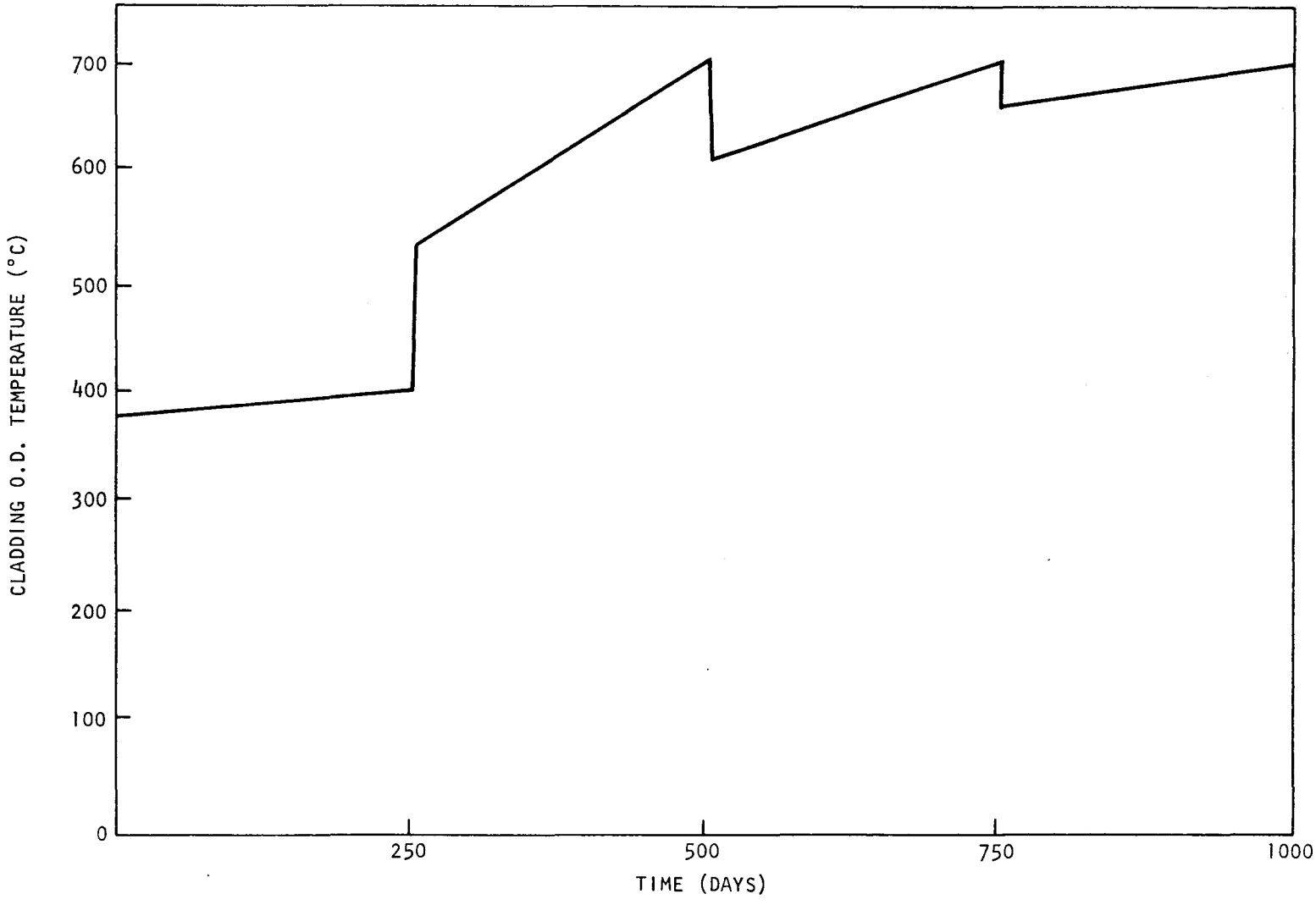

Fig. 6.2 Peak cladding temperature for thoria blanket rod 4-yr management scheme

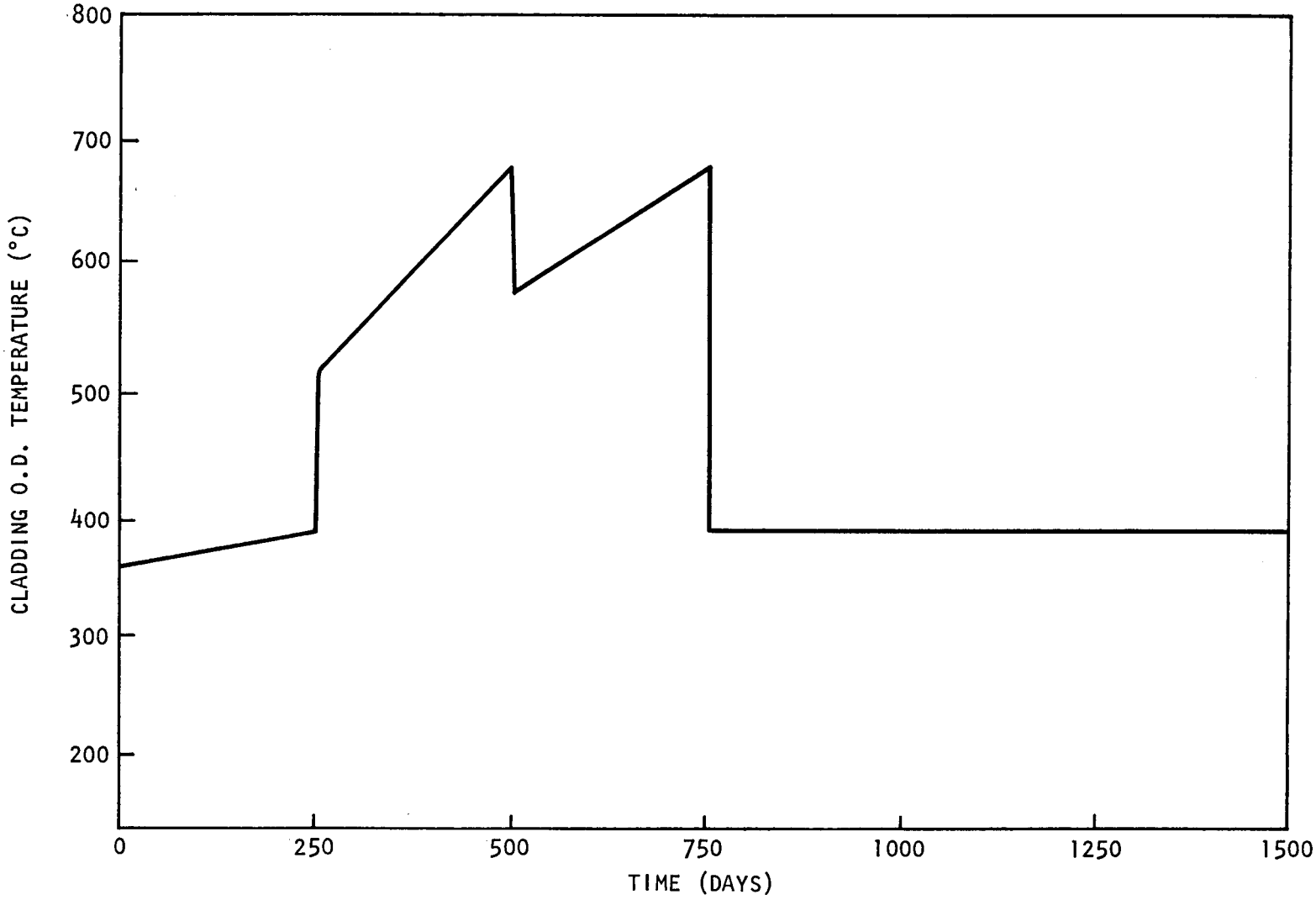

Fig. 6.3 Peak cladding temperature for thoria blanket rod 6-yr management scheme

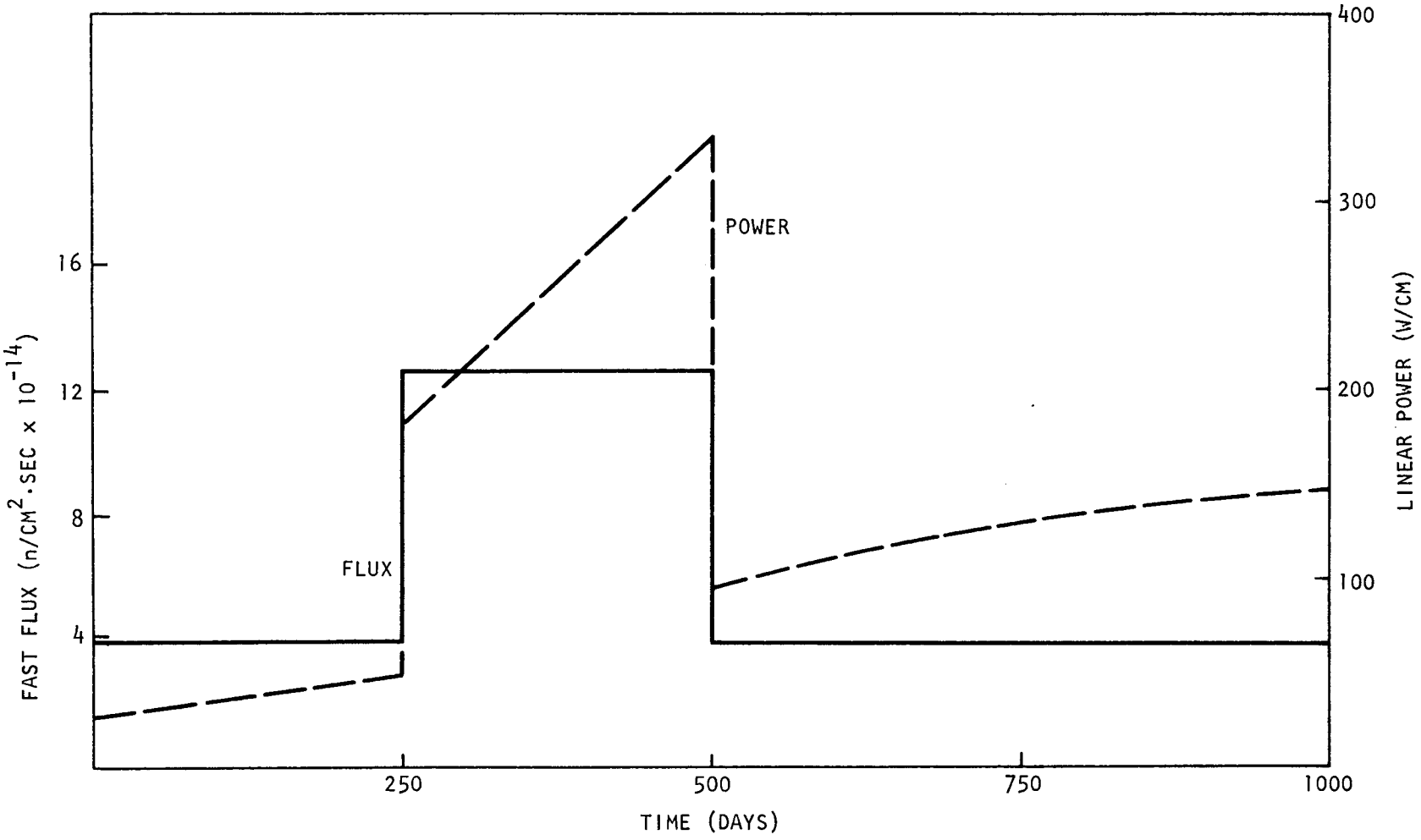

Fig. 6.4 Variation of peak power and fast flux in two-row thorium blanket with 37 rods (25.4-mm diameter), 4-yr residence, and in-out shuffling

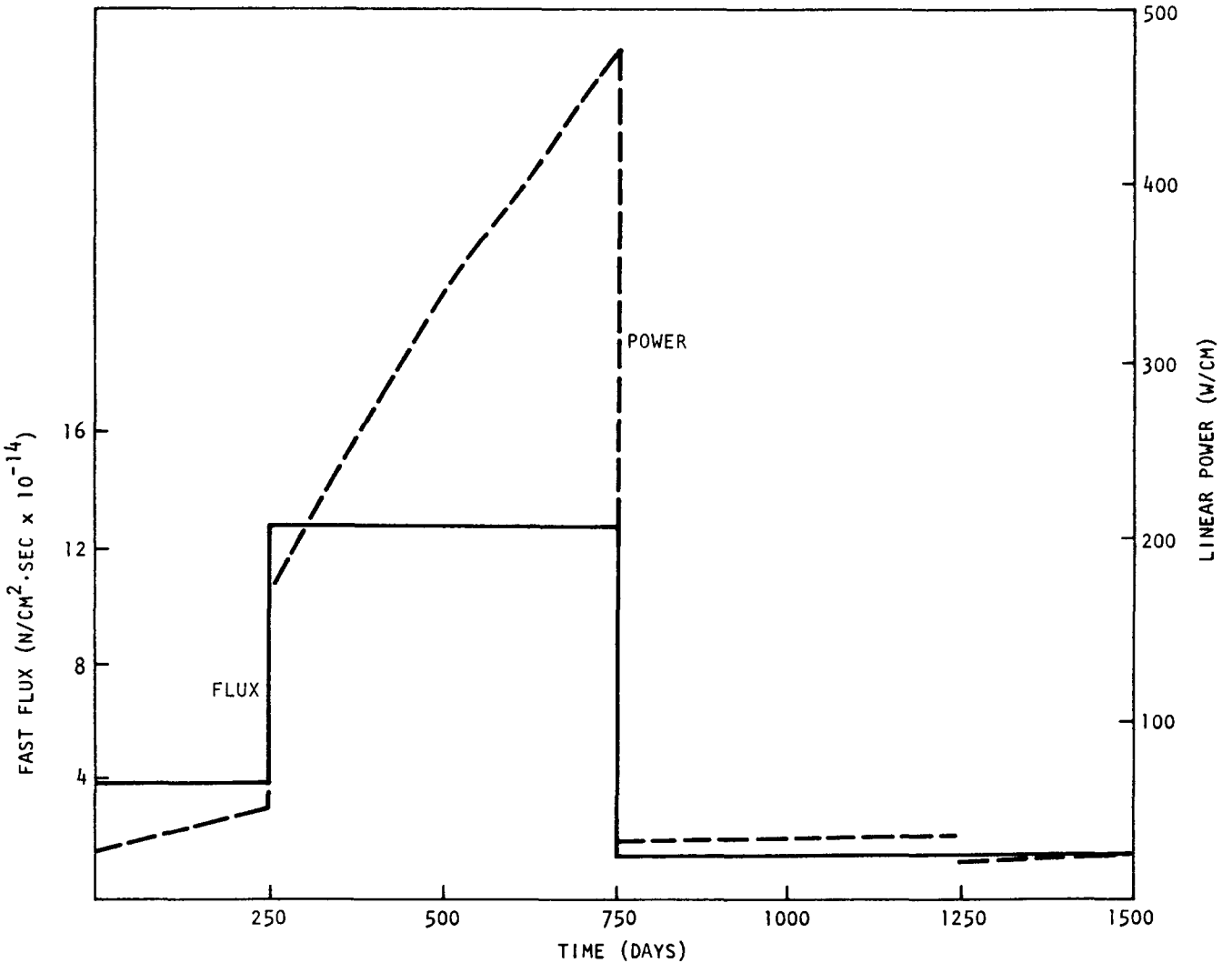

Fig. 6.5 Variation of peak power and fast flux in two-row thorium blanket with 37 rods (25.4-mm diameter), 6-yr residence, and in-out shuffling

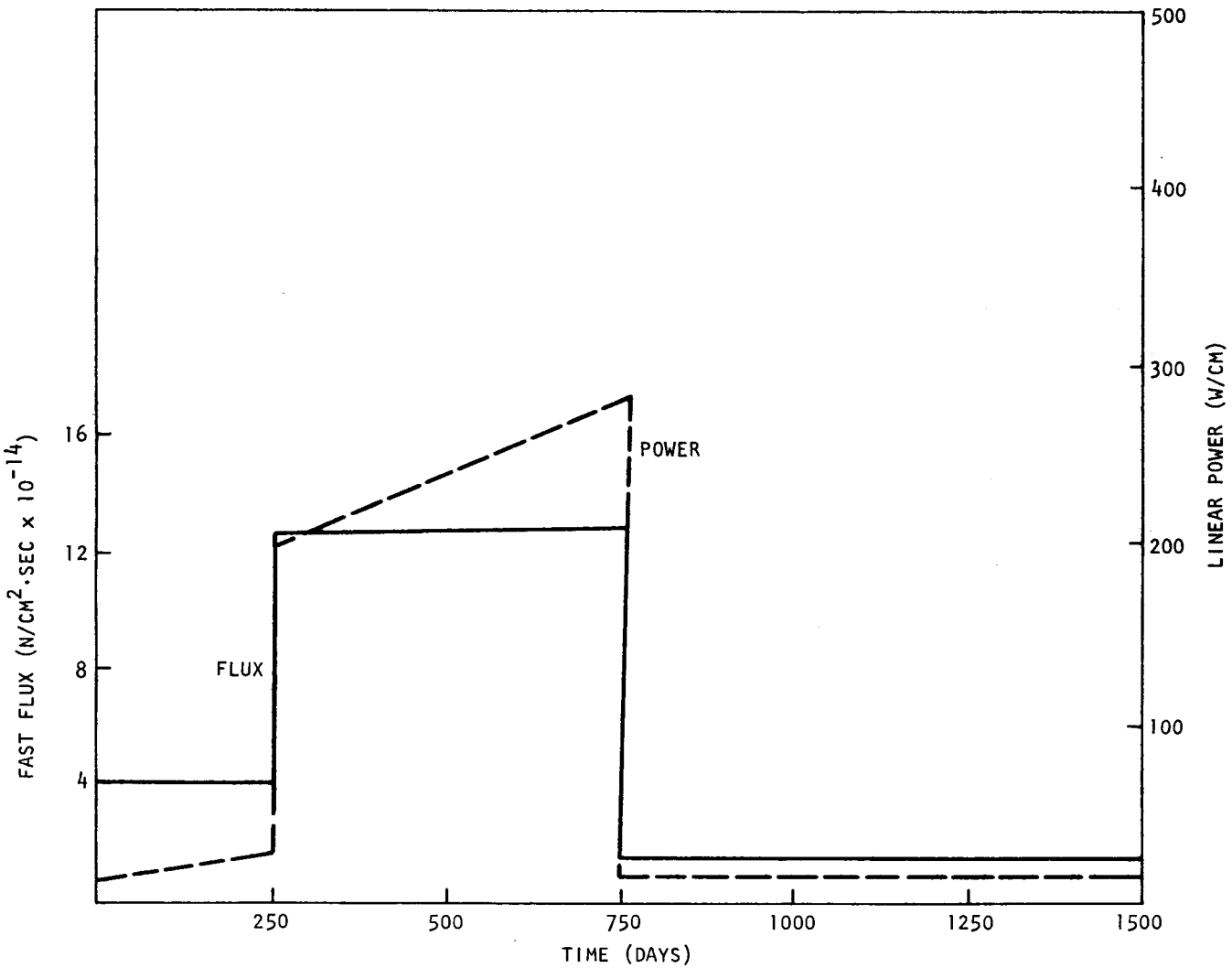

Fig. 6.6 Variation of peak power and fast flux for two-row thorium blanket with 61 rods (19.8-mm diameter), 6-yr residence, and in-out shuffling

for UO_2 or ThO_2 (conservative for ThO_2). In addition, any small difference in properties is also minimized by the fact that the blanket peak EOL burnup is very low compared to that of the fuel (<0.5 at-%).

To simulate vented rods, a very large plenum was postulated in such a way that the internal rod pressure never exceeded the external pressure by more than ~0.3 MPa, and the helium dilution by fission products in the gap did not exceed 10%.

The simulation resulted in the following findings:

1. The estimated power-to-melt for UO_2 is ~650 W/cm and for ThO_2 is ~850 W/cm, thus leaving a considerable margin-to-melt even under 15% overpower conditions (Fig. 6.7).

2. The EOL residual inelastic cladding strain never exceeded 0.1%, which is well below the design criterion limit of 1%.

3. The thermal creep strains are always less than 10^{-6} and are therefore negligible.

4. Negligible effects on temperatures, cladding strains, and power-to-melt result from changing the fuel/cladding gap from 0.18 to 0.15 mm and from changing the rod diameter from 20.3 to 25.4 mm.

5. The maximum fuel centerline temperature (2200°C) occurs at the end of the third cycle of the 25.4 mm diameter rods when the power reaches 476 W/cm.

This analysis was for the steady-state and did not consider the effects due to the differential irradiation-induced swelling and thermal gradient around the cladding circumference, which are the results of exposure to the flux gradient, especially at the interface between the fuel and blanket assembly.

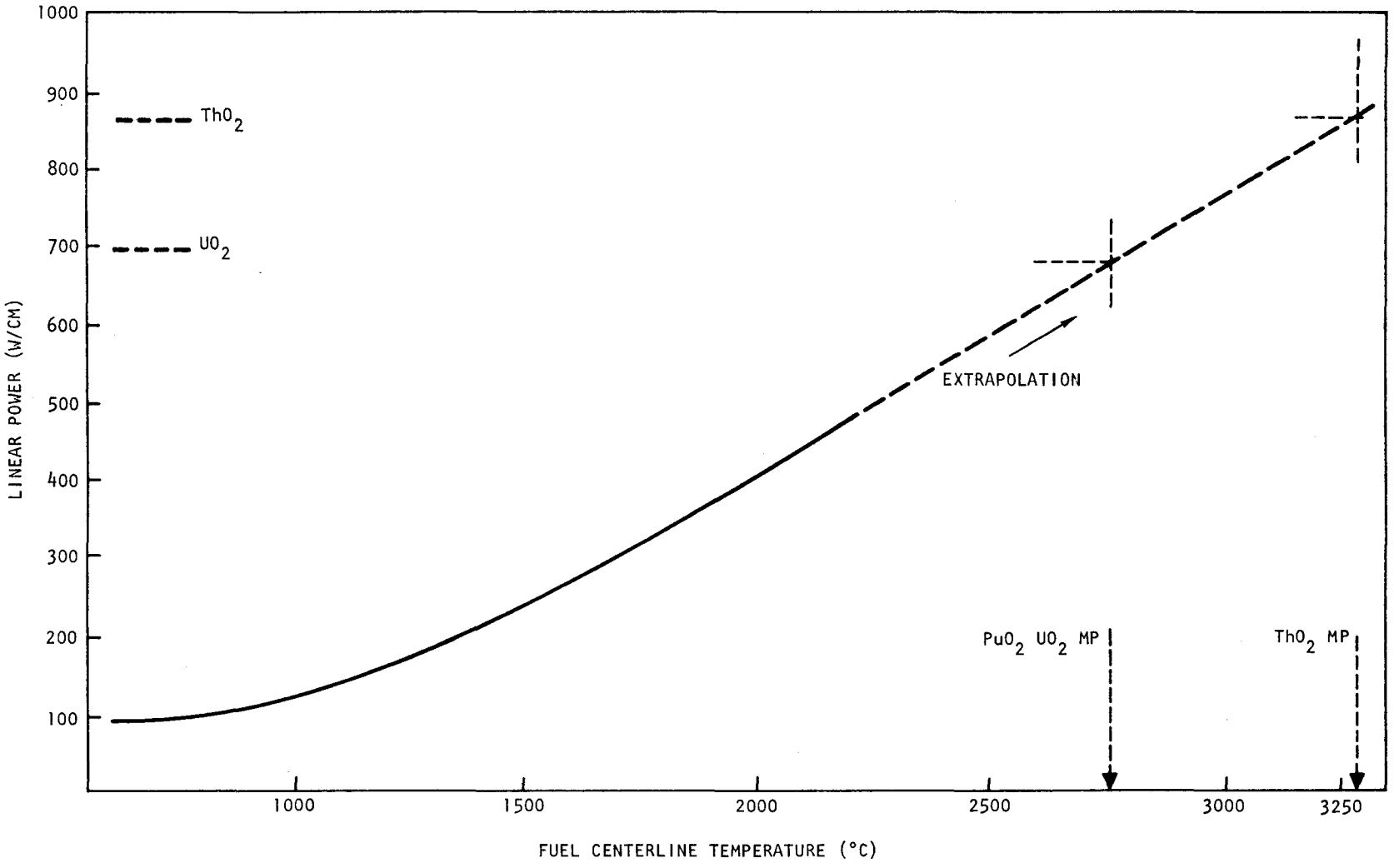

Fig. 6.7 Fuel centerline temperature vs linear power for radial blanket rods (25.4-mm diameter)

The proposed design has 19.8 mm diameter rods and a four-year management scheme. Although unanalyzed as yet, the results will be conservative with respect to the above analysis.

6.4.3. Fuel Rod Parametric Studies

Preliminary fuel rod parametric studies have been initiated using the LIFE-III code. The first parameter evaluated was the effect of utilizing solid fuel pellets versus the reference design pellet with a central void.

Preliminary results indicate that the absence of a fabricated central void results in an increase in fuel centerline temperature of about 120°C for the peak rod at 364 W/cm even at 15% overpower. The absence of the central void was compensated for by decreasing the fuel density (maintaining the fuel rod smear density).

Since the maximum centerline temperature is about 2000°C, the increase in centerline temperature (120°C) does not represent a significant decrease in the power-to-melt margin. No increase in EOL cladding inelastic strain was predicted for the analysis of the solid pellet of lower density.

6.4.4. Fuel Rod Transient Structural Analysis

A scoping model for the study of transient fuel cladding interactions has been developed using the TEPC structural analysis code. TEPC is a finite element code developed at General Atomic. It is one of the few codes that can perform combined thermal, elastic, plastic, and creep analyses on a single model. In addition, it is relatively simple and inexpensive to use.

The initial model employs 20 axisymmetric plane-strain finite elements to model a small section of the fuel rod, and was used to examine the suitability of the TEPC code for the fuel rod analysis. From the initial studies, it was found that it will be necessary to use separate models for

the thermal and mechanical portions of the analysis unless some modifications to the code are done. It was also found that the fuel/cladding gap could not be modeled directly in the structural models, but this is not a severe restriction in many cases. It has been concluded that the TEPC code can be used for preliminary studies of fuel rod transient structural behavior.

REFERENCE

1. Snyder, H. J., General Atomic, "Transmittal of Pre- and Post-Irradiation Data for Rods G-1 and G-3 from the F-1 Series Irradiations in EBR-II," unpublished data.

VII. NUCLEAR ANALYSIS AND REACTOR PHYSICS (189a No. SU008)

The scope of activities planned under this subtask encompasses the validation and verification of the nuclear design methods that will be applied to the GCFR core design. This will be done primarily by direct evaluation of the methods with a critical experiment program specifically directed toward GCFR development. Program planning and coordination activities, critical assembly design and analysis, and the necessary methods development will be carried out during the course of this program.

In the previous quarterly period, the Phase II core went critical with a radius close to that predicted by GA and ANL. Planning was completed jointly with ANL for a revised steam entry experiment to be performed in this phase. Post-analysis of the Phase I core was carried out with ENDF/B-IV nuclear data for criticality, polyethylene zone worth, central reactivity coefficients, and central reaction rate ratios in the as-built core configuration. Detailed specifications for an improved spectrum code were issued.

During this reporting period, planning for the inclusion of a steel reflector surrounding the Phase II and all subsequent assemblies was completed. Recalculation of steam and control boron worth, with the reflector in place, was accomplished. Post-analyses of the Phase I assembly, and in particular the steam zone experiment, were refined and continued. Methods development proceeded with the inclusion in the data files of ENDF/B-IV delayed-neutron data, and work was begun on speeding convergence of the 2DB two-dimensional diffusion code, which is to be used as a possible replacement for the more slowly converging ADGAUGE code.

7.1. PHASE I CRITICAL ASSEMBLY

7.1.1. Post Analysis of Phase I GCFR Critical Experiments

The post-analysis of the Phase I GCFR critical experiment is continuing. Reaction-rate mappings were generated from the two-dimensional diffusion calculations to compare with reaction-rate distributions measured via irradiations of uranium and plutonium foils. The comparisons show that the calculated power distributions, radially and axially, drop off faster than the measured fission-rate profiles; this indicates the calculated diffusion coefficients may be too low and/or that the calculations should include the effects of the steel support structure of ZPR-9 outside of the blankets, which are relatively thin.

7.1.2. Analysis of "Steam-Zone" Experiment

A refined analysis of the CH_2 flooding experiments in the central region of Phase I is under way. The previous ADGAUGE calculations for the 1/4- and 1/2-density CH_2 foam insertions utilized mixtures of two cross section sets: from the "dry" and full-density CH_2 GGC5 spectrum problems. For this re-analysis, separate GGC5 problems have been run to properly re-average the cross sections with the appropriate moderated spectra for each of the 1/4- and 1/2-density CH_2 cases. Using the updated 1/4-density (0.00875 g/cm^3 in void) GGC5 cross section set, new ADGAUGE calculations with the STOER exact perturbation theory capability were made. The re-analysis for the 1/4-density CH_2 worth yielded 131 Ih/kg, which compares well with the measured worth of 134 Ih/kg; calculations for the 1/2-density (0.0175 g/cm^3 in void) yielded a value of 158.8 Ih/kg, which is also in good agreement with the experimentally measured value of 160.2 Ih/kg.

Additional effort is being expended in this analysis using a 28 energy group structure instead of the usual 10 group partition.

7.2. PHASE II CRITICAL ASSEMBLY

7.2.1. Addition of Steel Reflector to Phase II

Foil irradiations in both Phases I and II have shown perturbations of the core and blanket flux profiles due to ZPR-9 structural components beyond the blankets, suggesting that the radial and axial blankets are neutronically too transparent. To mitigate this problem, an outer reflector of steel was proposed by ANL and agreed to by GA, and the construction was initiated during December. This reflector is constructed from 50.8 x 50.8 x 304.8 mm blocks of steel inserted into the matrix for two rows around the radial blanket and to a length of 152.4 mm beyond the axial blankets. In a first step to aid in the planning of the complete installation, and to provide a check on calculations, the reflector was installed around a quadrant of the blankets in one assembly half. The measured reflector-octant worth was about +85 inhours, extrapolating to about +0.7% $\Delta k/k$ for the full installation.

7.2.2. Analysis of Phase II GCFR Critical Experiment with Reflector

Pre-analysis ADGAUGE calculations for predicting the Phase II critical dimensions used a core radius of 59.0 cm yielding an eigenvalue of $k = 0.99952$. A repeat of this case using (1) a core radius of 58.14 cm, as derived from the designed core-cell fissile composition, (2) the ANL-specified critical mass, and (3) the average as-built blanket radius yielded an eigenvalue of $k = 0.99379$. Thus, with this model and using the directional diffusion coefficients to account for streaming, the calculational discrepancy amounts to a reactivity under estimate of 0.62% k or, conversely, an overprediction by 3% of the critical mass. However, the high blanket leakage from this assembly has led to a need for remodeling the analysis to include the structure of the ZPR-9 surrounding the basic core and blankets. When about 60 cm of homogenized matrix material is added radially around the radial blanket and 30 cm axially beyond the axial blankets, the calculated eigenvalue is raised to 0.99661, reducing the difference between measured and calculated eigenvalues to -0.34% k for the

Phase II study. These results are similar to the results for the ZPPR-2 benchmark calculations performed as part of the data testing for CSEWG.

The above calculations used directional diffusion coefficient modifiers to account for streaming except in the matrix material regions where isotropic diffusion was assumed (modifiers = 1.0). Repeat runs of the three ADGAUGE cases were made with all modifiers removed to evaluate the streaming effects on reactivity with the different models. Table 7.1 compares the results with and without streaming; also included in the table are cases with the steel reflector added. Reducing the core radius barely affects the streaming correction. The addition of the matrix reduces the streaming effect from 1.89 to 1.84% $\Delta k/k$. The largest effect on streaming worth resulted from adding the reflector, thus reducing the correction to about 1.7% $\Delta k/k$ (for a case without a change of core radius).

The last line in Table 7.1 gives the diffusion calculations of the reactivity change resulting from the addition of the Phase II reflector. Assuming a total steel density at about 91.8% by volume, the model dimensions for the reflector regions were specified to provide all the material in the designed reflectors plus the excess matrix structure beyond the reflectors. The calculated prediction using ADGAUGE is thus +1.04% Δk for the full reflector (relative to the matrix-added case). Extrapolation of the octant measurement already reported would give about +0.73% k.

7.2.3. Re-Analysis for CH_2 and B_4C Worths in Phase II with Steel Reflector

The reduced streaming and leakage provided by the steel reflector installed around the Phase II assembly will affect the polyethylene worth distributions and total "steam-ingress" effects. An analysis of the reactivity changes for the planned CH_2 foam insertions into the Phase II core and blanket void channels were therefore carried out for the steel-reflected model. At the planned maximum experimental density of 0.0175 g/cm^3 CH_2 in the channels, the reactivity gain (relative to the dry case) with the reflected assembly was calculated to be +0.89% k (about \$2.69), a value 24% less than without the reflector.

Table 7.1

STREAMING-EFFECT WORTHS CALCULATED FOR PHASE II WITH OUTER MATRIX OR REFLECTOR INCLUDED

Core Radius (cm)	ADGAUGE Model Reflector Region Specifications			Resulting k-value		Streaming Worth ($\Delta k/k_1 k_2$)
	Type	Radial Thickness (cm)	Axial Thickness (cm)	Direction Diffusion Modifiers	Isotropic Diffusion	
59.00	None	---	---	0.99952	1.01855	-0/0190
58.14	None	---	---	0.99379	1.01272	-0.0189
58.14	Homogenized Matrix	57.502	30.404	0.99661	1.01506	-0.0184
58.14	Steel Blocks	15.503	16.434	1.00704	1.02414	-0.0166

The plan for simulating steam entry into a rodded core has been finalized. Columns of B_4C are to be inserted into void spacers at the center of the reflected Phase II assembly and at eight additional symmetrical locations that are approximately 387 mm from the core center (about 2/3 of the distance to the core/blanket interface). The reactivity worths of these rods, and the change in worth with steam entry of various densities, have been computed with the 2-D code ADGAUGE and are exhibited in Table 7.2. As expected, rod worth increases with increasing steam entry, or alternatively, the reactivity worth of steam entry decreases in the rodded core. Successful calculation of this effect is expected to be a sensitive test of methods.

Table 7.2

WORTHS OF BORON CARBIDE COLUMNS INSTALLED IN PHASE II WITH VARIOUS REFLECTOR AND CH_2 FLOODING CONFIGURATIONS

CH_2 Density in Core and Blanket Void Channels (g/cm^3)	Outer Reflector Around Blanket Regions (with Constant Core and Blanket Dimensions)	Reactivity Change for B_4C Column Additions ($\Delta k/k_1/k_2$)	
		1 Column at Core Center	9 Columns Center plus Ring
None	None	-0.00491	---
None	Homogenized Matrix	-0.00478	-0.02417
None	Steel Blocks	-0.00449	-0.02438
0.00875	Steel Blocks	-0.00505	---
0.01750	Steel Blocks	-0.00564	-0.03092
0.03500	Steel Blocks	-0.00634	---

7.3. METHODS DEVELOPMENT

7.3.1. Version 4 Delayed Neutron Data

The GFE4 processing code has been modified to routinely process ENDF/B-IV delayed neutron data for the primary fissile and fertile nuclides.

7.3.2. Diffusion Code Development

A 28-group version of the 2-D diffusion code ADGAUGE has been developed and utilized for the dry Phase I assembly with a 28 x 25 mesh structure. The change in the eigenvalue going from 10 to 28 groups was $\Delta k = +0.0007$. Cases have been examined with and without the bidirectional diffusion coefficient modifiers; good agreement with the 10-group structure is obtained in both cases. The group structure effect on the first order perturbation worths of light elements, and in particular hydrogen, is now being examined.

The 2DB code was updated to accept the usual GCFR downscatter-only diffusion cross sections and checked against the ADGAUGE code for a GCFR Phase II critical assembly calculation (isotropic diffusion coefficients). It appears that 2DB is significantly faster than ADGAUGE for this problem and that 2DB converges stably and rapidly for both direct and adjoint calculations.

VIII. SHIELDING REQUIREMENTS (189a SU008)

The purpose of the shielding task is to verify the adequacy of the methods and data (physics and engineering) for the design of GCFR shields and to evaluate the effectiveness of various shield configurations. In addition, this task will coordinate and provide liaison with the analytical and experimental GCFR shielding activities at ORNL.

In the last quarterly period, results of radial shield studies including the effect of a two-row radial blanket on shielding requirements were reported. Shielding design criteria were examined, and a detailed method for determining fluence limits was developed. Preliminary analysis of the GA and ORNL benchmark calculations was conducted.

During this quarter, the effort was directed to the following areas:

1. A detailed analysis of the GA and ORNL shielding benchmark was carried out. The sources of differences in the absolute magnitude of the neutron transport and heating results were examined.

2. Additional analysis on the two-row blanket radial shield was conducted. The feasibility of incorporating a removable shield reflector element adjacent to the radial blanket was analyzed, and the effect of recent damage function data on the radial shield was investigated.

8.1. SHIELDING BENCHMARK CALCULATIONS

A detailed analysis was performed by GA and ORNL on the GCFR radial shield to serve as a benchmark calculation. The extended core version of the 1DFX code[1] was used by GA, and the ANISN[2] code was used by

ORNL. Both laboratories used neutron-coupled gamma-ray transport and heating cross sections throughout the core, blanket, shield, PCRV liner, and 30 cm of concrete in the PCRV.

The neutron-coupled gamma-ray cross section sets used at GA are reported in Refs. 3 and 4 and consisted of 24 neutron groups and 15 gamma-ray groups based on ENDF/B-III data. ORNL used its 51-neutron-group, 25 gamma-ray group library processed by the AMPEX code,[5] also based on ENDF/B-III data. Both laboratories used P_3 anisotropic scattering and S_6 angular quadratures.

Figure 8.1 shows the geometrical model used in the benchmark calculations. Table 8.1 gives a summary of the calculational parameters. Table 8.2 specifies the zone boundaries and material specifications.

8.1.1. Results and Discussion

The fundamental results of interest are presented in Figs. 8.2, 8.3, and 8.4. Figure 8.2 is a graph of the GA neutron flux versus radius for neutrons with E > 0.9 MeV; E > 0.086 MeV; E < 2.38 eV; and the total Figure 8.2 presents the ratios of ORNL results to GA results for the curves of Fig. 8.2, plus a few points for epithermal fluxes as a function of radius. Finally, Fig. 8.4 presents gamma-ray heating rates calculated at both laboratories in W/cm^3 versus radius, in the blanket (3-row nuclide densities), shield, liner, and concrete.

The ORNL neutron fluxes corresponding to the curves given in Fig. 8.2 can be obtained approximately by multiplying the magnitudes of the curve of interest in Fig. 8.2 by the appropriate ratio in Fig. 8.3.

Figure 8.2 is self-explanatory, with the various regions easily identified from the radii and materials given in Fig. 8.1. However, for the fuller appreciation of the agreement given in Fig. 8.3 for neutrons with E > 0.9 MeV, note that the magnitude of the fluxes with E > 0.9 MeV varies from $\sim 10^{15}$ to $\sim 4 \times 10^5$ $n/cm^2/sec$, or over nine orders of magnitude.

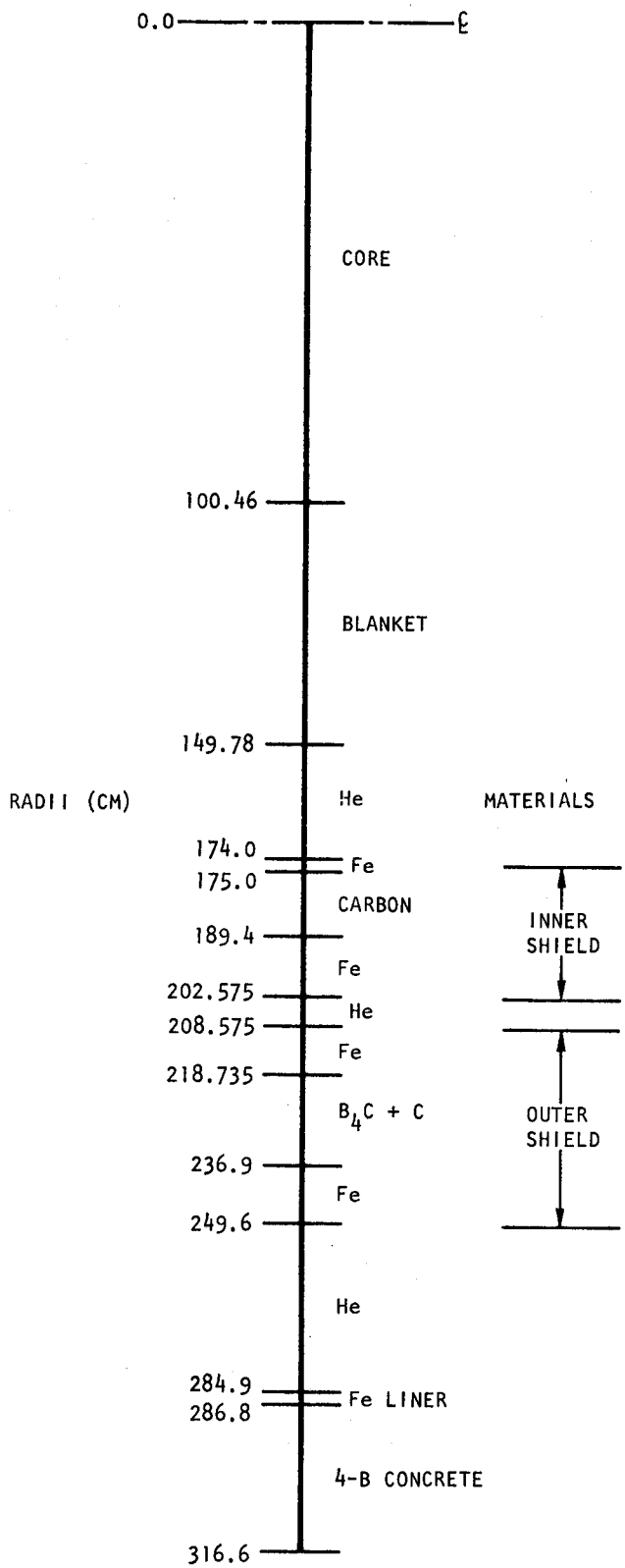

Fig. 8.1 Geometry for neutron-coupled gamma ray transport calculations

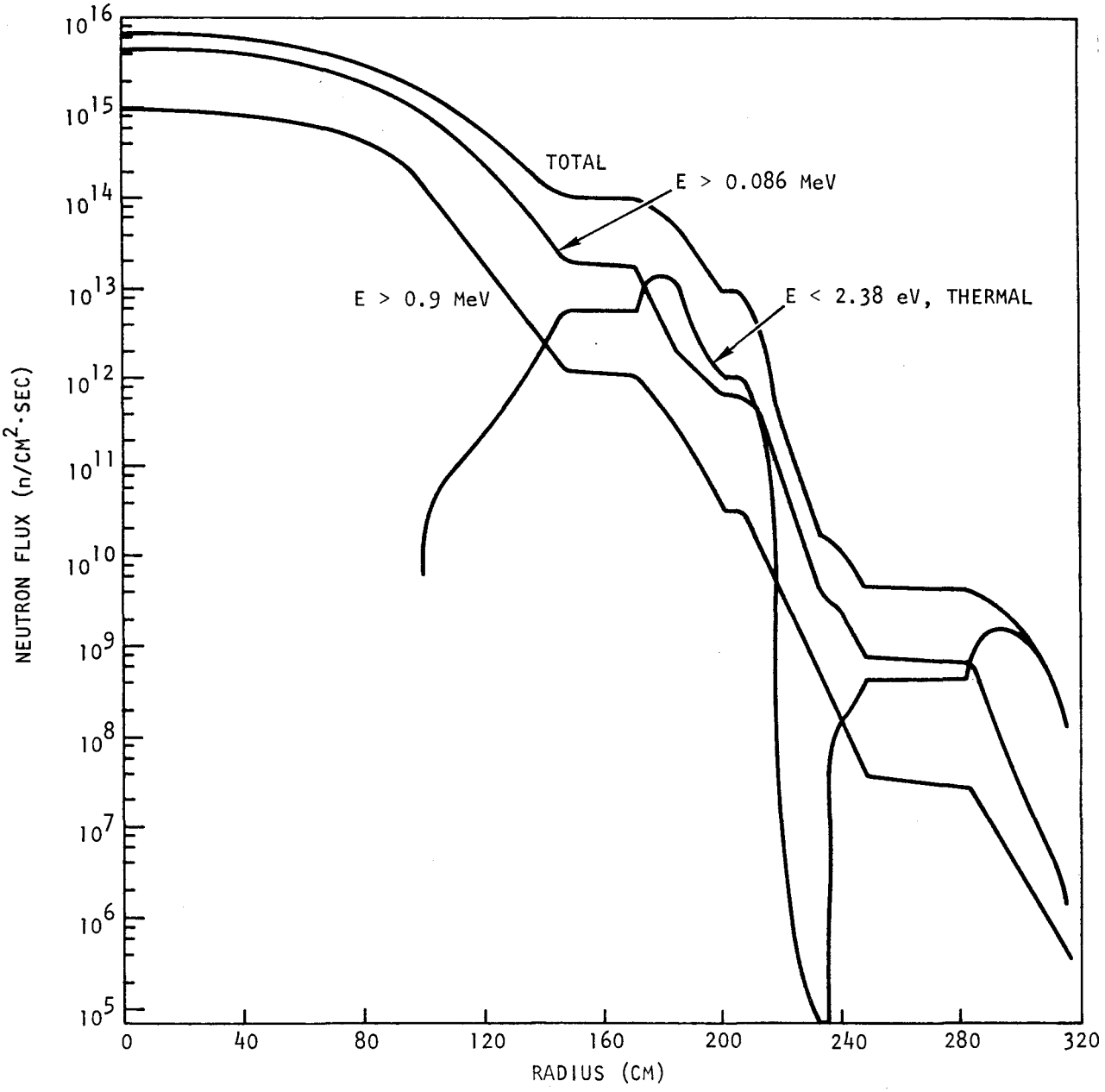

Fig. 8.2 GCFR benchmark neutron fluxes with E > 0.91 MeV, E > 0.086 MeV, thermal, and total

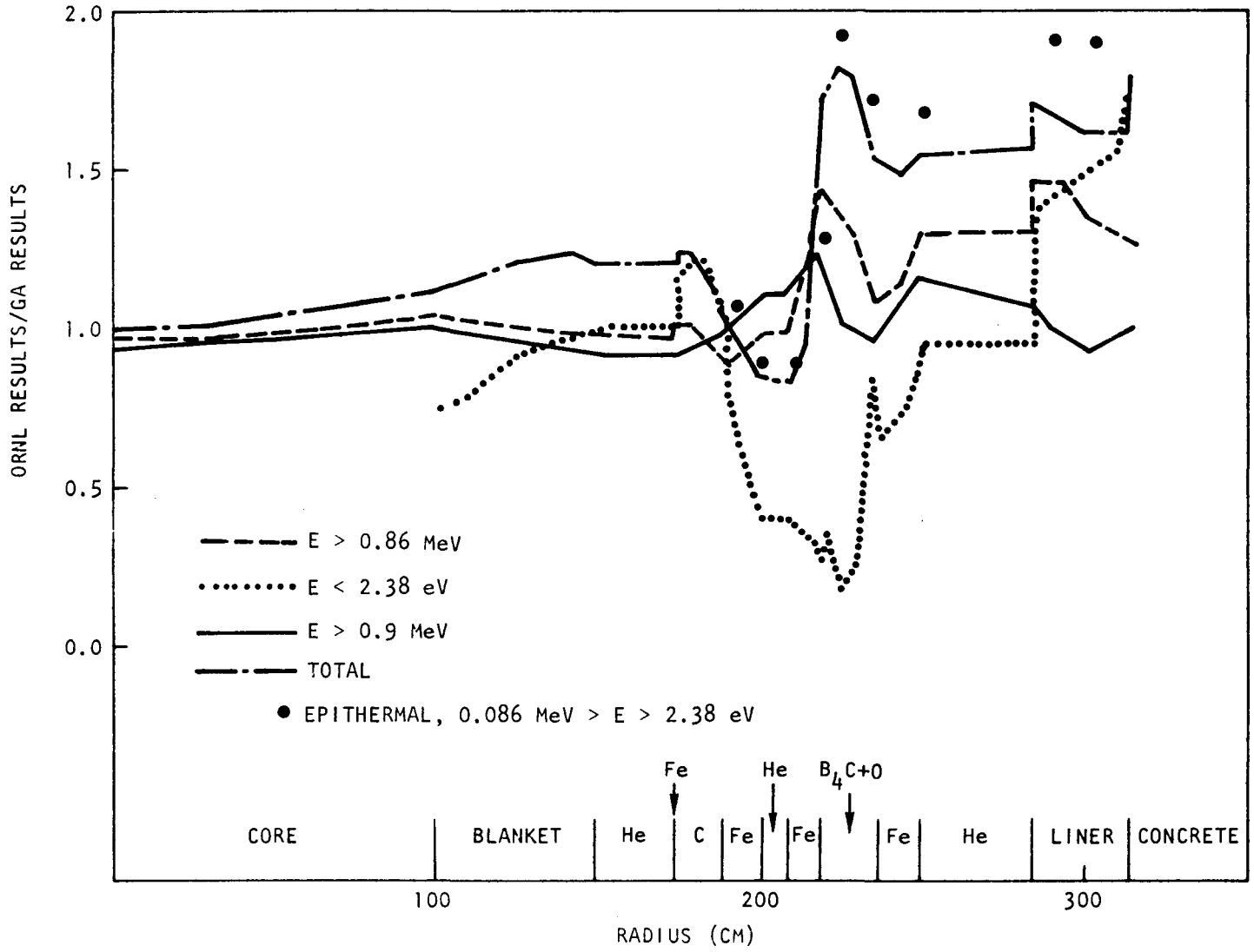

Fig. 8.3 Comparison of ORNL and GA GCFR benchmark results; ratios of neutron flux

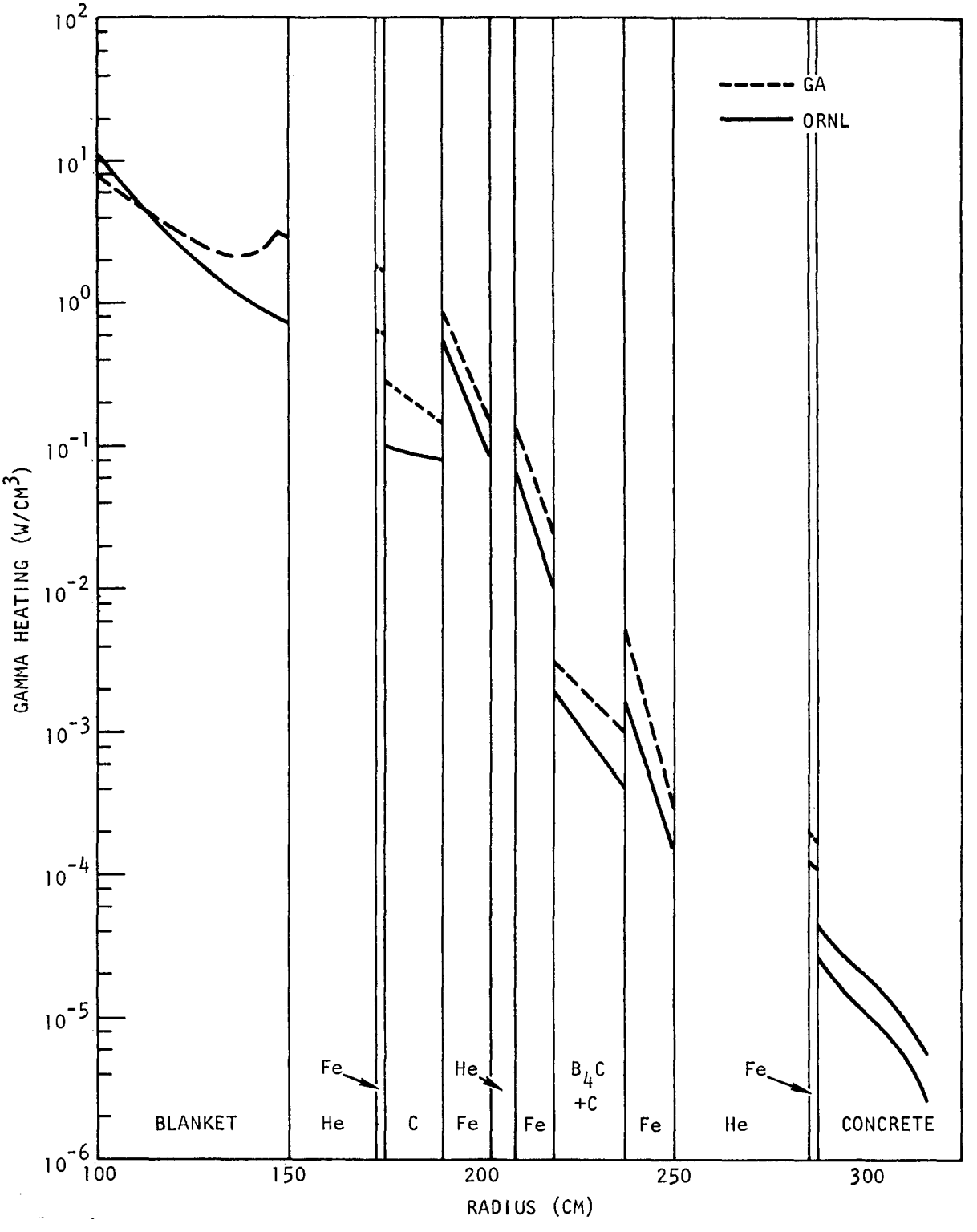

Fig. 8.4 Gamma heating for the GCFR benchmark

Table 8.1

PARAMETERS USED IN THE GCFR BENCHMARK, NEUTRON-COUPLED, GAMMA-RAY HEATING CALCULATIONS

Codes	
GA	1DFX, extended core version ED32 (July 19, 1975)
ORNL	ANISN
Quadrature	S_6
Scattering	P_3
Geometry	Cylinder
Boundary conditions	Reflective at origin, vacuum at right boundary
Number of material zones	13
Total number of fine-mesh intervals	187
Input guess	1.0 flux
Eigenvalue type	k-calculation
Number of energy groups	
GA	39 (24 neutron + 15 gamma)
ORNL	76 (51 neutron + 25 gamma)
Overall convergence criterion	0.001
Flux pointwise convergence criterion	0.001
Buckling factor	
GA	1.813857
ORNL	1.42089
Buckling total height	134.0
Buckling total depth	0.0
Eigenvalue obtained in the solution	
GA	1.136
ORNL	1.161

Table 8.2

RADII, FINE-MESH INTERVALS, AND MATERIALS

Zone	Radii (cm)	Number of Fine Mesh Intervals	Material
	0.0 - 2.00	2	
	2.0 - 8.0	2	
1	8.0 - 92.46	17	Core (averaged)
	92.46 - 98.46	2	
	98.46 - 100.46	2	
	100.46 - 102.46	2	
2	102.46 - 147.78	14	Blanket (averaged)
	147.78 - 149.78	2	
	149.78 - 151.78	2	
	151.78 - 155.78	2	
3	155.78 - 168.0	2	Helium
	168.0 - 172.0	2	
	172.0 - 174.0	2	
4	174.0 - 175.0	2	Fe
5	175.0 - 177.0	4	Carbon
	177.0 - 189.4	13	
	189.4 - 190.9	2	
6	190.9 - 200.9	8	Fe
	200.9 - 202.575	2	
7	202.575 - 208.575	6	Helium
	208.575 - 210.575	2	
8	210.575 - 216.735	3	Fe
	216.735 - 218.735	2	

Table 8.2 (continued)

Zone	Radii (cm)	Number of Fine Mesh Intervals	Material
	218.735 - 222.735	13	
9	222.735 - 232.9	20	B_4C + C
	232.9 - 236.9	12	
	236.9 - 238.9	2	
10	238.9 - 247.6	5	Fe
	247.6 - 249.6	2	
	249.6 - 253.6	2	
	253.6 - 261.6	2	
11	261.6 - 268.9	1	Helium
	268.9 - 280.9	3	
	280.9 - 284.9	2	
12	284.9 - 286.8	4	Fe
	286.8 - 289.2	5	
13	289.2 - 294.2	5	
	294.2 - 314.2	10	4-B
	314.2 - 316.6	2	Concrete

In Fig. 8.3, the result of particular interest is the ratio of ORNL to GA calculations for the neutron flux with E > 0.9 MeV. Throughout almost the entire range of the core, blanket, shield, liner, and concrete, the results differ by less than 10%. Also note the difference of less than 10% in neutron flux with E > 0.086 MeV throughout the core, blanket, and inner shield. Since the fast flux serves as a source for neutrons with energies less than 0.086 MeV, these very good agreements demonstrate that the basic methods and physical input used by GA and ORNL are in substantial agreement.

Therefore, the causes for the differences of about a factor of 1.5 to 2 in the epithermal flux in the outer shield and concrete, and in the thermal flux in the inner shield, outer shield and concrete, must be found in some differences in epithermal and thermal neutron cross sections and/or differences in the relative number of energy groups for neutrons with energies less than about 0.1 MeV. The curves of Fig. 8.3 suggested that the iron cross sections were the possible source of the trouble and were subsequently reviewed. ORNL made graphs of the iron ENDF data for iron with their broad groups superimposed. Plotting the GA epithermal cross sections revealed that the GA total cross sections were significantly higher than the ORNL total cross sections in this region.

The GA total and scattering cross sections for iron in the epithermal energy range are too large because of a well-known deficiency in the GA cross section codes GFE[6] and GGC-5[7]. Specifically, the GFE code prepares 99 fine-group cross sections for use in the GGC-5 code with a 1/E and/or fission spectrum within-fine-group weighting spectrum. The iron fine-group cross sections used in the benchmark calculation were 1/E-weighted below 820 keV and fission-spectrum weighted above 820 keV. This means that the iron fine-group sections were most appropriate for very dilute iron, whereas a massive iron region was used in the shield.

The present version of the GGC-5 code cannot be used to shield scattering cross sections even in the energy range below 7 keV in which a very detailed GAROL option calculation at some 13,700 energies was performed and used to prepare shielded capture and fission cross sections.

The benchmark calculation results indicate that the GFE code should be modified to incorporate a $1/[\sigma_t(E) + \sigma_0]$ within-fine-group weighting spectrum so that shielded fine-group cross-section libraries for the structural materials may be prepared for major compositions of interest. Alteration of the GAROL option of the GGC-5 code to prepare shielded scattering cross sections would be fine for the energy range below 7 keV but would not help in the important energy range above 7 keV in which iron is still strongly self-shielded.

A review of the curves of Fig. 8.3 at the carbon/iron interface of the inner shield and through the iron shows consistency with the above interpretation. Note that in the iron, the GA calculated fast flux is increasingly down-scattered into the epithermal range and then into the thermal range, relative to the ORNL calculations.

This interpretation is deduced from the slope of the appropriate curve of the ratio of ORNL/GA results versus radius. In general, if the slope of this ratio is positive, it means that the magnitude of the ORNL result is either increasing more quickly or decreasing more slowly than the GA results, as the radius increases. And if this slope is negative, the ORNL result is either increasing more slowly or decreasing more quickly than the GA results, as the radius increases. From Fig. 8.2, the fast flux and total flux always decrease as radius increases, therefore the second of the alternative interpretations applies. Hence, for a positive slope on a fast flux curve, the ORNL result is decreasing relatively more slowly (concomitantly, the GA result is decreasing relatively more quickly) with increase in radius; and for a negative slope, the ORNL result is decreasing more quickly (and the GA result is decreasing more slowly) with increase in radius.

Returning again to Fig. 8.3, in the iron of the inner shield the slopes of both fast flux curves ($E > 0.9$ MeV and $E > 0.085$ MeV) are positive, hence in the GA calculation, fast flux is scattered out of this range more quickly into the epithermal and then into the thermal energy range. (In this iron region, both the epithermal and thermal fluxes also decrease in magnitude with radius.) We note the relative change from epithermal to thermal flux is much greater in the GA calculations, resulting in a much greater magnitude of thermal flux in the iron. This is consistent with the above relative treatments of the iron cross sections in the resonance energy range.

Proceeding now to the first iron region in the outer shield, the above interpretation applies with the additional observation that the epithermal flux depletion is even faster in the GA results.

Finally, in the second iron region of the outer shield, the above interpretations still apply, but the slope of thermal flux curve is positive here, whereas it is negative in the other two iron regions. There is no contradiction in light of the fact that the thermal flux in the outer iron region of the outer shield is due mainly to thermal neutrons backscattered from the concrete of the PCRV.

Relative to the (B_4C + C) region, starting at the Fe/(B_4C + C) interface in the outer shield, a similar interpretation of the relative results through the (B_4C + C) in Fig. 8.3 suggests that the fast neutron flux in the ORNL calculations is down-scattered more quickly into the epithermal range and the thermal range, relative to the GA calculations. In the (B_4C + C) region, this effect may be due in part to the fact that in the GA results, the B_4C cross sections for the entire region were weighted with a 50/50 carbon/stainless steel spectrum. Due to the strong absorption of the thermals in the inner region, a harder spectrum is evident on the boron in the outer region. Hence, the GA absorption cross sections used in the outer part of the (B_4C + C) region could be too high. This could explain the relative increase in the thermal flux calculated by ORNL in the outer part of the (B_4C + C) region.

Finally, in Fig. 8.4, the main result of interest is the difference by a factor of approximately two in the gamma-ray heating throughout the shield, liner, and concrete calculated by GA and ORNL. However, from studies at GA reported in Ref. 4, gamma-ray heating in the concrete is dominated by gammas produced in the first iron region of the outer shield (about 20%). Consequently, the factor of two or more increase in the GA thermal flux in these regions would result in a factor of two or more increase in gamma production in these regions and would account for the major part of the higher gamma heating in the concrete shown in Fig. 8.4. Furthermore, since these gammas are produced isotropically, this same factor in the concrete gamma heating would contribute to the increased GA heating throughout the shield as well.

Therefore, allowing for the difference in the thermal neutron flux in the iron of the inner and outer shields, it was agreed that the gamma heating calculations by GA and ORNL are basically in agreement. This implies that gamma production and gamma transport calculations performed at both labs are also basically in agreement.

Finally, it is considered that the difference in heating rates at the blanket/shield interface (about a factor of four) is probably due to the differences in the gamma production in the iron of the shield as well as the effect of the thermal group structure on the gamma production rate in the U-238 assumed for the blanket. This problem will be given more consideration at a later date.

8.1.2. Conclusions

The results of the GCFR benchmark calculations performed at GA and ORNL lead to the following major conclusions:

1. The differences of 10% or less in the fast neutron fluxes throughout almost the entire core, blanket, shield, liner, and concrete demonstrate that the methods and physical input by both laboratories are in substantial agreement.

2. The differences in the calculated epithermal and thermal neutron fluxes in the iron of the shield can be identified with differences in shielding treatment of the iron cross sections in the resonance range, where GA used higher values than ORNL.

3. Allowing for the effects of conclusion 2, the gamma production and gamma transport calculations performed at both laboratories are basically in agreement.

4. The other differences in the gamma heating in the blanket and core can probably be related to the differences in the treatments

of cross sections and the energy group structure. This should be studied further in the future.

5. The 24 neutron energy groups and 15 gamma groups used in GA calculations are quite adequate for present GCFR shielding studies, with the more accurate ORNL 51-neutron, 25-gamma library serving as a check on results. However, in the future it is recommended that GA consider using at least four thermal neutron groups in shielding studies.

8.2. RADIAL SHIELD DESIGN STUDIES WITH A TWO-ROW RADIAL BLANKET

Additional analyses were performed for the radial shield with a two-row radial blanket. Specifically, the feasibility of incorporating removable shield-reflector elements adjoint to the radial blanket was examined.

Analysis was also performed using recent HEDL[8] damage function data which include temperature dependence.

8.2.1. Removable Shield-Reflector Element Studies

Two design concepts incorporating removable inner radial shield elements located adjacent to the radial blanket were considered in the analysis. These configurations are shown in Fig. 8.5.

Configuration 1 incorporates one row of hexagonal inner shield-reflector elements (54 in all) with the same overall outside dimensions as the core and blanket elements. The single row of removable elements is followed by an annular graphite/steel shield identical to that of the reference inner shield with reduced overall thickness.

Configuration 2 incorporates two rows of the hexagonal inner shield elements (54 in the first row and 60 in the second row), which constitute the entire inner radial shield.

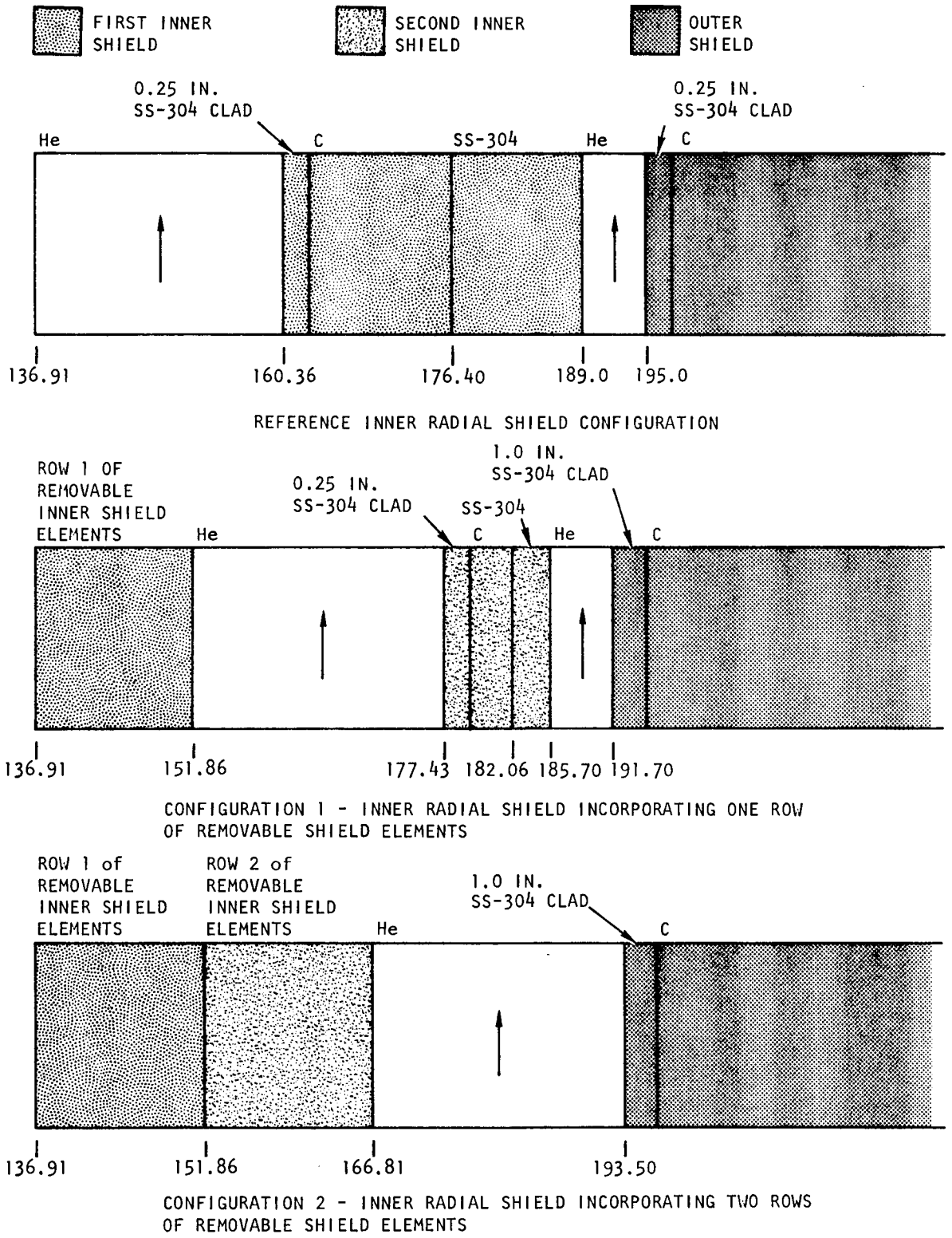

Fig. 8.5 Geometry for inner radial shield configurations (distances from core center are given below each configuration)

The graphite/stainless steel composition of the inner shield elements was varied to assess the shielding effectiveness of different mixtures. In these studies, the shielding effectiveness is limited by the 10% minimum residual ductility. This maximum ductility to be determined by detailed structural analyses yields the fluence limit for the inner shield. The objective is to minimize the number of required inner shield replacements while satisfying the fluence limit over the life of the plant.

Calculations were performed in cylindrical geometry (Z = 0) using the DTFX code[8] with P_3 anisotropic scattering and S_6 angular quadrature. All cross section sets were evaluated using the ENDF/B-IV data. Ten-group and 24-group eigenvalue calculations were performed to obtain a distributed source for use in subsequent calculations. The distributed sources were determined for the beginning-of-life, three-enrichment-zone, 121-element core and the large rod (0.595 ThO_2 volume fraction), two-row radial blanket. The blanket fissile inventory (U-233) linearly averaged in time over the equilibrium cycle for the four-cycle blanket management scheme was included to evaluate the radial blanket cross section sets. Three core regions and two blanket regions corresponding to the three core enrichment zones and the two blanket rows, respectively, were included. A homogeneous mixture of steel and graphite was assumed for the inner shield elements, and a 10% helium volume fraction was assumed to allow for shield element duct wall spacing and for coolant channels. The damage function used for the calculations is for type 304 stainless steel irradiated at 371°C (700°F). Ten-group (9 fast and 1 thermal) calculations were performed to determine the variation of shield effectiveness as a function of graphite/steel mixture. The 24 broad group damage functions were collapsed to 10 groups using a weighting spectrum typical of the inner shield region. This procedure minimizes the systematic error that will be introduced into the fluence limit calculation when both the damage function and the neutron spectrum vary greatly over a broad energy interval.

Table 8.3 summarizes the results of the fluence level and limit calculation for alternative cases using configurations 1 and 2. Note that,

Table 8.3

FLUENCE LEVELS AND LIMITS[a] AT THE INNERMOST REGION OF THE FIRST INNER SHIELD FOR VARIOUS INNER SHIELD ELEMENT COMPOSITIONS AND CONFIGURATIONS

Case	Inner Shield Configuration	Number of Neutron Groups in Calculation	SS-304 Atom Percent in Inner Shield Elements	Carbon Atom Percent in Inner Shield Elements	Total (E>0) Flux ($n/cm^2 \cdot sec$)	Total (E>0) Fluence (30 years at 0.8 load factor) (n/cm^2)	Total Fluence Limit[a] (n/cm^2)	First Inner Shield Lifetime (years at 0.8 load factor)
1	1	10	0	100	2.60 + 14	1.97 + 23	2.83 + 22	4.31
2	1	10	30	70	2.61 + 14	1.98 + 23	2.77 + 22	4.20
3	1	10	50	50	2.65 + 14	2.01 + 23	2.72 + 22	4.07
4	1	10	70	30	2.70 + 14	2.05 + 23	2.67 + 22	3.92
5	1	10	100	0	2.80 + 14	2.12 + 23	2.56 + 22	3.62
6	1	24	0	100	2.56 + 14	1.94 + 23	3.29 + 22	5.08
7	1	24	100	0	2.71 + 14	2.05 + 23	2.90 + 22	4.24
8	2	10	30	70	2.68 + 14	2.03 + 23	2.76 + 22	4.08
9	2	10	100	0	2.92 + 14	2.21 + 23	2.56 + 22	3.47

[a]Fluence limit based on a required 10% residual ductility based on total elongation for type 304 stainless steel.

although the total fluence is nearly the same, the total fluence limit, which depends only on the local spectrum, varies moderately for the different cases. It is seen that the first inner shield lifetime increases with increasing graphite concentration in the inner shield elements, a result of the greater moderating ability of graphite relative to that of SS-304. The time to reach the fluence limit is about 20% longer with the pure graphite inner shield elements than with the pure SS-304 inner shield elements. Comparing results for the 10-group calculations with those for the 24-group calculations indicates that the coarse group structure results in only a 15% underestimation of the shield lifetime.

Table 8.4 shows that the fluence level and the fluence limit at the innermost region of the second inner shield depend on the inner shield element composition. It is seen that the time to reach the fluence limit is about 20% longer for the equal graphite/SS-304 atom percent mixture relative to the cases with either pure graphite or pure SS-304 inner shield elements. As before, the coarse 10-group calculation predicts about a 15% shorter shield lifetime than the 24-group calculation. The shorter lifetime for configuration 2 is due primarily to reduced geometric (one-quarter) attenuation when the second inner shield is located closer to the core center.

The most significant result shown in Table 8.4 is that a single row of inner shield elements (configuration 1), regardless of the graphite/SS-304 mixture, adequately attenuates flux levels such that the type 304 stainless steel fluence limit for permanent structures (for a 30-year plant life at 0.8 load factor) is marginally met at the second inner shield. The second inner shield provides additional margin for calculational uncertainty to ensure that the fluence limit is not exceeded at the outer radial shield.

Table 8.5 gives the fluence levels and limits at the innermost region of the outer shield for the various cases. It is seen that in all cases the fluence limit for permanent shield structures is met with greater than

Table 8.4

LIFETIMES[a] OF THE OUTER RADIAL SHIELD FOR VARIOUS TEMPERATURES AND THERMAL RANGE DAMAGE FUNCTION WEIGHTING

Temperature (°C[°F])	Damage Function Type	Damage Function Weighting Over Thermal Energy Range	Percent Damage Response Due to E < 2.38 eV Flux	Percent Damage Response Due to E > 2.38 eV Flux	Outer Shield Lifetime (years at 0.8 load factor)
371 (700)	Nominal	1	22	76	42
371 (700)	Nominal	1/E	34	66	36
371 (700)	Upper Bound	1	36	64	10
371 (700)	Upper Bound	1/E	44	56	9
482 (900)	Nominal	1	28	72	115
482 (900)	Nominal	1/E	42	58	92
482 (900)	Upper Bound	1	42	58	25
482 (900)	Upper Bound	1/E	51	49	22
575 (1067)	Nominal	1	50	50	70
575 (1067)	Nominal	1/E	88	12	16

[a]Based on a required 10% residual total elongation for type 304 stainless steel.

Table 8.5

FLUENCE LEVELS AND LIMITS[a] AT THE INNERMOST REGION OF THE OUTER SHIELD FOR VARIOUS INNER SHIELD ELEMENT COMPOSITIONS AND CONFIGURATIONS

Case	Inner Shield Configuration	Number of Neutron Groups in Calculation	SS-304 Atom Percent in Inner Shield Elements	Carbon Atom Percent in Inner Shield Elements	Total (E>0) Flux ($n/cm^2 \cdot sec$)	Total (E>0) Fluence (30 years at 0.8 load factor) (n/cm^2)	Total Fluence Limit[a] (n/cm^2)	Fluence Margin at Outer Shield
1	1	10	0	100	3.17 + 13	2.40 + 22	6.30 + 22	2.6
2	1	10	30	70	2.94 + 13	2.23 + 22	6.28 + 22	2.8
3	1	10	50	50	2.92 + 13	2.21 + 22	6.17 + 22	2.8
4	1	10	70	30	2.97 + 13	2.25 + 22	5.97 + 22	2.7
5	1	10	100	0	3.22 + 13	2.44 + 22	5.51 + 22	2.3
6	1	24	0	100	3.48 + 13	2.63 + 22	8.69 + 22	3.3
7	1	24	100	0	2.90 + 13	2.19 + 22	7.09 + 22	3.2
8	2	10	30	70	1.90 + 13	1.44 + 22	7.21 + 22	5.0
9	2	10	100	0	1.82 + 13	1.39 + 22	4.78 + 22	3.5

[a]Fluence limit based on a required 10% residual ductility based on total elongation for type 304 stainless steel.

a factor of two margin. Note that the time to reach the fluence limit at the outer shield is a maximum with the 70% graphite/30% SS-340 inner shield elements.

In conclusion, the results indicate that a single row of the removable shield elements provides marginal flux attenuation to provide 10% residual ductility at the outer shield. The time to reach 10% ductility at the inner shield varies between four and five years depending on the inner shield composition and configuration. There does not appear to be any great incentive to fine-tune SS-304 to carbon atom percent ratios in the inner shield elements since this results in only a small increase in the shield effectiveness.

8.2.2. Effect of Recent Damage Function Data on the Radial Shield

Damage function data, to be included in the Nuclear Systems Materials Handbook[9] (NSMH), was reviewed to assess its impact on computed fluence limits for the radial shield. These new data include damage responses for various spectra and temperatures, thus providing upper bound solutions to the damage functions which enable estimation of fluence limits with a 2σ (95%) confidence level.

Based on the nominal (or expected) damage level, the results were in good agreement with previous analyses. However, the damage levels given by the new data based on the upper bound damage function for total elongation for the structural steel show that the time to reach the lower bound fluence limit at the inner shield may be less than previously predicted. Good agreement was found for the liner fluence limit.

The new NSMH damage functions for SS-304 total elongation indicate a strong temperature dependence. Above neutron energies of about 50 keV, where the primary damage mechanism is knock-on-atom displacement, the damage function decreases with increasing temperature which is due to the increased mobility and therefore enhanced annihilation of point defects.

Between thermal and 50 keV the neutrons produce little damage response. In the thermal energy range where helium production is important, the new damage function increases with increasing temperature apparently due to increased helium diffusion to grain boundaries.

Figure 8.6 shows a plot of the inner radial shield lifetime as a function of temperature for an inner radial shield design incorporating one row of pure stainless steel (with 10% helium volume fraction for coolant) shield-reflector elements (based on the spectrum for case 7 of Table 8.3). No rotation of the shield elements is assumed. The SS-304 temperature at the innermost region of the inner shield is near 650°C (1200°F). At this temperature, the time to reach 10% residual ductility is 2.5 years and greater than 6 years based on the lower bound and the nominal fluence limit, respectively. This time had been evaluated as 4.24 years based on the old data (Table 8.3).

Table 8.6 gives the times to reach 10% residual ductility at the outer radial shield for various temperatures based on the spectrum and fluence at the innermost SS-304 structure [2.54 cm (1 in.) thickness] facing the core (Case 6, Table 8.5). These times are for an inner shield consisting of one row of pure graphite shield elements followed by a second inner shield similar to the reference inner shield except with reduced thickness. The times are given based on the nominal and the lower bound fluence limits for three temperatures: 371, 482, and 575°C (700, 900, and 1067°F). The NSMH data do not include an upper bound solution for 575°C (1067°F). The 575°C (1067°F) temperature is representative of the maximum outer shield temperature, which is about 28°C (50°F) above the reactor outlet plenum temperature of 550°C (1022°F). A fairly soft spectrum with about 15% of the total flux with $E < 2.38$ eV results for the inner shield elements composed of graphite. The thermal flux damage is thus significant, and therefore results are given for both unity and 1/E weighting of the thermal range fine-group damage functions.

It is seen that the fluence limit, reflected by the times to reach the limit, varies considerably with temperature, increasing with temperature

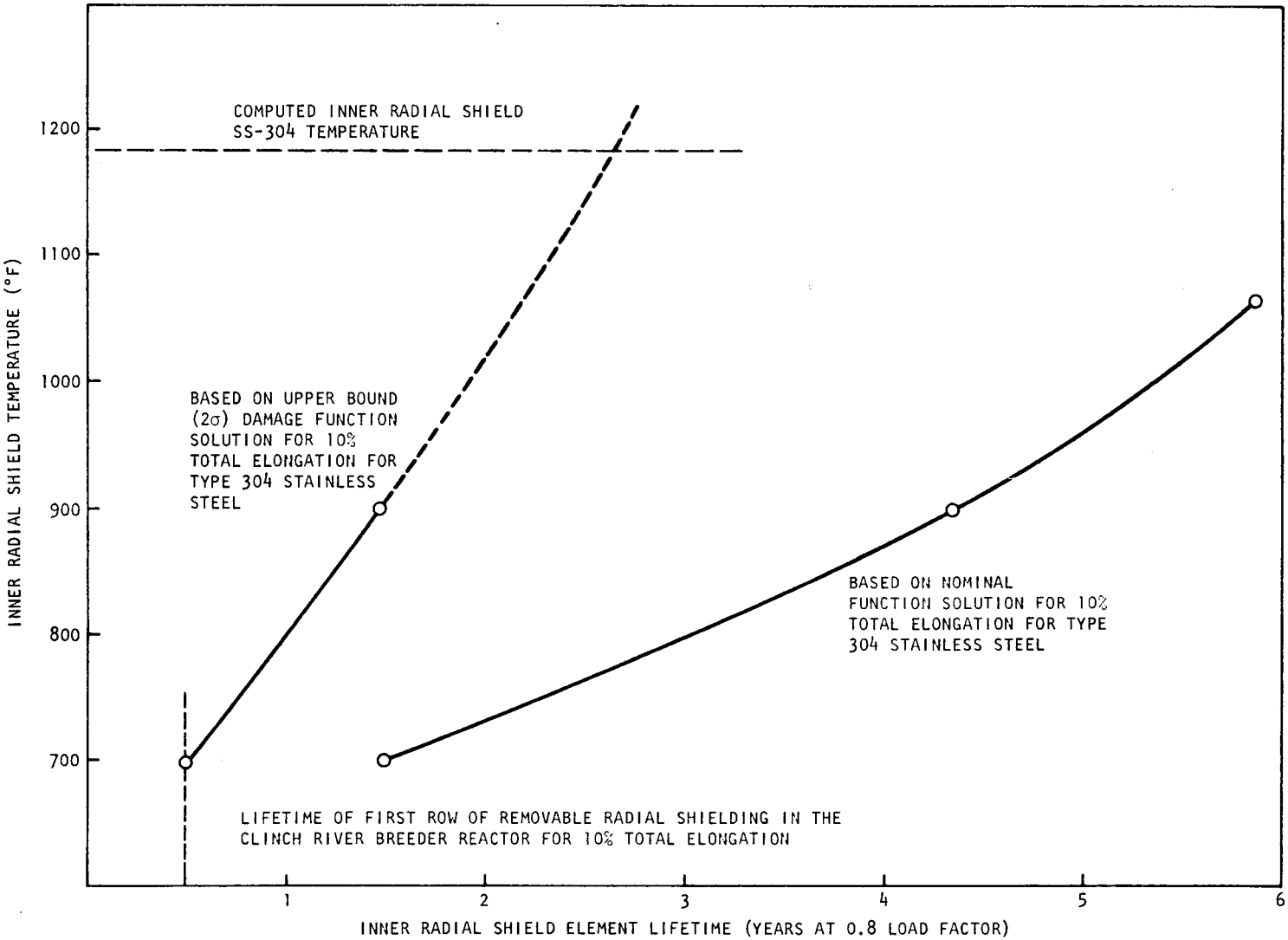

Fig. 8.6 Inner radial shield lifetime as a function of temperature

Table 8.6

FLUENCE LEVELS AND LIMITS[a] AT THE INNERMOST REGION OF THE SECOND INNER SHIELD FOR VARIOUS INNER SHIELD ELEMENT COMPOSITIONS AND CONFIGURATIONS

Case	Inner Shield Configuration	Number of Neutron Groups in Calculation	SS-304 Atom Percent in Inner Shield Elements	Carbon Atom Percent in Inner Shield Elements	Total (E>0) Flux ($n/cm^2 \cdot sec$)	Total (E>0) Fluence (30 years at 0.8 load factor) (n/cm^2)	Total Fluence Limit[a] (n/cm^2)	Second Inner Shield Lifetime (years at 0.8 load factor)
1	1	10	0	100	9.05 + 13	8.36 + 22	5.92 + 22	25.9
2	1	10	30	70	7.48 + 13	5.67 + 22	5.87 + 22	31.1
3	1	10	50	50	7.01 + 13	5.31 + 22	5.63 + 22	31.8
4	1	10	70	30	6.76 + 13	5.12 + 22	5.25 + 22	30.8
5	1	10	100	0	6.75 + 13	5.11 + 22	4.54 + 22	26.6
6	1	24	0	100	9.24 + 13	7.00 + 22	8.43 + 22	31.6
7	1	24	100	0	6.34 + 13	4.80 + 22	5.52 + 22	34.5
8	2	10	30	70	1.07 + 14	3.11 + 22	6.05 + 22	22.4
9	2	10	100	0	9.98 + 13	7.56 + 22	4.07 + 22	16.2

[a]Fluence limit based on a required 10% residual ductility based on total elongation for type 304 stainless steel.

between 371 and 482°C (700 and 900°F). The fluence limit decreases with temperature above about 482°C (900°F) due to the increasing damage contribution of the thermal flux. The upper bound fluence limits and thus the times to reach 10% ductility are about a factor of four lower than those based on the corresponding nominal damage function, indicating a large uncertainty in the energy dependence of the damage function over the spectral range of interest. It is also important to note that at higher temperatures the fluence limit is very sensitive to the spectral detail of the thermal flux. The times to reach 10% ductility are computed to be 70 years for unity and 16 years for 1/E thermal energy range weightings, for the 575°C (1067°F) case. However, including an absorbing material such as boron in the inner shield or excluding graphite from the inner shield would significantly reduce the thermal flux damage in the outer shield.

REFERENCES

1. Archibald, R., K. D. Lathrop, and D. Mathews, "1DFX - A Revised Version of the 1DF (DIF-IV) SN Transport Theory Code," Gulf General Atomic Report Gulf-GA-B-10820, September 1971.

2. Engle, W. W., "A Users Manual for ANISN, A One-Dimensional Discrete Ordinates Transport Code with Anisotropic Scattering," USAEC Report K-1693, Union Carbide, 1967.

3. Nagel, M., and R. J. Cerbone, "Neutron-Coupled Gamma-Ray Cross Section Requirements for Gas-Cooled Fast Breeder Reactors," USAEC Report GA-A13329, General Atomic, March 1975.

4. Cerbone, R. J., et al., "Shielding Analysis of the 300-MW(e) GCFR," USERDA Report GA-A13558, General Atomic, August 1975.

5. "AMPEX Modular Code System for Generating Coupled Multigroup Neutron Gamma-Ray Cross-Section Libraries from ENDF/B," USAEC Report ORNL-TM3706, Oak Ridge National Laboratory, September 1973.

6. Archibald, R. J., and D. R. Mathews, "The GAF/GAR/GAND Fast Reactor Cross Section Preparation System, GAND2 and GFE2 - Computer Programs for Preparing Input Data for the GAFGAR, GGC, and MICROX Codes From an ENDF/B Format Data File," v. II, USAEC Report GA-7542, Gulf General Atomic, March 1973.

7. Nathews, D. R., et al., "GGC-5, A Computer Program for Calculating Neutron Spectra and Group Constants," Gulf General Atomic Report GA-8871, September 21, 1971.

8. Lathrop, K. D., "DTF-IV - A Fortran IV Program for Solving the Multigroup Transport Equation with Anisotropic Scattering," Los Alamos Scientific Laboratory Report LA-3373, July 1965.

9. Nuclear Systems Materials Handbook, Draft Copies of Final Pages on Damage Functions for Volumes I and II, Hanford Engineering Development Laboratory (TID-26666), unpublished data.

IX. REACTOR SYSTEMS ENGINEERING (189a No. SU019)

Under this task, reactor system development activities are being defined and carried out. Analytical methods and models applicable to the assessment of thermal-hydraulic performance of the GCFR reactor core are being developed and utilized to define operating strategies. Methods and materials behavior models are being evaluated to assess the capability of the PCRV internal structures to serve as a post-accident fuel containment (PAFC); and GCFR plant control systems are being developed, including establishing the interface requirements between these control systems, the plant protection system, the operational protection system, and the plant operator.

9.1. CORE THERMAL-HYDRAULIC PERFORMANCE

Activities in this subtask are devoted to the development of accurate computer models for the evaluation of core thermal-hydraulic performance. In addition, the methods and requirements for core temperature monitoring are being investigated.

In previous reporting periods, the development of the core thermal-hydraulics computer program, GACOOL, was described, and preliminary results were reported. During the current reporting period, computer program development and documentation were continued. Several test cases were also run to compare the results of GACOOL to those of an alternative core design program.

Efforts to define the feasibility of an alternative core temperature monitoring concept and to quantify the system benefits from the use of an alternative concept were continued.

9.1.1. GACOOL Development

GACOOL development activities continued during this quarterly period. An improved method of calculating node-point heat fluxes from input mid-node-point power densities was added. An improved pressure drop model, based primarily on information obtained from previous calculations done by the Fuel Element Development Branch, was added to the program. This model consists of an overall loss coefficient for the entire inlet section of the core element as determined by detailed calculations and also includes direct calculations of outlet losses and losses in the fuel rod bundle due to acceleration, friction, and spacers. The model considers the presence of the core element duct wall and changes in the fuel rod diameter at various positions along the rod. An average Reynolds number is used to determine the friction factor in each of the four fuel rod assembly sections: the upper axial blanket, the smooth fueled section, the roughened fuel section, and the lower axial blanket. In addition, special consideration is given in determining an effective friction factor for the roughened region of the core. This effective friction factor is determined by combining a friction factor for the smooth perimeter of the core element duct wall with a friction factor based on Swiss Federal Institute for Reactor Research (EIR) data for the roughened perimeter of the fuel rods. An effort has also been initiated to obtain and incorporate in GACOOL improved correlations for Stanton numbers and friction factors as a function of Reynolds number and relative roughness in the roughened portion of the fuel rod. These correlations are being obtained from the Fuel Element Development Branch and are based on recently developed transformation techniques using the latest raw EIR data. The heat transfer and pressure drop models for the control rod elements have also been refined to include the perimeter of the control rod guide tube in the hydraulic diameter calculation. All of the above mentioned pressure drop model changes and the revised GASFLO subroutine discussed in the last ERDA quarterly progress report[1] have been verified by independent hand calculations.

During this reporting period, a change was also made in the programming structure of GACOOL. GACOOL was originally written using variable dimensions to allow the size of arrays to be adjusted easily from run-to-run to accommodate different numbers of core elements, axial nodes, or time points. However, this method has proven to be cumbersome. In order to increase the flexibility of GACOOL and to ease the addition or deletion of arrays, the program was changed from variable dimensioning to a PARAMETER statement approach. This new method will decrease the errors associated with array changes and also will aid during debugging while still allowing flexibility in the size of arrays from run to run.

In addition to the above development activities, several test cases were run to compare the results of GACOOL and an alternative core design code. The test cases included cores with different numbers of core elements and different core pressure drops. Results for coolant flow rates, coolant outlet temperature, and core pressure drop were compared and found to be in close agreement for all cases.

Work also continued on the draft document for GACOOL.

9.1.2. Alternative Methods for Core Temperature Monitoring

Work in the area of alternative methods for core temperature monitoring has continued. In addition to the infrared system discussed in previous reports, another alternative has been identified. Preliminary information has been received from ORNL about the noise thermometer that is being developed by them.

9.2. POST-ACCIDENT FUEL CONTAINMENT

The objectives of this subtask are (1) to assess the capability of the structures at the bottom of the reactor cavity to contain core debris associated with a postulated core meltdown arising from a series of very low probability failures and (2) to define the analytical and experimental

studies needed to verify thermal processes associated with core debris containment.

In the previous quarterly report,[1] results of the study of upward heat removal with forced circulation were reported. During the current reporting period, work has been completed on upward heat removal without helium circulation. As part of the computer program development, a comparison of the NUTAP[2] and SINDA[3] computer programs has been prepared.

9.2.1. Upward Heat Removal

Detailed results of the upward heat removal analysis with forced helium flow were reported in the previous quarterly reporting period.[1] The present analysis uses the same initial configuration and assumptions, the only exceptions being the absence of helium flow, and decay heat sources are assumed to be retained in the fuel melt. The cavity liner cooling system is assumed to be operational.

The computational model is shown in Fig. 9.1. Temperature histories at various surface locations (marked in Fig. 9.1) are shown in Fig. 9.2. Initially, two cases were considered in this study: (1) the reference design with the thermal barrier (Kaowool) and (2) the lower portion of the thermal barrier replaced by graphite (cross-hatched area in Fig. 9.1). The second case, which permits more heat to be removed by the liner cooling system, is made possible by the alternative design concept, which moved the lower portion of the thermal barrier (silica) to the top of the lower shield assembly.[1] In Fig. 9.2 are shown the time spans before reaching the melting point of stainless steel (1427°C) at critical surface locations inside the reactor cavity. The temperature histories for the remainder of the locations indicated on Fig. 9.1 are shown in Fig. 9.3.

Before the melting point is reached, structural failure due to stress rupture is possible; however, there is uncertainty about this temperature. Since at 1300°C, stainless steel still retains about 3% of its original tensile strength and the stress in the outer radial shield steel casing

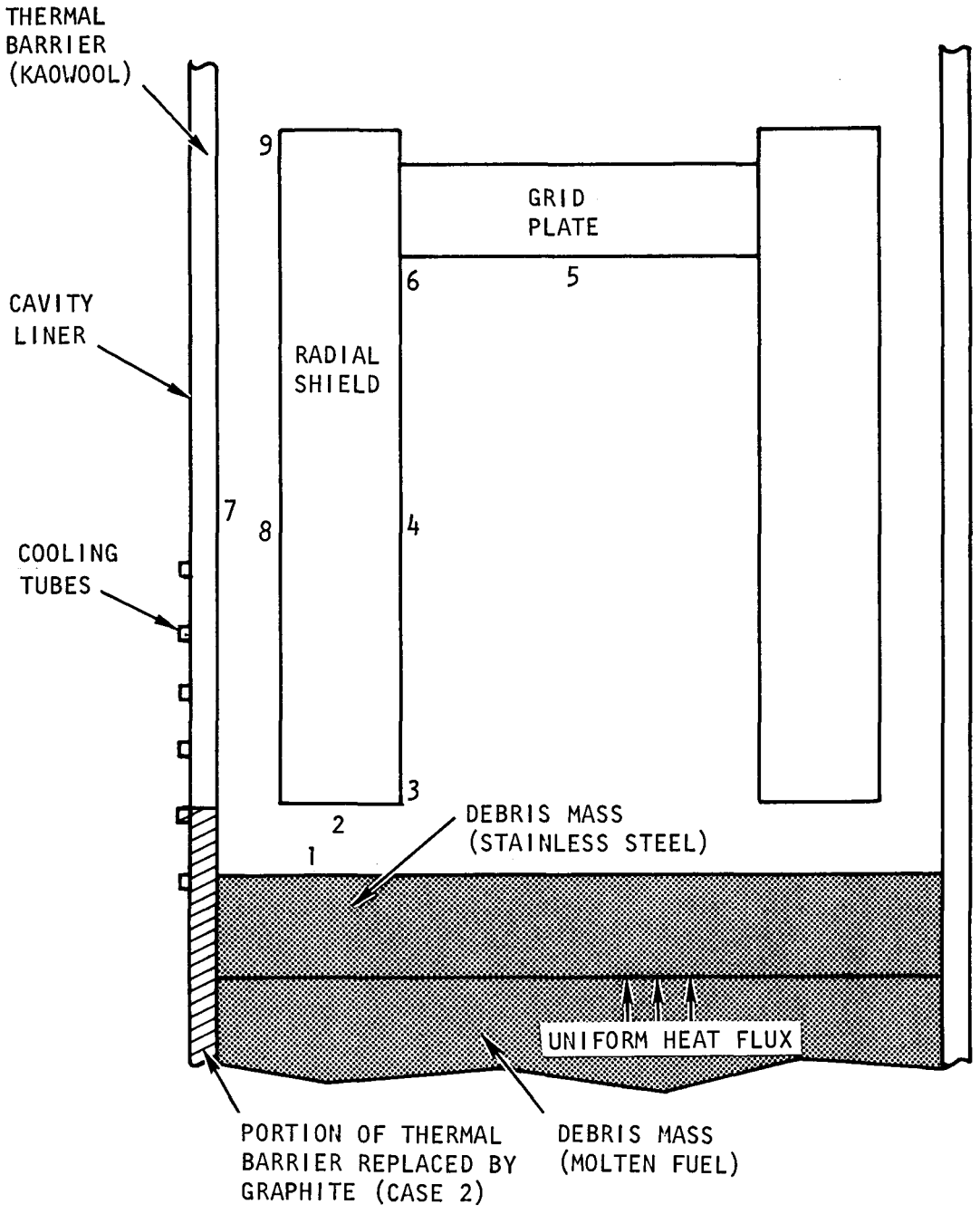

Fig. 9.1 Conceptual model for upward heat removal analysis

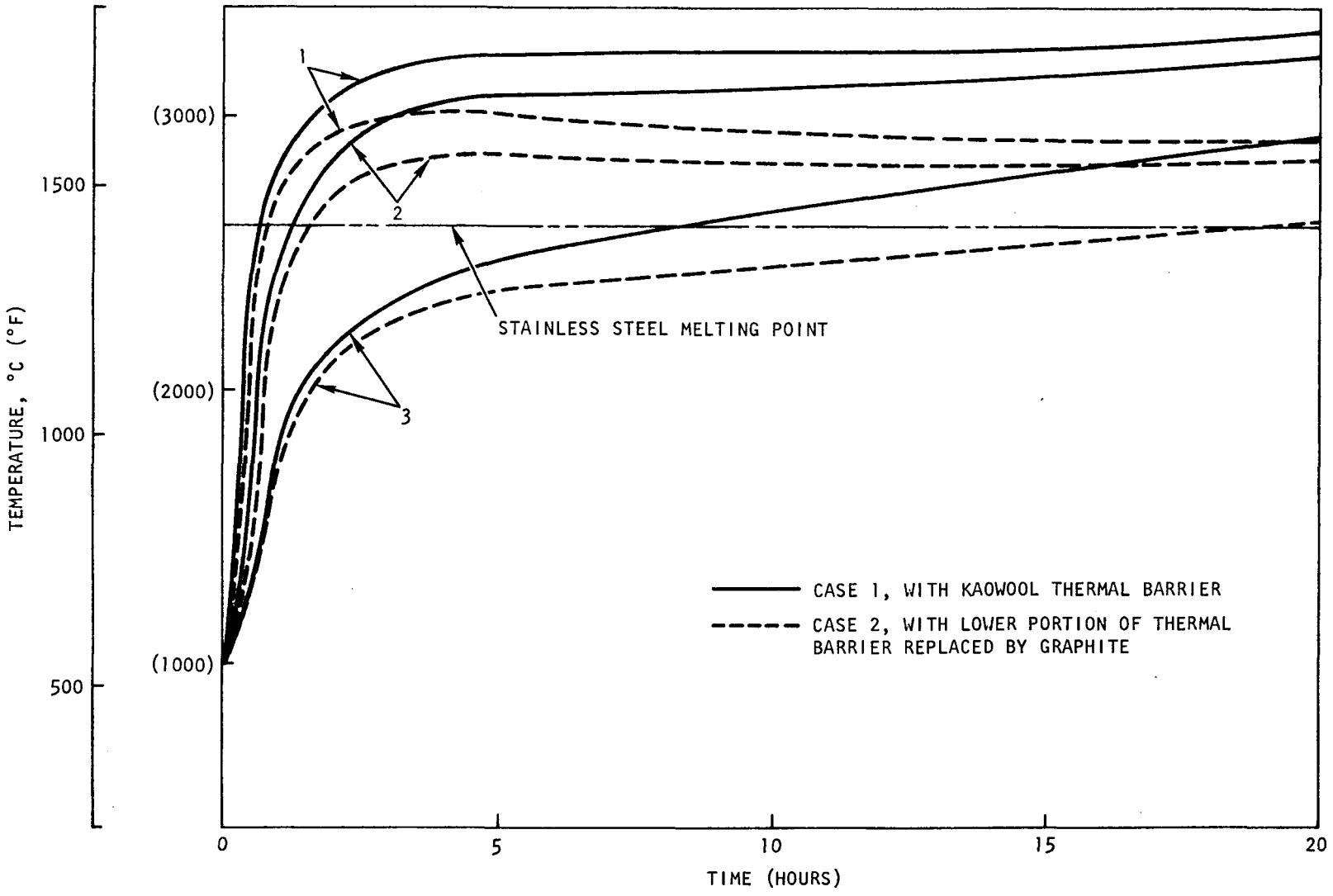

Fig. 9.2 Surface temperature history at critical reactor cavity locations

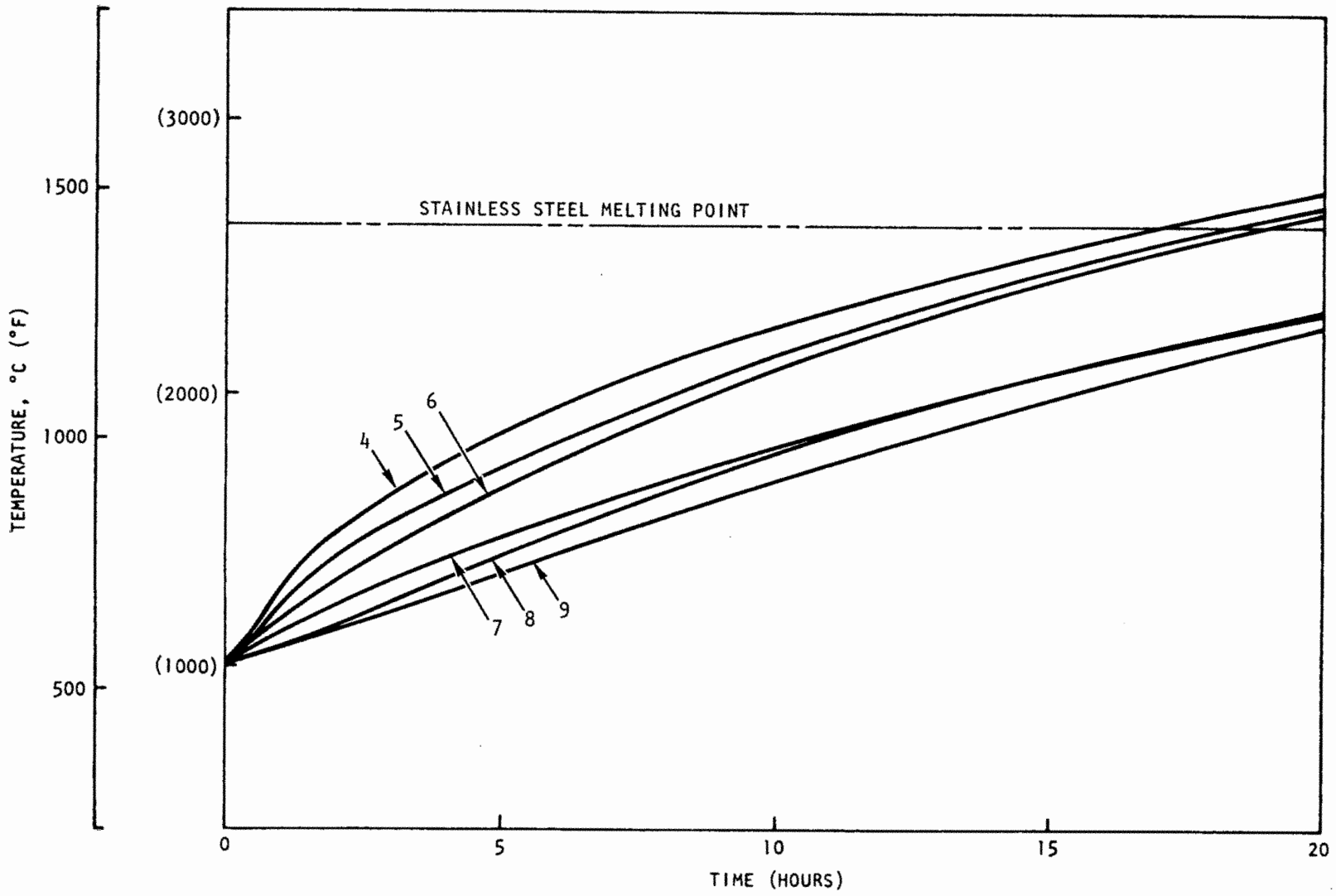

Fig. 9.3 Surface temperature history at some additional reactor cavity locations

is due only to its own weight and that of graphite, structural failure may not occur even at a temperature close to the melting point.

In addition, the structures of the outer radial shield and its support are the occasion of some uncertainties in the actual failure mechanism. In the reference design, the outer radial shield is supported by graphite posts clad in stainless steel. It is questionable whether these graphite posts will maintain their structural integrity while submerged in the liquid fuel pool. It is possible that these posts may fail before melting occurs at any outer radial shield location. Two alternative support concepts are considered to prevent this possibility; the first one is to relocate the support posts within the wrapped-around portion of the lower shield; the second and more favored concept is to have the outer radial shield supported from above, either as a permanent or backup design. In addition, the graphite blocks inside the outer radial shield can be interlocked with each other. With this design, the graphite blocks will be held together and in place even if the stainless steel casing should melt. Thus, an outer radial shield failure is only possible if the support structure itself fails. This support structure, however, is in a relatively cool region of the reactor cavity and will not be exposed to the hot radiation source unless the grid plate and support flange have melted.

Radiation heat transfer within the reactor cavity is very effective and tends to equalize the surface temperatures of the internal structures. As seen in Fig. 9.3, surface temperatures in the core region at locations 4, 5, and 6 are similar. Also in the annular region at locations 7, 8, and 9, similar surface temperatures prevail. It is surprising that during the first ten hours the temperature at location 3, about 0.3 m above the lower end of the outer radial shield (location 2), is about 200°C lower than at location 2. The reason for this large temperature difference between two neighboring surface points is that at location 2 only the hot molten pool surface can be seen, whereas at location 3 all the cold surfaces of the core region can be viewed. As can be expected, the temperatures at all locations increase monotonically with time and tend to reduce their differences.

In addition, a third case, with the cavity liner cooling eliminated, has been studied. Results appear similar to case 1 which has the Kaowool thermal barrier. Temperatures for this case are thus not shown in Fig. 9.2. However, a melting time comparison of all three locations is given in Table 9.1.

Table 9.1

COMPARISON OF TIMES TO REACH MELTING POINT FOR DIFFERENT STUDY CASES

Case		Time to Reach Melting Point at Various Locations (hr)		
		1	2	3
1	Full thermal barrier (Kaowool)	0.7	1.3	8.0
2	Lower portion of the thermal barriers replaced by graphite	0.8	1.5	19.0
3	No cavity liner cooling	0.7	1.3	7.5

The time to reach the melting point at locations 1 and 2 is about the same for all 3 cases. At location 3, a much longer melting time is shown for case 2; this is due to the increased heat flow to the cavity liner cooling system.

The history of heat flow in the debris bed and heat removal by cavity liner cooling is shown in Fig. 9.4. As for case 1, four hours after the postulated accident the heat radiated upward from the debris surface follows closely the decay heat curve. This indicates that only a small amount of heat is transferred sideward from the debris bed. For case 2, the sideward heat removal accounts for almost 50% of the upward heat removal prior to t = 20 hours. At this time, the heat removal by cavity liner cooling approaches 25% of the upward flowing decay heat for case 1 and almost

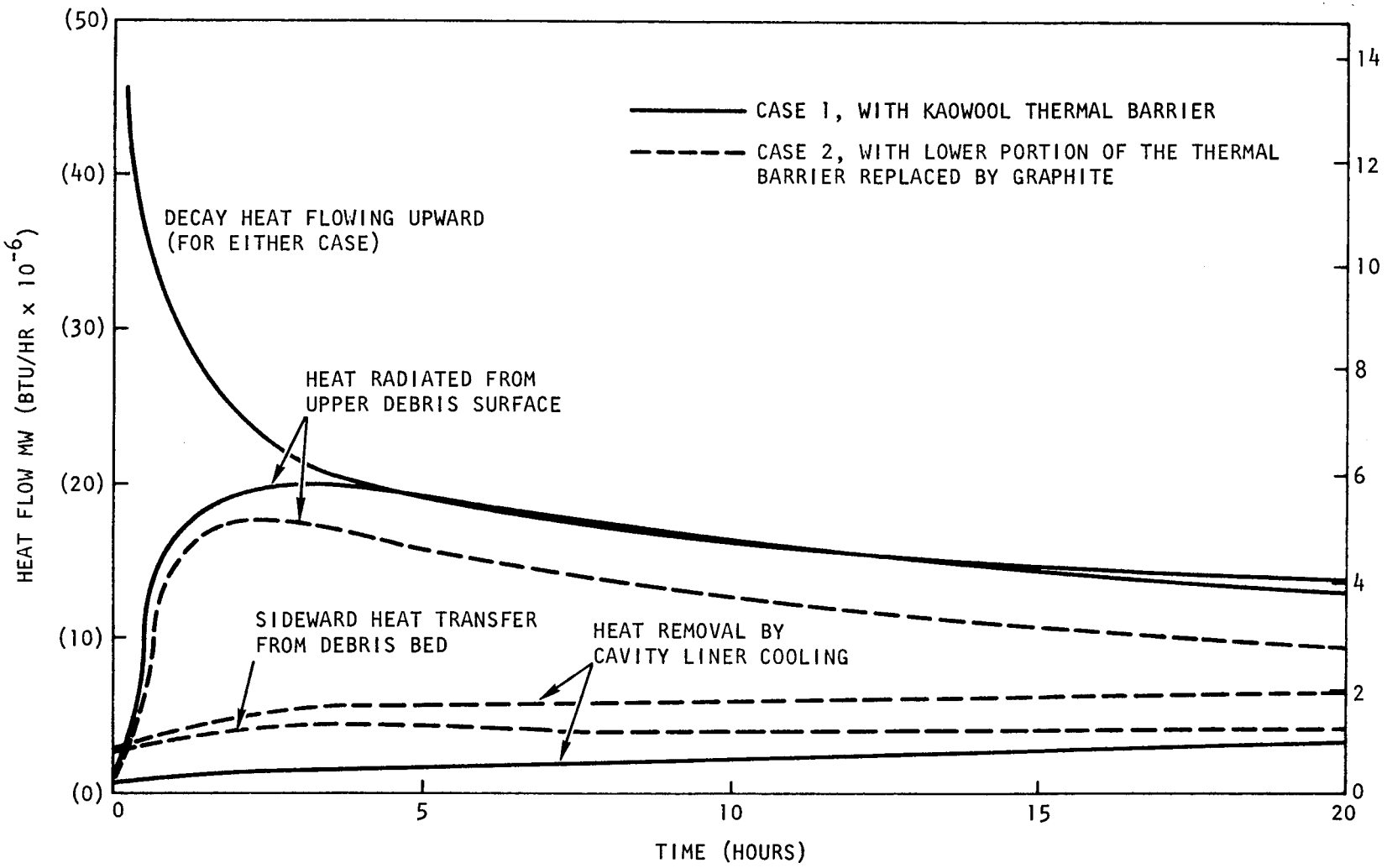

Fig. 9.4 History of debris bed heat transfer and liner cooling

50% for case 2. However, this increasing cooling rate is due to the rise of liner temperature. Melting of the reactor internal structures and eventual melt-through of the cavity liner are likely to occur before enough heat can be removed through the cavity liner. Therefore, without any helium circulation, the present design of the cavity liner cooling system does not provide adequate heat removal capacity for extended post-accident heat removal.

9.2.2. Computer Program Development

Two network-type digital thermal analyzer programs were tested and compared with respect to their accuracy, ease of problem input preparation, running time, and cost. The test problem involved solidification of molten material in a mold.[4] The two computer programs, NUTAP and SINDA, were found to give almost identical solutions to the problem. NUTAP required fewer input cards and less computer time. Also, the cost of a run with NUTAP was less than with SINDA. SINDA has an advantage over NUTAP when the thermal network is large and the pre-processed network structure can be saved from run to run.

It was recommended to use NUTAP for the initial PAFC studies while developing and testing new thermal models. However, for parametric studies requiring multiple runs, it appears advantageous to use SINDA.

9.3. CONTROL SYSTEMS

Mathematical models have been developed for the steam generator and resuperheater. The development of the digital computer program that incorporates these individual models into a simulation of the primary and secondary loops is about twenty percent complete.

REFERENCES

1. "Gas-Cooled Fast Breeder Reactor Quarterly Progress Report for the Period August 1, 1975 through October 31, 1975," USERDA Report GA-A13766, General Atomic, January 1976.

2. Leach, C. E., and E. L. Kelley, "TAP-LOOP: A Stable Thermal Analyzer Code for Thermal Analysis of Closed Hydraulic Systems," USAEC Report BNWL-1172, January 1970.

3. Smith, J. P., "SINDA User's Manual," TRW Systems Group, Reprint 14690-H001-RO-00, Revision 1, October 1972.

4. Lazaridis, A., "A Numerical Solution of the Multidimensional Solidification (or Melting) Problem," Intern. J. Heat Mass Transfer, 13, 1459-1477 (1970).

X. COMPONENT DEVELOPMENT (189a No. SU025)

10.1. REACTOR VESSEL

The scope of this subtask is to assure that the design of the PCRV and the related components that contribute to the integrity of the pressure boundary are satisfactory and to test critical component configurations to make certain that they attain the design objectives.

This subtask will demonstrate by analyses and tests that the PCRV with its penetrations and closures will meet the design criteria. It will provide assurance that the design of the thermal barrier will satisfactorily protect the liner and PCRV from the effects of high temperatures and that flow restrictors for the large penetrations can be developed to limit the flow of helium from the primary coolant systems to acceptable levels in the event of structural failure of a penetration or closure component.

During this reporting period, in support of the scale model testing program for the PCRV cavity closures, the placement of the reinforcing bars in the prototype closure, drawing 1304-0354, was forwarded to ORNL. The drawing included a table detailing for each type of rebar the shape, dimensions, diameter, developed length, and total footage required.

As part of the coordination task, a set of certified-for-construction drawings was received from ORNL. These drawings, showing the modeling of the rebars for the 1/15 scale test model, were reviewed and found to duplicate suitably those of the prototype closure. Also received from ORNL was a copy of the verification results[1] demonstrating by proof-testing that the steel balls to be used in the support fixture for the model test are capable of withstanding the highest loading condition to be expected.

Based on the reference design of the reactor cavity closure, a drawing of a prototype configuration has been initiated. The details of machining and supporting the steel tubes used for penetrations for the reactivity control mechanisms are being studied. Shear rings will be used to transfer the shearing forces to the supports; and as a means of reducing the deflections on the lower plate caused by the coolant pressure forces, the plate will be internally braced.

For the structural analysis of the PCRV, the results of the 3D finite element stress analysis performed by the structural mechanics group for the 300-MW(e) PCRV reference design were reviewed and evaluated. The 3D analysis of the PCRV was modeled using a newly developed 3D creep-crack computer program, which was run using the forces generated by the prestressing system and the maximum cavity pressure. From the review, it was concluded that the mathematical model should include the liners in order to reflect a more realistic picture of the stress distributions around the cavities and penetrations. The model is being revised to incorporate this change.

A literature search has been initiated in preparation for the draft of the GCFR thermal barrier test specifications and a topical report on GCFR pressure boundary integrity was issued during this quarter.

10.2. CONTROL AND LOCKING MECHANISMS

The primary objective of this task is the preparation of a comprehensive development plan for the control and locking mechanisms for a 300-MW(e) GCFR demonstration plant.

The "System Description" section of the "Control and Locking Mechanisms Development Plan" was completed. This section consists of a comprehensive description of the following components for the reference design.

1. Element locking mechanism.
2. Control rod drive.

3. Shutdown rod drive.

4. Pressure housings.

5. Element locking machine.

10.3. FUEL HANDLING DEVELOPMENT

Three subtasks are covered under fuel handling development: conceptual studies and system optimization, spent fuel shipping studies, and post-irradiation examination (PIE) facility evaluations.

1. Conceptual Studies and System Optimization

   Due to very limited applied efforts, no reportable results were obtained during this quarter.

2. Spent Fuel Shipping Studies

   Compilation of a substantial topical reference bibliography was completed. The bibliography contains over 50 recent publications directly related to the shipping of radioactive materials and specifically spent fuel. Most of these reference publications have been obtained and are on file, while the remainder have been ordered.

3. Post-Irradiation Examination (PIE) Facility Evaluations

   The initial task of obtaining the required input data from the Fuel Element Development Branch was completed in the form of a request that listed specific parameters by which the PIE facility will be capable of performing the planned inspection of a fuel or blanket element.

10.4. CORE SUPPORT STRUCTURE

The purpose of this subtask is to assure the availability of the structural analysis methods and materials mechanical behavior required to assess the structural integrity of the GCFR core support structure

under all anticipated operational and safety-related loading conditions in the GCFR environment.

In the previous quarterly report[2] analytical solutions of stresses and displacements of the grid plate were obtained from the anisotropic elasticity theory. In addition, a 15% scale model of the grid plate and the core elements was constructed for the determination of the structural characteristics and the dynamic response of the grid plate.

During this quarter, the core support structure model test effort has continued. The contract to perform the test was awarded to San Diego State University. The test setup was constructed and some preliminary data were taken for immediate analysis. In structural analysis, the problem of the structural interaction between the grid plate and the support cylinder was investigated. An analytical solution was obtained to determine the interactive moment between the grid plate and the lower flange and the discontinuity shear force and bending moment at the junction between the lower flange and the support cylinder. A small computer program to determine the results was written. Also, the draft of the report for the core support structure development plan was completed.

10.4.1. Structural Analysis

The problem of the structural coupling between the grid plate and the support cylinder has been investigated. The purpose of this study is to find the interactive moment between the grid plate and the support cylinder to determine the effect of the local flexibility of the support cylinder on the grid plate deflection.

The problem was formulated in such a way that the grid plate is a part of the integrated core support structure so that when subjected to load, the grid plate, the support cylinder, and its lower flange rotate together. In the analysis, the support cylinder was treated as a long, thin cylindrical shell, and the lower flange was treated as a short, thin cylindrical shell. To simplify computation, thin plate theory was applied

to the equivalent solid plate of the grid plate, and the solid rim effect was ignored.

As is shown in Fig. 10.1 the core support structure is subjected to a uniformly distributed load P. The free body diagram in Fig. 10.2 shows the interactive force and moment between the grid plate and the support cylinder due to clamping and the discontinuity shear force and bending moment at the joint section of the support cylinder and its lower flange.

Based on the assumptions, the equations for the rotations and displacements of the grid plate, the support cylinder, and its lower flange can be written as follows:[3]

Rotation at the Edge of the Grid Plate

$$\theta_p = \frac{3\,(1-\nu^*)\,PR^3}{2E^*\,H^3} - \frac{12\,(1-\nu^*)\,RM_1}{E^*\,H^3} \quad , \tag{1}$$

where E^* = effective Young's modulus of the grid plate,
ν^* = effective Poisson's ratio of the grid plate.

Support Cylinder

Rotation at the Lower End

$$\theta_c = \frac{M_2}{\beta_c\,D_c} - \frac{S_2}{2\beta_c^2\,D_c} \quad , \tag{2}$$

where $\beta_c = \left[\frac{3\,(1-\nu^2)}{R_c^2\,H_c^2}\right]^{1/4}$,

$$D_c = \frac{E\,H_c^3}{12\,(1-\nu^2)} \quad ,$$

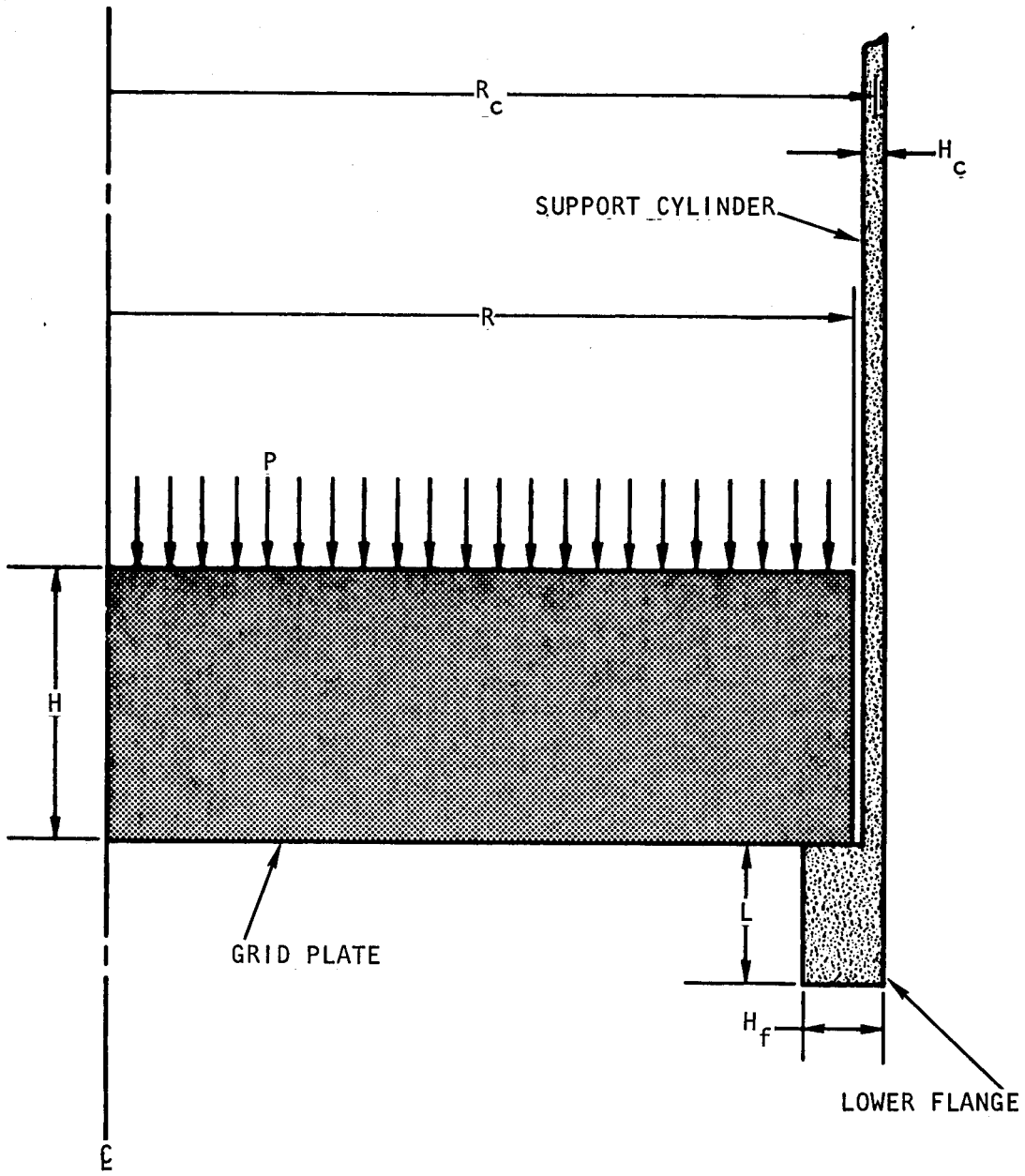

Fig. 10.1 Core support structure subjected to a uniform pressure load on the grid plate

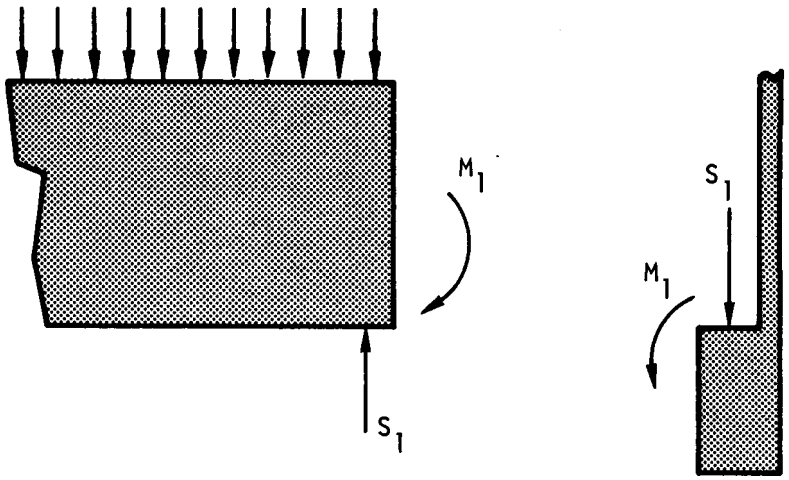

(A) INTERACTIVE FORCE AND MOMENT BETWEEN THE GRID PLATE AND THE SUPPORT CYLINDER

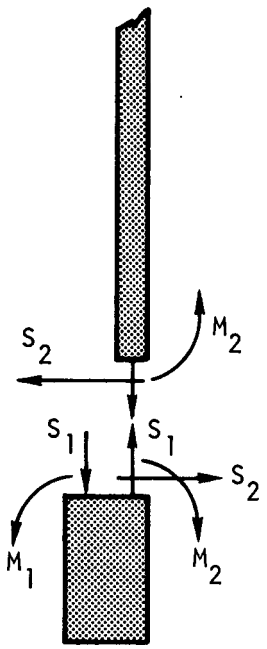

(B) DISCONTINUITY SHEAR FORCE AND BENDING MOMENT AT THE CYLINDER AND FLANGE JOINT SECTION

Fig. 10.2 Free-body diagram of the core support structure

E = Young's modulus ,

ν = Poisson's ratio .

Radial Displacement at the Lower End

$$W_c = \frac{M_2}{2\beta_c^2 D_c} - \frac{S_2}{2\beta_c^3 D_c} \quad . \tag{3}$$

Lower Flange

Rotation at the Upper End

$$\theta_f = \frac{A_1 S_2}{2\beta_f^2 D_f} + \frac{A_2 (M_2 - M_1 - S_1 H_f/2)}{2\beta_f D_f} \quad , \tag{4}$$

where $\beta_f = \left[\frac{3 (1-\nu^2)}{R_f^2 H_f^2}\right]^{1/4}$,

$$D_f = \frac{E H_f^3}{12 (1-\nu^2)} \quad ,$$

$$A_1 = (\cosh 2\beta_f L - \cos 2\beta_f L)/2(\sinh^2 \beta_f L - \sin^2 \beta_f L) \quad ,$$

$$A_2 = (\sinh 2\beta_f L + \sin 2\beta_f L)/(\sinh^2 \beta_f L - \sin^2 \beta_f L) \quad .$$

Radial Displacement at Upper End

$$W_f = \frac{B_1 S_2}{2\beta_f^3 D_f} + \frac{B_2 (M_2 - M_1 - S_1 H_f/2)}{2\beta_f^2 D_f} \quad , \tag{5}$$

where $B_1 = (\sinh 2\beta_f L - \sin 2\beta_f L)/2 (\sinh^2 \beta_f L - \sin^2 \beta_f L)$,

$B_2 = A_1$.

If the grid plate is rigidly clamped to the support cylinder, then

$$\theta_p = -\theta_f = \theta_c \quad ; \tag{6}$$

moreover,

$$W_c = W_f \quad . \tag{7}$$

Substituting equations (1) to (5) into equations (6) and (7) and performing a rearrangement, it gives

$$\frac{A_1}{2\beta_f^2 D_f} S_2 - \left[\frac{12\ (1-\nu^*)\ R}{E^*\ H^3} + \frac{A_2}{2\beta_f\ D_f}\right] M_1 + \frac{A_2}{2\beta_f\ D_f} M_2$$

$$= \frac{A_2\ S_1\ H_f}{4\ \beta_f\ D_f} - \frac{3\ (1-\nu^*)\ PR^3}{2E^*\ H^3} \quad , \tag{8}$$

$$\left[\frac{1}{2\beta_c^2 D_c} - \frac{A_1}{2\beta_f^2 D_f}\right] S_2 + \frac{A_2}{2\beta_f\ D_f} M_1 - \left[\frac{A_2}{2\beta_f\ D_f} + \frac{1}{\beta_c\ D_c}\right] M_2$$

$$= \frac{A_2\ S_1}{4\beta_f\ D_f} \quad , \tag{9}$$

$$\left[\frac{B_1}{2\beta_f^3 D_d} + \frac{1}{2\beta_c^3 D_c}\right] S_2 - \frac{B_2}{2\beta_f^2 D_f} M_1 + \left[\frac{B_2}{2\beta_f^2 D_f} - \frac{1}{2\beta_f^2 D_c}\right] M_2$$

$$= \frac{B_2\ S_1}{4\ \beta_f^2\ D_f} \quad , \tag{10}$$

where

$$S_1 = \frac{\pi R^2 P}{2\pi R} = \frac{PR}{2} \quad .$$

Consequently, the unknowns, S_2, M_1, and M_2 can be determined.

A computer program based on these analytical results was written, and the numerical results were obtained for the core support structure of the 300-MW(e) plant. The following geometric and material constants were used:

$R = 1.743$ m (68.625 in.), $H = 0.6096$ m (24 in.),

$R_c = 1.765$ m (69.5 in.), $H_c = 0.0446$ m (1.75 in.),

$R_f = 1.705$ m (67.125 in.), $H_f = 0.1651$ m (6.5 in.),

$E = 1.724 \times 10^{11}$ Pa (25×10^6 psi), $L = 0.3048$ m (12 in.),

$E^* = 3.447 \times 10^{10}$ Pa (5.0×10^6 psi), $\nu = 0.3$,

$P = 2.896 \times 10^5$ Pa (42 psi), $\nu^* = 0.76$.

It was found that

$S_2 = 9.396 \times 10^3$ N/m (53.65 lb/in.),

$M_1 = -1.609 \times 10^4$ N·m/m (-3618 lb-in./in),

$M_2 = 1.539 \times 10^3$ N·m/m (346 lb-in./in.).

It is of interest to note that the negative sign of the interactive moment (M_1) indicates that an additional rotation of the grid plate is caused by M_1 because of the larger rotation of the more flexible support cylinder. This result will be used to arrive at a satisfactory design configuration for the junction between the grid plate and the core support cylinder.

10.4.2. Core Support Structure Model Test

The test of the grid plate is in progress, and the major part of this static test has been completed.

For these static tests a fixture was built and a uniform pressure load was applied to the grid plate by inflating a tire tube. Due to practical considerations, water is used to insure required pressures in the tire tube. Figure 10.3 illustrates the general setup of the test, where the fixture and instrumentation of the grid plate model can be observed. The perforated plate is placed between two thin steel rings (9.52 mm [0.375 in.]) and this assembly is supported by the table of a universal tensile machine. The tube is placed inside of the lower ring between the plate and the test table. To insure a sufficient reaction force from the pressure load of the tube on the plate, an arbitrary preload is applied at the upper ring by the four columns of the tensile machine. As this figure illustrates, the four columns of the tensile machine act as a large C-clamp. The instrument gauge of the tensile machine may be seen on the right side of the figure; and the mounting arrangement of the dial indicators and the dial indicators for measuring the absolute and relative displacements of the grid plate are also shown. Figure 10.4 shows an enlarged version of the mounting arrangement of the dial indicators, which are mounted on the thick, heavy table (254 mm [10 in.]) of the tensile machine. Figure 10.5 shows a somewhat different view of the plate and the use of the dial indicators.

To verify that the tire tube is applying a uniform pressure to the plate, the measured pressure load applied to the plate by the tube is compared with the measured total reaction force on the upper ring measured by the tensile test machine. The correspondence of the two measurements confirms that the tube is indeed applying a uniform pressure load to the plate.

10.4.3. Core Support Structure Development Plan

The first draft of the core support structure development plan was completed and reviewed within the branch. The report elaborates the areas of the core support structure that require further research and development and therefore will be used as a guideline for future activities. The report also provides a timetable that is compatible with the overall GCFR program plan.

Fig. 10.3 General test setup

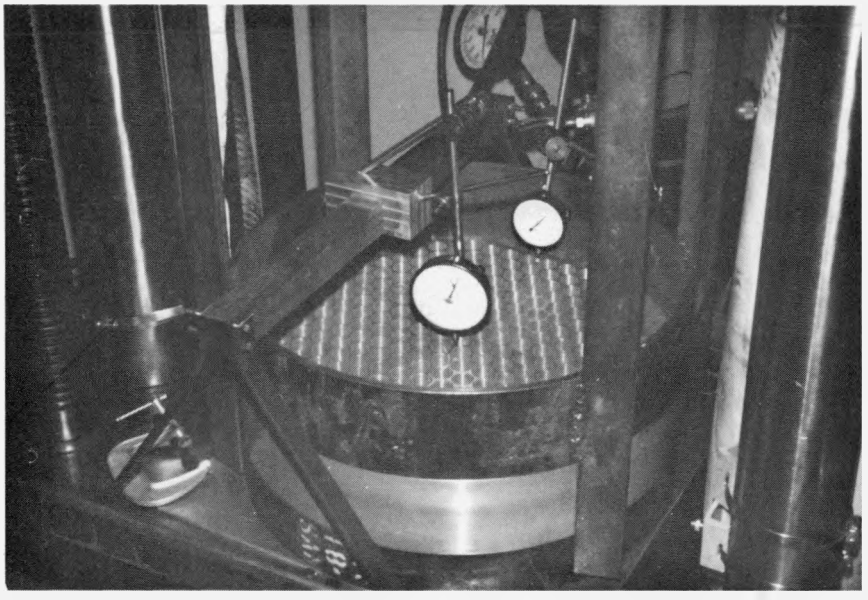

Fig. 10.4 Mounting arrangement

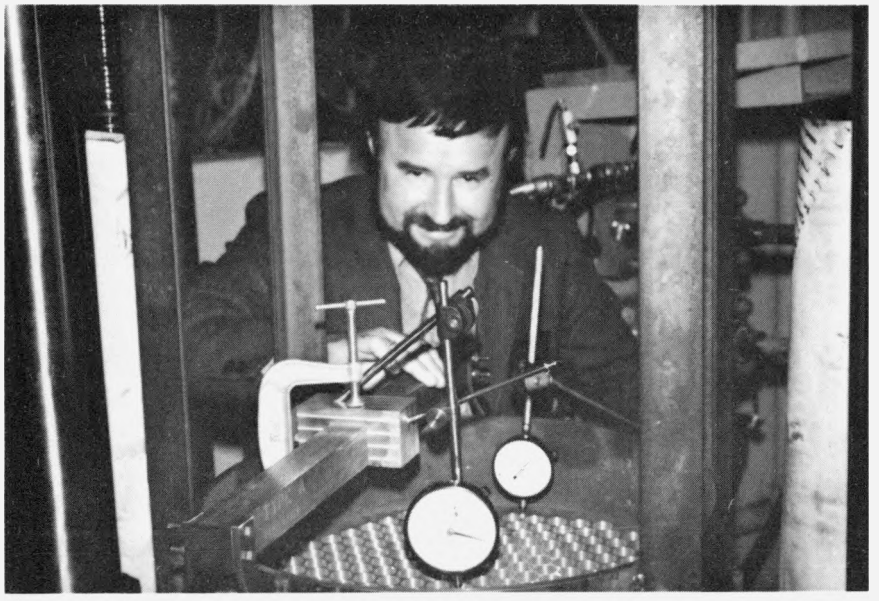

Fig. 10.5 Dial indicators

10.5. REACTOR SHIELDING

The primary objective of the reactor shielding task is the development of analytical and experimental methods to construct a reliable structure and to insure an efficient thermal-hydraulic design of the shields. In the previous quarterly reporting period, a simplified stress analysis of the radial shields was initiated and has been continued with increased emphasis on the question of ductility limits and the lifetime of the inner radial shield. Parallel to this effort, a review of the shield status is also being conducted, and the different design concepts are compared according to their technical and economic merits. This study is nearly completed.

Temperature distribution studies of the radial shields were also carried out for several design configurations with two-row blankets.

10.5.1. Shielding Structural Analysis and Shield Status

In connection with the structural analysis of the shields, the current publications of the fast breeder programs were reviewed. Reference 4 is an investigation of the combined effects of high temperatures and long term fluences on various candidate steel materials. It provides a great deal of information on the combined effects of irradiation and high temperature, although the duration of the test data is less than half of the desired GCFR requirements. An excellent review of the shielding materials is given in Ref. 5, which is a study of the material properties of the various graphites and boronated graphites. This work also examines the applicability of the different alloys for cladding and structural uses. Among the recent technical papers, Ref. 6, though brief, is the one most applicable to the shielding problems of the GCFR. At this stage of the study, the preliminary safety analysis report of CRBR (Ref. 7) appears to be the most detailed effort in this field. This report encompasses the safety aspects and design criteria of the shields, however, it has not supplied any detailed background information for these criteria. A current technical book (Ref. 8) covers the state-of-the-art and includes

information and techniques involving high temperature, long term effects, and extrapolation methods applied to creep rupture.

In the last quarterly report,[2] some results of a simplified preliminary stress analysis were reported for the radial shield. Since then these calculations have been further detailed. In the simplified stress analysis of the radial shields, steady state mechanical, thermal, and flux loads were considered. The corresponding thermal stresses, thermal expansions, creep, and relaxation were estimated. In this analysis, two failure mechanisms were found to be important: (1) creep rupture and (2) residual ductility. The creep rupture curves of Ref. 4 were applied to determine the allowable stress limits. In cases where the required range of the stress calculation has exceeded the range of the creep rupture curves of Ref. 4, the curves were extrapolated according to the methods of Ref. 8. Since the computed stresses are low, even with conservative assumptions, a significant margin of safety may exist between the computed stress from the different loads and the creep rupture stress limits. The application of the ductility limits was also uncertain. Because of the lack of pertinent information, the ductility criteria of Ref. 7 were tentatively adopted for this study. On this basis, refinements are being made in the ductility calculations, distinguishing between structural and non-structural components of the radial shields and accounting for the flux and fluence distribution along the longitudinal direction of the radial shields. Considering the longitudinal distribution of the flux, an order of magnitude reduction can be obtained in the fluence levels between the center and the end points of the radial shields where the more sensitive structural attachments may be located.

The objective of this study is to show that both the inner and outer radial shields may be designed as non-removable components, and then to show that the same conclusion can be obtained for the upper and lower shielding configurations. This is being done by first performing simplified analyses and then by further detailed analyses considering interaction effects between the different physical phenomena such as creep, cycling, residual ductility, etc.

The report will be divided into two parts; the first part presents a descriptive discussion of the reference shield design and the various recently proposed shield configurations, and the second part will investigate the following different problem areas: (1) structural analysis, (2) material and radiation damage, (3) support to PCRV, (4) construction, and (5) cost effectiveness. In this second section the interaction between the shields and adjacent components of the reactor will also be investigated and the functional requirements of each component will be explored.

10.5.2. Heat Transfer and Hydrodynamic Analyses

The objectives of this subtask are as follows:

1. To define and validate (as necessary) the analytical methods for determining the flow distribution and pressure drops related to coolant flow in and around the GCFR shielding structures.

2. To define methods for and perform evaluations of the temperature distribution in the shielding structures.

In the previous quarterly report,[2] the coolant flow rates and pressure drops were established for the main flow path and parallel flow paths through a single loop of the primary coolant system. Four flow networks were considered in the analysis, and the results were reported. In addition, based on the flow rates, thermal analyses of the radial shielding structures were performed for some alternative design configurations. During this reporting period, similar analyses were carried out for other alternative design configurations with two-row blankets.

10.5.3. Temperature Distribution

The steady-state temperature distribution in the radial shield at the core midplane was evaluated by using an existing two-dimensional heat

transfer computer code. Energy deposition rates in the shield were obtained from physics analyses, based on the following assumptions:[3]

1. A 121-element core with three enrichment zones.
2. A large rod, two-row, ThO_2 radial blanket (0.595 ThO_2 volume fraction).
3. A beginning-of-cycle radial blanket element material composition, i.e., no fissile material buildup.

The two alternative design configurations and the temperature profiles corresponding to these configurations are shown in Figs. 10.6 and 10.7. For design configurations 1 and 2, the peak temperature in the graphite region of the inner radial shield is 832°C (1529°F) and occurs at approximately 166 cm (65 in.) from the centerline of the core. This temperature is about 68°C (114°F) higher than the corresponding temperature in Ref. 1 for the three-row blanket design. The surface temperatures (i.e., at the graphite/steel interfaces) of the inner radial shield graphite range from 771°C (1420°F) to 795°C (1463°F). These temperatures are approximately 44°C (80°F) to 54°C (98°F) higher than the corresponding temperatures in Ref. 1.

In the steel cladding around inner radial shield graphite, the outer surface temperatures (i.e., at the coolant boundaries) range from 592°C (1098°F) to 611°C (1131°F); the inner surface temperatures (i.e., at the steel/graphite interfaces) of the steel cladding range from 601°C (1114°F) to 622°C (1151°F). These temperatures are approximately 8°C (14°F) to 17°C (31°F) higher at the inner surfaces and 6°C (12°F) to 14°C (24°F) higher at the outer surfaces than the corresponding temperatures in Ref. 1.

The peak temperature in the supporting steel section of the inner radial shield is 646°C (1195°F), 24°C (43°F) higher than the corresponding temperature in Ref. 1. It occurs at approximately 184 cm (72.5 in.) from the core centerline. The surface temperatures, at the coolant boundaries of this steel section, range from 584°C (1084°F) to 604°C (1119°F).

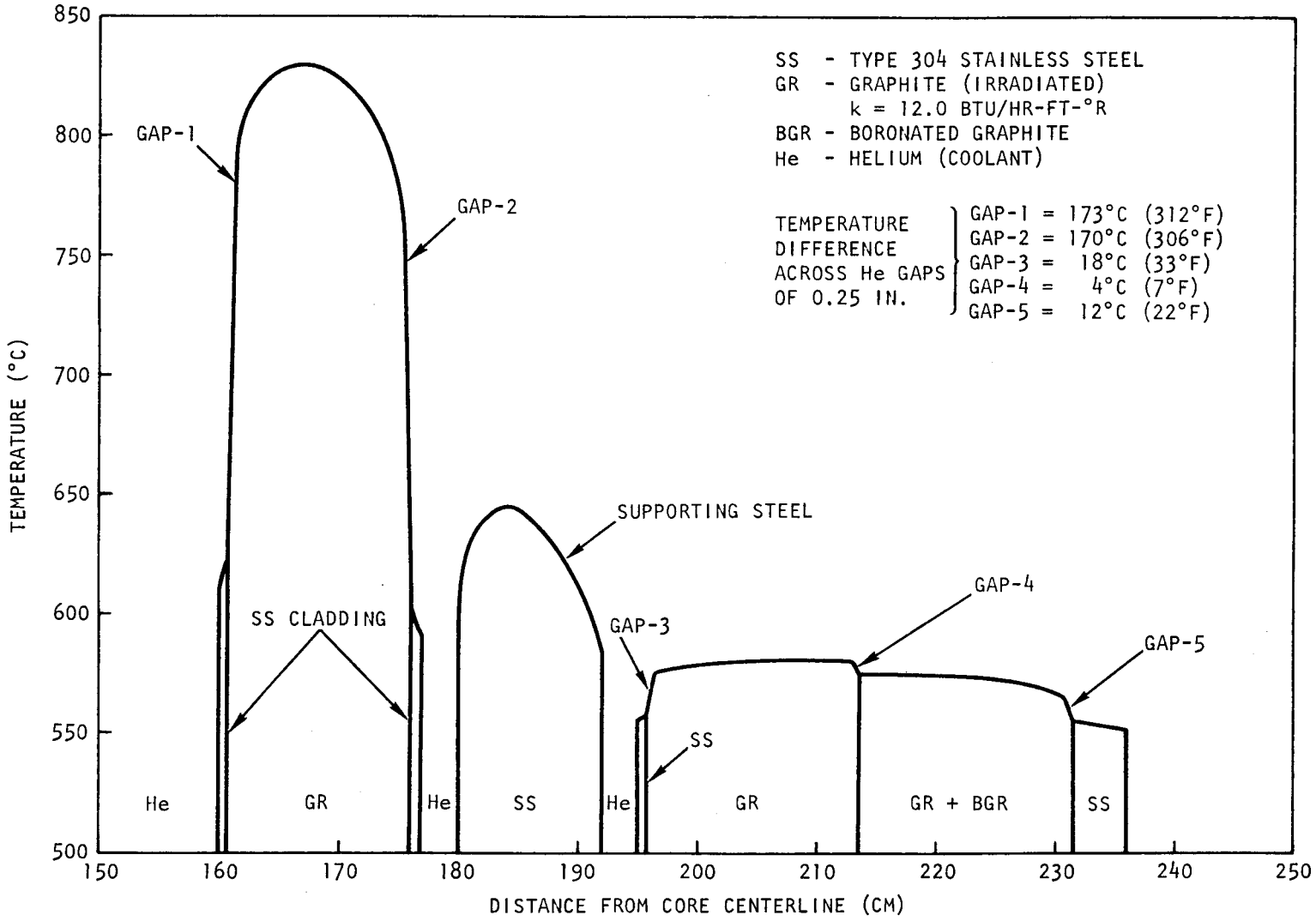

Fig. 10.6 Temperature distribution in the GCFR radial shield at the core midplane for configuration 1 with four coolant passages

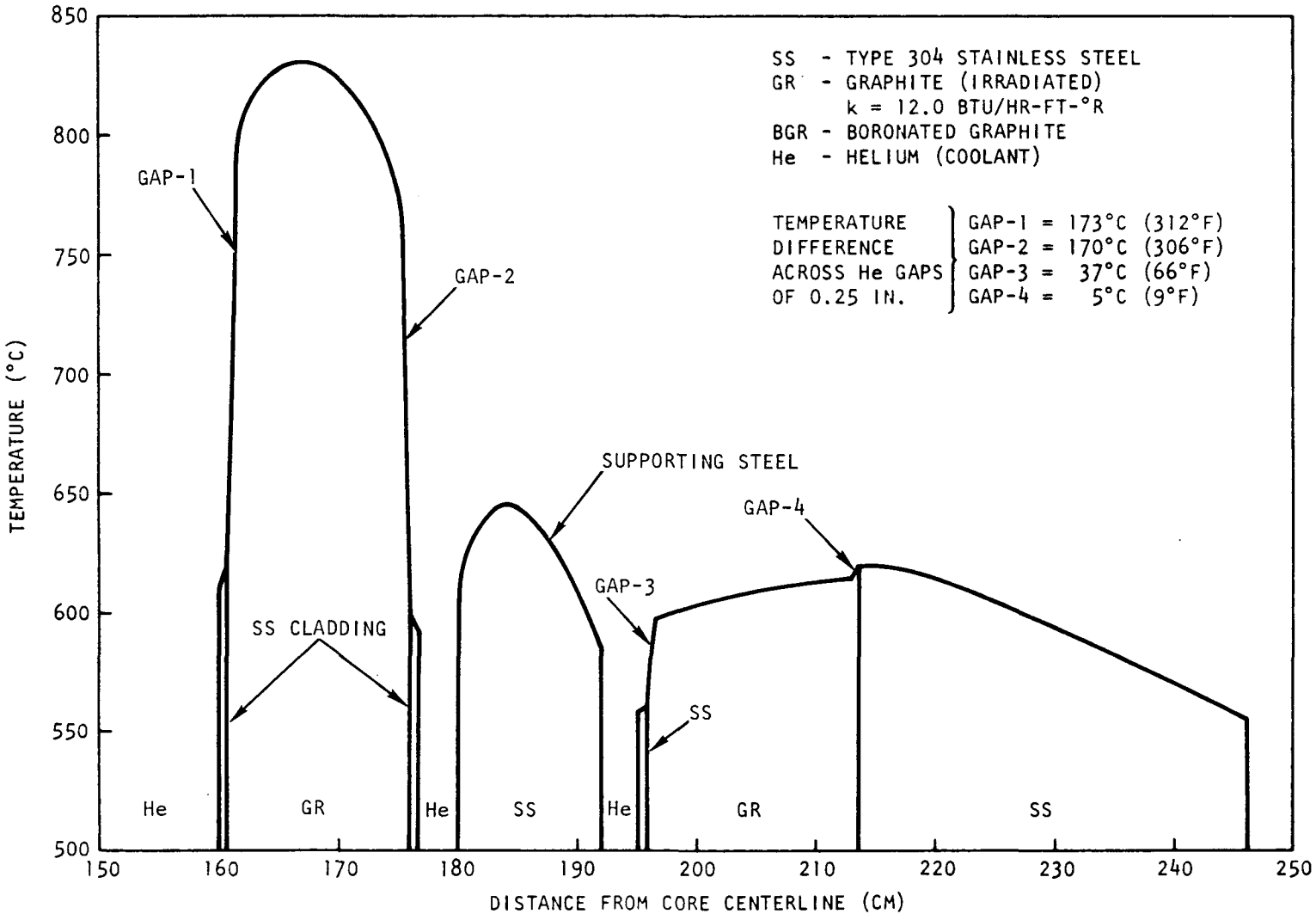

Fig. 10.7 Temperature distribution in the GCFR radial shield at the core midplane for configuration 2 with four coolant passages

In conclusion, the results of this study show that the temperature profiles in the radial shield for the two-row blanket design are higher than those previously reported in Ref. 1 for the three-row blanket design. This is primarily due to approximately 50% and 20% increases in the energy deposition rates in the inner and outer radial shields, respectively, for the two-row blanket design. The increase in the energy deposition rates can be attributed to a reduction in the neutron attenuation associated with the removal of the three-row blanket. Although the temperatures for the two-row blanket design are higher than for the three-row blanket design, these temperatures are within the range found satisfactory in other reactor applications for these materials.

10.6. MAIN HELIUM CIRCULATOR, VALVE AND SERVICE SYSTEM

The objective of this task is to prepare a topical report evaluating alternative main loop isolation valve conceptual designs.

The scheduled December start for this task was delayed due to manpower limitation and priority of ERDA CACS task. Initial scoping work for a review of alternative main loop isolation valve designs is now in progress.

10.7. STEAM GENERATOR

The purpose of this task is to develop a steam generator that meets the operational, performance, and safety requirements of the GCFR. During FY-76, several steam generator designs will be analyzed and evaluated and the merits of each design will be compared.

As part of the evaluation of alternative steam generator designs, a unit using straight tubes, instead of helically coiled tubes, is being investigated. Since the last quarterly reporting period, straight tube and helical coil steam generators have been sized for a modified cycle [helium temperature in = 549°C (1020°F), out = 340°C (644°F)], in which the helium outlet temperature is 29°C (53°F) higher than in the reference cycle. This modified cycle, with a steam exit temperature of 510°C (950°F),

permits the elimination of the resuperheater, a considerable reduction (about 30%) in heat transfer surface, and simplification of the piping arrangement.

Sizing of straight tube units for this modified cycle for bundle diameters of 1.83, 2.13, and 2.44 m (6, 7, and 8 ft) was performed. Figure 10.8 shows surface area, number of tubes, and bundle length as a function of bundle diameter. Figure 10.9 shows bundle helium pressure drop for friction, spacers, and entrance plus exit.

Referring to Fig. 10.8, it is seen that an increase in bundle diameter from 1.83 to 2.44 m (6 to 8 ft) increases the required surface area by about 46% but reduces the bundle length by only about 17% because as bundle diameter increases, both the inside (water) heat transfer coefficient and the outside (helium) heat transfer coefficient decrease and thus lower the overall heat transfer coefficient.

Figure 10.9 shows the variation of helium pressure drop (bundle friction, tube spacers, entrance plus exit) with bundle diameter. The upper curve shows that the total pressure drop decreases by about 50% when the bundle diameter increases from 1.83 to 2.44 m (6 to 8 ft). The spacer pressure drop is based on a free flow area fraction of 70% because free flow area fractions less than this produce a very much higher pressure drop.

For the above cycle, comparison of a helical coil steam generator with a similar straight tube unit shows that for equal bundle helium pressure drop the bundle diameter and length are very similar. However, because of the lower overall heat transfer coefficient, the surface area required for the straight tube unit is about twice that of the helical coil unit.

For the modified cycle, additional size comparisons were made for straight tube and helical coil tube steam generators using a resuperheater. Because of the increased available helium to steam temperature difference, the required surface area was significantly reduced for both types of units.

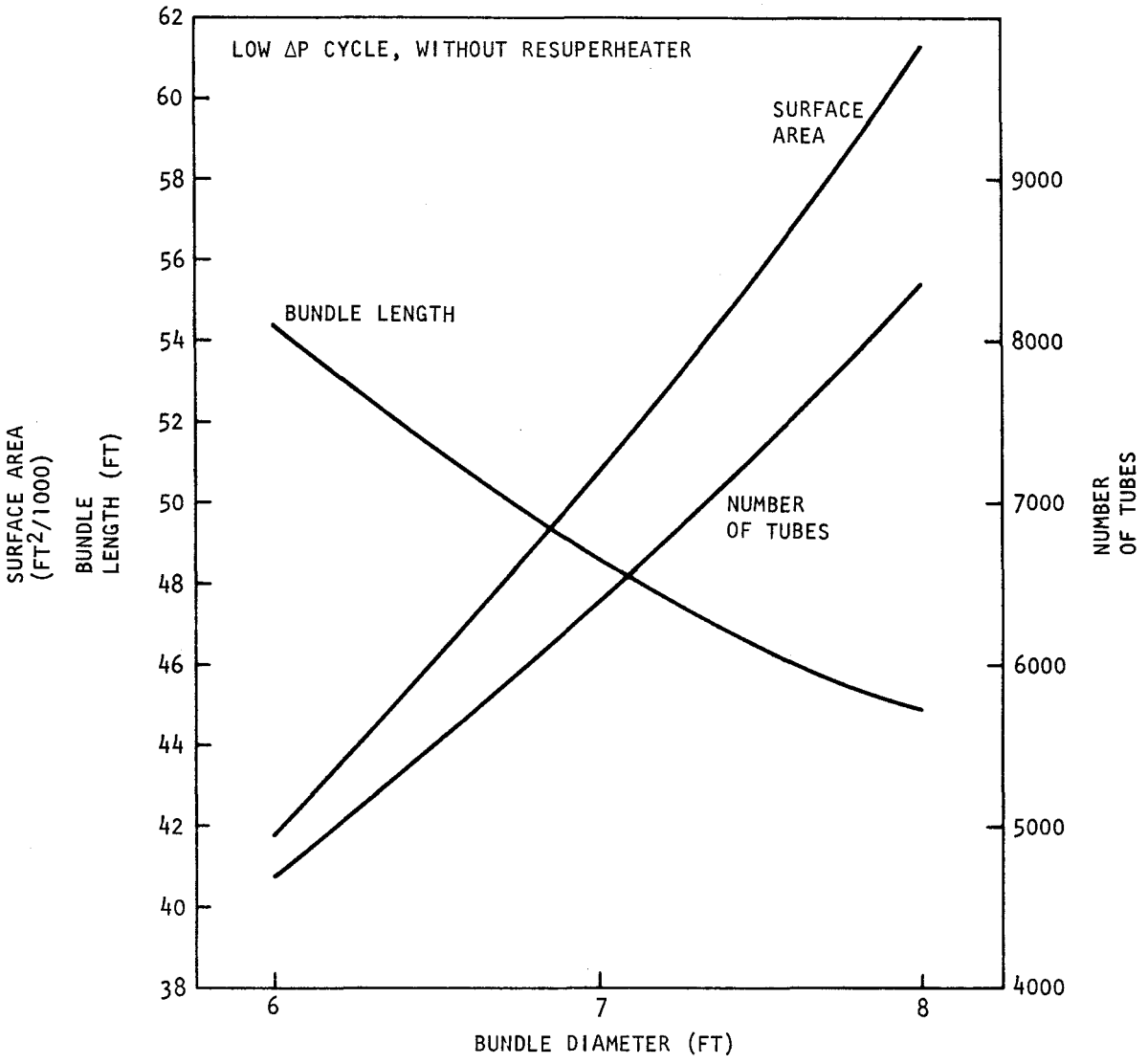

Fig. 10.8 Bundle length, surface area, and number of tubes for straight-tube steam generator

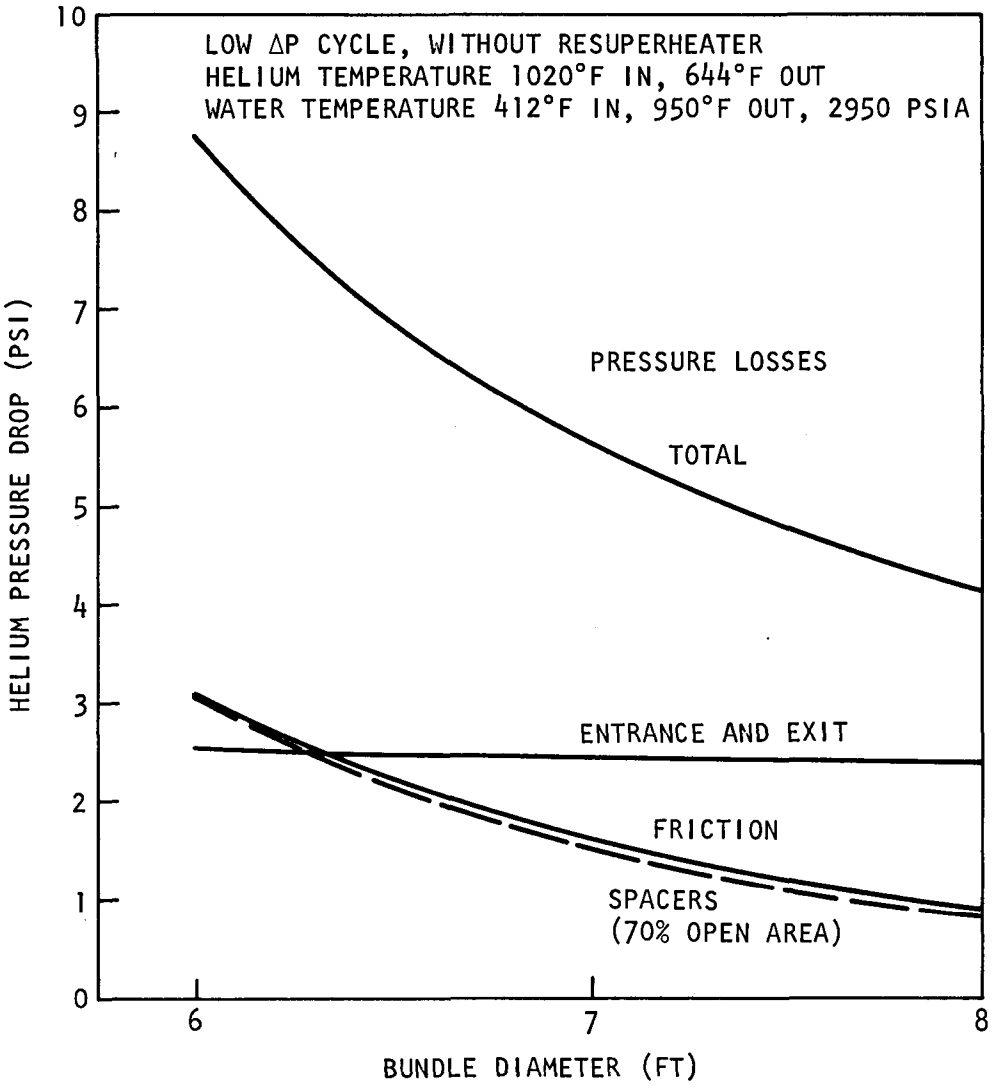

Fig. 10.9 Helium pressure drop vs bundle diameter for straight-tube steam generator

10.8. AUXILIARY CIRCULATOR, VALVE AND SERVICE SYSTEM

The primary objective of this task is to prepare and issue a CACS component development plan document. The purpose is to develop components for the CACS system to meet the reliability and safety criteria and to demonstrate the performance and reliability of critical components by testing under anticipated operating conditions.

The review and evaluation of design and development requirements for the GCFR CACS components have been completed. A first draft of the development plan for the CACS components that require development and test verifications has been written. The following components have been included:

1. Auxiliary circulator.
   a. Auxiliary circulator and service system development.
   b. Auxiliary circulator bearing lubrication and seal system.
   c. Auxiliary circulator qualification tests.
2. Auxiliary circulator electric motor and cooling system.
3. Core auxiliary heat exchanger (CAHE).
   a. CAHE gas side inlet flow distribution.
   b. CAHE corrosion/erosion tests.
4. CACS loop isolation valve.
5. Auxiliary circulator motor drive control system.

REFERENCES

1. Robinson, G. C., "Verification of the Use of Balls in Support Fixtures of 1:15 Scale Model Tests of 300 MW(e) GCFR-PCRV Closures," Oak Ridge National Laboratory Report GCR:75-20, October 1975.

2. "Gas-Cooled Fast Breeder Reactor Quarterly Progress Report for the Period August 1, 1975 through October 31, 1975," USERDA Report GA-A13766, General Atomic, January 1976.

3. "ASME Boiler and Pressure Vessel Code," Section III (ASME 111/2).

4. Soo, P., "Analysis of Structural Materials for LMFBR Coolant-Boundary Components, Materials Property Evaluations," Westinghouse Electric Report WARD-3045T3-5, November 1972.

5. Simnad, M., "Evaluation of Materials for the GCFR Radial Upper and Lower Shield," General Atomic, to be published.

6. Wrights, G. N., "Clinch River Breeder Reactor (CRBR) Shielding Considerations to Assure Structural Integrity," Trans. Am. Nucl. Soc. 22, 788-789 (1975).

7. "Clinch River Breeder Reactor Plant, Preliminary Safety Analysis Report," v. 4, Project Management Corporation, July 1975.

8. Penny, R. K., and D. L. Marriott, Design for Creep, McGraw-Hill, London, 1971.

XI. HELIUM CIRCULATOR TEST FACILITY (189a No. SU046)

The objective of this task is to develop a test facility for qualification testing of the GCFR main helium circulator. The scope of this task involves the evaluation of alternative test facility concepts in terms of technical feasibility and cost, the identification of the most promising test facility concepts, the preparation of specifications for the selected test facility concept, an architect/engineer (A/E) preliminary design study, and final design, construction, and checkout of the facility.

A draft of a topical report describing the full power (100%) circulator test facility concept and evaluation, including cost estimates, is in final review prior to publication.

The FY-76 work plan and an updated Schedule 44 for the helium circulator test facility were issued during the last quarter. Estimated costs used in the Schedule 44 were for a closed steam loop system powered by electric motor driven steam compressors.

Cost estimates for a 25% power test facility using the same system concepts as the 100% power scoping study are complete. A report is being prepared.

During the first quarter of FY-76, RRD requested an evaluation of the Rocketdyne Components Test Laboratory V (CTL-V) as a possible GCFR helium circulator test facility site (HCTF). The CTL-V site is located at the Rocketdyne Division of Rockwell International's Santa Susana field test laboratory near Canoga Park, California. The facility contains a multimotor electric drive and gear box, which has potential as a drive for the steam compressor in a closed loop helium circulator test facility. A preliminary study to investigate this application of the CTL-V facility has now been completed.

Anticipated costs for additional equipment and refurbishing of CTL-V for 100% and 25% circulator power test facilities have been assembled and compared to a completely new and independent facility located on a new and as yet undeveloped site. The cost of a 100% circulator power test facility located at CTL-V is estimated to be $22,100,000 based on May 1975 dollars. A completely new and independent facility located on a new and as yet undeveloped site is estimated at $22,900,000. Both figures include construction cost, engineering design and support, operating cost, and a 30% contingency. The CTL-V cost includes an estimated $1,000,000 Rocketdyne facility rental charge.

A 25% circulator power HCTF located at CTL-V would cost an estimated $12,700,000 compared to $13,300,000 for a new facility located on an undeveloped site. Rocketdyne's facility rental fee is included in the former cost.

A summary of this study has been prepared and is currently undergoing management review.

XII. REACTOR SAFETY (189a No. SU021)

The purpose of this task is to study the reactor safety aspects of the GCFR. Logical probabilistic methods are employed to determine the probabilities associated with various accident initiation and progression sequences and to identify potential design modifications that would help reduce risks. The thermal behavior of the fuel element duct walls under conditions of loss of shutdown heat removal is studied to determine the relative timing of duct wall melting and fuel melting. This task also includes liaison between GA and the RRD-funded GCFR Safety Task at Argonne National Laboratory (ANL).

12.1. ACCIDENT INITIATION AND PROGRESSION ANALYSIS (AIPA)

Applying the AIPA analysis techniques developed in FY-74, work is being directed toward the probabilistic analysis of potential accident sequences leading to low-probability, high-consequence sequences of events, also under study at ANL on "GCFR Safety Aspects on Fuel and Core." The principal AIPA effort is directed at the 300-MW(e) demonstration plant with scoping type analyses to be performed for larger plant sizes. The three principal accident classes under investigation are loss of flow (LOF) with shutdown, LOF with failure to shut down, and transient overpower (TOP). Work during this period has been directed at the first two accident classes, namely LOF with and without shutdown.

12.1.1. Loss of Flow with Shutdown Accidents

Emphasis in this area has been directed at identifying the means and probability of decay heat removal failure in the GCFR. Work performed previously under this subtask (as reported in Refs. 1 and 2) was complemented during this period by the calculation of the accident sequence probability error bands and by bunching all accident sequences into three

accident groups for summary purposes. For propagating the accident sequence error bands, the method employed by the Reactor Safety Study group was used with the aid of the "SAMPLE"[3] computer program for error estimation. The numerous accident sequences that lead to loss of flow with shutdown accident outcomes that were considered were then bunched into similar consequence groups. Since analyses at ANL have indicated that no key accident variable exists for LOF accidents with shutdown in terms of consequences to the primary activity barrier provided by the core, these accidents may be treated as generically similar in consequence, except in the way they may affect the secondary activity barriers, namely the PCRV and containment. This consideration leads to the assignment of three accident event groups:

1. Transients: events potentially leading to an LOF in a pressurized reactor. Secondary barriers are not impacted by these events.

2. Loss of preferred power supply: events potentially leading to an LOF in a pressurized reactor due to the unavailability of electrical power. Active containment systems are potentially impacted by these events.

3. Depressurization: events potentially leading to an LOF in a depressurized reactor. The integrity of the PCRV as an activity barrier is limited as a result of these events.

Table 12.1 summarizes the median total cooling failure probability that has been calculated for each of these event groups as well as the uncertainty factor that has been calculated about this median. The uncertainty factor has been calculated by the methods described previously and represents the statistical propagation of the initiating event and failure data ranges but does not include consideration of uncertainties in design performance. The latter has been accounted for by generally selecting conservative performance requirements.

Table 12.1 also summarizes the individual contribution of independent component failures, allowing for test and maintenance unavailability, and

Table 12.1

SUMMARY OF THE PROBABILITY OF DECAY HEAT REMOVAL FAILURE

Accident Group	Decay Heat Removal Failure Probability (per year)				
	Component Failures Only	Test and Maintenance Unavailability Only	Common Mode Failures Only	Total	Uncertainty Factor[a]
Transient events	5×10^{-9}	1×10^{-8}	3×10^{-6}	3×10^{-6}	10
Loss of preferred power supply	2×10^{-7}	1×10^{-7}	5×10^{-6}	5×10^{-6}	9
Depressurization	9×10^{-11}	4×10^{-10}	5×10^{-10}	1×10^{-9}[b]	30

[a]This is the uncertainty factor for a 90% probability interval.

[b]Dominated by depressurization occurring due to a small pipe break. The design basis depressurization accident (DBDA) leading to decay heat removal failure has a probability orders of magnitude below this.

including the potential for common mode failures employing the HTGR-AIPA beta factor approach.[1,4] For pressurized accidents, the redundancy provided by the residual heat removal (RHR) systems, particularly the core auxiliary cooling system (CACS), is high, and therefore the assumed common mode failures are very significant. For the depressurized accidents, the redundancy provided, and hence the effect of common mode failures, is not as significant.

As indicated by Table 12.1, the AIPA estimates to date show that the failure of decay heat removal in the GCFR may have a frequency of slightly less than 10^{-5} per year. Many initiating events and accident paths contribute to this assessment; however, the dominant sequences involve failures of residual heat removal by the main loops, which place moderately urgent requirements (15 minutes to 1 hour following trip) on providing CACS cooling, coupled with the common mode failure of all three CACS loops to start. A brief summary of the dominant accident sequences under each event group is given below:

1. Transient Events

   Based on estimates to date, a demand may be expected to be placed on the CACS due to transients not involving a loss of normal power supplies approximately once in a hundred years. The unavavailability of the CACS following this event has been calculated to be 3×10^{-4}, based upon a calculated loop failure of approximately 10^{-2}, of which 3% are assumed to be common mode in nature. The resulting total failure probability is thus 3×10^{-6} per year.

2. Loss of Preferred Power Supply

   Several events may lead to a loss of preferred power, including loss of offsite power (LOSP) occurring during a plant outage, LOSP occurring while the plant is at power with turbine control and trip, and turbine trip leading to network instabilities and subsequent LOSP. In all cases, approximately 30 minutes

or more is available to restore power. Failing this, main loop cooling would be lost with a total frequency of approximately 5×10^{-3} per year. The failure of the CACS following this is now dominated by common mode failure of the emergency diesels with a frequency of 10^{-3} giving a total failure probability of 5×10^{-6} per year.

3. Depressurization

Studies to date indicate that the failure of decay heat removal as a result of depressurization accidents has a frequency well below that of pressurized transients. The dominant event in this case has been identified as a small piping failure occurring with a frequency of 10^{-3} per year, resulting in a slow depressurization. The failure of main loops and CACS loops following this event is calculated as approximately 10^{-3} apiece, resulting in a total failure probability of 10^{-9} per year. All other depressurization events, including the DBDA, are much less probable since the initiating event frequency decreases more rapidly than the cooling system failure probability increases.

12.1.2. Loss of Flow Without Shutdown Accidents

During this period work has been initiated on loss of flow without shutdown accidents. The emphasis, thus far, has been to identify the most significant initiating events which lead to partial or total loss of coolant, whether operational protection system action is adequate, and the number and type of plant protection system trip signals available to prevent these events from ultimately leading to core damage. For each initiating event, where possible, an attempt was made to identify the time available for manual action if all automatic protection action fails, to identify the critical item which provides the time for manual action (e.g., steam generator water inventory in the case of loss of feed), and to estimate how fast the reactor coolant flow rate would be reduced if no protective action were taken. Identification of these events is necessary for further probabilistic work on loss of flow without shutdown accidents.

12.2. THERMAL ANALYSIS OF FUEL ELEMENT DUCT WALLS

Under the subtask "Safety Related Analytical and Experimental Studies" analyses are in progress to determine the heatup and melting of duct walls relative to the fuel during a loss of coolant flow in the shutdown reactor. Analyses from previous reporting periods have indicated that the duct wall will melt prior to any fuel melting within the element, and the time lag between duct melting and fuel melting was shown to be insensitive to large variations in the physical parameters and in the accident scenario.[1]

12.2.1. Effects of a Residual Flow and of Gamma Heating in Steel

During the current reporting period, the effects of a residual coolant flow and of gamma heating in steel structures on the duct and fuel melting sequence have been analyzed using an expanded version of the one-dimensional slab geometry code BOXRAD. A small residual coolant flow reduces the heatup rate of both the fuel and the duct wall, thereby increasing the time to melting, as shown in Fig. 12.1. Cooling of the declad fuel rods is the dominant effect, so that the time lag between duct melting and fuel melting increases with increasing flow. For flow rates in excess of about 0.2% of the normal full power flow, no fuel melting is calculated to occur; at the same time, duct melting is prevented by coolant flow rates in excess of about 0.6%. Thus, duct melting always occurs prior to fuel melting, if it occurs at all. The flow rates that are calculated to prevent fuel and duct melting are small, and in the event that molten cladding does not fully block the coolant channels by refreezing in the lower axial blanket, such low flow rates could probably be established by natural convection effects. Buoyancy forces would preferentially result in up-flow through the core elements and down-flow through the blanket elements. The heat capacities of the upper axial blanket, the grid plate, and the inlet plenum region would serve as temporary heat sinks.

Gamma heating in the cladding and duct wall reduces the time to melting of the duct wall, because the gamma heating represents an internal

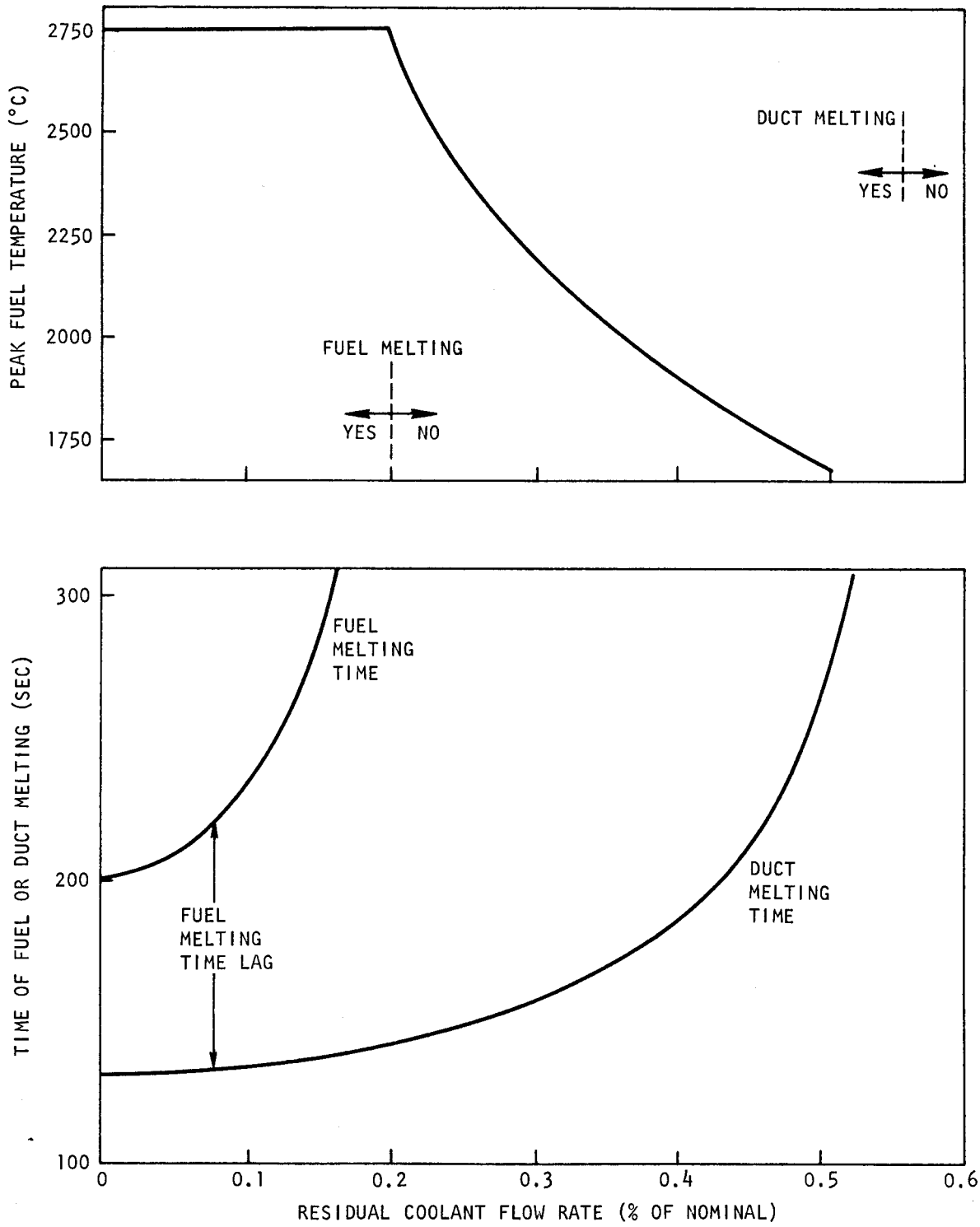

Fig. 12.1 Influence of residual coolant flow on duct and fuel melting in the central element

heat source in the duct in addition to the heat transport into the duct by conduction, radiation, and convection from the fuel rod bundle. The time to fuel melting is not influenced, and the net effect of gamma heating in steel is an increase of about 15% in the time lag between duct melting and fuel melting.

12.2.2. Detailed Rod Bundle Geometry Analyses

In parallel to these one-dimensional calculations, detailed analyses of an actual rod bundle geometry model, using the SINDA[5] code, are proceeding.[2] The emphasis of these detailed analyses is two-fold: (1) to verify the results of the simpler BOXRAD analysis and thus enhance the confidence in the results of the sensitivity study and (2) to address effects which cannot readily be analyzed with the BOXRAD model, such as the duct corner melting delay, the effect of unfueled corner support rods, and the behavior of control fuel elements. The detailed SINDA analyses for a fuel element with fueled corner rods and for an element with unfueled corner support rods have been completed during this reporting period. The results from these analyses, summarized in Table 12.2, show very good agreement with the results from BOXRAD analyses for the mid-flat region of the duct wall. Objective 1 has thus been accomplished.

For an element with fueled corner rods, the analysis shows that the duct corner melts 18 seconds after the first duct melting occurs at the mid-flat area. The duct corner still melts 59 seconds before any fuel melting occurs. For an element with unfueled corner support rods, the duct corner melting delay increases to 51 seconds because the corner support rod has to melt before the duct corner can melt. However, the duct corner still melts 29 seconds before fuel begins to melt. These analyses include the effect of gamma heating in the duct wall and in the corner support rod. If the effect of direct gamma heating is neglected, the duct corner would still melt 13 seconds before any fuel melting would commence. It is thus concluded that for a fuel element near the core center, the ducts would melt circumferentially before fuel melting would begin in either element design. The analyses of duct melting during a loss of

Table 12.2

CLADDING, DUCT, AND FUEL MELTING SEQUENCE DURING A TOTAL LOSS OF FLOW ACCIDENT IN THE SHUTDOWN REACTOR

Location	Melting Time (sec)		
	Slab Model (BOXRAD)	Rod Bundle Model (SINDA)	
	Fueled Corner Rods	Fueled Corner Rods	Unfueled Corner Rods
First cladding	35	40	40
Last cladding	---	106	111
First support rod node	---	---	135
Last support rod node	---	---	156
First duct wall node	122	121	118
Last duct wall node	---	139	169
First fuel rod	198	198	198

flow in the shutdown reactor are being concluded with an analysis of a control fuel element, and a summary report is in preparation.

12.2.3. Test Size Requirements for Duct Melting Experiments

A scoping study of test size requirements for duct melting experiments has been completed. The objective was to determine the minimum size test assembly that would allow a simulation of the phenomena that contribute to duct melting during a loss of flow accident. The slab geometry code, BOXRAD, was used to analyze the test configuration shown in Fig. 12.2, which consists of an inner duct wall, a variable number of fuel rod rows, an outer duct wall, a thermal insulation layer, and a cooled outer wall. Prototypic GCFR dimensions were used in the analysis. In order to be reasonably confident that an experiment simulates all the phenomena that contribute to duct melting, it is necessary to simulate both the heat fluxes into the duct wall and the peak fuel temperatures that would be expected in the accident situation. The results of the study indicate that an experiment with three to five rows of fuel between the inner and

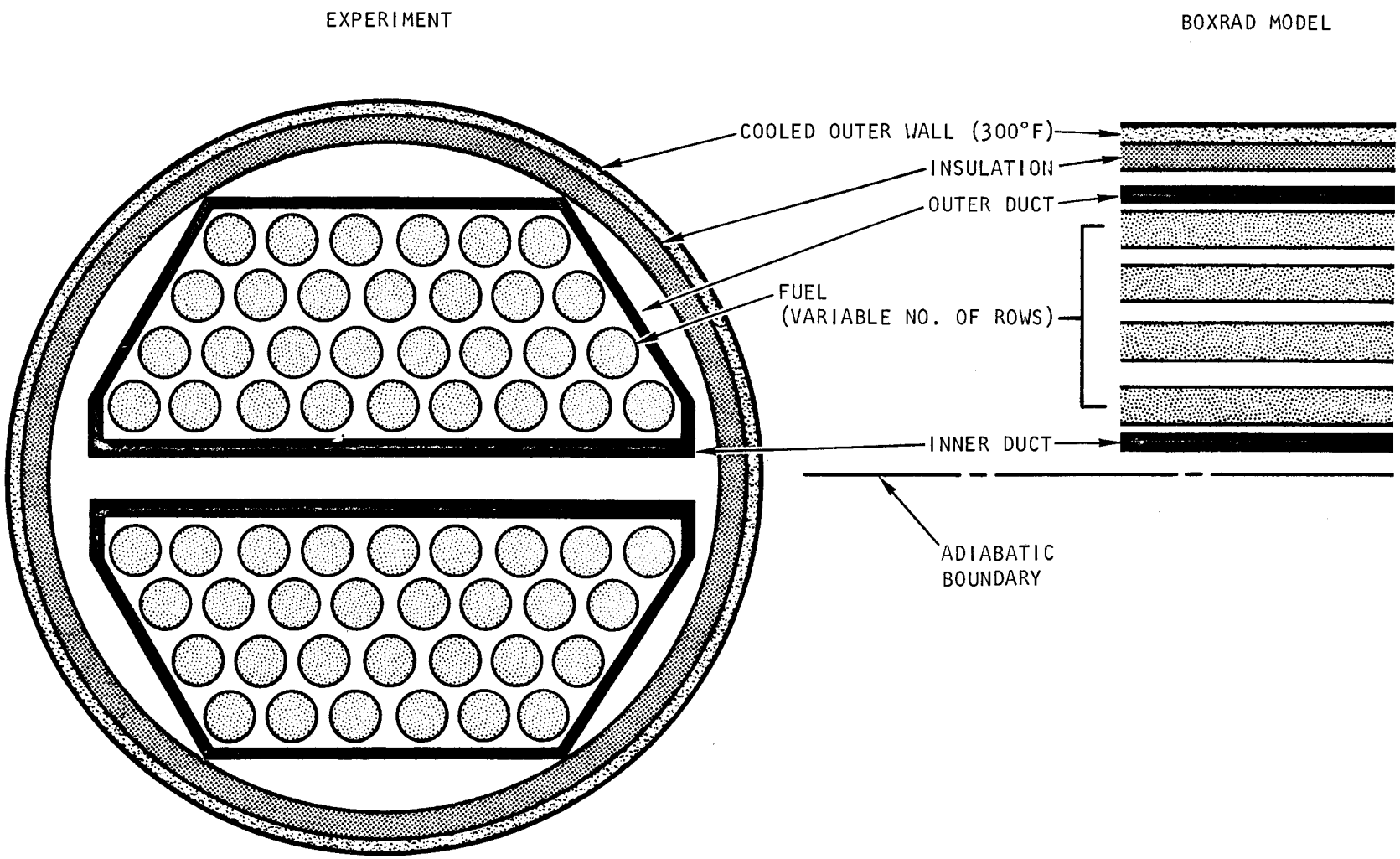

Fig. 12.2 Schematic of the experiment cross section and of the BOXRAD model

the outer duct wall could well simulate the heat flux into the inner duct wall and thus reproduce the time of duct melting. However, even under optimum assumptions for the thermal insulation, the outer duct is calculated to melt at least 15 seconds after the inner duct. This delay will most likely require a mechanical decoupling of the inner and the outer duct if duct dropping is to be simulated in such a test.

A simulation of the expected peak fuel temperatures in an experiment is more difficult. Figure 12.3 shows the peak fuel temperature at the time of inner duct melting with increasing test bundle size. Large test sizes, exceeding seven rows of fuel between the inner and the outer duct, would be necessary to approach the expected accident fuel temperatures. The test fuel temperature can, however, be effectively increased by test power-density optimization. As indicated, an experiment with five rows of fuel can approach the desired peak fuel temperature if the test power is held constant at the initial value of 6% of full power instead of decreasing the test power according to the fission product decay heat. However, in such a test, the heat fluxes into the duct wall would be larger than desired.

The results of this study indicate that it may be possible to devise in-pile tests in near-term facilities to simulate the important phenomena involved in melting duct walls at decay heat levels. Additional analyses will be necessary to confirm this preliminary conclusion, but it seems evident that not all the phenomena can be reproduced in one single test. This may, however, be acceptable for the purpose of verifying analytical predictions of duct melting times and circumferential incoherence of duct melting.

It is important, however, to recognize that the usefulness of an experimental program to investigate duct melting phenomena will be enhanced if it also leads to a definition of the conditions that are necessary for the dropping of GCFR fuel elements after the duct wall has melted. This is a difficult task, because it requires the definition of interference patterns among fuel elements with fully and partly melted duct walls and

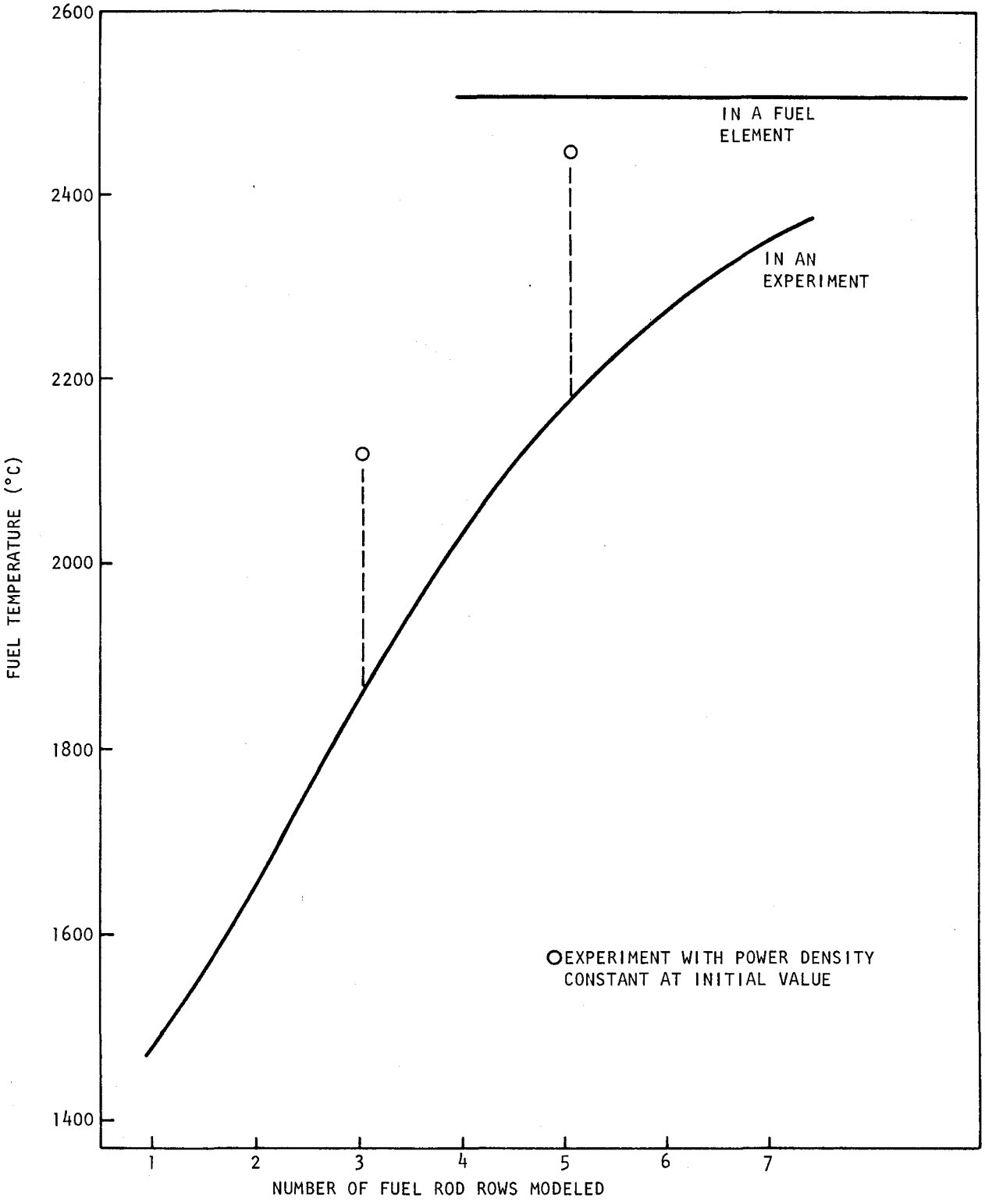

Fig. 12.3 Maximum fuel temperature at the time of inner duct melting vs number of fuel rows modeled

detailed test design considerations to reproduce these interference effects during an experiment. The incentive for clarifying these criteria for duct dropping is to allow a mechanistic description of the accident progression and thus reduce the need to consider unduly conservative assumptions regarding the coherence of fuel relocation.

12.3. SAFETY RESEARCH AND DEVELOPMENT LIAISON

The two General Atomic members of the GCFR Safety Program Review Committee attended the GSPRC meeting in Denver on December 10-11. General Atomic's written comments on both the October 31, 1975 GCFR Safety Program Summary document and on the GSPRC Charter were distributed to the other committee members. A list of the safety information needs was prepared at the meeting and the suitability of several existing and proposed test facilities for providing the information was discussed.

REFERENCES

1. "GCFR Reactor Safety Progress Report for the Period July 1, 1974 through June 30, 1975," USERDA Report GA-A13703, General Atomic, December 1975.

2. "Gas-Cooled Fast Breeder Reactor Quarterly Progress Report for the Period August 1, 1975 through October 31, 1975," USERDA Report GA-A13766, General Atomic, January 1976.

3. "Reactor Safety Study - An Assessment of Accident Risks in U.S. Commercial Nuclear Power Plants," (Draft) v.1, USAEC Report WASH-1400, August 1974, App. II.

4. "HTGR Accident Initiation and Progression Analysis Status Report," v. II, USERDA Report GA-A13617, General Atomic, October 1975.

5. Smith, J. P., "SINDA Users Manual," TRW Systems Group Report 14690-Hool-RO-00, April 1971.

XIII. IN-PILE SAFETY TEST PROGRAM-GRIST (189a No. SU015)

13.1. INTRODUCTION

The Gas Reactor In-Pile Safety Test (GRIST) program is being evaluated by ERDA-RRD, Argonne National Laboratory (ANL), Aerojet Nuclear Company (ANC), and General Atomic (GA) as a potential follow-on to analytical and experimental programs being conducted under the LMFBR and GCFR programs. Important data for the design basis of the GCFR demonstration plant would be provided by in-pile endurance testing of the 12-rod GCFR test assemblies in the BR-2 in Mol, Belgium, and by out-of-pile tests with the core flow test loop (CFTL) described in Section IV. The objective of the GRIST program is to go beyond the design basis accidents and, in particular, to investigate the behavior of melted cladding and fuel. However, testing of GCFR type fuel assemblies in the GRIST program may include less severe transients of core power, coolant flow, and coolant pressure in order to investigate the effects of upset, emergency, and faulted conditions on the performance of fuel assemblies for gas-cooled fast breeder reactors. These tests would provide information that is projected to be of importance for improving the performance of commercial GCFR plants.

The studies were initiated in FY-74 and included (1) a comprehensive review of potential program objectives, (2) design trade-off studies, (3) schedule and cost estimates for the in-pile loop facility to be installed in the Engineering Test Reactor at Idaho National Engineering Laboratory (INEL), and (4) a conceptual design study for a reference test bundle.

During this quarterly period, efforts were devoted to a preliminary scoping analysis of test space requirements for duct wall melting tests employing multisection test assemblies. The test assemblies being considered would be designed to prototypically simulate transient temperature

behavior of the duct wall during severe temperature transients involving duct wall melting.

13.2. SCOPING ANALYSIS OF TEST SPACE REQUIREMENTS FOR DUCT WALL MELTING TESTS

Duct wall melting tests have been considered to experimentally verify and demonstrate that during severe operational accidents (LOF, LOC) involving melting of cladding, flow ducts, and fuel, the GCFR fuel assembly will drop out of the core prior to gross fuel melting. Several stringent requirements have to be imposed on duct wall melting and assembly dropping tests:

1. A test assembly has to consist of several sections, each representative of a partial section of a GCFR fuel assembly.

2. Each section has to include a large enough number of rods to provide good simulation of transient duct wall temperatures.

3. For complete demonstration of element dropping, circumferential duct wall melting has to be achieved and nonprototypical refreezing of molten material has to be eliminated.

Because of limited test space and power provided by any test reactor, the full dropping test cannot be conducted in-pile. However, it was concluded that partial tests can be performed which would demonstrate and verify certain aspects of the dropping hypothesis. Phenomena that may be separately tested are, for example, the melt-through rate and melting progression of (1) the flat sections of the flow duct and (2) the corner sections behind the unfueled spacer support rods. The results from these tests may be employed to check calculational methods and analytical approaches to the dropping phenomenon. It must be remembered, however, that the final demonstration of dropping still has to be experimentally done to ensure that cocking of the assembly and refreezing of molten material does not prevent the assembly from dropping out of the core.

A scoping study was proposed to look into test space requirements of duct wall melting tests using multisection test assemblies. The scoping analysis was conducted using the BOXRAD code. BOXRAD is a GA-developed thermal analysis code applying heat transfer by radiation to multilayer slab geometries. In spite of the significant geometric simplification, the code shows excellent agreement with other, more sophisticated analytical tools as long as the fuel rod configuration to be analyzed represents a symmetric geometry. Irregular configurations, such as those represented by the corner rods of fuel assemblies, cannot be analyzed with BOXRAD. Thus, additional analyses which would focus on thermal analyses of fuel assembly corners using the SINDA code have been proposed to ERDA.

The preliminary BOXRAD calculations are described in Section 12.2. Because of the code limitations, the calculations focused on thermal analyses of the flat sections of the duct wall. The results indicate that five rows of fuel rods are needed on either side of two adjacent duct walls to achieve a good representation of the real heat flux into the duct walls during a loss of coolant flow test. It has to be emphasized that this requirement does not account for unfueled rods needed for spacer support.

13.3. PRELIMINARY DESIGN CONSIDERATIONS AND TEST SPACE REQUIREMENTS FOR MULTISECTION TEST ASSEMBLIES

Preliminary design considerations and minimum test space requirements have been developed using the BOXRAD results. For melting tests with duct wall flats, double-section test assemblies which provide large sections of adjacent flat duct walls (Fig. 13.1) are envisioned. The minimum test space requirement can be deduced from a configuration which provides about six fueled rods along the duct walls and about five rows of rods on either side of the flat duct walls to be tested. The effect of the unfueled corner tie rods has not yet been analyzed.

As shown in Table 13.1, the minimum test space requirement of double-section test assemblies corresponds to that of a 127-rod test assembly with the basic hexagon configuration and thus would require a net in-pile

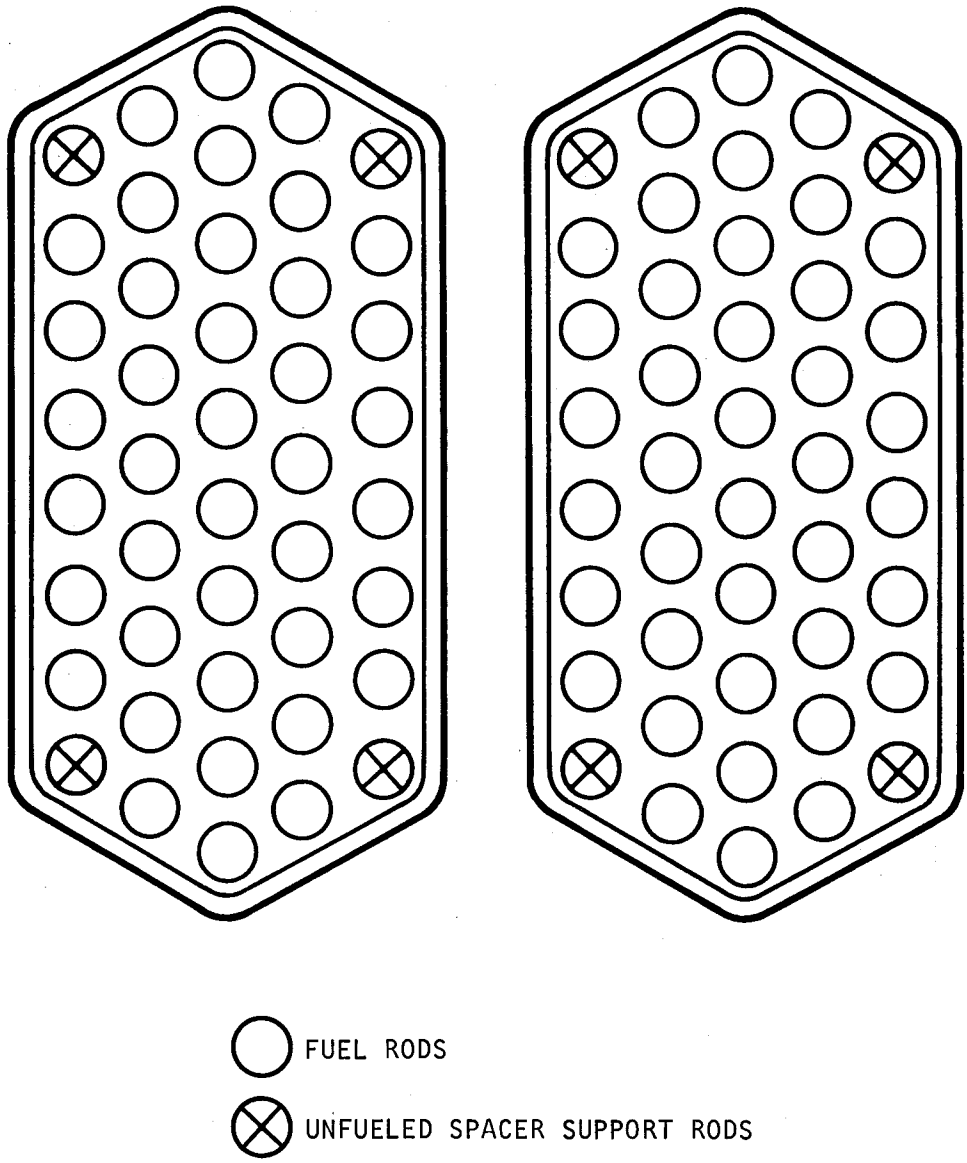

Fig. 13.1 Preliminary cross section of double-section test assembly

Table 13.1

TEST SPACE REQUIREMENTS[a]

Number of Rods in Basic Fuel Assembly Configuration	Test Diameter Including Attemperation Flow and Insulation (mm)			Triple-Section Test Assembly			Double-Section Test Assembly			Control Assembly	
	100%	90%	80%	Rows	Arrangement	Rods	Rows	Arrangement	Rods	Rows	Rods
37	111.4	100.3	89.1	3			2			--	
61	133.0	119.7	106.4	4			3			1	
91	154.6	139.1	123.7	5	5 x 5	75	4			2	
127	176.2	158.6	141.0	6	6 x 6	108	5	2 x 44	88	3	90
169	197.8	178.0	158.2	7	7 x 7	147	6	2 x 59	118	4	132
217	219.4	197.5	175.5							5	180
271	241.0	216.9	192.8							6	234

[a]Design assumptions: fuel rod pitch = 10.8 mm; space for insulation and attemperation flow = 25 mm on the diameter.

tube diameter of 176.2 mm. If further analyses of the effect of unfueled corner rods results in the requirement of an additional row of fueled rods, the test space requirement would be raised to 197.8 mm for the test tube inner diameter. Scaling of the test size by 10% and 20% would reduce the test space requirement to 178 mm and 158.2 mm, respectively. The effect of scaling on thermal test conditions and transient simulation has not yet been investigated.

For melting tests with duct wall corners, triple-section test assemblies (Fig. 13.2) are envisioned. The minimum test space requirement can be deduced from a test assembly consisting of a total of 108 rods. Again, this test assembly would fulfill test requirements based on BOXRAD calculations which neglect the unfueled rods. Investigation of the effect of unfueled rods may raise the minimum space requirement to that of configurations with a total of 147 rods. As shown in Table 13.1, triple-section test assemblies with 108 and 147 rods would require test tubes with 176.2- and 197.8-mm inner diameters, respectively.

The third test assembly listed in Table 13.1 represents control assemblies with an inner duct around the control rod. Melting tests for this inner duct would require about five rows of rods (a total of 180 rods) around the duct, which would result in a test tube diameter of 219.4 mm. If the test control assembly were scaled down by 20%, the tube diameter could be reduced to 175.5 mm.

ANC has been requested to look into the net in-pile tube diameter at a 228.6 by 228.6 mm test position in ETR and the test reactor power supply situation if more than 100 fuel rods are included in the test assemblies. ANC reported that the net test diameter may range from 175 to 185 mm and a uniform power distribution may be achieved in a 100-rod test assembly if the power density is kept at about 30% to 40% of GCFR power density at full load. For comparison, the power requirements of LOC and LOF accidents correspond to about 6% of GCFR full-load power density.

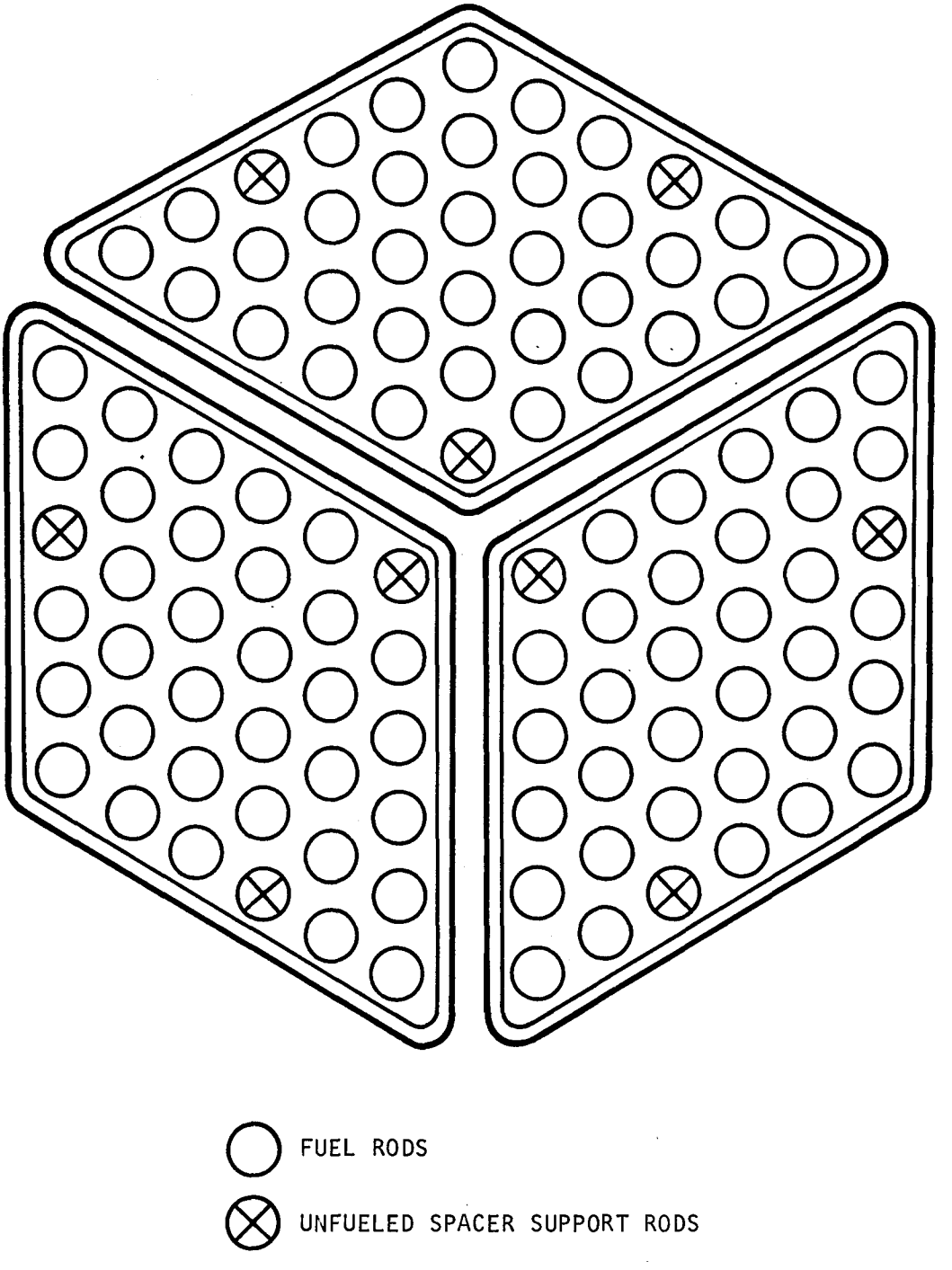

Fig. 13.2 Preliminary cross section of triple-section test assembly

The above results indicate that multisection test assemblies may be feasible and selected aspects of duct wall melting and dropping phenomena may be tested in-pile in the ETR. To confirm these findings, additional analyses using a more detailed and accurately simulating computer code (SINDA) and further conceptual design work for multisection test assemblies have been proposed.